The Impact and Durability Performance of Adhesively-Bonded Metal Joints

By

Ambrose Cornelis Taylor

Department of Mechanical Engineering,
Imperial College of Science, Technology & Medicine,
Exhibition Road, London SW7 2BX.

A thesis submitted for the Degree of Doctor of Philosophy of the University of London and for the Diploma of Imperial College

June 1997



Abstract

In recent years there has been an increasing use of adhesives in industry as manufacturers have become aware of the advantages that adhesives can offer over conventional joining techniques. However, the mechanical properties of an adhesive joint can decrease considerably under impact conditions, or with exposure to water and cyclic fatigue loads. The present work discusses the effect of these important factors on the fracture behaviour of adhesive joints.

Fracture mechanics is an established technique to analyse the behaviour of adhesive joints, and allows the propagation of flaws to be expressed mathematically. A fracture mechanics approach was therefore used to characterise the fracture behaviour of adhesively-bonded aluminium-alloy and steel joints. The adherends were prepared using a gritblast and degrease, or a chromic-acid etch, surface treatment. A range of structural epoxy adhesives were used.

Three-point bend and tapered double-cantilever beam tests were used to determine the reduction in adhesive fracture energy, G_c, with increasing test rate for bulk adhesive and adhesive joint specimens. Reductions of between 8 and 36 % were noted for rates of between 10^{-5} and 1 m/s. These fracture mechanics results were compared to the results measured using an impact wedge-peel test method, where there is a significant amount of plastic deformation of the adherends. However, a correlation between the measured cleavage force (from the impact wedge-peel test) and the adhesive fracture energy, G_c, was identified. Further, the behaviour of the impact wedge-peel test could be quantitatively modelled using a finite element analysis method, coupled with a knowledge of the value of G_c for the adhesive.

A fracture mechanics approach was also used to determine the relationship between the rate of crack growth and the maximum applied fracture energy, G_{max}, under cyclic fatigue loading. These tests were conducted at room temperature in 55 % relative humidity or with the specimen immersed in distilled water at 28°C. The data indicated a threshold value of G_{max}, below which crack growth did not occur. This value was unique for each combination of test conditions, and was far lower than the fracture energy, G_c, at a constant (slow) displacement rate. These data were used to predict theoretically the lifetime of single lap joints, using an analytical and a finite element method. The predictions were found to give good agreement with the experimental data. Finally, the mechanisms of water attack have been identified from using various surface analytical techniques.

To B.E. Taylor

Acknowledgements

This work was funded by the Department of Trade and Industry as part of the Measurements, Technology & Standards programme on the performance of adhesive joints. Additional funding came from the Engineering and Physical Sciences Research Council.

I would like to thank my supervisor Tony Kinloch for his advice throughout.

I would express my gratitude to my colleagues at Imperial College, especially Bamber Blackman, Jag Jethwa, Matthew Little and Hugh MacGillivray, plus Yu Wang and Andy Curley for their help with the finite element analysis. I would also like to thank Pat Pathak, Tom Robinson, Peter Savage, Nick Tailor and Glenn Wallington for their assistance with the test equipment. For his help with the thermography work, thanks go to Gero Farruggio.

I would also like to acknowledge the support and assistance of Roger Davis and Paul Fay at Ford UK, Geoff Eckold, John McCarthy and Tony Sampson at AEA Technology, and Gary Critchlow at Loughborough University. Thanks are also due to Ciba Polymers, Permabond and Hysol Dexter for the supply of materials.

Special thanks go to my family and friends for their encouragement and support throughout.

Contents

Abstract i

Dedication ii

Acknowledgements iii

Table of Contents iv

Nomenclature xiii
English Alphabet xiii
Greek Alphabet xv
Abbreviations xv

1 Introduction 1

2 Literature Review 3
2.1 Introduction 3
2.2 Interfacial Contact: Surface Energy and Wetting 3
2.3 Mechanisms of Adhesion 4
2.3.1 Introduction 4
2.3.2 Mechanical Interlocking 5
2.3.3 Diffusion Theory 5
2.3.4 Electronic Theory 5
2.3.5 Adsorption Theory 6
2.4 The Role of Surfaces 6
2.4.1 Introduction 6
2.4.2 Surface Modification 6
2.4.3 Surface Treatments 7
2.5 Adhesives 7
2.5.1 Introduction 7
2.5.2 Adhesive Types 7
2.5.3 Toughening 8
2.5.4 Energy Absorbing Mechanisms 8
2.5.4.1 Rubbery Particle Toughening 8
2.5.4.2 Rigid Particle Toughening 9
2.6 Fracture Mechanics 10
2.6.1 Introduction 10

2.6.2 Failure Modes 11
2.6.3 Fracture Energy 11
2.6.4 Stress Intensity Factor 13
2.6.5 Specimen Width 14
2.6.6 Plastic Zone Size 15
2.7 Impact Tests for Adhesive Joints 16
2.7.1 Introduction 16
2.7.2 Effect of Test Rate 16
2.7.2.1 Polymer Properties 16
2.7.2.2 Dynamic Effects 17
2.7.3 Non-Fracture Mechanics Test Methods 18
2.7.3.1 Block Shear Test 18
2.7.3.2 Impact Wedge-Peel Test 19
2.7.3.3 Lap Joints 19
2.7.4 Fracture Mechanics Test Methods 20
2.7.4.1 Introduction 20
2.7.4.2 Three-Point Bend Test 20
2.7.4.3 Compact Tension Test 22
2.7.4.4 Double-Cantilever Beam Test 23
2.7.4.5 Tapered Double-Cantilever Beam Test 24
2.8 Environmental Attack of Adhesive Joints 25
2.8.1 Introduction 25
2.8.2 Mechanisms of Attack 26
2.8.2.1 Introduction 26
2.8.2.2 Interfacial Attack by Water 27
2.8.2.3 Interfacial Attack: Thermodynamic Considerations 28
2.8.2.4 Oxide Attack by Water 29
2.8.2.5 Bulk Adhesive Attack by Water 30
2.8.3 Kinetics of Attack 31
2.8.3.1 Introduction 31
2.8.3.2 Bulk Diffusion 31
2.8.3.3 Interfacial Diffusion 33
2.9 Durability Test Methods 33
2.9.1 Introduction 33
2.9.2 'Boeing' Wedge Test 33
2.9.3 Lap Joints 35
2.9.3.1 Introduction 35
2.9.3.2 Residual Strength 35
2.9.3.3 Constant Stress 35

2.9.3.4 Cyclic Fatigue of Lap Joints 36
2.9.4 Fracture Mechanics Tests: Cyclic Fatigue 36
2.9.5 Other Methods 37
2.9.6 Fatigue Crack Propagation 38
2.10 Conclusions 38

3 Materials 40
3.1 Introduction 40
3.2 Adhesives 40
3.3 Adherends 42
3.4 Surface Treatments 44
3.4.1 Introduction 44
3.4.2 'As Received' Material 44
3.4.3 Gritblast & Degrease Treatment 46
3.4.4 Chromic-Acid Etch Treatment 48
3.5 Adhesive Application 50
3.5.1 Single-Part Epoxy 50
3.5.2 Two-Part Epoxy 51
3.6 Conclusions 51

Part 1: Impact Performance - Results and Discussion

4 Tapered Double-Cantilever Beam Tests 52
4.1 Introduction 52
4.2 Experimental Procedure 52
4.2.1 Specimen Manufacture 52
4.2.2 Low Rate Tests 53
4.2.3 High Rate Tests 53
4.2.4 High-Speed Photography 54
4.3 Methods of Analysis 57
4.3.1 Introduction 57
4.3.2 General Analysis 57
4.3.3 Force Method 58
4.3.4 Force/Displacement Method 59
4.3.5 Dynamic Effects 59
4.3.6 Displacement Method 61
4.3.7 Constant Crack Velocity Analysis 61
4.3.8 Analysis of Stick/Slip Crack Propagation 62

4.3.9 Comparison of Analysis Methods 62
4.4 Results 64
4.4.1 Introduction 64
4.4.2 Variation of Fracture Energy with Crack Length 64
4.4.3 Variation of Fracture Energy with Test Rate 65
4.4.4 Fractography 65
4.5 Conclusions 73

5 Three-Point Bend Tests 74
5.1 Introduction 74
5.2 Experimental Procedure 74
5.2.1 Introduction 74
5.2.2 Specimen Manufacture 75
5.2.2.1 Bulk Specimens 75
5.2.2.2 Joint Specimens 75
5.2.3 Pendulum Machine Tests 79
5.2.4 High-Speed Servo-Hydraulic Machine (HSSHM) Tests 81
5.3 Analysis 81
5.4 Dynamic Effects 82
5.4.1 Introduction 82
5.4.2 Mass/Spring Model of Dynamic Effects 84
5.4.3 ESIS Protocol Method for 'Allowable' Dynamic Effects 88
5.5 Results 90
5.5.1 Introduction 90
5.5.2 Bulk Specimen Results 91
5.5.3 Joint Specimen Results 94
5.5.4 Comparison of Bulk and Joint Specimen Results 94
5.5.5 Kinetic Energy Correction 97
5.5.6 Fractography 98
5.5.7 Comparison with TDCB Results 101
5.6 Conclusions 103

6 Impact Wedge-Peel Tests 104
6.1 Introduction 104
6.2 Discussion of Published Work 104
6.3 Experimental Procedure 107
6.3.1 Specimen Manufacture 107
6.3.2 High Rate Testing 107
6.3.3 High Speed Photography 113

6.4 Thermography 114
6.5 Analysis of the IWP Test Data 118
6.5.1 Introduction 118
6.5.2 Types of Crack Growth in the IWP Specimen 119
6.5.2.1 Stable Crack Growth 119
6.5.2.2 Unstable Crack Growth 119
6.5.3 Methods of Analysis 121
6.5.3.1 The ISO Standard Method 121
6.5.3.2 Criticisms of the ISO Standard Method 121
6.5.3.3 Other Methods of Analysis 123
6.5.3.4 Effect of IWP Specimen Geometry 124
6.5.3.5 Analysing Unstable Failure 127
6.5.3.6 Preferred Method of Analysis 127
6.6 Correlation of IWP Results and Adhesive Fracture Energies 127
6.6.1 Introduction 127
6.6.2 High Rate Tests 128
6.6.3 Effect of Adherend Material 129
6.6.4 Effect of Test Temperature 130
6.6.5 Effect of Test Rate 133
6.7 Finite Element Modelling 135
6.7.1 Modelling the IWP Test 135
6.7.2 Universal Crack Closure Method 137
6.7.3 Effect of Friction 137
6.7.4 Comparison of Predictions and Experimental Results 138
6.7.5 Effect of Adherends 140
6.7.6 Conclusions from the Modelling Work 140
6.8 Conclusions 141

7 Impact Performance: Summary 143
7.1 Introduction 143
7.2 Fracture Mechanics Tests 143
7.2.1 Tapered Double-Cantilever Beam (TDCB) Tests 143
7.2.2 Three-Point Bend (TPB) Tests 144
7.2.3 Comparison of Test Methods 144
7.3 Impact Wedge-Peel Tests 145
7.4 Correlations Between IWP Cleavage-Force and Adhesive Fracture Energy 145
7.5 Modelling the Behaviour of the Impact Wedge-Peel Test 145
7.6 Concluding Remarks 146

Part 2: Durability Performance - Results and Discussion

8 Durability of Adhesive Joints: A Fracture Mechanics Approach..... 147
8.1 Introduction..... 147
8.2 Experimental Procedure..... 148
8.3 Crack Length Measurement Using Crack Propagation Gauges..... 149
8.3.1 Introduction..... 149
8.3.2 Gauge Application..... 150
8.3.3 Experimental Procedure..... 151
8.3.4 Comparison of Potential Drop and Optical Methods..... 151
8.4 Analysis..... 152
8.5 Results - Constant Displacement Rate Tests..... 155
8.5.1 Introduction..... 155
8.5.2 'AV119' Adhesive..... 156
8.5.3 'LMD1142' Adhesive..... 158
8.6 Results - Fatigue Tests..... 158
8.6.1 Introduction..... 158
8.6.2 Diffusion of Water into Adhesive Joints..... 159
8.6.3 'AV119' Adhesive Fatigue Test Results..... 160
8.6.3.1 Chromic-Acid Etched Aluminium-Alloy..... 160
8.6.3.2 Gritblasted & Degreased Aluminium-Alloy..... 168
8.6.3.3 Steel..... 173
8.6.3.4 'AV119' Fatigue Data Summary..... 179
8.6.4 'LMD1142' Adhesive Fatigue Test Results..... 181
8.6.4.1 Chromic-Acid Etched Aluminium-Alloy..... 181
8.6.5 Load Control Tests..... 187
8.6.6 Discussion..... 189
8.7 Conclusions..... 192

9 Lifetime Prediction of Bonded Joints and Components..... 195
9.1 Introduction..... 195
9.2 Bonded Joints..... 195
9.2.1 Introduction..... 195
9.2.2 Experimental Procedure..... 196
9.2.2.1 Specimen Manufacture..... 196
9.2.2.2 Constant Displacement Rate Tests..... 196
9.2.2.3 Fatigue Tests..... 197
9.2.3 Experimental Results..... 198

9.2.3.1 Constant Displacement Rate Tests 198
9.2.3.2 Fatigue Tests 202
9.2.3.3 Summary of Experimental Results 206
9.2.4 Crack Detection Using a Backface Strain Technique 209
9.2.4.1 Introduction 209
9.2.4.2 Experimental Procedure 210
9.2.4.3 Backface Strain Results 211
9.2.5 Lifetime Prediction Modelling 214
9.2.5.1 Introduction 214
9.2.5.2 Analytical Approach 214
9.2.5.3 Finite Element Approach 218
9.2.5.4 Modelling the Fracture Mechanics Durability Data 223
9.2.6 Comparison of Theoretical Predictions and Experimental Results 225
9.2.7 Effect of Boundary Conditions on Predicted Lifetimes 226
9.2.7.1 Introduction 226
9.2.7.2 Effect of Initial Flaw Size 226
9.2.7.3 Effect of Modified Paris Law Parameters n_1 & n_2.. 228
9.2.7.4 Effect of Single Crack or Interfacial Failure 231
9.2.7.5 Dominant Mode of Failure 234
9.2.8 Lap Joint Summary 236
9.3 Bonded Components 238
9.3.1 Introduction 238
9.3.2 Experimental Procedure and Results 238
9.3.2.1 Specimen Manufacture 238
9.3.2.2 Constant Displacement Rate Tests 240
9.3.2.3 Fatigue Tests 243
9.3.3 Lifetime Prediction Modelling 248
9.3.3.1 Finite Element Modelling 248
9.3.3.2 Modelling the Fracture Mechanics Data 250
9.3.4 Comparison of Predictions and Experimental Results 251
9.3.5 Component Summary 252
9.4 Conclusions 253

10 Durability Performance: Summary 255
10.1 Introduction 255
10.2 Fracture Mechanics Tests 255
10.2.1 Constant Displacement Rate Tests 255
10.2.2 'Dry' Fatigue Tests 257

10.2.3 'Wet' Fatigue Tests 257
10.3 Predicting the Lifetime of Bonded Joints 258
10.3.1 Introduction 258
10.3.2 Crack Mechanics 258
10.3.3 Lap Joints 259
10.3.4 Component 259

11 Conclusions 260
11.1 Introduction 260
11.2 Impact Performance 260
11.2.1 Introduction 260
11.2.2 Tapered Double-Cantilever Beam Tests 261
11.2.3 Three-Point Bend Tests 261
11.2.4 Comparison of Test Methods 261
11.2.5 Impact Wedge-Peel Tests 262
11.3 Durability Performance 263
11.3.1 Introduction 263
11.3.2 Fracture Mechanics Fatigue Tests 263
11.3.3 Bonded Single Lap Joints 264
11.3.4 Bonded Component 265
11.4 Concluding Remarks 265

12 Recommendations for Future Work 267
12.1 Introduction 267
12.2 Impact Wedge-Peel Tests 267
12.3 Fracture Mechanics Durability Tests 268
12.4 Crack Mechanics 269
12.5 Lifetime Prediction Modelling 269

References 271

Appendices 281
Appendix 1 Material Properties for FE Modelling 281
Appendix 2 TDCB Impact Tests, Example Results 284
Appendix 3 Three Point Bend Tests, ϕ Values and Example Results 285
Appendix 4 Confidence Limits for Linear Regression 287
Appendix 5 Impact Wedge-Peel Tests, Example Results 290
Appendix 6 TDCB Durability Tests, Example Results 291

Appendix 7	Bonded Lap Joint Test Results.....	293
Appendix 8	Bonded Component Tests, Example Results.....	296
Appendix 9	Publications.....	298

Nomenclature

English Alphabet

A	Area
A_f	Modified Paris Law Coefficient
a	Crack Length
a_o	Griffith Flaw Size
a_f	Crack Length at Final Failure
$\dot{a}$	Crack Velocity
b	Width
C	Compliance
C	Concentration of Water
C	Intercept
c	Half Overlap Length
c	Wave Speed
D	Diffusion Coefficient
D	Modified Paris Law Coefficient
d	Depth
E	Young's Modulus
E_a	Young's Modulus of Adhesive
E_s	Young's Modulus of Adherend
e	Stiffness
F	DCB Large Displacement Correction
f	Gradient
G	Fracture Energy, Strain Energy Release Rate
G_c	Fracture Energy (Constant Displacement Rate)
G_{max}	Maximum Fracture Energy
G_{min}	Minimum Fracture Energy
G_{th}	Threshold Fracture Energy
H_v	Hardness (Vickers)
h	Adherend Thickness
K	Bending Moment Factor
K	Stress Intensity Factor
K_c	Critical Stress Intensity Factor
k	Intercept
k	Spring Stiffness

l	Half Thickness
l_p	Dugdale Plastic Zone Length
M	Gradient
M	Mass
M_e	Bending Moment
m	Mass
m_b	TDCB Geometry Factor
N	Number of Cycles
N_f	Number of Cycles to Failure
n	Modified Paris Law Exponent
n_1	Threshold Region Curve Fitting Constant
n_2	Fast Fracture Region Curve Fitting Constant
P	Force
P_c	Critical Force
P_{max}	Maximum Force in Fatigue Cycle
P'	Dimensionless Force
p	Power Law Coefficient
Q	Geometry Factor
q	Modified Paris Law Exponent
r	Polar Coordinate
r	Power Law Exponent
r_p	Irwin Plastic Zone Radius
T	Load per Unit Width
T	Temperature
T_g	Glass Transition Temperature
t	Time
t_a	Adhesive Layer Thickness
t_f	Time to Failure
U	Energy
U_c	Energy Absorbed in Test
U_e	Strain Energy
u	Displacement
$\dot{u}$	Velocity
v	Striker Velocity
W_A	Work of Adhesion in Air
W_{AL}	Work of Adhesion in Liquid
W_d	Work Done
X	Bending Stiffness
x	Distance

z	Height

Greek Alphabet

α	Confidence Interval
α	Ratio of Spring Stiffnesses
β	Element Width
γ	Surface Energy
δ	Displacement
$\dot{\delta}$	Velocity
ε	Coefficient of Restitution
ε	Strain
ε_p	Plastic Strain
ε_y	Yield Strain
θ	Polar Coordinate
μ	Coefficient of Friction
ρ	Density
σ	Stress
σ_a	Tensile Strength of Adhesive
σ_p	Plastic Stress
σ_y	Yield Stress
τ	Shear Stress
υ	Poisson's Ratio
ϕ	Geometry Factor for Three Point Bend Test
χ	DCB Shear Correction Factor
ω	Natural Frequency

Abbreviations

AES	Auger Electron Spectroscopy
ASTM	American Society for Testing and Materials
BS	British Standard
CAE	Chromic-Acid Etch
CFRP	Carbon-Fibre Reinforced Plastic
DCB	Double-Cantilever Beam
DSC	Differential Scanning Calorimetry
ESIS	European Structural Integrity Society
FCP	Fatigue Crack Propagation
FE	Finite Element

FEA	Finite Element Analysis
GB&DG	Gritblasted and Degreased
HSSHM	High-Speed Servo-Hydraulic Machine
ISO	International Standards Organisation
IWP	Impact Wedge-Peel
LEFM	Linear-Elastic Fracture-Mechanics
LMD	Lost Motion Device
LVDT	Linear Variable Displacement Transducer
MTS	Measurement, Technology and Standards Adhesives Programme
PAA	Phosphoric-Acid Anodise
SEM	Scanning Electron Microscopy
TDCB	Tapered Double-Cantilever Beam
TEM	Transmission Electron Microscopy
TPB	Three-Point Bend
XPS	X-ray Photoelectron Spectroscopy

Chapter One

Introduction

In recent years the use of adhesives has increased as manufacturers have become aware of the advantages that adhesives can offer compared with conventional joining techniques. However, to be confident in their use it is necessary to evaluate the performance of adhesive joints, especially as the mechanical properties of the joints tend to decrease with impact loading, and with exposure to moisture or fatigue loading. The main aims of the present work are to investigate how epoxy adhesives perform under these conditions when used to bond steel or aluminium-alloy adherends.

Firstly, various methods will be used to evaluate the impact performance of a range of epoxy adhesives. Two fracture mechanics approaches will be used, the tapered double-cantilever beam and the three-point bend test methods. It has been shown that the tapered double-cantilever beam (TDCB) test, typically used with adhesives at quasi-static loading rates, can also be used successfully at high rates of test. Thus TDCB tests will be performed to investigate the variation of the mode I fracture energy, G_c, of the adhesives with loading rate. Three-point bend tests will be used to determine any differences in the fracture energies obtained from bulk and joint specimens at high test rates. Additionally, the recently introduced ISO Standard[1] method for the impact testing of adhesive joints, the impact wedge peel (IWP) test, will also be evaluated. The results obtained from the IWP test will be compared with the values of the appropriate adhesive fracture energies, to investigate whether a correlation exists between the test methods. The force versus time response will also be modelled. This work will concentrate on the impact wedge peel test, as no finite element modelling has previously been published on this geometry. The model will be used to predict the IWP cleavage force from the measured value of the adhesive fracture energy. From this research, recommendations will be made as to the best test methods for evaluating adhesives at high rate.

Secondly, the present research will investigate the effect of an aqueous environment on the adhesive fracture energy of two adhesive systems under cyclic loading (i.e. dynamic fatigue loading) using the TDCB specimen geometry. A low impact performance epoxy adhesive will be used to bond steel and aluminium-alloy adherends prepared with either a gritblast and degrease, or a chromic-acid etch surface treatment. The results will be compared with those from a high impact performance epoxy. These tests will identify the

relationship between the rate of crack growth per cycle, da/dN, as a function of the maximum applied fracture energy, G_{max}. These fatigue tests will be conducted both in a 'dry' environment of 23±1°C and 55 % relative humidity, and a 'wet' environment of immersion in distilled water at 28±1°C. From these data it will be possible to determine whether a threshold applied fracture energy, G_{th}, exists, below which crack growth does not occur. These data will then be used to predict the life of bonded single lap joints under fatigue loading in an aqueous environment. An analytical and a finite element method will be used to model the variation in G_{max} with crack length in the joints. Knowing the relationship between the fatigue crack growth rate and G_{max} from the TDCB fatigue tests allows the predicted number of cycles to failure to be calculated. The predictions will be compared with experimental results, and the accuracy of the two methods assessed. Similarly, a finite element model will be used to predict the rate of crack growth in a bonded component subject to fatigue loading, using the data from the TDCB tests. The predictions will be compared to experimental results.

The reductions in performance, if any, due to impact or fatigue and exposure to water will be compared, and their relative importance discussed. Surface analytical techniques will be used to identify the mechanisms responsible for any reduction in performance. Finally, recommendations for future work will be made.

Chapter Two

General Literature Review

2.1 Introduction

This Chapter provides a brief review of the aspects of adhesion science, fracture mechanics and mechanical testing that are relevant to the present work. Some of the most relevant topics are dealt with in more detail later on, where a Chapter concentrates on a specific area. Thus Chapters 4 to 6 will consider the tapered double-cantilever beam (TDCB) test, the three-point bend test and the impact wedge-peel test in more detail, when used at high test rates. The problems of dynamic effects will also be discussed further in Chapter 5. Chapters 8 and 9 will consider the TDCB and lap joint specimens when used under fatigue loading.

This Chapter first considers the interfacial contact between the adhesive and the adherend, and then discusses the various theories of adhesion that have been proposed. The effects of surface treatments are also discussed. As the present work concentrates on structural epoxy adhesives these are considered, along with the mechanisms of toughening. The principles of fracture mechanics are introduced in Section 2.6, followed by a summary of the effects of test rate on adhesive joints. Some of the methods for testing adhesive joints under impact conditions are also discussed. The effects of environmental attack are then considered, and finally some of the test methods to investigate the durability of joints are discussed.

2.2 Interfacial Contact: Surface Energy and Wetting

Intimate molecular contact between an adhesive and an adherend is required to form a strong joint. This requires that the adhesive spreads across the surface of the adherend, and displaces air, and other contamination, that would otherwise become trapped and hence reduce the subsequent joint strength. To do so the adhesive requires a relatively low viscosity and an ability to wet the surface.

Surface tension, in a liquid or a solid, exists due to the attraction of the bulk material for the surface. This reduces the number of molecules at the surface, and increases the inter-molecular distance. Work must be done to return this structure to the 'bulk' state. This is the surface free energy, or surface tension. In general, polymers have low surface

energies and metal oxides have high surface energies. As a low surface energy liquid will wet a high energy surface, so a polymeric adhesive would be expected to wet a metal surface. This can be checked by performing a contact angle test[2-4]. A drop of the liquid polymer is placed on the surface of the adherend. The angle between the surface and the edge of the drop is measured, see Figure 2.1. A near zero contact angle indicates that the adhesive wets the surface well, and the drop will have spread out across the surface.

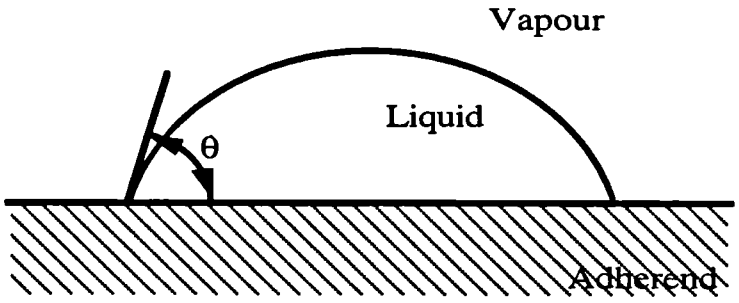


Figure 2.1: Measurement of contact angle, θ, using a drop of liquid polymer on surface of adherend.

However, high energy surfaces will tend to absorb water vapour, hydrocarbons, and other airborne contaminants, thus reducing the surface energy. For example, work by Poole and Watts[5] using X-ray Photoelectron Spectroscopy (XPS) has shown high levels of carbon contamination on adherends due to adsorption of such airborne contaminants.

2.3 Mechanisms of Adhesion

2.3.1 Introduction

Four main theories of adhesion have been proposed:

Mechanical interlocking;
Diffusion theory;
Electronic theory;
Adsorption theory.

Each of these theories has been shown to be applicable in some cases. However, the adsorption theory is considered to be the most widely applicable[6]. Each of the theories will now be described briefly.

2.3.2 Mechanical Interlocking

This is the simplest explanation of adhesion, and involves the adhesive keying into irregularities in the surface of the adherend. This may be significant on porous surfaces, and those where ink-bottle, or other types of re-entrant cavities, are present. However, most surfaces do not exhibit these features, and it has also been shown that good adhesion may be obtained on smooth surfaces, e.g. glass[6] or mica[7-9]. Roughening of the surface, chemically or mechanically, does increase the strength of a joint, as shown by various authors[10, 11]. This effect could be due to improved wetting or the increased surface area available for bonding. However, it is unlikely that mechanical interlocking is the main mechanism of adhesion.

2.3.3 Diffusion Theory

This theory proposes that there is mutual diffusion of molecules across a polymer/polymer interface[12, 13]. For this to occur the molecules must be sufficiently mobile, and mutually soluble[14]. However, if the solubility parameters of the two components are not similar, or the polymers are crosslinked, crystalline, or above their glass transition temperatures, T_g, then this mechanism is unlikely to be applicable[6]. Thus it is unlikely to occur with the adhesives used in this work, or with metal surfaces[15]. However, mutual diffusion has been shown to occur in some cases of polymer/polymer bonding[16].

2.3.4 Electronic Theory

The electronic theory proposes that the electrostatic forces at the interface of an adhesive and an adherend cause high joint strength[17]. Contact between materials with different electronic band structures may result in electron transfer and the formation of a double layer of electrical charge. Thus the joint is treated in the same way as a capacitor, and the attractive forces across the charged layers provide the adhesion. The theory is supported by experimental measurements, though the electrical phenomena are observed only at fracture. Thus a process of fracture is used to explain the process of adhesion. However, the electrostatic forces may be a result of high joint strength rather than the cause of it. Experiments have also shown that the contribution of an electrostatic component to the intrinsic adhesion for a typical adhesive joint is likely to be small compared to the van der Waals contribution, as reported by Kinloch[6].

2.3.5 Adsorption Theory

The adsorption theory proposes that materials adhere due to interatomic and intermolecular forces across the interface. This requires intimate molecular contact between the surfaces. Van der Waals forces are considered to be the most common interactions[6]. These are grouped together with hydrogen bonds, and described as secondary bonds. Stronger, primary, bonds can also occur[18, 19]. This category covers ionic, covalent, or metallic bonds which can be formed across the interface. The experimental evidence to support this theory includes work which showed that measured joint strengths can be accounted for by secondary interactions alone[20, 21].

However, many adhesive joints fail in a cohesive-in-adhesive manner, and pure interfacial failure is rare. Even when pure interfacial failure does occur, the dominant energy absorption mechanism will usually be the deformation of the adhesive rather than the fracture of interfacial bonds[22]. However, the interface becomes of major importance when environmental attack occurs, see Section 2.8.

2.4 The Role of Surfaces

2.4.1 Introduction

In their 'as received' state most materials will have a poor surface for bonding. Metals will often be covered with a weak oxide, and deposits of grease or airborne contamination. These form a weak layer, which will cause premature joint failure, and thus these must be removed prior to bonding. Additionally the surface energy must be high enough to allow wetting and intimate molecular contact to be attained.

2.4.2 Surface Modification

Roughening the surface by gritblasting or abrasion has an effective surface cleaning action. The irregular surface may also prevent cracks from propagating along a line of interfacial weakness. A rough surface may also increase the energy dissipation in the adhesive by promoting plastic deformation and energy absorption in the adhesive[6, 10]. The contribution from mechanical interlocking due to simple abrasion is probably not significant.

Increasing the surface energy will give improved molecular contact, and will also form stronger interactions between adhesive and adherend, hence improving the bond. This can be achieved with chemical treatments, after removing any surface contaminants.

2.4.3 Surface Treatments

A range of surface treatments are used prior to bonding. These range from a simple surface degrease to complex chemical procedures. One of the most common treatments used is an abrade and degrease, which removes any weak surface oxide and provides an oil-free surface for bonding. The chromic-acid etch (CAE) treatment uses a solution containing sulphuric acid and sodium dichromate to etch the surface of the adherend, and provide a stable oxide and/or better wettability and intrinsic adhesion. This treatment also gives better durability performance than a simple abrade and degrease treatment. Phosphoric acid anodising (PAA) is used in the aircraft industry, and though complex and expensive, provides excellent joint durability[23]. This process uses a chemical etch to remove any weak layer on the surface, then the anodising process builds up pore-like oxide structures on the surface into which the adhesive can penetrate, resulting in a 'micro-composite' surface structure[24].

2.5 Adhesives

2.5.1 Introduction

The present work investigates the effect of test rate and durability on a range of structural epoxy adhesives. A structural adhesive can be considered to be one which has a relatively high modulus and strength when cured. Hence it can be used to join rigid adherends as an integral part of a load-bearing structure. Epoxy adhesives are only one type of many used in industry. One of the major applications for epoxies will be the automotive industry. Manufacturers are currently investigating the possibility of replacing the spot-welding of vehicle bodies with adhesive bonding[25, 26]. Some parts of cars and trucks are already bonded, for example adhesives are used to bond and seal the inner door skin to the outer. They are also used to bond stiffeners to doors, bonnet and boot panels[27]. The use of adhesives as a primary joining method has so far not reached mass-production manufacturing, though they have achieved penetration in the lower volume end of the market, for example in the Lotus 'Elise'. The increased stiffness imparted to a body structure compared with spot-welding, the good surface finish and the ability to join dissimilar materials makes the use of adhesives attractive.

2.5.2 Adhesive Types

Epoxy adhesives typically fall into two categories, the two-part adhesive requiring a room temperature cure, and the single-part adhesive with an elevated temperature cure. Epoxies are thermosetting polymers, and during cure crosslinks are formed between the polymer chains. Thus the adhesive changes from a paste to a solid that is capable of bearing loads once incorporated into a structure. The automotive industry is investigating

elevated-temperature curing epoxies for use in the fabrication of vehicles[25, 26]. The adhesive would be applied, and the vehicle body tacked together with a few spot-welds, before the body was painted. The adhesive would cure when the body passed through the paint-curing ovens. Thus many of the adhesives investigated in the present work cure at approximately 180°C. However, the same adhesive could not be used in crash repairs, as it would not be possible to expose the vehicle to temperatures of 180°C without causing damage to the interior and trim. Thus a room temperature curing adhesive would be required. Alternatively, an adhesive with a cure temperature of up to approximately 50°C could be used, as this temperature may be achieved by using heat lamps. This latter method is currently used for repairs to aircraft[28].

2.5.3 Toughening

Epoxies, in their untoughened state, are very brittle materials, and thus are unsuitable as structural adhesives. During fracture, some energy is absorbed by shear yielding, but this mechanism is localised to a very small area at the crack tip, and hence the energy absorbed is very limited. Untoughened epoxies, in common with other highly crosslinked polymers, do not have sufficient mobility of the polymer chains to allow crazing to occur[6, 29]. However, if discrete particles of rigid, elastic, or viscoelastic material are dispersed through the matrix, the fracture toughness can be improved, as described in Section 2.5.4 below. However, care must be taken that any increase in fracture toughness is not at the expense of other properties, e.g. modulus or glass transition temperature. The mechanisms of toughening will now be considered.

2.5.4 Energy Absorbing Mechanisms

2.5.4.1 Rubbery Particle Toughening

Toughening agents can be introduced into an epoxy adhesive as liquid rubbers, and will undergo a phase separation during adhesive cure to form discrete particles. Typically 5 to 20 % by weight of rubber is added, which increases the fracture toughness of the epoxy, see Table 2.1. Initial explanations of the mechanisms of toughening postulated that the rubber particles were bridging the fracture surfaces of the crack, and thus additional energy was required to tear the rubber particles. Kunz and Beaumont[30] proposed this type of particle stretching and tearing mechanism. However, this model did not fully explain some of the other effects of rubber toughening such as the high toughness at high temperature, and the large plastic deformations and stress whitening observed.

Huang and Kinloch[31-33] proposed that the rubber tearing was only a secondary mechanism, and most of the energy was being absorbed by plastic yielding. The triaxial

Table 2.1: Comparison of typical properties of untoughened and rubber toughened epoxy adhesives, from[6].

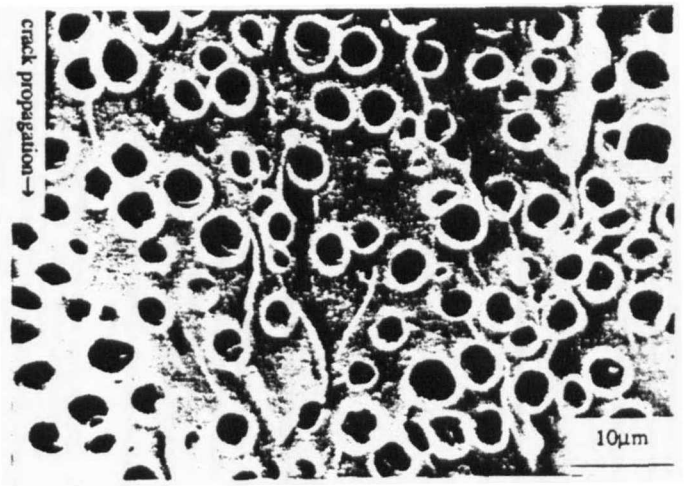
	Modulus, E_a, GN/m^2	Fracture energy, G_c, J/m^2
Untoughened	4	60
Rubber toughened	3	3500

stresses at the crack tip cause plastic expansion of the matrix and cavitation of the rubber particles. Stress whitening is caused by light being scattered by the microvoids, i.e. holes, resulting from this process. Plastic shear yielding occurs between the holes formed by the cavitated particles, and can be seen as furrows in the fracture surface at 45° to the direction of the maximum tensile stress, i.e. in the plane of the maximum shear stress, see Figure 2.2. Thus plastic deformation of the matrix, initiated by cavitation, absorbs the extra energy. Li et al[34] have shown that there is massive shear yielding only when cavitation occurs. The plastic deformation will blunt the crack tip, reducing the local stress concentration, and requiring a greater energy input to cause fracture, increasing the measured toughness of the material.

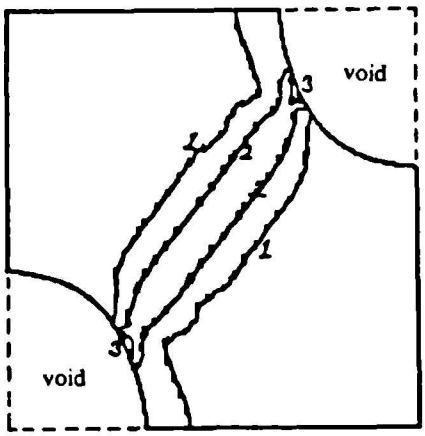
2.5.4.2 Rigid Particle Toughening

As discussed above, deformation of the toughening particles is not the main mechanism of energy absorption, instead the energy is absorbed by the shear yielding and plastic deformation initiated by cavitation. Thus an epoxy can also be toughened by the addition of rigid particles. Here cavitation of the matrix at the surface of the particle will initiate the energy absorbing mechanisms.

In an epoxy with a less ductile matrix crack pinning will also absorb energy. When the crack front reaches a line of rigid particles it becomes pinned at the particles, but will bow out between them. When it has bowed out sufficiently it breaks away and the crack front reforms. This mechanism is supported by investigation of the fracture surfaces[35, 36]. However, in general toughening with rigid particles is less effective than with rubbery particles.



(a) Scanning electron micrograph of cavitated rubber particles.



(b) Finite element prediction of plastic shear bands initiated by rubber particle cavitation.

Figure 2.2: Rubber-toughening of an epoxy adhesive, (a) scanning electron micrograph of cavitated rubber particles, and (b) finite element prediction of plastic shear bands initiated by rubber particle cavitation, from [31].

2.6 Fracture Mechanics

2.6.1 Introduction

The theoretical strength of a material, based on the molecular forces within it, is several orders of magnitude greater than that observed experimentally. The explanation for this was first proposed by Griffith[37] in 1920. He postulated that all solids must contain cracks or flaws. There will be a stress concentration at the tip of any flaw, and hence the theoretical strength is reached locally though the nominal stress is well below that required for fracture. The effect of these flaws explains the observations made in the

fifteenth century by Leonardo daVinci, as reported by Irwin[38]. He noted that the strength of a piece of wire decreased with increasing length. This would be due to the increased probability that the wire would contain large flaws due to the increased volume.

Thus, the basic tenet of fracture mechanics is that intrinsic flaws are present in any material, which propagate and cause premature failure. Fracture mechanics aims to model this process, and allow the engineer to predict the observed strength.

2.6.2 Failure Modes

Loads may be applied to a crack in three modes, as shown in Figure 2.3. Tensile opening, mode I, is considered the most important as it is the most commonly seen, and the mode in which fracture requires the smallest energy input. Mode II is the in-plane shear mode, and mode III the anti-plane shear or tearing mode.

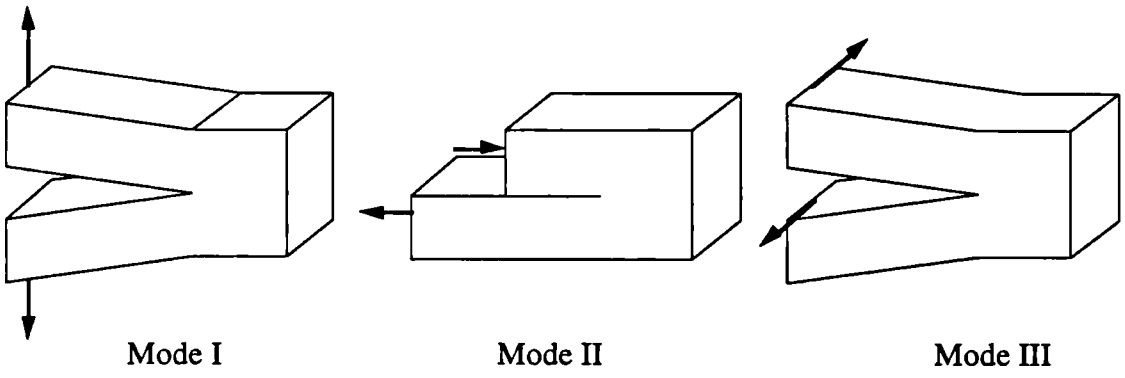


Figure 2.3: Modes of failure.

2.6.3 Fracture Energy

Fracture mechanics proposes that fracture occurs when sufficient energy is released by the growth of a crack to supply the energy requirements of the new surface formed. This energy comes from the stored elastic energy of the body or the potential energy of the loading system[39]. Hence for a body of width, b,

$$\frac{1}{b}\frac{\partial(W_d - U_e)}{\partial a} \geq 2\gamma_m \qquad (2.1)$$

where the increase in surface area, dA, is equal to 2b.da. The term W_d is the work done by the external force, U_e is the stored elastic, or strain, energy and γ_m is the surface energy.

The initial work on this fracture criterion was performed on perfectly brittle materials, e.g. glass. Thus other authors[40, 41] found that the energy required for crack growth in most materials was greater than $2\gamma_m$. Although this term reflects the energy required to rupture secondary bonds, it does not include the contribution from primary bonding or, most importantly, the energy dissipated through viscoelastic and plastic processes. Thus a modified version of Equation 2.1 was formulated,

$$\frac{1}{b}\frac{\partial(W_d - U_e)}{\partial a} \geq G_c \qquad (2.2)$$

where G_c includes all the energy losses around the crack tip. This is the fracture energy, the total energy required for a unit increase in crack length within a body of unit width. The fracture energy, G_c, is a material property.

The value of G_c can be calculated by considering a general elastic body containing a crack of length, a, subjected to a load. Crack growth by a length, da, causes the load to drop from P_1 to P_2, while the displacement increases from u_1 to u_2, see Figure 2.4.

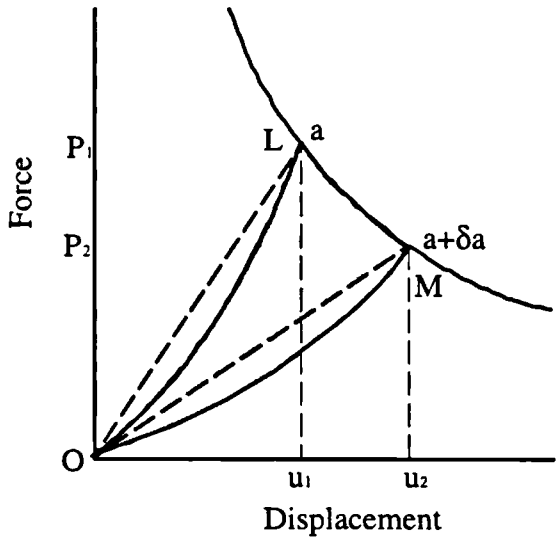


Figure 2.4: Area method for determining fracture energy, after[39].

The strain energy stored prior to crack growth is represented by the area OLu_1, shown as a solid line in Figure 2.4, and OMu_2 is the energy remaining in the body after the crack grows by a length, da. Thus the change in strain energy is (OMu_2 - OLu_1). The external work done is given by the area u_1LMu_2. Thus the total change in energy is the area OLM, shown shaded, and hence the fracture energy is given by

$$G = \frac{\delta U_e}{b\delta a} = \frac{\text{area OLM}}{b.\delta a} \tag{2.3}$$

If the load versus displacement response is linear, then the curves OL and OM are replaced by straight lines, shown dashed in Figure 2.4, hence

$$G = \frac{1}{2b\delta a}(P_1 u_2 - P_2 u_1) \tag{2.4}$$

The compliance of the specimen, C, can be defined as a function of the crack length, where

$$C = \frac{u}{P} \tag{2.5}$$

Hence, by substitution into Equation 2.4,

$$G = \frac{P^2}{2b}\frac{dC}{da} \tag{2.6}$$

The overall loading response of the specimen can be considered to be linear elastic providing any plasticity is localised to a small zone around the crack tip. These conditions allow linear elastic fracture mechanics (LEFM) to be used, thus simplifying the analysis, providing no large scale plastic deformation has to be taken into account. The specimens used in the present work allow this simplification to be used[6].

2.6.4 Stress Intensity Factor

An alternative method to the energy approach discussed above is to consider the stress distribution around the crack tip, as shown in Figure 2.5. Equations to describe this stress field were developed by Westergaard[42] and subsequently modified by Irwin[38]. These follow the general form

$$\sigma_{ij} = \frac{K}{(2\pi r)^{1/2}} f_{ij}(\theta) \tag{2.7}$$

where σ_{ij} is a component of the stress tensor, K is the stress intensity factor, and f_{ij} is a dimensionless function of θ. The polar coordinates r and θ are defined in Figure 2.5, with the origin of the coordinates at the tip of the crack.

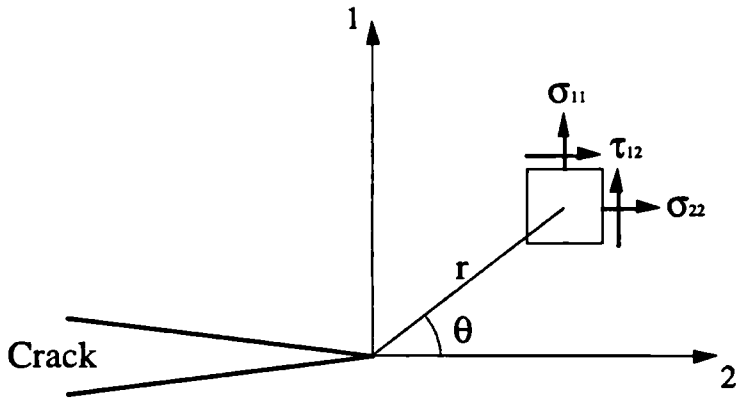


Figure 2.5: Stress intensity factor approach for evaluating fracture toughness.

Fracture is said to occur when the stress intensity factor is equal to the critical value, K_c, which is a material property. Equation 2.7 shows that there is a stress singularity at the crack tip, produced by the $1/r$ term. Problems are encountered close to an interface where no satisfactory model of the crack tip behaviour yet exists, due to the additional complications these conditions impose[6]. Thus the fracture energy approach is generally considered to be the simpler method.

For mode I plane-strain conditions, the fracture energy, G_c, and the critical stress intensity factor, K_c, are related by

$$G_c = \frac{K_c^2\left(1-\upsilon^2\right)}{E} \qquad (2.8)$$

where υ is the Poisson's ratio and E is the Young's modulus of the material.

2.6.5 Specimen Width

The value of fracture energy has been found to vary with specimen width. The plane stress value is higher than the plane strain value, as the yield stress of a material is greater under a triaxial stress (plane strain) than under a biaxial stress (plane stress). This results in less plasticity at the crack tip in plane strain. The value required for engineering applications will be the lowest, i.e. the plane strain value. Plane strain conditions are present in the centre of specimens, thus the specimen must be sufficiently wide for this condition to dominate[39]. The minimum width is given by

$$b \geq 2.5\left(\frac{K_c}{\sigma_y}\right)^2 \qquad (2.9)$$

where K_c is the plane strain fracture toughness, and σ_y is the yield stress of the material.

2.6.6 Plastic Zone Size

A plastic zone will form ahead of the crack tip in a material, the boundary of which encloses plastically deformed material. The measured toughness of an adhesive will be reduced if the size of this zone is restricted by the adherends. The size of this zone has been estimated by Irwin[38] and Dugdale[43]. The Irwin model, shown in Figure 2.6, assumes that the plastic zone is circular, with a radius r_p, where for plane-strain conditions,

$$r_p = \frac{1}{6\pi}\left(\frac{K_c}{\sigma_y}\right)^2 \qquad (2.10)$$

where K_c is the fracture toughness, and σ_y the yield stress of the material. For plane stress, the value of r_p is three times the plane strain value.

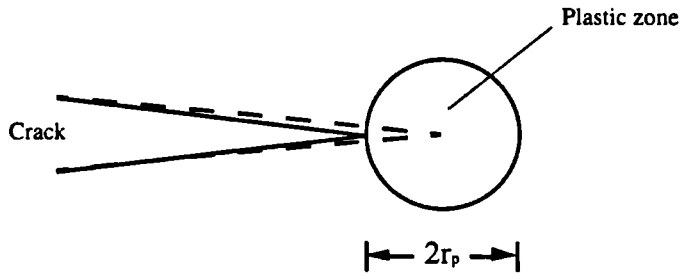


Figure 2.6: Irwin model of plastic zone at crack tip.

The plastic zone size for the main epoxy adhesive used in the current work ('AV119' from Ciba Polymers) can be calculated knowing that the fracture energy G_c = 700 J/m^2, the modulus E = 3 GPa, and the Poisson's ratio υ = 0.35. Hence, using Equation 2.8, these data[44] give a fracture toughness of K_c = 1.55 MN/m$^{3/2}$. Thus, as the yield stress σ_y = 40 MN/m^2, the radius of the plastic zone, r_p = 0.08 mm under plane strain conditions.

The Dugdale model proposes an elongated plastic zone[43], as shown in Figure 2.7, where the zone length, l_p, is given by

$$l_p = \frac{\pi}{8}\left(\frac{K_c}{\sigma_y}\right)^2 \qquad (2.11)$$

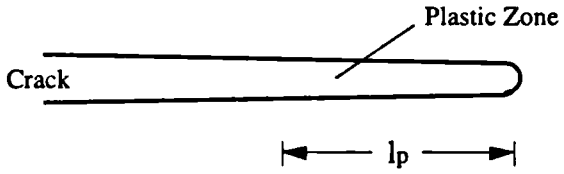


Figure 2.7: Dugdale model of plastic zone at crack tip.

Again, for the main epoxy adhesive used in the current work, l_p = 0.6 mm.

Both models imply that the actual crack length should be considered to be longer, e.g. by r_p for the Irwin model, than that observed. However, these corrections are small, and can be ignored for most practical applications.

2.7 Impact Tests for Adhesive Joints

2.7.1 Introduction

The test methods that may be used to evaluate the performance of adhesive joints at high loading rates can be broadly split into two categories, those that use a fracture mechanics approach, and those that use some other measure of the joint performance. The fracture mechanics tests use a specimen with an artificially introduced flaw, or pre-crack, from which crack propagation will occur. The other methods use specimens with no pre-crack, and these will be discussed first. However, first of all, the effects of test rate will be considered, as these affect the polymer properties and cause dynamic effects.

2.7.2 Effect of Test Rate

2.7.2.1 Polymer Properties

Polymers are viscoelastic materials, and as such fall between the elastic, where the stress is proportional to the strain, and the viscous, where the stress is proportional to the strain rate and independent of the applied strain[45].

Increasing the test rate, or decreasing the test temperature, will decrease the size of the plastic zone, and hence decrease the measured toughness of a material. Conversely when the test rate is reduced the plastic zone size will increase. It should be noted however that the zone size may be restricted by the adherends in an adhesive joint. The toughening mechanisms that operate at low rate still operate at high rate or low temperature, but are not as effective. Thus the measured value of fracture energy would be expected to decrease with an increased test rate or low temperatures[46].

2.7.2.2 Dynamic Effects

At high test rates, dynamic effects can become significant. Large oscillations are superimposed on the quasi-static force versus time response. These can be caused by elastic stress waves reflecting within the specimen and interacting with the propagating crack[47]. However, if the timescale of the test is long compared with the time taken for the reflection of the stress waves then this mechanism will not be dominant.

A more significant cause can be vibrations in the testing system leading to oscillations in the measured response. When a specimen is loaded rapidly, e.g. when struck with a pendulum or a falling weight, it will vibrate. This motion will be recorded as an oscillating force by a load-cell in contact with the specimen. The inertial loads within the testing system can result in the force in the specimen not being equal to that measured by a load-cell mounted on the testing machine. This difference is important because to calculate the fracture energy of a material the force that is required is that acting in the specimen, from which the energy gained by the specimen is calculated. If this force is not the same as that measured by the load-cell, erroneous energy values will be calculated. This effect is negligible at low impact velocities, but pronounced differences can occur as the test velocity is increased.

For example, with the three-point bend test described in Section 2.7.4.2, oscillations in the force response are measured due to the specimen flexing and losing contact with the supports and the striker, and hence with the load-cell mounted on the striker. The measured load may even become negative. Thus there can be large differences between the measured forces and those acting in the specimen[48, 49]. Hence the measured force versus time data does not accurately record the forces acting on the specimen, and hence the energy calculated from these data becomes meaningless. The problems of dynamic effects in the three-point bend test will be discussed further in Chapter 5.

The magnitude of the oscillations caused by dynamic effects varies with test rate as mentioned above, but also with the test geometry. For example, the three-point bend test

tends to exhibit more significant dynamic effects than the tapered double-cantilever beam test, at the same test velocity. The oscillations depend on the specimen type and how the specimen is loaded, as will be shown in subsequent Chapters.

2.7.3 Non-Fracture Mechanics Test Methods

2.7.3.1 Block Shear Test

This test method is specified by ASTM D950[50] and BS 5350[51]. Until the impact wedge-peel test was introduced, see below, these were the only Standards governing the impact testing of adhesive joints. The block shear test is basically a comparative test, it does not give any material parameters. The specimen consists of a 25 mm square, by 10 mm thick, block bonded to a larger base block, see Figure 2.8. This is tested on an Izod pendulum machine. The energy required to remove the upper block, i.e. the energy lost by the pendulum, is taken to be the impact strength of the adhesive. No starter crack is used with this test.

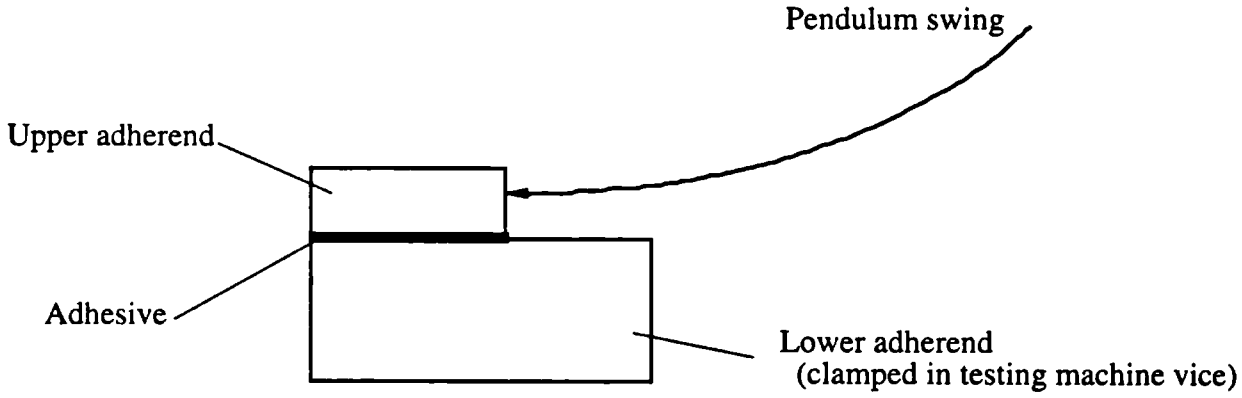


Figure 2.8: The block shear specimen.

The block shear test is poor at discriminating between adhesives, even over a large range of brittle to very tough adhesives[52]. The results have also been found to be highly dependent on the testing machine used, and thus can only indicate the relative strengths of the adhesives used[53]. Failure also tends to be apparently interfacial. This is a result of the joint geometry, as there is a stress concentration at the corner of the adhesive and the lower adherend[53]. Thus the block shear test is a poor method for evaluating the impact performance of adhesives.

2.7.3.2 Impact Wedge-Peel Test

The impact wedge-peel (IWP) test was introduced as an International Standard in 1993[1]. This specifies the use of 20 mm wide, sheet metal adherends, between 0.6 and 1.7 mm thick. These are bonded over a length of 30 mm, the unbonded arms being formed to give a 'tuning fork' profile. The free arms of the specimen are clamped, and a wedge is driven through the bonded portion, see Figure 2.9. The wedge velocities specified by the Standard are 2 m/s for steel adherends, and 3 m/s for aluminium. The energy and average cleavage-force required to drive the wedge through the specimen are recorded, neglecting the first 25 % and last 10 % of the force versus time trace.

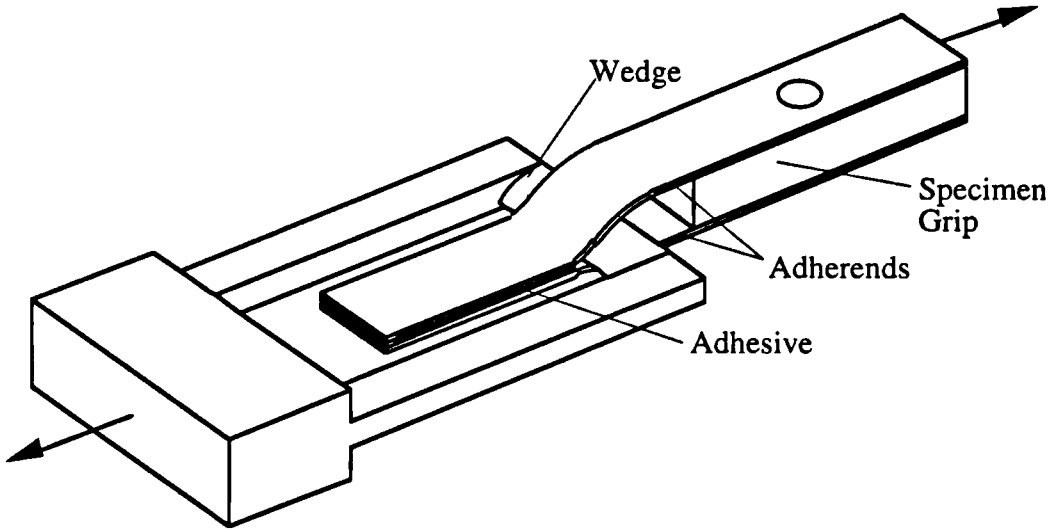


Figure 2.9: The impact wedge-peel test.

Extensive plastic deformation of the specimen occurs, and so this test method measures the ability of the adhesive/adherend system to absorb energy. It is popular in the automotive industry where it is used to evaluate the relative performance of adhesives. It is also considered to be a useful predictor of the impact performance of larger structures, e.g. bonded box beams or vehicle front ends, as the plastic deformation of the adherend is taken into account[26]. This test method will be discussed in more detail in Chapter 6.

2.7.3.3 Lap Joints

The lap joint is one of the simplest test geometries, see Figure 2.10, and is probably the closest to how adhesives would be used in industry. Though it would appear to be a

mode II joint, failure is usually by peeling of the ends of the overlap, and thus the mode I component is considered to dominate failure[54].

However, the scatter in the experimental data is large, especially at high rates of test. Work by Tomczyk[55] showed scatter of up to 70 % in the energy absorbed prior to fracture using lap joint specimens tested at up to 8 m/s. Thus it may be concluded that the lap joint geometry is unsuitable as an impact test.

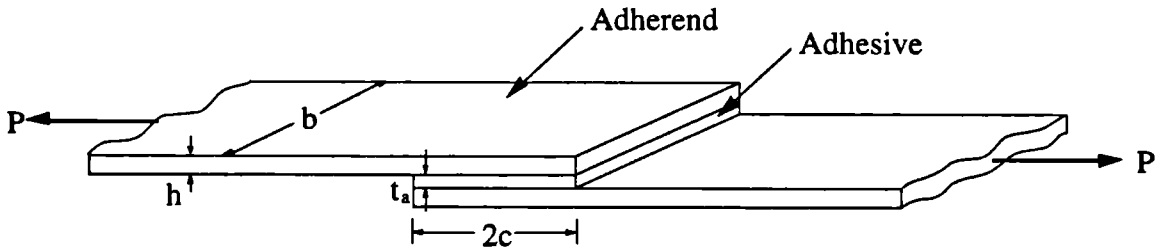


Figure 2.10: Single lap joint.

2.7.4 Fracture Mechanics Test Methods

2.7.4.1 Introduction

As discussed in Section 2.6 above, the resistance to fracture of a material can be quantified using fracture mechanics, and this Section discusses some of the test methods that may be used to calculate the adhesive fracture energy, G_c, in both bulk and joint configurations. All tests are performed using a constant test rate.

The basic analysis[56] is common to all the methods, calculating G_c using Equation 2.6

$$G = \frac{P^2}{2b}\frac{dC}{da} = \frac{P}{2b}\left(\frac{u}{C}\right)\frac{dC}{da} = \frac{1}{2b}\left(\frac{u}{C}\right)^2\frac{dC}{da} \qquad (2.6)$$

where P is the force, C is the compliance, u is the displacement, a is the crack length, and b is the width of the specimen.

2.7.4.2 Three-Point Bend Test

The three-point bend (TPB) or Charpy test is a Standard method for measuring the fracture energy of metals[57] and polymers[58], see Figure 2.11. It has also been used with bulk adhesive and joint specimens[59, 60], as shown in Figure 2.12. However, the dynamic effects associated with this test make analysis of the force versus displacement

response, and hence calculation of the fracture energy, difficult at high test rates. Models of these dynamic effects have been proposed[61, 62], which will be discussed further in Chapter 5. The use of damping material at the contact point has recently been recommended[58] to reduce the force oscillations to less than ±5 % of the maximum force, and hence allow a 'valid' G_c value to be calculated.

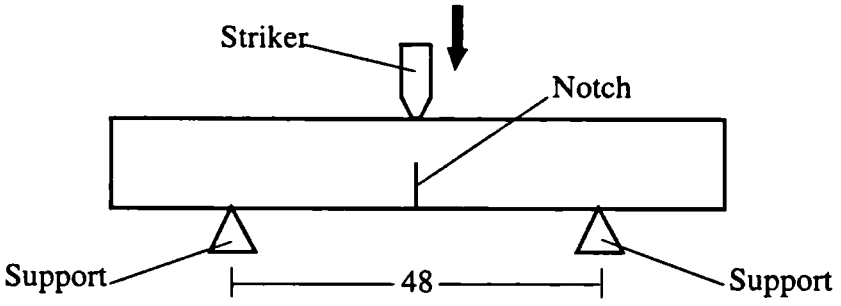
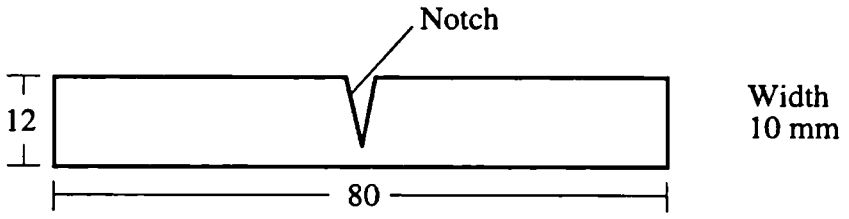
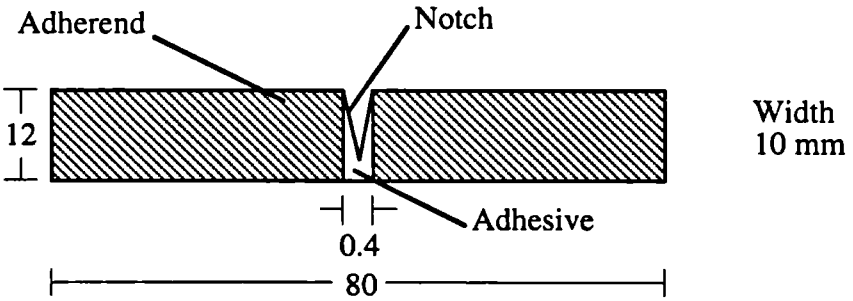


Figure 2.11: The three-point bend test. Typical dimensions are shown, in millimetres.



(a) Bulk adhesive specimen.



(b) Adhesive joint specimen.

Figure 2.12: Three-point bend specimens, (a) bulk adhesive specimen, (b) adhesive joint specimen. Typical dimensions in millimetres are shown.

The analysis to calculate G_c for this test method uses Equation 2.6, which states

$$G = \frac{P^2}{2b}\frac{dC}{da} \tag{2.6}$$

Introducing a dimensionless geometry factor, ϕ, where[58]

$$\phi = \frac{C}{\left(\frac{\partial C}{\partial\left(a/d\right)}\right)} \tag{2.12}$$

gives an expression for the fracture energy,

$$G_c = \frac{U_c}{bd\phi}. \tag{2.13}$$

Here U_c is the energy absorbed in the test, b is the width and d is the depth of the specimen. Values of the geometry factor, ϕ, are available in tabular form[58]. Hence the fracture energy is the gradient of a plot of the energy consumed in the test against $bd\phi$, where ϕ is dependent on the initial crack length. Thus a number of specimens with a range of crack lengths are required to generate a value of G_c. The ESIS protocol[58] recommends that fifteen specimens are tested for each fracture energy value required. This test method will be discussed further in Chapter 5.

2.7.4.3 Compact Tension Test

The compact tension specimen, as shown in Figure 2.13, can be used to test bulk adhesive or joint specimens[63, 64] The stress intensity factor, K_c, can be calculated from

$$K_c = \frac{P_c Q}{bd^{1/2}} \tag{2.14}$$

where P_c is the critical load, Q is a geometry factor, b is the width and d is the length of the specimen. The value of the geometry factor can be found from published tables[58], or from knowledge of dC/da, determined either experimentally or by finite element methods.

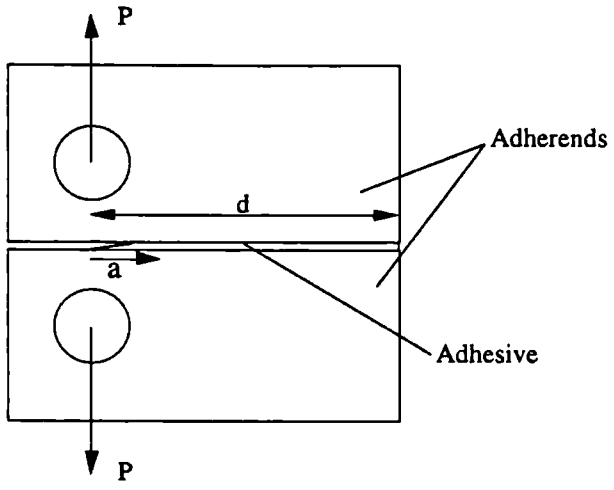


Figure 2.13: The compact tension specimen.

2.7.4.4 Double-Cantilever Beam Test

The double-cantilever beam (DCB) specimen, see Figure 2.14, uses a pair of flat adherends, loaded using holes drilled near the end of the adherends or with bonded end-blocks[47, 65].

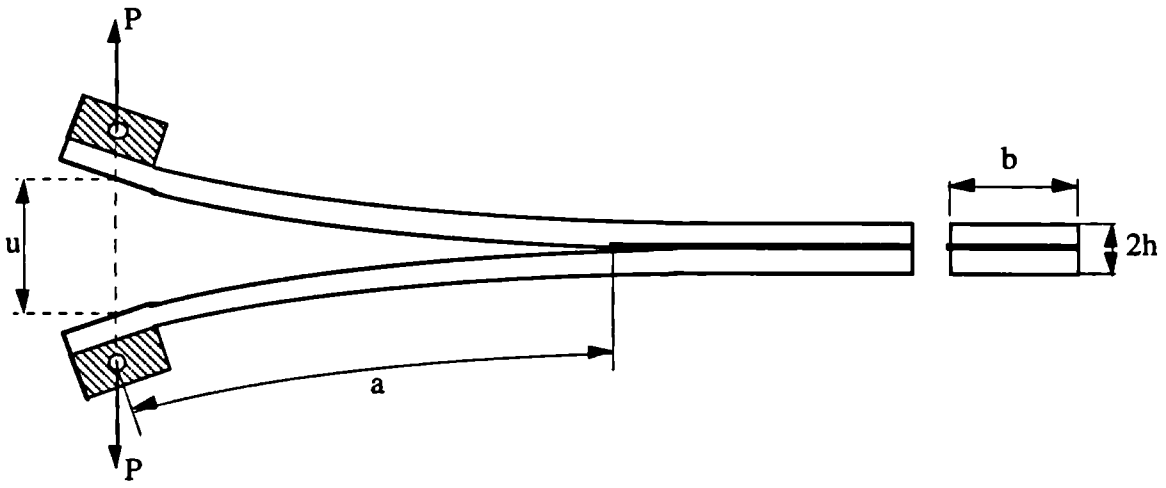


Figure 2.14: Double cantilever beam (DCB) specimen.

The fracture mechanics analysis uses the load form of Equation 2.6, the value of dC/da being determined either experimentally or analytically. Any analytical method must take into account the stiffening effect of any end-blocks, the shear rotation and the large

displacements[47, 66]. Thus for the specimen shown in Figure 2.14 the analytical solution would be

$$G = \frac{12FP^2(a+\chi h)^2}{b^2h^3E_s} \tag{2.15}$$

where F is the large displacement correction factor, and χ is the shear correction term. These correction terms are more important when using reinforced (e.g. with glass or carbon fibres) plastic adherends, where the adherends may be anisotropic and possess a low transverse modulus, than using metal adherends[47].

2.7.4.5 Tapered Double-Cantilever Beam Test

The tapered double-cantilever beam (TDCB) specimen, as shown in Figure 2.15, is a modification of the DCB described above[67, 68]. The height of the adherends, z, is machined such that the compliance increases linearly with crack length, and hence dC/da is constant,

$$\frac{dC}{da} = \frac{8m_b}{E_s b} \tag{2.16}$$

where E_s is the modulus of the adherend, and

$$m_b = \left(\frac{3a^2}{z^3} + \frac{1}{z}\right) = \text{Constant} \tag{2.17}$$

where z is the height of the adherend.

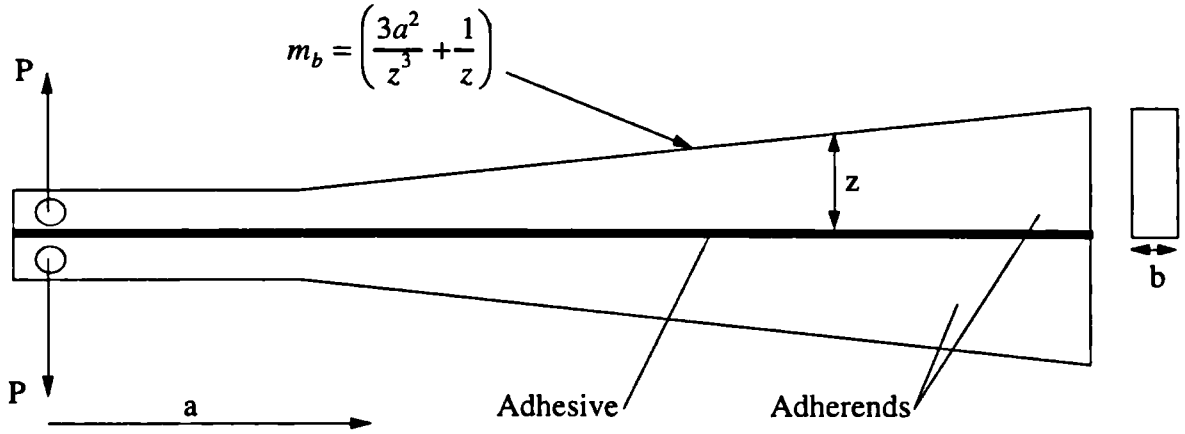


Figure 2.15: The tapered double-cantilever beam specimen.

Substituting Equation 2.16 into Equation 2.6 gives

$$G = \frac{4P^2 m_b}{E_s b^2} \qquad (2.18)$$

The calculated value of the fracture energy is independent of the crack length. Thus the analysis for the TDCB is simpler than that for the DCB specimen, as the crack length does not need to be measured during testing to calculate the fracture energy.

At high test rates the measured force may become unreliable due to dynamic effects, thus a load-independent analysis may be required. This will be discussed in more detail in Chapter 4, which discusses the use of the TDCB geometry at test rates up to 0.5 m/s.

2.8 Environmental Attack of Adhesive Joints

2.8.1 Introduction

Adhesive joints made with metal adherends are particularly susceptible to environmental attack by water as metals have high surface energy, polar surfaces[69]. Water is a polar molecule, and so it is strongly attracted to the polar metal surface, where, for example, it may displace the adhesive or cause hydration and weakening of the metal oxide. In general, water tends to force the locus of failure from a cohesive-in-adhesive path to an apparently interfacial one[65].

Hence, water is one of the most aggressive environments for adhesive joints, as comparative tests in water and simple alcohols have demonstrated. Indeed, work by Kerr, MacDonald and Orwan[70] showed that methanol and ethanol do not cause loss of adhesion, whereas water does. They suggested that the combination of hydrophilic and hydrophobic groups made these alcohols better plasticisers than water[70]. The effect of plasticisation is discussed in Section 2.8.2.5. Another explanation is the thermodynamic argument that the alcohols do not tend to displace the adhesive from the adherend, as discussed in Section 2.8.2.3.

Also, it has been shown[71-73] that increasing the relative humidity that an adhesive joint is exposed to may reduce the strength and accelerate failure. Salt water, either as immersion or as a salt spray may accelerate failure, and is often used by the automotive industry to simulate the effect of driving on salted roads[74]. However, it should be noted that the exact performance will vary from one adhesive system to another.

2.8.2 Mechanisms of Attack

2.8.2.1 Introduction

Water can affect the strength of adhesive joints, as reported by Comyn[75], by attacking the adhesive, the adherend, or the interface between them. It can reach these areas by diffusion through the adhesive or by transport along the interface[75-77]. These processes will be discussed below. Some of the other possible processes, such as diffusion through the adherends, are not applicable to the present work, as the metal adherends are non-porous.

The mechanisms by which the joint can be weakened can include[78]

Reversible alteration of the adhesive properties, e.g. plasticisation;
Irreversible alteration of the adhesive properties, e.g. hydrolysis;
Swelling stresses in the adhesive;
Displacement of the adhesive from interface;
Hydration and weakening of the metal oxide at interface.

These mechanisms are mostly detrimental to joint durability, but some may be beneficial, for example plasticisation allows the adhesive to relax, causing blunting and reducing the stress concentration at the crack tip. Thus an increased adhesive toughness may be measured as a result of this effect.

Various authors[71, 73, 79] have pointed to the existence of a critical concentration of water in the joint, below which the water has no effect on the strength of the joint. This is evident from the experimental data which shows that there is no significant loss of joint strength with time if the joint is exposed to a low relative humidity (say 50 %). However, if a joint is exposed to a high relative humidity (say 90 %), the strength now decreases.

A possible explanation for a critical concentration is offered by Bowditch[80] who suggests that there are two main mechanisms operating. Plasticisation would tend to raise the joint strength, while interfacial attack would lower it. Thus there could be an equilibrium water concentration below which the two effects cancel each other out, the net effect being that the joint strength is unaffected. Evidence for this is provided by test results which have shown an increase in joint strength over short exposure times, when an adhesive joint is immersed in water or exposed to a high relative humidity, but a decrease in strength over longer times[80, 81].

Note that much of the published work which attempts to explain losses in joint strength, and changes in the loci of joint failure, proposes interfacial bond-weakening theories.

These assume that adhesion occurs by the adsorption theory, as discussed in Section 2.3.5.

2.8.2.2 Interfacial Attack by Water

As discussed above, the effect of water on an adhesive joint tends to force the locus of failure from a cohesive-in-adhesive path to an apparently interfacial one. Further, purely interfacial failure absorbs significantly less energy than cohesive-in-adhesive fracture due to the reduced size of the plastic zone. Hence there is less viscoelastic and plastic energy dissipation at the crack tip.

Secondary forces (van der Waals and hydrogen bonds) are considered to be the most common interactions between the adhesive and the adherend[6, 82, 83]. However, stronger, primary forces may also occur due to ionic or covalent bonding[18, 19, 75].

If only secondary bonding occurs, a thermodynamic approach[20, 21] may be used to predict the stability of the interface, see Section 2.8.2.3. As water and metal oxides are both highly polar, the work of adhesion for an epoxy/metal interface in water is negative[69]. Hence there is a driving force for debonding, and once an adhesive is displaced from the surface, it is not sufficiently mobile to reattain contact[75]. However, it is unlikely that water would displace the adhesive completely if there were interfacial primary forces present, and hence joints do not tend to fall apart completely upon water immersion. Hydrogen bonds between the polymer and the metal oxide may also be displaced or interrupted by water[82].

The primary forces that may occur across the interface include ionic and covalent bonding, although these may also be affected by water. Comyn[75] suggests that ionic forces may occur across the interface of adhesive joints, especially as amine groups are common in adhesives. However, water tends to weaken these ionic forces at the interface. Covalent bonds may occur between the adhesive and the adherend[75], although a chemical reaction involving their destruction would be accelerated by an applied stress, i.e. there would be an apparent lowering of the activation energy.

Watts and his co-authors[84, 85] investigated the effect of water immersion and subsequent drying on joint strength and the locus of joint failure, using aluminium-alloy specimens bonded with an epoxy adhesive, immersed at 50°C. They found that some of the strength lost by the joints upon water immersion was recoverable on drying. The locus of joint failure changed from fully cohesive-in-adhesive to a mixed failure locus that was partly apparently interfacial. The mechanism of hydrolysis of the oxide, see Section

2.8.2.4, does not allow for this reversible behaviour. They suggest that though this hydrolysis mechanism is partially responsible, as not all the strength is recoverable, there is a second mechanism operating simultaneously. They suggest that there is an aggregation of water, at or near the epoxy/metal interface, which reduces the joint strength by forming a weak boundary layer, although the description given is rather vague. This water can be partially removed by drying the specimen. The authors also identified a loss of joint strength due to the leaching of a constituent of the adhesive at the elevated temperature used.

2.8.2.3 Interfacial Attack: Thermodynamic Considerations

It is possible to use a thermodynamic approach to determine whether the interface in a joint is susceptible to environmental attack. The work of adhesion, W_A, can be calculated from the surface energies using the Dupré equation, assuming there are only secondary forces acting between the surfaces. Thus this analysis assumes there are no primary forces acting across the interface, and no mechanical interlocking, interdiffusion or chemisorption present[86]. For an adhesive joint in air, the Dupré equation states[6],

$$W_A = \gamma_x + \gamma_y + \gamma_{xy} \qquad (2.18)$$

where γ_x is the adherend surface energy, γ_y is the adhesive surface energy and γ_{xy} is the interfacial free energy of the adherend/adhesive interface. If W_A, is greater than zero, the interface is stable. However, a negative value of W_A indicates that the interface is liable to dissociate.

In the presence of a liquid, denoted by the subscript L, the work of adhesion is given by

$$W_{AL} = \gamma_{xL} + \gamma_{yL} + \gamma_{xy} \qquad (2.19)$$

where γ_{xL} is the interfacial free energy of the adherend/liquid interface, γ_{yL} is the interfacial free energy of the adhesive/liquid interface and γ_{xy} is the interfacial free energy of the adherend/adhesive interface. As above, a negative value of W_{AL} indicates that the interface is unstable, and will tend to dissociate.

The work of adhesion for steel and aluminium-alloy adherends, calculated using the above Equations, both in air and exposed to liquid, are shown in Table 2.3. This shows that in air W_A is positive, and hence the joints are stable. This is also the case with ethanol, though the value of W_{AL} is now smaller. However, when exposed to water the work of adhesion is negative, and thus there is a driving force for the displacement of the adhesive

at the interface by water. Hence interfacial debonding would be expected, and was observed by the authors[21, 86].

Table 2.3: Work of adhesion values for epoxy adhesive with steel and aluminium-alloy adherends, from[20, 21].

Adherend	W_A (Air), mJ/m^2	W_{AL} (Ethanol), mJ/m^2	W_{AL} (Water), mJ/m^2
Fe_2O_3 (Steel)	291	22	-255
Al_2O_3 (Aluminium)	232	-	-137

2.8.2.4 Oxide Attack by Water

As discussed above, the effect of water on an adhesive joint tends to force the locus of failure from a cohesive-in-adhesive path to an apparently interfacial one, and may cause the failure path to move into the metal oxide. Exposure to water can cause weakening of the metal oxide on the surface of the adherend, forming a weak link in the joint through which failure can occur more easily. Further, Minford[87] suggests that the additional strain energy in the first few microns of the metal surface at the interface increases its susceptibility to corrosive attack by moisture. This leads to weakening of the oxide and early bond failure.

Transmission electron microscopy (TEM) has been used to investigate whether a process of hydration and swelling of the oxide occurs ahead of the crack tip in aluminium-alloy joints bonded with an epoxy adhesive. Jethwa[65], found no evidence of thickening of the oxide due to hydration, at 28°C. This observation confirms observations by Davies and Kinloch[88] though contradicting the proposed mechanism of Davis[89] who postulated that swelling of the oxide occurred. The conclusion of Jethwa was that a subtle process of hydration was occurring which did not affect the oxide thickness, and that the transformation to a weak pseudo-boemite structure, as proposed by Venables[90], and as observed using unbonded specimens, was not occurring beneath the adhesive layer. However, post-failure hydration and thickening of the oxide has been observed using adhesive joints[21, 65, 69, 88]. Note that oxide hydration and breakdown can occur at the same time as displacement of the adhesive from the surface of the adherend, as observed by Cayless[91] .

2.8.2.5 Bulk Adhesive Attack by Water

Exposing an adhesive to an aqueous environment will result in water being absorbed. The 'AV119' epoxy adhesive used in the present work absorbs approximately 5% by weight of water before saturation is reached[92]. Water uptake will alter the mechanical properties of the adhesive, as it will plasticise the polymer, as mentioned previously. It has been shown that water decreases the Young's modulus, E_a, of the adhesive[92, 93]. The shear modulus, Poisson's ratio, υ, and yield stress, σ_y, are also reduced[92, 94]. For example, the Young's modulus of the 'AV119' adhesive used in the current work is reduced from 3.2 GPa when dry to 2.8 GPa when saturated with water[92], see Table 2.4. The glass transition temperature, T_g, is also reduced, probably due to the presence of physically, rather than chemically, bound water, as the reduction is recoverable on subsequent drying[93]. For example, the T_g of the 'AV119' adhesive used in the present work is reduced from 113°C when dry to 87°C when saturated with water[76].

Table 2.4: Mechanical properties of the 'AV119' epoxy adhesive used in the present work when 'dry', and when saturated with water[76, 92].

Adhesive state	Modulus, GPa	T_g, °C	Shear modulus, GPa	Poisson's ratio
'Dry'	3.2	113	1.13	0.42
Saturated	2.8	87	1.0	0.36

As described above, plasticisation will increase the measured toughness of an adhesive[95]. However, the ingress of water may also cause swelling, which increases the stresses in the adhesive. This in turn will increase the susceptibility to environmental attack by lowering the activation energy required for bond rupture. Both plasticisation and swelling are reversible processes, the changes in properties induced being recoverable on drying.

Hydrolysis of the bulk adhesive is an irreversible process, involving chemical degradation of the adhesive, due to the presence of water. This will also affect the durability of an adhesive as it will change the chemical microstructure. However, this mechanism is unlikely to occur below about 70°C in the case of most epoxy-based structural adhesives[6].

2.8.3 Kinetics of Attack

2.8.3.1 Introduction

Section 2.8.2 has shown that water can attack the bulk adhesive, the oxide layer on the surface of the adherend, or the interface between them. However, before this can occur, water must reach these areas. The kinetics of water attack are controlled by the rate at which water can enter the joint. The two possible routes are diffusion through the bulk adhesive or along the interface. (Since, as the metal adherends used in the current work are not porous, water cannot diffuse through the adherend.)

2.8.3.2 Bulk Diffusion

Water can enter a joint by diffusion through the adhesive, a process that can often be modelled using Fick's second law of diffusion, providing that the adhesive is at a temperature below its glass transition temperature, T_g. If one-dimensional diffusion is assumed, (i.e. diffusion is limited to the x-direction, for example in a thin film), the concentration of water, C, at any point in a joint to be found after a time, t, using the relation[96]

$$\frac{\partial C}{\partial t} = D\frac{\partial^2 C}{\partial x^2} \qquad (2.20)$$

where D is the diffusion coefficient of the material. Note that above their T_g, epoxy adhesives can exhibit non-Fickian behaviour[63].

For a semi-infinite film of material immersed in water, i.e. where diffusion will be one-dimensional, a solution to the above equation is given by[75]

$$\frac{C_t}{C_\infty} = 1 - \frac{4}{\pi}\sum_{n=0}^{\infty}\frac{(-1)^n}{(2n+1)}\exp\left[\frac{-D(2n+1)^2\pi^2 t}{4l^2}\right]\cos\left[\frac{(2n+1)\pi x}{2l}\right] \qquad (2.21)$$

where the film thickness is 2l.

Equation 2.21 can be integrated to give the mass of water at any point in the film, expressed as the fractional mass uptake, M_t/M , assuming that the film is initially free from water,[75]

$$\frac{M_t}{M_\infty} = 1 - \frac{8}{\pi^2}\sum_{n=0}^{\infty}\frac{1}{(2n+1)^2}\exp\left[\frac{-(2n+1)^2\pi^2 Dt}{4l^2}\right] \qquad (2.22)$$

At short times this may be simplified to

$$\frac{M_t}{M_\infty} = \frac{4}{l}\left(\frac{Dt}{\pi}\right)^{\frac{1}{2}} \qquad (2.23)$$

The value of the diffusion coefficient, D, can be found by immersing a film of adhesive, typically 0.3 to 1 mm thick, in water and measuring the mass increase at intervals[75, 78, 92] The value of D can be calculated from initial slope of a plot of M_t/M_∞ versus t/l, using Equation 2.23. This relationship is typically linear up to $M_t/M_\infty = 0.6$.

Once the value of D has been calculated, the concentration of water at any distance, x, from the edge an adhesive joint can be estimated from Figure 2.16, or calculated using Equation 2.21. The curves shown in this Figure correspond to various values of Dt/l^2. The calculation of water concentrations in an adhesive joint will be discussed further in Chapter 8.

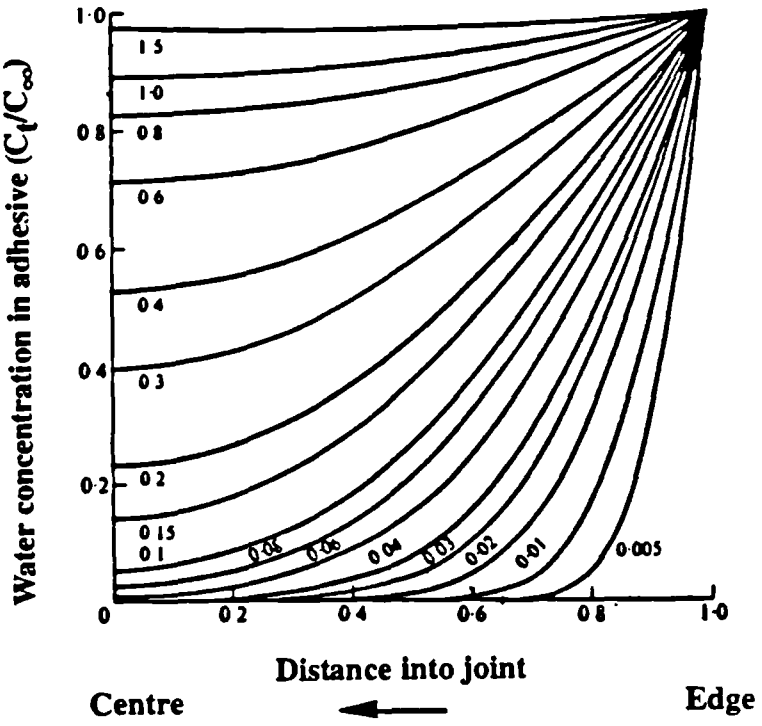


Figure 2.16: Water uptake plot, from Crank[96], showing concentration of water versus proportion of distance from centre of joint for varying values of Dt/l^2.

The rate of diffusion increases with increasing temperature[21]. For example, for the 'AV119' adhesive used in the present work, it is reported[76, 92] that $D = 3.2 \times 10^{-14}$ m²/s at 30°C, but at 60°C, it is 64×10^{-14} m²/s. This is an increase of twenty times over a

temperature range of only 30°C. However, the present work uses a water temperature of 28°C, as higher temperatures may cause leaching of components of the adhesive, as discussed previously.

2.8.3.3 Interfacial Diffusion

Water can also enter an adhesive joint by transport along the interface. In metallic joints this can be the main diffusion mechanism[92]. Work by Ebtahaj[77] has indicated that the interfacial diffusion coefficient may be approximately ten times the bulk value in an aluminium-alloy joint bonded with an epoxy adhesive. Zanni-Deffarges and Shanahan[97] exposed bonded joints to 100 % relative humidity at 70 °C for various time intervals. The torque required to rotate the joint through a set angle in torsion was measured. The effective modulus of the adhesive was calculated, and related to the 'dry' and 'wet' modulii measured using tensile tests. Thus an estimate of the amount of water that had entered the joint could be made. The authors estimated that the interfacial coefficient of diffusion in epoxy/stainless steel joints was approximately four to ten times the bulk adhesive value. They postulated that the increase was due to surface tension effects near the interfacial region increasing the effective driving force for water penetration. Thus with some systems, diffusion along the interface rather than bulk diffusion may dominate the rate of water penetration into the joint.

2.9 Durability Test Methods

2.9.1 Introduction

The most realistic test to evaluate the durability of an adhesive joint is simply to expose it to its 'in-service' conditions and evaluate how well it performs. However, the required life of a joint may be tens of years, and thus laboratory testing aims to accelerate the mechanisms of attack, without introducing new mechanisms that a joint would not experience in service[80, 98] Various methods have been used to test the durability of joints under laboratory conditions, some of the most commonly used of which are outlined below.

2.9.2 'Boeing' Wedge Test

The 'Boeing' wedge test is a simple method to compare the durability of adhesive systems. A DCB-type specimen is prepared, and a wedge used to load the joint, as shown in Figure 2.17. The increase in crack length over a given time is measured, giving a qualitative estimate of the durability performance, see Figure 2.18. However, the results can be misleading if the adhesive creeps excessively, as this will relieve the local

stresses[99]. This test method has proved useful as a quality control test, and if care is taken, for example to generate reproducible initial cracks, it can be considered a useful comparative method. However, the detection level is relatively low and so only serious quality degradation will be identified[5, 100].

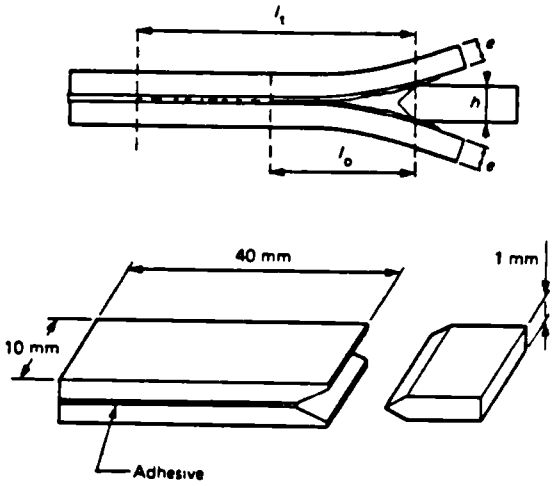


Figure 2.17: Schematic of the 'Boeing' wedge test, from[99], showing typical dimensions used.

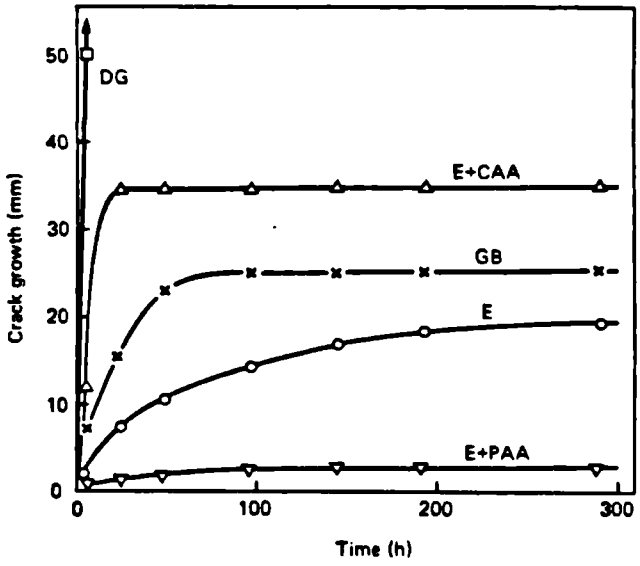


Figure 2.18: Example results from 'Boeing' wedge tests, from[5]. Longer crack growth indicates poor durability. Treatments used: degrease only (DG), chromic-acid etch plus chromic acid anodise (E+CAA), gritblast (GB), chromic-acid etch (E), chromic-acid etch plus phosphoric-acid anodise (E+PAA).

2.9.3 Lap Joints

2.9.3.1 Introduction

The lap joint is one of the simplest test geometries, see Figure 2.19, and is probably the closest to how adhesives would often be used in industry. Although it would appear to be a mode II joint, failure is usually by peeling of the ends of the overlap, and thus the mode I component is considered to dominate failure[54].

This joint geometry may be used to evaluate the durability of adhesive joints in several ways, as discussed below.

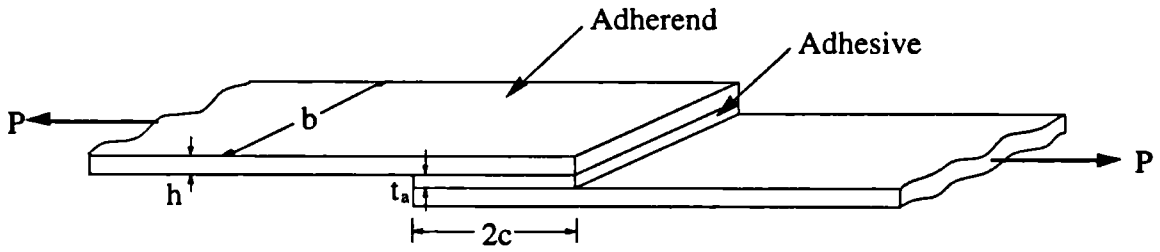


Figure 2.19: Single lap joint.

2.9.3.2 Residual Strength

This method typically uses single, or double, lap joints, which are exposed to a given environment. The joints are not stressed during exposure, but a proportion are removed at intervals and tested at a constant displacement rate[11, 101]. The residual strength is expressed as a percentage of the strength of unexposed joints. Joints may also have holes drilled through the overlap to reduce the time taken for a relatively high water concentration to be achieved[102]. However, constant displacement rate tests on lap joint specimens tend to show significant scatter in the data, so the sensitivity of this method is limited. This test method can also be considered to be unrealistic as most joints will be stressed during service.

2.9.3.3 Constant Stress

Applying a constant stress to a lap joint and exposing it to an environment is a popular method for comparing the durability of adhesive joints[74, 103, 104]. A number of single lap joints, typically six, are bolted together in series and placed in a perforated tube. A spring is used to apply a constant load to the joints, which are exposed to the environment until one fails. The failed specimen is removed and replaced by a blank. This process is repeated until all the joints have failed. The time to failure of the joints is

recorded, giving a relationship between applied load and time to failure, see Figure 2.20. The times to failure are compared, and hence the relative performance of adhesive systems is indicated.

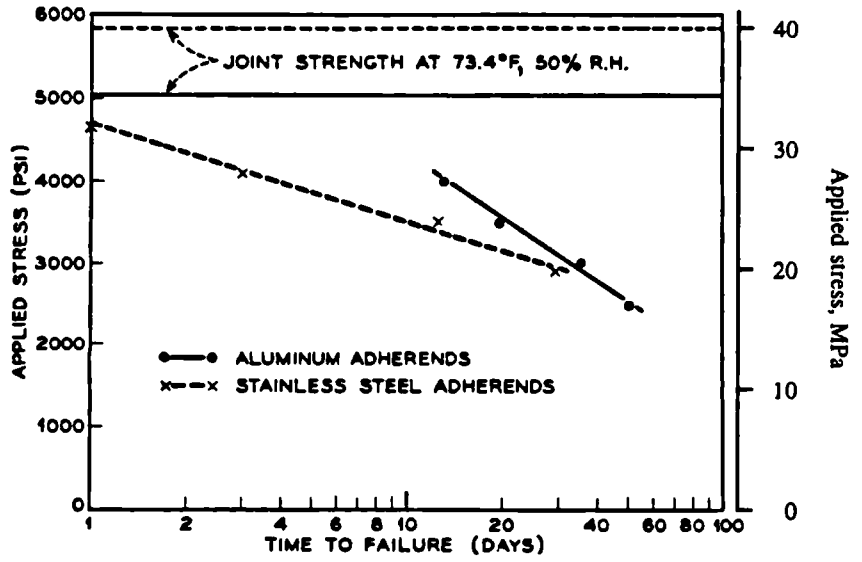


Figure 2.20: Example results from bonded stainless steel and aluminium single lap joints subjected to constant load, from[104]. Test temperature 23°C.

2.9.3.4 Cyclic Fatigue of Lap Joints

Lap joints are also commonly tested in fatigue, at a given percentage of the nominal failure stress measured using a constant displacement rate test[65, 105, 106]. The number of cycles to failure is recorded. The data obtained are equivalent to the S-N curves frequently obtained for metals or plastics. These tests are performed to evaluate whether a threshold stress exists, below which failure will not occur. This is a comparative method. It should also be noted that, as discussed in Section 2.6.4, the joint is loaded with a combination of mode I and mode II stresses. The use of the lap joint when tested at a constant displacement rate and in fatigue will be discussed further in Chapter 10. This method gives an indication of the relative performance of the adhesives.

2.9.4 Fracture Mechanics Tests: Cyclic Fatigue

This method uses either the DCB or TDCB specimen mentioned above[65, 106]. These are subjected to fatigue loading in the presence of an environment, and the rate of crack growth per fatigue cycle, da/dN, measured against the maximum applied fracture energy, G_{max}, see Figure 2.21. The rate of crack growth can alternatively be plotted against ΔG (i.e. $G_{max} - G_{min}$), but there is concern that surface debris prevents the crack from closing

properly, and hence gives an artificially high value of G_{min} [107, 108]. This method will be discussed further in Chapter 8.

A given adhesive and adherend combination will typically show a threshold value of G_{max}, denoted by G_{th} (I in Figure 2.21), below which crack growth does not occur. This is a quantitative test method, and the results can be used to predict the life of other joint geometries, as discussed in Chapter 9. The value of G_{th} can also be used as a 'fail-safe' design limit.

2.9.5 Other Methods

The above methods are some of those most commonly used to evaluate the durability of adhesive joints, but many others exist. These include the notched coating test[109], which uses a thin layer of adhesive exposed to the environment, and hence takes a relatively short time to reach equilibrium water uptake compared with lap joints or DCB specimens. The peel test has also been successfully used to investigate the effect of relative humidity[73, 110] or immersion in water[84] on durability.

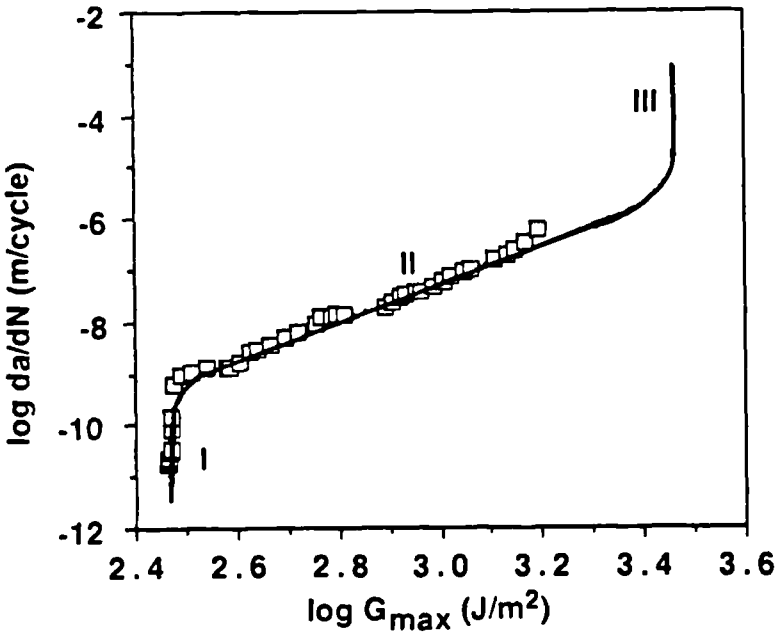


Figure 2.21: Example results from bonded composite DCB specimens tested in cyclic fatigue, from[107].

2.9.6 Fatigue Crack Propagation

As a significant portion of the current work will use the fatigue TDCB test, it is therefore useful to look at the factors affecting fatigue crack propagation (FCP).

Problems can occur with fatigue testing if the chosen frequency is too high. As mentioned above, adhesives are polymeric, and hence are viscoelastic materials. Thus hysteresis will occur, and the adhesive temperature will rise until the heat input equals that lost by conduction and convection. If the glass transition temperature is approached or exceeded, failure may occur by excessive plastic deformation. Thermal effects can also lower the yield stress of the adhesive, causing crack blunting and increased toughness. A frequency of 5 Hz is generally considered low enough to eliminate these effects. This suggestion was supported by thermal imaging work conducted by Harjoprayitno[111] which showed no heating effect at the crack tip of an aluminium-alloy TDCB specimen bonded with a structural epoxy adhesive at frequencies up to 30 Hz.

The effect of test frequency on the rate of crack growth in polymers is dependent on the polymer being studied[29]. For example, the FCP rate decreases with increasing frequency for polystyrene and PMMA, but increases for polycarbonate and nylon 66. In general, those materials that craze easily are more frequency sensitive than those which do not, thus epoxy-based adhesives, which do not tend to craze, are likely to be insensitive to the applied frequency. For adhesives also the effect of frequency is dependent on the adhesive used; some authors have found no effect of test frequency[106, 112], although at very low frequencies, there may be a creep effect which can increase the crack growth rate per cycle[113].

For epoxy adhesives the shape of the loading waveform, be it sinusoidal, square or triangular, does not affect the FCP growth rate, though it can with other polymers[29]. The level of mean stress applied to a joint can also affect the FCP rate, a higher mean stress tending to increase the crack propagation rate. It has been shown[29] for some epoxies that using an R-ratio (P_{min}/P_{max}) of 0.5 will increase the FCP rate compared with an R-ratio of 0.1. However, an R-ratio of 0.1 can also lead to a higher crack propagation rate than using a value of 0.5, as shown by Osiyemi[106].

2.10 Conclusions

This Chapter has reviewed some of the general aspects of adhesion and adhesives to provide background information for the work presented in later Chapters. One aspect that is clear from the work reviewed here is that it is necessary to consider the adhesive joint as

a 'system', (i.e. the adhesive, the adherends and the surface pretreatment used), especially in the durability work where failure can occur at a number of locations.

In the next Chapter, the materials, i.e. the adhesives and adherends, used throughout the current work are discussed. Details of the surface treatments used are also given.

Chapter Three

Materials

3.1 Introduction

This Section provides details of the materials and surface treatments that are common for many of the test methods used in the current work. Structural epoxy adhesives and aluminium-alloy, or steel, adherends were used throughout.

3.2 Adhesives

A range of rubber-toughened structural epoxy adhesives were used in the current work, as listed in Table 3.1. The main adhesive used was the 'AV119' adhesive produced by Ciba Polymers. All the adhesives listed were used for the impact work, while the 'AV119' and 'LMD1142' adhesives were additionally used for the durability tests. These two adhesives were chosen because they represent an older-generation, 'poor' impact-performance adhesive, and a modern 'good' impact-performance adhesive, respectively. Thus the effect of fatigue and water immersion on a 'poor' and a 'good' impact-performance adhesive can be investigated. Further, it can be seen whether the adhesive with a 'poor' impact-performance possesses the better durability.

Stress versus strain data for some of the adhesives are available in the literature. For example, data from tensile tests using the 'AV119' adhesive[44] are shown in Figure 3.1. These data are required for some of the modelling work discussed in Chapter 9, and are also given in Appendix 1.

The glass transition temperatures, T_g, of all the adhesives used were measured using differential scanning calorimetry (DSC)[114]. This technique uses a small sample of adhesive, which is heated from below its expected T_g to about 50°C above it. The heat input and output are measured, and the value of T_g may be calculated from the position of the point of inflection in the response. The measured T_g values are shown in Table 3.1.

Table 3.1: Adhesives used in the current work.

Adhesive	No.	Manufacturer	Form	Cure temperature °C	Recommended cure time	Glass transition Tg, °C
'AV119'	1	Ciba Polymers	Single-part	120	60 min	113
'EA9309'	2	Hysol Dexter	Two-part	23	5 days	79
'ESP110'	3	Permabond	Single-part	150	45 min	107
'LMD1142'	4	Ciba Polymers	Single-part	180	30 min	98
'XB5315'	5	Ciba Polymers	Single-part	190	70 min	85
'XW1044'	6	Ciba Polymers	Single-part	155	50 min	95

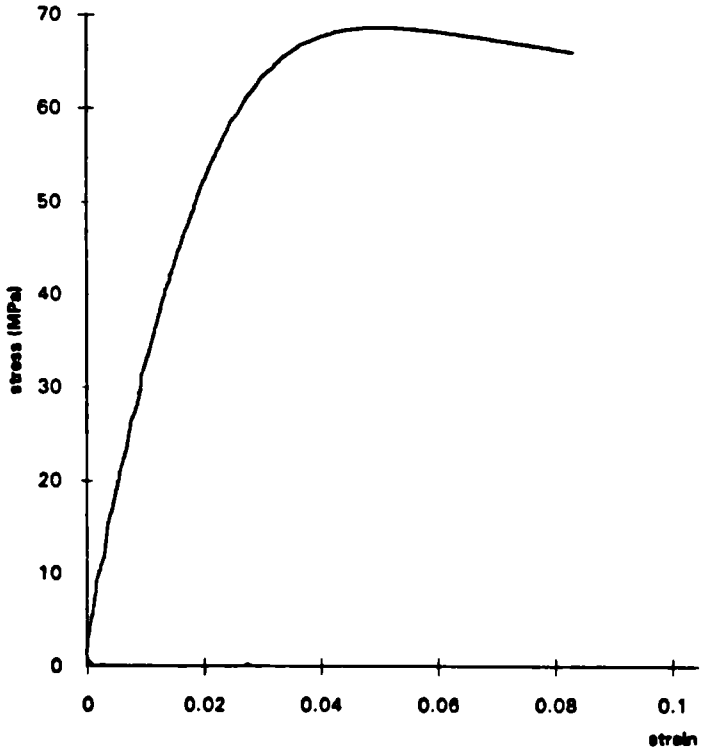


Figure 3.1: Tensile test data for 'AV119' adhesive, from[44].

3.3 Adherends

The current work used mild steel and aluminium-alloy adherends throughout. Mild steel grade 'EN 32B' was used for the adherends of the three point bend and TDCB geometries. This grade is a hardened mild steel which is not available in the thin sheet required for some of the specimen geometries. Thus grade 'EN 3A' was used for these specimens - the impact wedge peel, lap joint and bonded component specimens. There is, however, little difference between these two grades of steel.

The aluminium-alloy used for the impact wedge-peel tests was grade 'EN AW 5251' (alloy designations are taken from British Standard EN 485-2[115]). Originally this was also specified for the TDCB tests, but it was found to plastically deform during testing. As the adherends should remain elastic for this geometry, grades with higher yield stress values were required. Grade 'EN AW 5083' was used for the majority of these tests, though grade 'EN AW 2014A' was required for the 'LMD1142' adhesive as the yield stress of the 'EN AW 5083' was insufficient. The approximate yield stresses, and the measured hardnesses, of the aluminium-alloys used in the present work are shown in Table 3.2. The hardness can be used to differentiate between the alloys. The elemental compositions of the alloys used are given in Table 3.3.

Tensile tests were performed using the steel and aluminium-alloy adherends used for the impact wedge-peel test, and examples of such data are shown in Figure 3.2. The material properties of the 'AV119' adhesive, and the grade 'EN AW 5251' aluminium-alloy and 'EN 3A' steel adherends are summarised in Appendix 1. These data are required for use with the finite element modelling discussed in the present work, for example of the IWP test discussed in Section 6.6 and the modelling work discussed in Chapter 9.

Table 3.2: Yield stress, from[116], and Vickers hardness of aluminium-alloys used in current work.

Alloy	Yield stress, σ_y, MN/m^2	Hardness, H_v
'EN AW 5251'	110	52
'EN AW 5083'	175	87
'EN AW 2014A'	430	160

Table 3.3: Percentage elemental composition of adherends used in present work, from[117], (a) aluminium-alloys and (b) steel.

(a) Aluminium-alloys.

Alloy, 'EN AW'	Si	Fe	Cu	Mn	Mg	Cr	Zn	Ti
'5251'	0.4	0.5	0.15	0.1-0.5	1.7-2.4	0.15	0.15	0.15
'5083'	0.4	0.4	0.1	0.4-1.0	4.0-4.9	0.05-0.25	0.25	0.15
'2014A'	0.5-0.9	0.5	3.9-5.0	0.4-1.2	0.2-0.8	0.1	0.25	0.15

Notes:

(1) Balance is aluminium.

(2) 'EN AW 2014A' also contains 0.1 % Nickel.

(b) Steel.

	C	Mn	P
'EN 3A'	0.2	0.7	0.06

Note: Balance is iron.

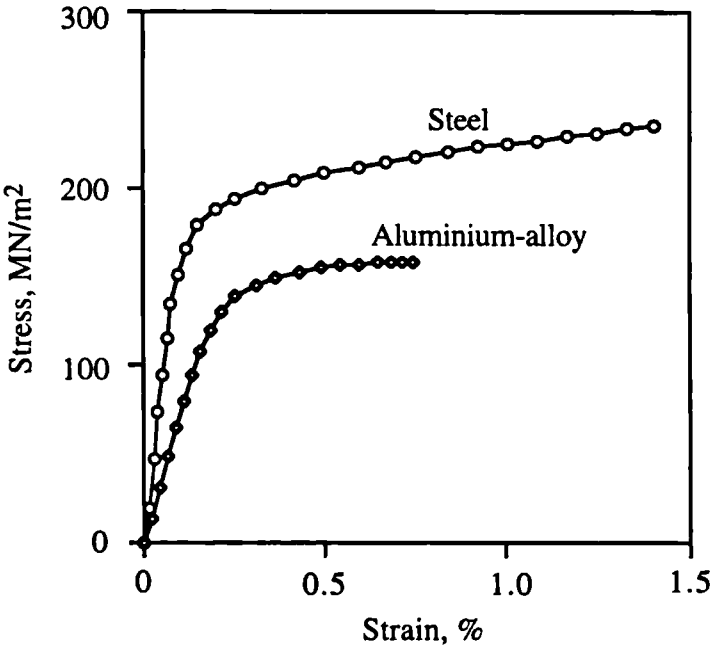


Figure 3.2: Tensile stress versus strain response of aluminium-alloy ('EN AW 5251') and steel ('EN 3A') adherends used for IWP test, at a test rate of 1 mm/min.

3.4 Surface Treatments

3.4.1 Introduction

The basic surface treatment used in the current work was a gritblast and degrease (GB&DG) process. However, a chromic-acid etch (CAE) treatment was used for some aluminium-alloy adherends, as this treatment encourages cohesive-in-adhesive failure. The bonding operation was always completed as soon as possible after surface preparation of the adherends to reduce the risk of surface degradation or contamination[118].

3.4.2 'As Received' Material

The aluminium-alloy and steel adherend materials, in their 'as received' condition, showed a relatively smooth surface, with rolling or machining lines clearly visible using scanning electron microscopy (SEM), see Figure 3.3. The steel adherend material was often received with a thick coating of grease on the surfaces, used to prevent corrosion. This was removed using acetone before any further surface treatment was used.

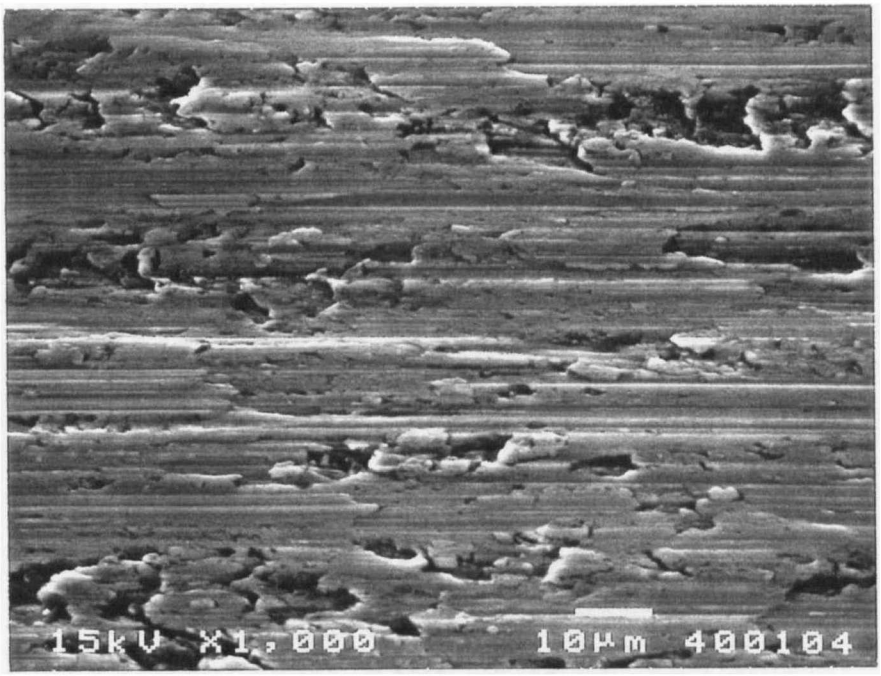


Figure 3.3: Scanning electron micrograph of 'as received' aluminium-alloy, showing machining marks.

The chemical composition of the degreased 'as received' 'EN AW 5251' aluminium-alloy surface was investigated using Auger Electron Spectroscopy (AES). Depth profiling allowed the chemical composition to be analysed at various depths below the surface. In this method, the surface is eroded using an ion beam for a known time, the erosion time having been calibrated using a range of standard materials, and thus the analysis depth is known. An AES analysis is performed, and the process repeated. The results of the AES analyses are shown in Table 3.4. As the depth of the analysis is increased the proportion of aluminium oxide decreases, while the proportion of elemental aluminium increases, as shown by the increasing aluminium to oxygen ratio. These data show that there is carbon contamination on the surface, accounting for 25 % of the total, but this disappears quickly, less than 2 % being present at 1.3 nm below the surface. Surface contamination by carbon may be anticipated because metal surfaces possess a high surface energy and thus attract airborne contaminants, as discussed in Section 2.4.

The AES analysis also shows that there is preferential movement of the magnesium to the surface, as there is up to 8.4 % close to the surface, but only 1.6 % at a depth of 160 nm. The bulk 'EN AW 5251' alloy typically contains 1.7 to 2.4 % magnesium[119].

Table 3.4: Auger electron spectroscopy (AES) data for degreased 'as received' aluminium alloy, grade 'EN AW 5251', showing elemental composition by atomic percentage.

Depth, nm	O	Al	S	C	Ca	Mg	Si
0	51.7	14.6	1.1	24.6	0.6	7.4	0
1.3	59.3	30.0	0	1.6	0.8	8.4	0
5.3	54.6	36.7	0	1.3	0.6	6.9	0
10.7	54.5	39.1	0	0.7	0.4	5.1	0.2
16	43.0	52.7	0	0	0	3.5	0.7
21.5	36.6	60.5	0	0	0	2.3	0.5
29.5	24.7	72.8	0	0	0	2.0	0.5
40	17.5	80.3	0	0	0	1.8	0.4
53.5	15.7	81.9	0	0	0	1.8	0.5
80	11.9	85.9	0	0	0	1.7	0.5
128	8.3	89.7	0	0	0	1.6	0.5
160	6.6	91.4	0	0	0	1.6	0.5

3.4.3 Gritblast & Degrease Treatment

Relatively large adherends were wiped with acetone until the tissue used remained clean after each stroke, showing that no further contamination was being removed. They were then gritblasted with 180/220 mesh alumina grit at 60 or 80 psi for aluminium-alloy and steel adherends respectively. The grit was sprayed at an angle of 45° to the surface so that the particles bounced off the surface rather than becoming embedded in it. The adherends were then degreased again by wiping with acetone as above.

Relatively small adherends were degreased in a bath of 'Genklene N' (Trimite Ltd.), a commercial name for 1,1,1-Trichloroethane. This was later changed to 1,1,1-Trichloroethylene ('Triklone N', Trimite Ltd.) for environmental reasons. They were immersed in the hot liquid solvent for 5 minutes, before being removed and allowed to dry and cool for 5 minutes. After this time they were placed in the vapour for another 5 minutes. They were then gritblasted as above and degreased again in the 'Genklene' as before.

A scanning electron micrograph of the surface produced by the gritblast and degrease treatment is shown in Figure 3.2. The surface roughness has been increased from the 'as received' state, though there is little evidence of re-entrant cavities that might aid mechanical interlocking.

Surface chemical analysis data from gritblasted and degreased (GB&DG) aluminium-alloy surfaces are shown in Tables 3.5 and 3.6 for the 'EN AW 5251' and 'EN AW 5083' alloys respectively. These data show that there is carbon contamination on the surface, accounting for 35 to 40 % of the total. The carbon is relatively tenacious compared with the 'as received' material, several percent remaining at a depth of 40 nm on both specimens. This is probably a function of the surface roughness. The oxide layer is thinner than that seen on the 'as received' sample, 50 % aluminium being present at 10 nm on the GB&DG samples, but only at 16 nm on the 'as received' sample. Small amounts of other contaminants, e.g. sulphur and chlorine, are also identified, but only at the surface.

The 'EN AW 5251' aluminium-alloy (with the lowest yield stress of those used in the present work) contains less magnesium than the 'EN AW 5083' alloy, the bulk compositions typically containing 1.7 to 2.4 % and 4.0 to 4.9 % respectively[116, 119]. However, the surface segregation of the magnesium is evident with both specimens, more magnesium being present at the surface than in the bulk. Further, a depleted zone exists, where the magnesium content is less than in the bulk alloy, i.e. 1 % compared with over 4 % in the bulk for the 'EN AW 5083' alloy, see Table 3.6.

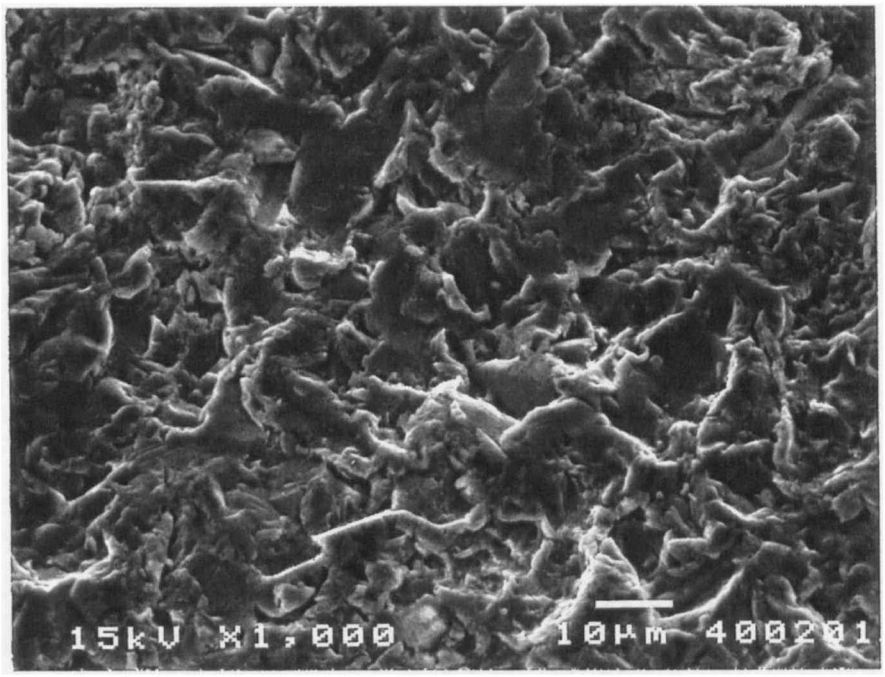


Figure 3.4: Micrograph of gritblasted and degreased (GB&DG) aluminium-alloy surface.

Table 3.5: AES data for gritblasted and degreased aluminium-alloy adherends, grade 'EN AW 5251', showing variation of elemental composition with depth.

Depth, nm	Al	Mg	S	Si	Cl	C	O
0	11.2	5.0	0.9	0	0.8	36.3	45.9
2	29.3	3.6	0.6	0	0	13.4	53.0
6	47.7	2.1	0	0	0	10.0	40.1
10	60.9	2.0	0	0.2	0	7.6	29.3
16	73.8	1.0	0	0.4	0	5.2	19.5
28	80.4	0.8	0	0.3	0	3.5	15.0
40	84.1	0.7	0	0.3	0	2.4	12.5

Table 3.6: AES data for gritblasted and degreased aluminium-alloy adherends, grade 'EN AW 5083', showing variation of elemental composition with depth.

Depth, nm	Al(o)	Al(e)	Mg	Cl	C	N	O
0	10.8	0	6.2	1.0	38.2	1.2	42.6
2.8	30.5	0	7.7	0.5	14.3	0	47.0
6	32.7	2.3	6.1	0	11.1	0	47.8
9.2	26.9	25.0	4.0	0	9.3	0	34.7
12.5	26.0	25.4	4.1	0	9.4	0	35.1
16	16.3	45.4	4.3	0	7.4	0	26.5
20	9.3	65.5	1.5	0	5.4	0	18.4
28	6.1	73.9	1.3	0	4.7	0	14.1
40	4.0	79.2	1.2	0	3.4	0	12.3
56	4.2	81.1	1.1	0	2.5	0	11.0
80	3.3	84.0	1.1	0	2.2	0	9.4
120	3.6	85.1	1.1	0	1.8	0	8.5
240	3.0	86.9	1.0	0	1.7	0	7.4

Note:
Al(o) and Al(e) are the percentages of aluminium in the oxide and elemental forms respectively.

3.4.4 Chromic-Acid Etch Treatment

The aluminium-alloy adherends were first prepared using a gritblast and degrease treatment as described above. They were then placed in a bath of chromic-acid etch (CAE) at 68°C for 10 minutes[118]. They were then rinsed with tap water and placed in a bath of tap water for 15 minutes before being rinsed with distilled water and dried in warm air.

The chromic-acid etch bath is composed of sulphuric acid, sodium dichromate, powdered aluminium and copper sulphate, see Table 3.7. The chromic-acid etch (CAE) treatment produces a surface with rounded pits a few microns in diameter and about 200 nm deep[65], as shown in Figure 3.5. Transmission electron microscopy (TEM) has shown that the oxide is typically about 60 nm thick[65, 120].

Table 3.7: Composition of chromic-acid etch treatment bath, from[65].

40 litres distilled water.
7.2 litres analar quality sulphuric acid (s.g. 1.84).
3.87 kg sodium dichromate.
0.6 kg powdered aluminium.
0.1 kg copper sulphate.

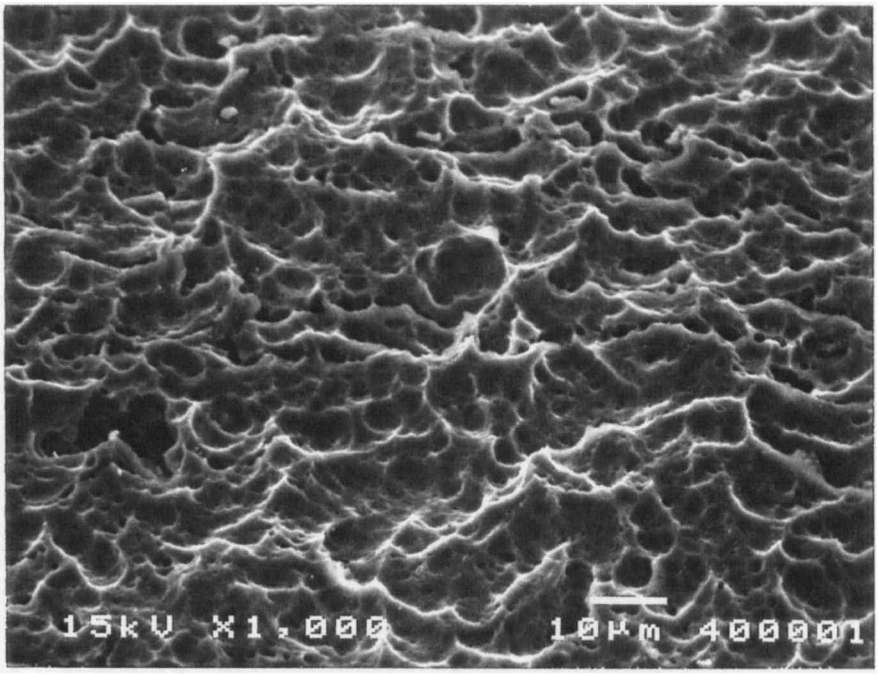


Figure 3.5: Micrograph of chromic-acid etched aluminium-alloy surface.

The AES analysis data shows that the oxide layer produced by the CAE treatment is approximately 15 to 20 nm thick, see Table 3.8. The percentage of magnesium increases from 2.8 % at the surface to 4.8 % at a depth of 18 nm, then decreases to 0.6 % at a depth of 54 nm. The decreased percentage at the surface, compared with the GB&DG treated material, is probably due to the magnesium being preferentially dissolved compared with the aluminium during etching[121].

The calcium present on the surface probably comes from the rinse water. Surface contamination by sulphur, phosphorous and carbon is also identified, although the carbon is only present on the surface of the specimen and none is detected at a depth of

BIBL LONDON UNIV

Table 3.8: AES analysis data for a 'BS AW 5083' aluminium-alloy surface after CAE treatment. Elemental composition by atomic percentage is shown.

Depth, nm	Al(o)	Al(e)	Mg	Cr	P	S	Ca	C	O
0	27.8	0	2.8	0.7	3.9	1.0	2.0	2.8	59.0
2.8	35.8	0	3.1	0.9	0.9	0.6	1.6	0	57.1
6	36.9	0	3.3	0.9	0.9	0.6	1.1	0	56.4
10	34.5	10.6	2.9	0.5	0.9	0.5	1.1	0	49.0
14	23.9	23.9	4.1	0.5	0	0.3	0.4	0	46.9
18	9.4	72.8	4.8	0	0	0	0	0	12.9
28	2.2	92.0	0.9	0	0	0	0	0	5.0
36	2.2	93.3	0.7	0	0	0	0	0	3.7
48	1.3	95.8	0.7	0	0	0	0	0	2.2
54	1.2	96.8	0.6	0	0	0	0	0	1.3

Note:
Al(o) and Al(e) are the percentages of aluminium in the oxide and elemental forms respectively.

2.8 nm. Chromium is also identified in the oxide, up to 0.9 % being present. The presence of chromium is probably a result of the surface treatment, as it is only detected in the oxide. However, the bulk alloy does typically contain 0.05 to 0.25 % chromium[116].

3.5 Adhesive Application

3.5.1 Single-Part Epoxy

After surface preparation of the adherends, a bead of adhesive was applied to both sides of the joint and spread with a spatula until the entire surface was covered. Care was taken not to trap air bubbles. The joint was closed, and the adhesive cured, using the conditions shown in Table 3.1.

The time required to cure the adhesive was calculated by adding the manufacturer's recommended cure time to the time required for the joint to reach the specified cure temperature, as measured by a thermocouple placed in the bondline of a sample joint.

3.5.2 Two-Part Epoxy

The 'EA9309' adhesive is a two-part system consisting of a resin and a hardener, which were used in the ratio of 100:22 by weight. The adhesive was mixed thoroughly, whilst attempting to minimise air entrapment. A bead of adhesive was applied to both surfaces and spread with a spatula. The joint was closed and allowed to cure at room temperature. Full strength is obtained after 3 to 5 days.

3.6 Conclusions

This Chapter has provided details of the adhesives, adherends and surface treatments used in the present work. These are considered in more detail in later Chapters where applicable.

The next part of the present work investigates the impact performance of the adhesives, first considering the tapered double-cantilever beam test.

Chapter Four

Tapered Double-Cantilever Beam Tests

4.1 Introduction

The tapered double-cantilever beam (TDCB) test, as shown in Figure 4.1, is a fracture mechanics test method that is commonly used at test rates in the order of 1 mm/min (10^{-5} m/s), as discussed in Chapter 2. However, recent work has shown that it may also be used successfully at high test rates[114]. Tapered double-cantilever beam tests were performed to determine fracture energy, G_c, values for a range of adhesives. Test rates between 10^{-5} and 1 m/s were used to investigate the effect on the fracture energy from increasing the test rate. The data obtained also allow comparisons to be made with the fracture energies obtained from the three-point bend tests using bulk adhesive and joint specimens, see Chapter 5. Further, these data will be used to investigate the correlation between the adhesive fracture energy and the cleavage-forces measured using the impact wedge-peel tests, as discussed in Chapter 6.

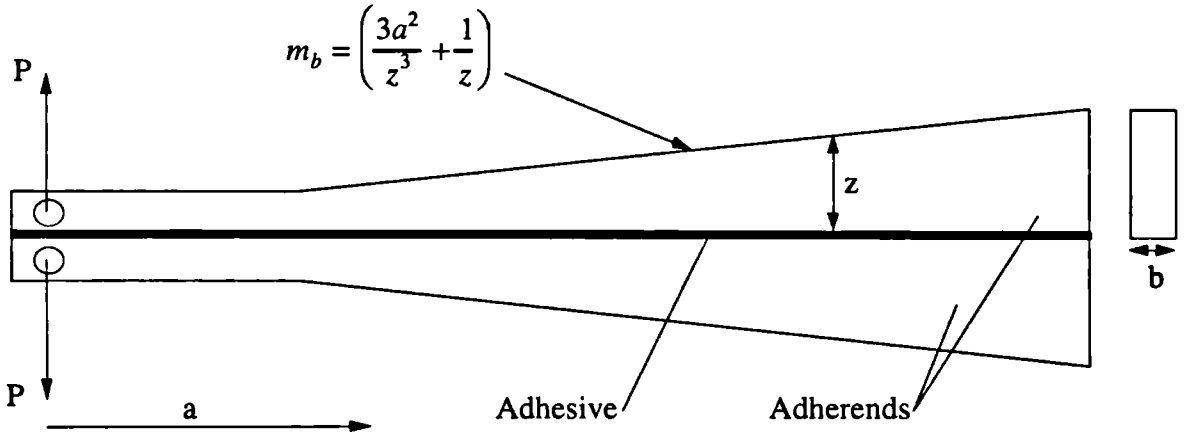


Figure 4.1: The tapered double-cantilever beam specimen.

4.2 Experimental Procedure

4.2.1 Specimen Manufacture

The tapered double-cantilever beam specimens used aluminium-alloy adherends, 10 or 12.5 mm thick. This thickness is sufficient to ensure that plane strain conditions dominate, as discussed in Chapter 2. The tapered profile of the beams was milled on a

computer numerically-controlled milling machine. The surfaces to be bonded were chromic-acid etched, as described in Chapter 3.

The adhesive was applied as a bead to both surfaces and spread over them. Pieces of 0.4 mm diameter stainless steel wire were placed at each end of the joint to control the adhesive layer thickness. Alternatively glass spheres, 0.4 mm in diameter, were dispersed through the adhesive. Both methods gave a constant adhesive layer thickness of 0.4 mm. A double layer of aluminium foil coated with release agent was placed in the middle of the adhesive layer to act as a starter crack, and encourage the adhesive to fail in a cohesive-in-adhesive manner. The two halves of the beam were brought together in a jig, which was pre-heated where applicable. The top and bottom platens of the jig are shaped such that pressure is applied to three points along the length of the beam. The bolts securing the two platens were tightened to a torque of about 5 Nm.

After curing, most of the excess adhesive on the side of the specimens was carefully removed using a chisel, the remainder being sanded off. It was also possible to remove the excess from the specimens bonded using the softer adhesives with a razor blade, doing this as soon as the specimens were removed from the oven after curing. A 20 mm wide strip on the side of the specimen, spanning the adhesive layer, was painted white and marked every 10 mm from the loading point. This enabled the length of the crack to be measured during testing.

4.2.2 Low Rate Tests

Tests were conducted using a screw-driven 'Instron' testing machine, using a test rate of either 0.5 or 1 mm/min (10^{-5} m/s), in order to achieve a crack velocity of approximately 10^{-4} m/s. This will allow comparisons to be made with the results from the impact wedge-peel (IWP) tests discussed in Chapter 6, at the same crack velocity. The force versus time response of each specimen was recorded. A travelling microscope was used to follow the crack tip, and the force versus time response was marked when the crack crossed one of the lines marked on the specimen. This enabled the variation of fracture energy with crack length to be plotted.

4.2.3 High Rate Tests

The beams were tested using a high-speed servo-hydraulic 'Instron' testing machine (HSSHM). Test rates of 0.05 or 0.1 m/s were used, to give a crack velocity of approximately 2 m/s, and hence allow comparisons to be made with the IWP test results, at an equivalent crack velocity. Tests were also conducted at test rates of 0.5 or 1 m/s to

investigate whether the fracture energy of the adhesives decreased with increasing test rate. Force and displacement versus time data were recorded. The tests were filmed using a high-speed camera, as described in Section 4.2.4, as measuring the force can be problematic at high test rates, due to dynamic effects. Analysis of the high-speed films enabled the specimen displacement and crack length data to be obtained.

A schematic of the testing arrangement used for the high rate TDCB tests is shown in Figure 4.2. The test apparatus uses a lost-motion device (LMD), which allows the testing machine ram to accelerate for a short distance and reach the required velocity before it picks up the specimen. The contact between the ram and the LMD is damped using rubber washers to reduce any oscillations when the LMD is picked up. The loading shackles, and other components of the test rig that are attached to the machine ram, as shown in Figure 4.2, are made from titanium to reduce the mass, and hence the inertia of the system. The loading pins used allow the halves of the beam to rotate freely as they deform elastically.

The force on the specimen was measured using a small piezo-electric load-cell, with a natural frequency of 70 kHz and a rise time of 10 μs. A transient recorder oscilloscope was used to record the force versus time data from the load-cell, and the displacement versus time data from the linear variable displacement transducer (LVDT) on the machine ram. A schematic of this arrangement is shown in Figure 4.3. These data were transferred to a computer for analysis. The nominal test rate was calculated from the gradient of the displacement versus time data from the LVDT.

4.2.4 High-Speed Photography

A 16 mm 'Photec IV' rotating prism high-speed camera ('Hadland Photonics') was used to film the high rate tests, to provide crack length and crack velocity data, and hence enable the fracture energy to be calculated using the displacement or crack velocity methods, as discussed in Section 4.3. The specimens were illuminated with floodlights and a focused tungsten spotlight. These were activated immediately before testing to prevent any heating of the specimen. Tungsten-balanced 'Eastman 7250' colour film was used.

A typical TDCB test at 1 m/s lasts about 10 ms. To enable sufficient data to be taken from the film to calculate the fracture energy, the camera was run at its maximum speed of 5000 frames per second. The camera was fitted with a half-frame converter, enabling two pictures to be taken on each frame of film, giving a total of 10,000 pictures per second (pps). This would be expected to give about 100 pictures of a test lasting 10 ms. However, the film used was 100 feet long, and so when the specimen was tested, it would

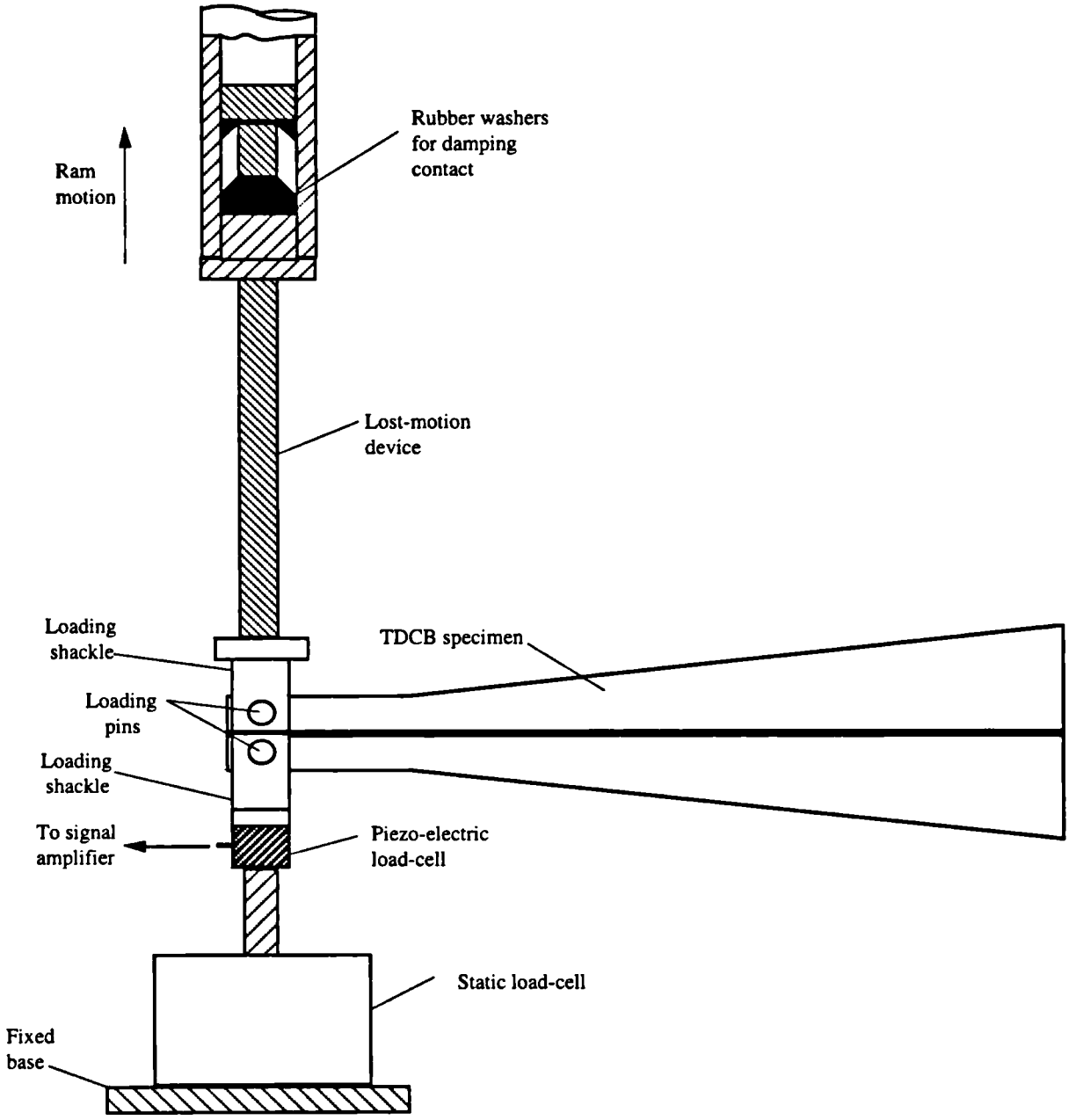


Figure 4.2: High rate TDCB testing rig, showing lost motion device and damping unit.

still be accelerating. Thus the final framing rate was less than that specified. However, as the camera printed a timing mark on the film every millisecond, the exact framing rate attained during the test could be obtained. Further, this enabled the duration of the test to be calculated and compared to the force versus time response. Analysis of the films showed that a framing rate of approximately 6000 pps was attained, giving about 60 pictures of a test lasting 10 ms, i.e. at a test rate of 0.5 to 1 m/s.

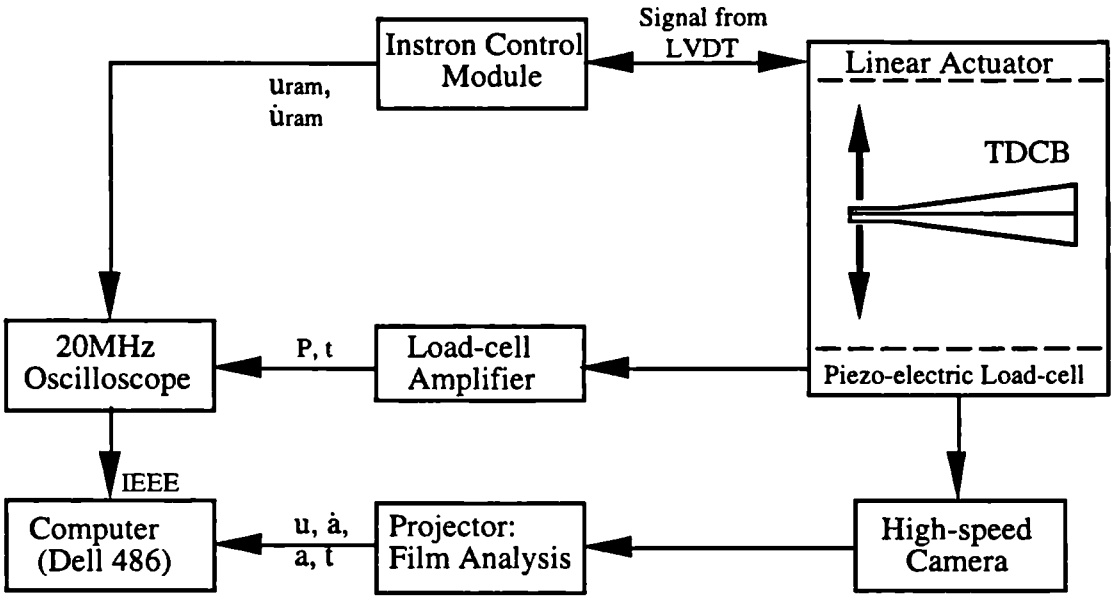


Figure 4.3: Schematic of testing arrangement for TDCB specimens at high test rates.

A disadvantage with using such high framing rates is that as the film speed is increased, the picture quality deteriorates, producing a grainy picture. The picture also becomes darker as less light is absorbed by the film when it is travelling faster, and hence receives a shorter exposure time. These effects combine to make the crack tip, and the edges of the loading pins, difficult to locate on the final image, and may lead to errors in the subsequent analysis of the films.

To analyse the high-speed films, they were projected onto a screen. The displacement of the loading pins and the crack length were measured from the image. The projection magnification factor was calculated from the projected size of the specimen.

The displacement measured using the high-speed photography is the actual specimen displacement. This may not be equal to the displacement calculated from the LVDT on the machine ram. For example, if there is insufficient damping between the lost-motion device and the machine ram then the lost-motion device may bounce. Hence the specimen will not experience a constant displacement rate, and the specimen displacement will not equal that measured by the LVDT. However, there was excellent agreement between the displacement from the LVDT and that from the high-speed photography for the tests in the present work, see Figure 4.4.

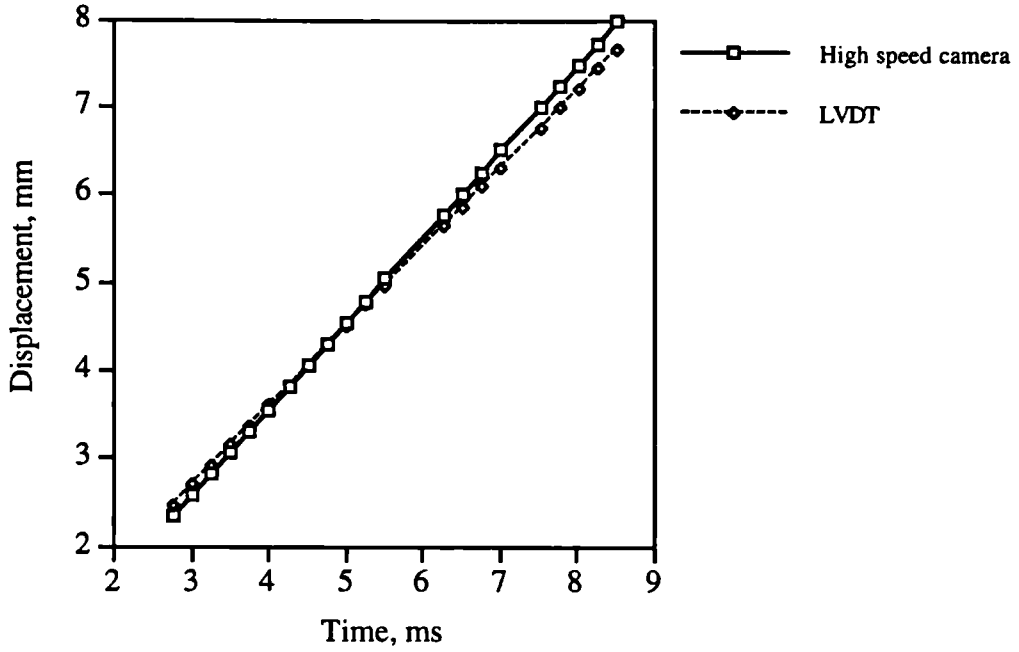


Figure 4.4: Displacement versus time response of aluminium-alloy TDCB specimen bonded with 'LMD1142' adhesive, at a test rate of 1 m/s. Displacement measured using high-speed camera and LVDT on testing machine ram. Note excellent agreement between the two methods.

4.3 Methods of Analysis

4.3.1 Introduction

The tapered double-cantilever beam test is a fracture mechanics test method which is used to measure the fracture energy, G_c, of adhesives. This Section considers various analysis methods that may be used to calculate the fracture energy. Note that all the specimens used in the present work failed in a cohesive-in-adhesive manner, i.e. through the centre of the adhesive layer.

As the fracture energy is a material property, it would be expected that the value would not vary down the length of the beam, and indeed this was found to be the case, see Section 4.4.2. Hence a single average value of the adhesive fracture energy for crack propagation can be quoted.

4.3.2 General Analysis

It has been shown[48, 67] that for a general linear elastic double-cantilever beam, the strain energy release rate, G, is given by

$$G = \frac{P^2}{2b}\frac{dC}{da} = \frac{P}{2b}\left(\frac{u}{C}\right)\frac{dC}{da} = \frac{1}{2b}\left(\frac{u}{C}\right)^2\frac{dC}{da} \qquad (2.6)$$

where P is the measured force, b is the width of the specimen, C is the compliance, a is the crack length, and u is the displacement. Fracture occurs at a critical value of the strain energy release rate, i.e. G_c, the adhesive fracture energy

As discussed in Section 2.7.4.5, the tapered double-cantilever beam (TDCB) geometry is designed such that the value of dC/da is constant as the crack grows through the specimen[122]

$$\frac{dC}{da} = \frac{8m_b}{E_s b} \qquad (2.16)$$

where E_s is the modulus of the adherend and

$$m_b = \left(\frac{3a^2}{z^3} + \frac{1}{z}\right) = \text{Constant} \qquad (2.17)$$

where z is the height of the adherend, see Figure 4.1, and $m_b = 2\ mm^{-1}$.

Integrating Equation 2.16 with respect to the crack length gives an expression for the specimen compliance

$$C = \frac{8m_b a}{E_s b} \qquad (4.1)$$

where a is the crack length.

4.3.3 Force Method

TDCB specimens are commonly used at quasi-static test rates, i.e. 10^{-5} m/s. At these rates the adhesive fracture energy can simply be calculated from the crack propagation force, using the expression derived in Chapter 2, by substituting Equation 2.16 into Equation 2.6,

$$G_c = \frac{4P_c^2 m_b}{E_s b^2} \qquad (2.18)$$

Hence, the adhesive fracture energy can be calculated using the crack propagation force, P_c. At low test rates the crack propagation force is approximately constant as the crack grows through the TDCB specimen, as shown in Figure 4.5a.

At high test rates, dynamic effects, see Section 4.3.5, cause the measured force versus displacement response to become more oscillatory, as shown in Figure 4.5b. An average crack propagation force is calculated and substituted into Equation 2.18.

4.3.4 Force/Displacement Method

Alternatively if force and displacement data are available, by substituting Equations 2.16 and 4.1 into Equation 2.6, the fracture energy may be calculated using

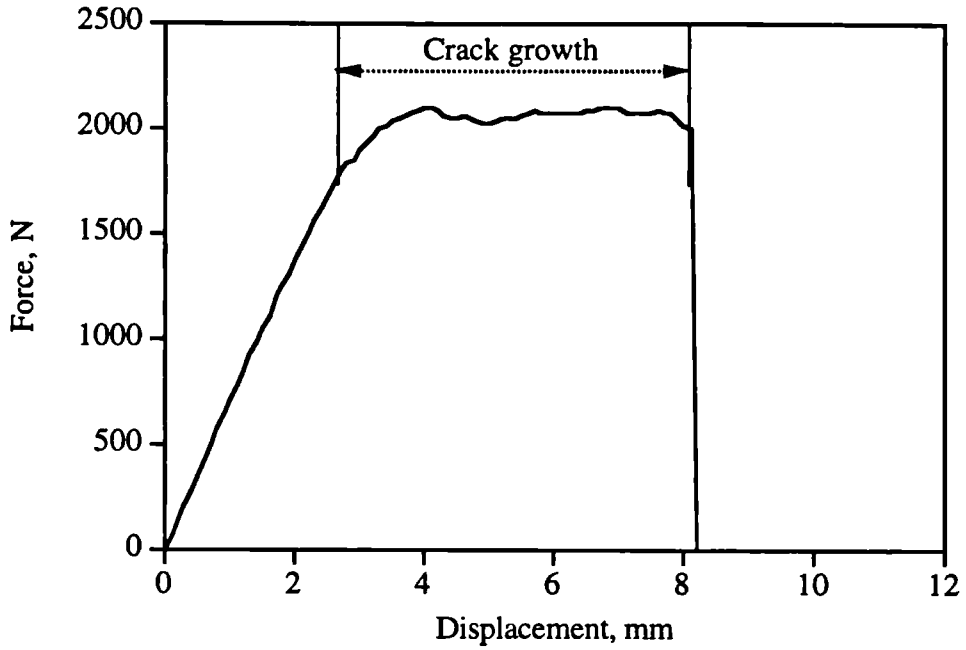
$$G_c = \frac{Pu}{2ba} \tag{4.2}$$

Although the measured displacement increases linearly with time, as shown in Figure 4.4, because the test rate is constant, the measured force may be oscillatory, as discussed in Section 4.3.5. However, the fracture energy may be calculated using the average crack propagation force.

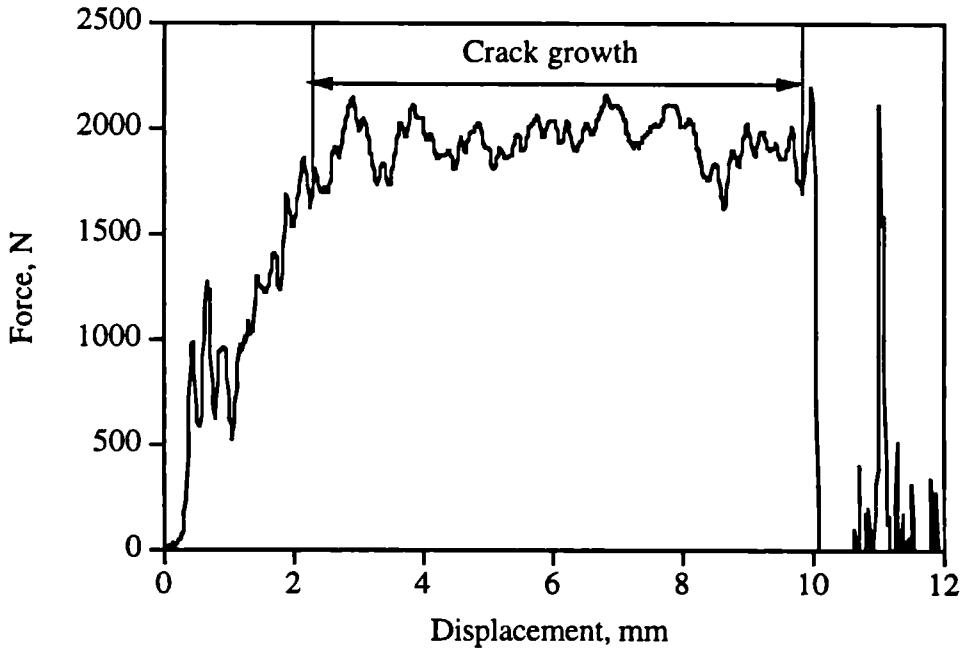
4.3.5 Dynamic Effects

At low test rates the crack propagation force is approximately constant as the crack grows through the TDCB specimen, as shown in Figure 4.5a. As the test rate is increased, dynamic effects can become significant. These dynamic effects cause the measured force versus displacement response to become more oscillatory, as shown in Figure 4.5b. These oscillations mean that a single value of P_c is difficult to determine, as discussed above and shown in Figure 4.5b. These dynamic effects can be caused by high contact stiffness between the testing machine and the specimen, or by the loss and regaining of contact between the two, as discussed in Chapter 2. The oscillations may be reduced by damping the contact, here between the testing machine ram and the lost motion device, using rubber washers, as shown in Figure 4.2.

Oscillations can also be caused by inertial effects, and the repeated reflection of stress waves in the specimen. However, the effect of stress waves is likely to be limited at the test rates used in the present work as the time to failure of the TDCB specimens is large compared to the reflection time[123]. The speed, c, of the longitudinal waves can be calculated using



(a) Slow, test rate of 10^{-5} m/s, crack velocity approximately 10^{-4} m/s.



(b) Fast, test rate of 1 m/s, crack velocity approximately 20 m/s.

Figure 4.5: Force versus displacement response of TDCB specimens bonded using the 'LMD1142' adhesive, (a) slow, test rate of 10^{-5} m/s, crack velocity approximately 10^{-4} m/s, and (b) fast, test rate of 1 m/s, crack velocity approximately 20 m/s.

$$c = \sqrt{\frac{E}{\rho}} \tag{4.3}$$

where E is the modulus and ρ is the density of the specimen. As the thickness of the adhesive layer is small compared to the height of the adherends, the specimen properties are approximately equal to those of the aluminium-alloy. Thus using $E_s = 70$ GN/m^2 and $\rho = 2720$ kg/m^3, the wave speed is approximately 5100 m/s. For the TDCB specimens, which are 300 mm long, the wave travels 600 mm, and the reflection time will be 0.12 ms. Thus even for the tests at 1 m/s, where a test lasts approximately 10 ms, the reflection time is relatively small. Hence the effect of stress waves will be limited, and the loss and regaining of contact between the machine ram and the LMD is likely to be the main cause of dynamic effects.

4.3.6 Displacement Method

As the crack propagation force can oscillate due to dynamic effects, an alternative is to use a force-independent method of analysis. Substituting Equations 4.1 and 2.16 into Equation 2.6 gives

$$G_c = \frac{u^2 E_s}{16 m_b a^2} \tag{4.4}$$

Hence the fracture energy, G_c, can be calculated from the displacement and crack length data obtained using the high-speed photography. Thus the calculated value of G_c is unaffected by the oscillations in the measured force. However, the accuracy of the calculated value of the fracture energy depends on how accurately the displacement and crack length data can be obtained from the high speed films. As discussed in Section 4.2.4, obtaining these data can be difficult at high test rates, due to the relatively poor quality of the pictures. This will lead to some inaccuracies in the calculated fracture energy.

4.3.7 Constant Crack Velocity Analysis

Analysis of the high speed films of the TDCB tests has shown that the test rate and the crack velocity are constant as the crack grows along the length of the specimen (except when stick/slip failure occurs, see Section 4.3.8). Thus the fracture energy can be calculated using a modified form of Equation 4.4,

$$G_c = \frac{E_s}{16 m_b}\left(\frac{\dot{u}}{\dot{a}}\right)^2 \qquad (4.5)$$

where $\dot{u}$ is the test rate, and $\dot{a}$ is the crack velocity measured from the high speed films. For the TDCB specimens tested in the current work the crack velocity is approximately twenty to fifty times the test rate, a larger ratio giving a smaller value of fracture energy. For example, if a crack velocity of 2.2 m/s is measured at a test rate of 0.1 m/s, the fracture energy calculated using Equation 4.4 would be 4.5 kJ/m^2. Hence, a tough adhesive has a relatively low crack velocity compared with a brittle adhesive at the same test rate.

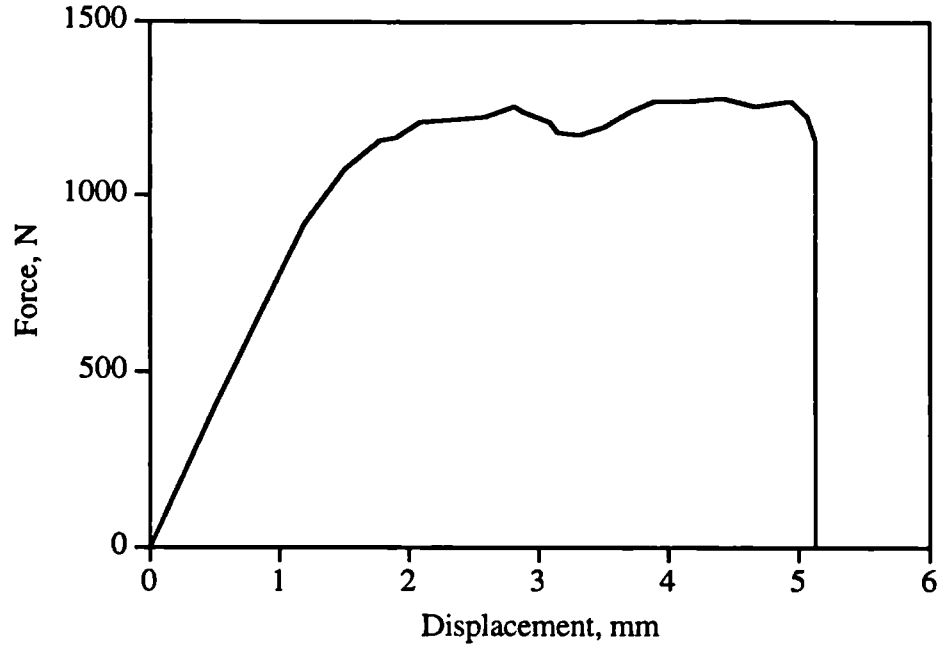
Use of this force-independent method of analysis requires small increments of crack length and displacement to be measured from the high-speed films. This can be difficult, as discussed in Section 4.2.4. Thus the simplest way is to calculate the mean crack velocity and test rate over the period of crack growth, and then to calculate a single value of the fracture energy.

4.3.8 Analysis of Stick/Slip Crack Propagation

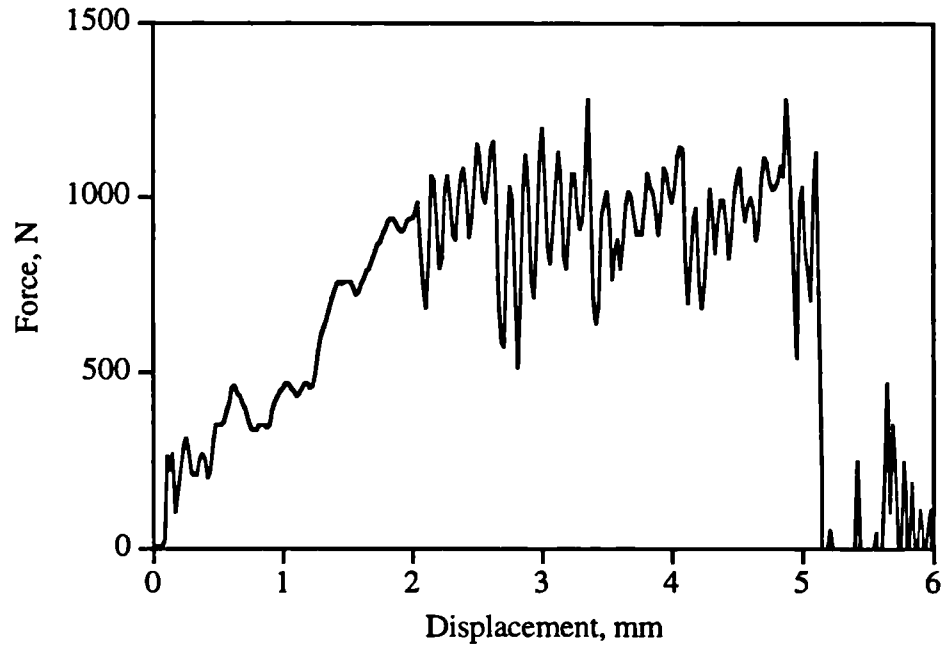
Almost all of the specimens tested failed in a stable, continuous manner. The exceptions were the specimens bonded using the 'ESP110' adhesive at a test rate of 0.5 m/s. These failed in a stick/slip manner, see Figure 4.6b. This behaviour was only observed at for this adhesive and at this test rate; the 'ESP110' adhesive failed in a stable manner at lower test rates, as shown in Figure 4.6a. This type of failure may be analysed by calculating an initiation and/or an arrest value of the fracture energy. However, it should be noted that stick/slip failure may involve crack blunting and the development of a large plastic zone at the crack tip before crack propagation occurs, and hence the initiation values may be artificially high[44]. Thus the magnitude of the reduction of fracture energy with increasing test rate may be underestimated for this adhesive ('ESP110') at this test rate (0.5 m/s).

4.3.9 Comparison of Analysis Methods

All the test results reported in the present work have shown a good correlation between all the analysis methods used. Example results for the 'LMD1142' adhesive are shown in Table 4.1. Similar results were obtained for all the adhesives used in the present work. Thus at test rates of 1 m/s and below, any method of analysis may be used. The calculated



(a) Test rate 10^{-5} m/s



(b) Test rate 0.5 m/s, showing oscillations in the measured force showing stick/slip failure and oscillations caused by dynamic effects.

Figure 4.6: Force versus displacement response of TDCB specimens bonded using the 'ESP110' adhesive, (a) test rate 10^{-5} m/s, and (b) test rate 0.5 m/s, showing stick/slip failure and oscillations in the measured force caused by dynamic effects.

fracture energies were found to be constant with crack length, i.e. no R-curves were seen, as discussed in Section 4.4.2.

Table 4.1: Average fracture energies calculated using various methods of analysis for three tests using the 'LMD1142' adhesive, at test rates of 10^{-5}, 0.1 and 1 m/s. Force versus displacement responses at test rates of 10^{-5} and 1 m/s are shown in Figure 4.5.

Method of analysis	Fracture energy, kJ/m^2		
	10^{-5} m/s	0.1 m/s	1 m/s
Force	4.51	4.18	3.99
Force/displacement	4.47	4.08	3.84
Displacement	4.43	4.00	3.76
Crack velocity	4.40	4.08	3.97

Perhaps the simplest method to calculate the fracture energy is to calculate an average crack propagation force, and calculate the fracture energy using the force method, i.e. using Equation 2.18. The present work has shown that this method produces values of the fracture energy that agree well with those obtained using the other methods. However, obtaining higher test rates than these experimentally using this specimen geometry is difficult, and hence for practical purposes, this method of analysis is applicable at most practical test rates. Further, this method requires only an instrumented testing machine. The other methods require the additional use of high-speed photography.

4.4 Results

4.4.1 Introduction

All the tests conducted in the present work have shown a good correlation between all the analysis methods used, see Section 4.3.9. However, the simplest analysis method to use is the force method, and hence all the fracture energies quoted in this Section were calculated using this method.

4.4.2 Variation of Fracture Energy with Crack Length

For all of the adhesives tested the value of the fracture energy, G_c, was constant with increasing crack length, i.e. there were no R-curves present. This would be expected as the fracture energy is considered to be a material property. Example results are shown in

Figure 4.7, for the 'LMD1142' adhesive (also see Appendix 2). At the low test rate, 10^{-5} m/s, the relationship between fracture energy and crack length is flat, as shown in Figure 4.7a. At the higher test rate, the relationship is not as flat, but the fracture energies calculated using all the methods fall within the range of the fracture energies calculated using the force method, which is indicated using the error bars, see Figure 4.7b.

4.4.3 Variation of Fracture Energy with Test Rate

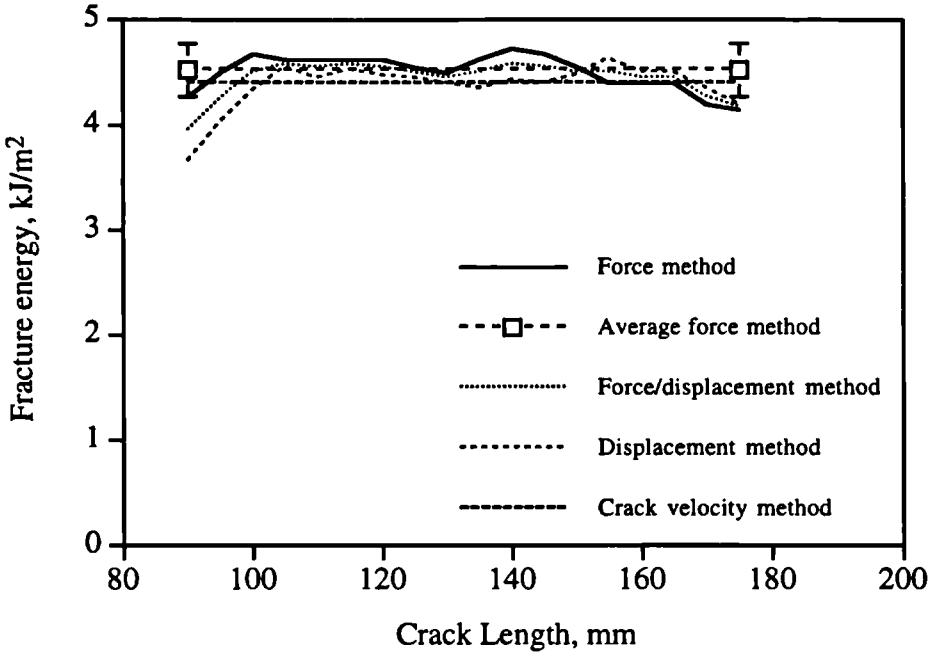
The fracture energies obtained for the range of epoxy adhesives tested in the present work were plotted against the test rate, see Figure 4.8. These data are also shown in Table 4.2 for test rates of 10^{-5} and 0.5 - 1 m/s. All the failures were cohesive-in-adhesive, i.e. failure was approximately through the centre of the adhesive layer.

The measured fracture energies decreased with increasing test rate. Reductions in fracture energy of 12 to 36 % were measured between test rates of 10^{-5} and 1 m/s. Note that the 'ESP110' adhesive failed in a stick/slip manner at a test rate of 0.5 m/s, and thus this value may be artificially high. Hence the quoted fracture energy reduction of 8 % may underestimate the true magnitude of the reduction in performance for this adhesive.

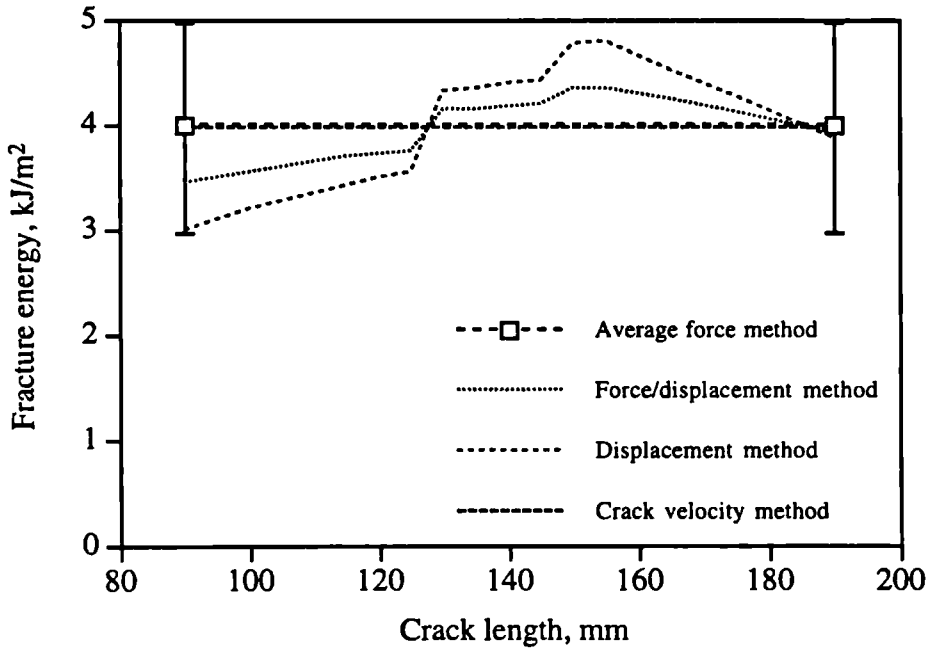
There is no correlation between the fracture energy at low test rate and the value measured at high test rates. Thus a high fracture energy at low test rates does not indicate that the impact performance of the adhesive will be good. For example, the fracture energy of the 'EA9309' adhesive was 3.8 kJ/m^2 at 10^{-5} m/s, but was reduced by 31 % when the test rate was increased to 1 m/s. Conversely low fracture energy adhesives can also exhibit poor performance at the higher test rates. For example the fracture energy of the 'AV119' adhesive was reduced by 36 %, from 0.7 to 0.45 kJ/m^2 as the test rate was increased from 10^{-5} to 0.5 m/s.

4.4.4 Fractography

The fracture surfaces of the TDCB specimens were examined visually and using scanning electron microscopy (SEM). All the specimens used in the present work failed in a cohesive-in-adhesive manner. The fracture surfaces of the specimens bonded using the 'LMD1142' and 'AV119' adhesives were examined in detail, as these adhesives represented the extreme cases of high and low fracture energy amongst the adhesives used in the present work. Both of these adhesives are rubber toughened epoxies, although the 'LMD1142' adhesive probably has polyurethane added to the matrix to improve its fracture properties[124].



(a) Slow, test rate of 10^{-5} m/s.



(b) Fast, test rate of 1 m/s.

Figure 4.7: Comparison of fracture energy values obtained from various analysis methods versus crack length, using TDCB specimens bonded with 'LMD1142' adhesive (a) slow, test rate of 10^{-5} m/s, and (b) fast, test rate of 1 m/s. The relevant force versus displacement responses are shown in Figure 4.5.

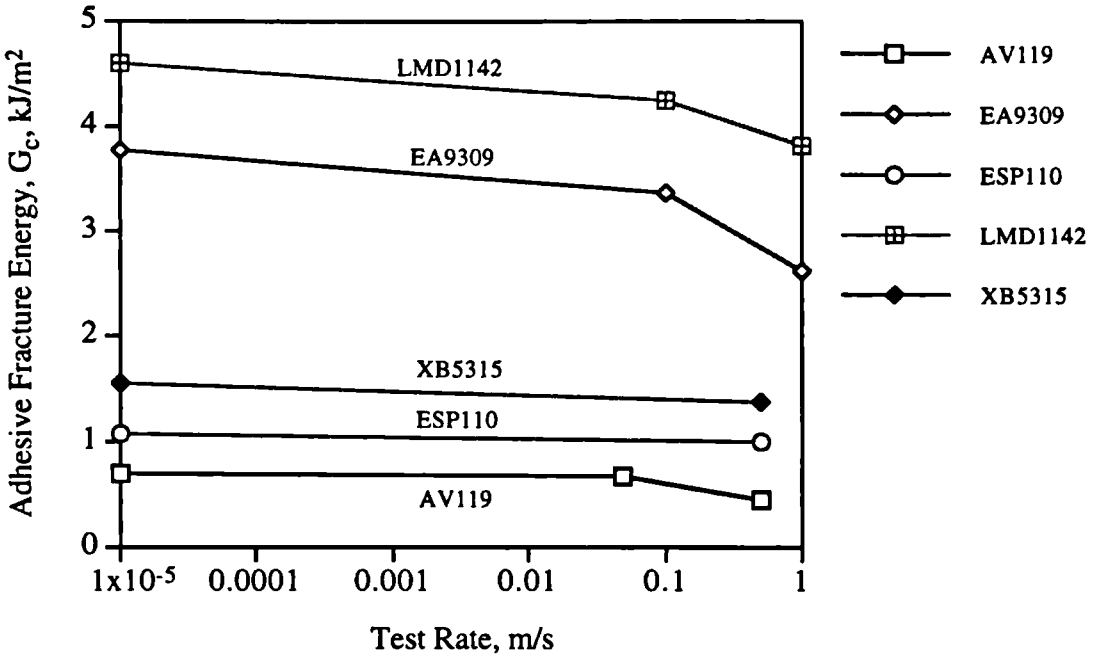


Figure 4.8: Variation in fracture energy with test rate (linear-log axes), from impact TDCB tests. Also see Table 4.1.

Table 4.2: Variation of adhesive fracture energy with test rates of 10^{-5} and 0.5 to 1 m/s, TDCB tests, also see Figure 4.8. Note that the crack velocities are approximately 10^{-4} and 20 m/s respectively.

Adhesive	Fracture Energy, G_c, kJ/m^2		Reduction, %
	Slow (10^{-5} m/s)	Fast (0.5 - 1 m/s)	
'AV119'	0.70	0.45	36
'EA9309'	3.76	2.61	31
'LMD1142'	4.59	3.81	17
'XB5315'	1.55	1.37	12
'ESP110'	1.06	0.98*	8*

* Note:
The 'ESP110' adhesive failed in stick/slip manner at 0.5 m/s.

The micrographs of the fracture surfaces of the 'LMD1142' and the 'AV119' adhesives show significant differences, see Figures 4.9 and 4.10. It should be noted that the crack velocity in both cases was approximately equal, at 10^{-4} m/s. The fracture surfaces of the 'AV119' adhesive are virtually featureless at a magnification of fifty times, see Figure 4.10a. However, the surface of the 'LMD1142' adhesive appears to be composed of a series of 'plates', see Figure 4.9a. The greater deformation and the crack branching which occurs contributes to the greater toughness, and hence the higher fracture energy, of the 'LMD1142' adhesive (4.6 kJ/m^2) compared to the 'AV119' adhesive (0.7 kJ/m^2), as shown in Table 4.2.

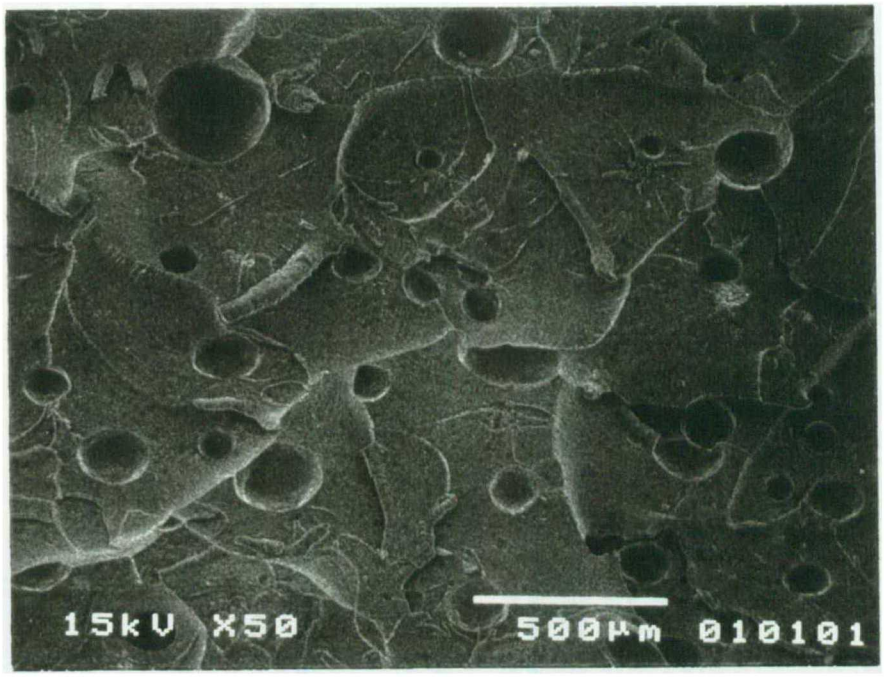
However, it was at a higher magnification that the most significant differences are visible, see Figures 4.11 and 4.12. Cavitated rubber particles can be seen on the fracture surfaces of the 'LMD1142' adhesive. These appear as dark circles, approximately 1 μm in diameter, see Figure 4.11. As discussed in Chapter 2, the cavitation of these particles initiates energy-absorbing mechanisms in the epoxy matrix. The matrix of the 'LMD1142' adhesive is believed to be tougher than the matrices of other commercial epoxy adhesives, due to the addition of polyurethane[124]. Thus large amounts of energy are absorbed by the deformation, resulting in a very high fracture energy, compared with the other epoxy adhesives. In contrast, there was little rubber particle cavitation evident on the micrographs of the fracture surfaces of the 'AV119' adhesive, see Figure 4.12. This is consistent with the low fracture energy of the 'AV119' adhesive relative to that of the 'LMD1142' adhesive.

Differences were also visible for both adhesives at the different test rates. The fracture surfaces of the 'AV119' adhesive appeared rougher at the lower test rate, indicating more deformation had occurred, see Figure 4.10. This lesser degree of deformation is consistent with the lower fracture energy measured at the higher test rate. An average fracture energy of 0.7 kJ/m^2 was measured at 10^{-5} m/s, and 0.45 kJ/m^2 at 1 m/s for the 'AV119' adhesive. The same was true for the 'LMD1142' adhesive, where the surfaces of the 'plates' on the fracture surface appeared rougher at the lower test rate, see Figure 4.9. Further, at high test rates, less rubber particle cavitation is evident, see Figure 4.11b, and hence a lower fracture energy is measured. The fracture energies measured at the test rates shown were 4.6 and 3.8 kJ/m^2 at 10^{-5} and 0.5 m/s respectively for the 'LMD1142' adhesive.

These observations agree with those in the literature, which indicate that the toughening mechanism of shear yielding initiated by the rubber particles does occur at high rates, as the adhesive fracture toughness is not reduced to that of the adhesive without the rubber particles[60,169]. However, the toughening mechanism is less effective at high rates.

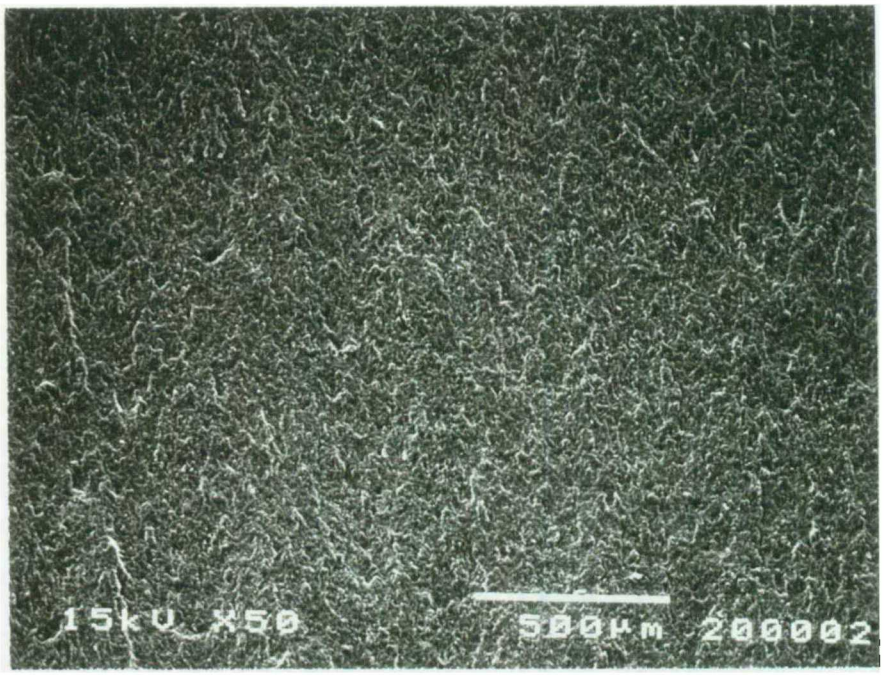


(a) Test rate 10^{-5} m/s, crack velocity approximately 10^{-4} m/s.

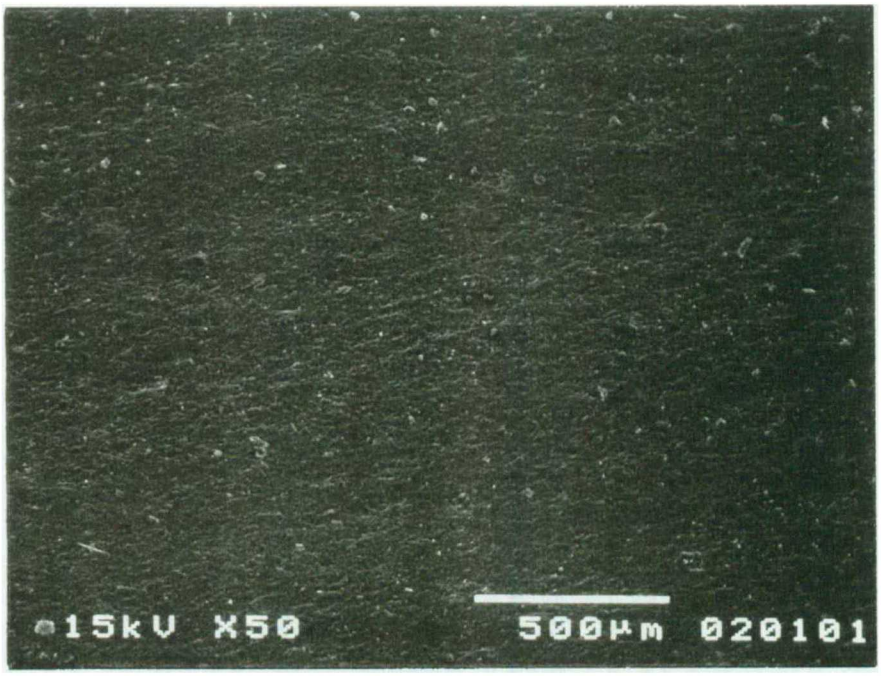


(b) Test rate 1 m/s, crack velocity approximately 20 m/s.

Figure 4.9: Micrographs of fracture surfaces of aluminium-alloy specimens bonded with the 'LMD1142' adhesive, (a) test rate 10^{-5} m/s, and (b) test rate 1 m/s. (Note that the relatively large (0.4 mm diameter) circles shown are the glass beads used to control the adhesive layer thickness.) (Crack propagation is from top to bottom.)

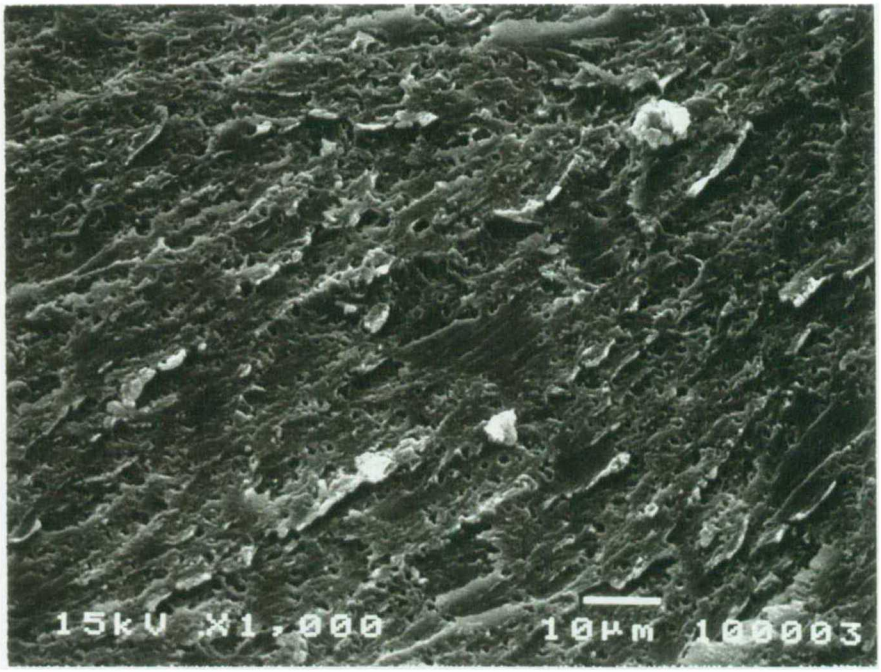


(a) Test rate 10^{-5} m/s, crack velocity approximately 10^{-4} m/s.

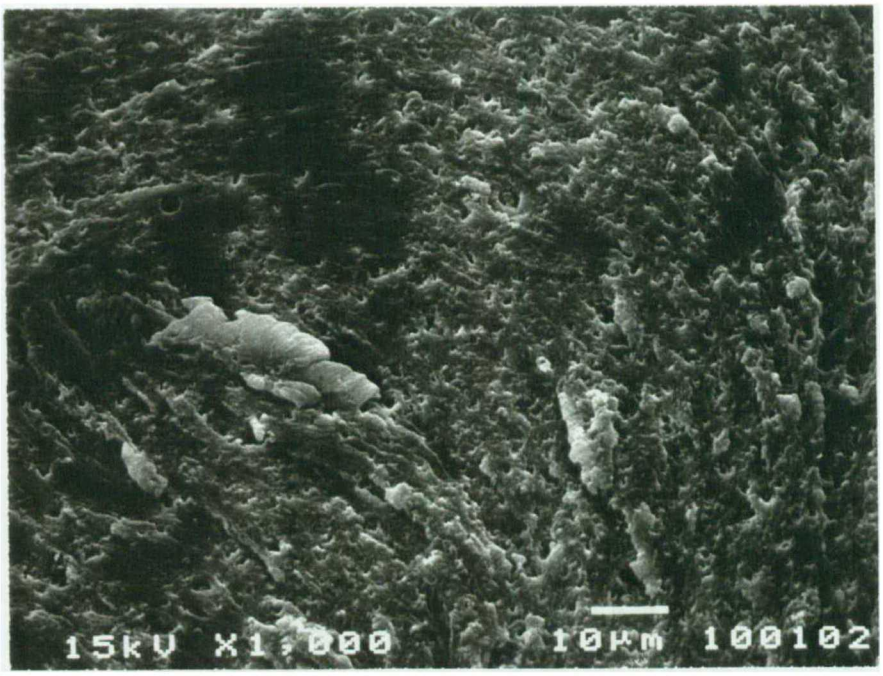


(b) Test rate 0.5 m/s, crack velocity approximately 20 m/s.

Figure 4.10: Micrographs of fracture surfaces of aluminium-alloy TDCB specimens bonded with the 'AV119' adhesive, (a) test rate 10^{-5} m/s, and (b) test rate 0.5 m/s. (Crack propagation is from top to bottom.)

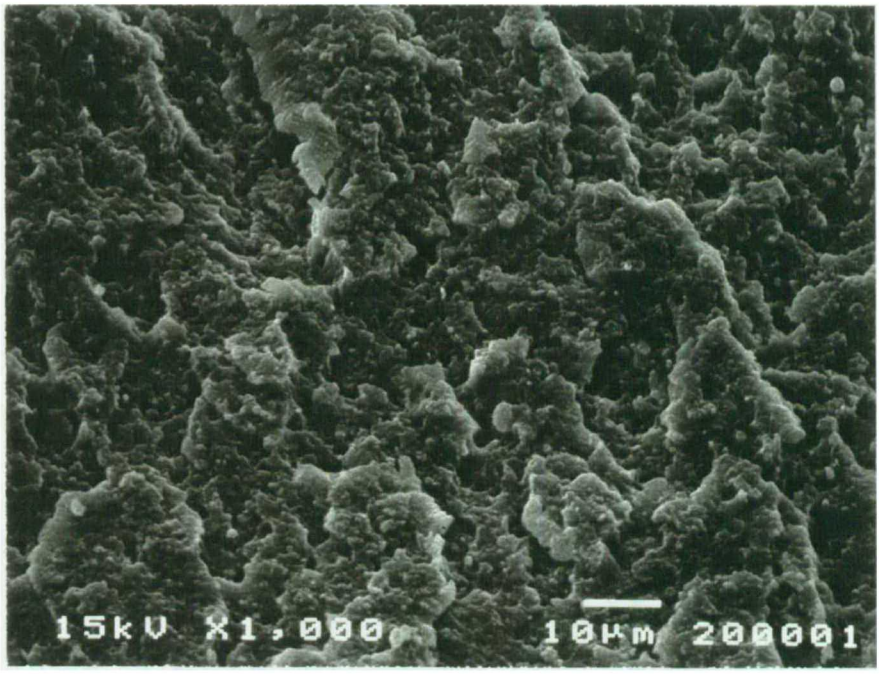


(a) Test rate 10^{-5} m/s, crack velocity approximately 10^{4} m/s.

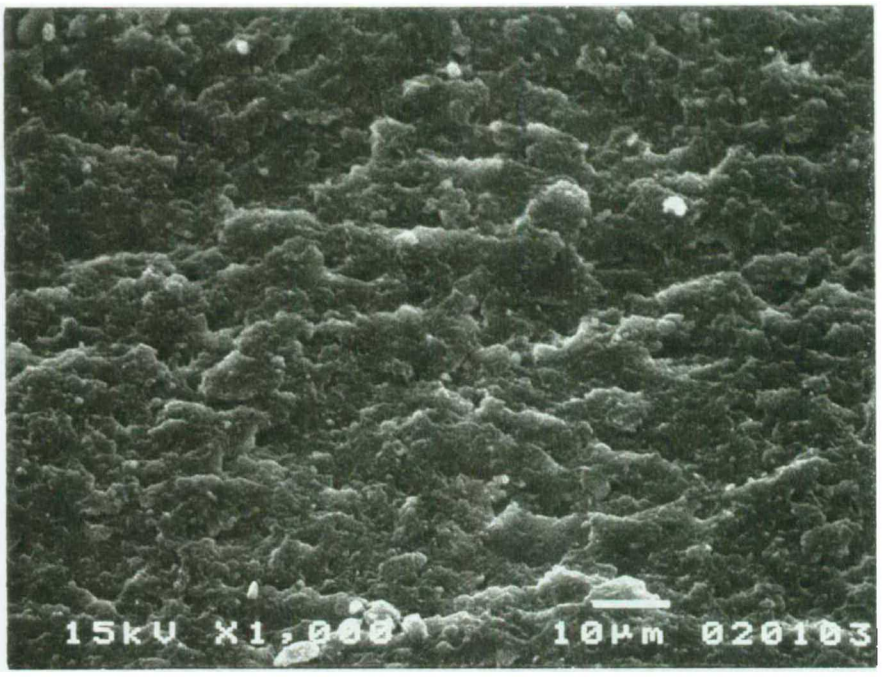


(b) Test rate 1 m/s, crack velocity approximately 20 m/s.

Figure 4.11: Micrographs of fracture surfaces of aluminium-alloy specimens bonded with the 'LMD1142' adhesive, (a) test rate 10^{-5} m/s, and (b) test rate 1 m/s. (Crack propagation is from top to bottom.)



(a) Test rate 10^{-5} m/s, crack velocity approximately 10^{-4} m/s.



(b) Test rate 0.5 m/s, crack velocity approximately 20 m/s.

Figure 4.12: Micrographs of fracture surfaces of aluminium-alloy TDCB specimens bonded with the 'AV119' adhesive, (a) test rate 10^{-5} m/s, and (b) test rate 0.5 m/s. (Crack propagation is from top to bottom.)

4.5 Conclusions

The fracture energies of a range of structural epoxy adhesives were measured over a range of test rates between 10^{-5} and 1 m/s. For all of the adhesives tested, the value of the fracture energy, G_c, was constant with increasing crack length, i.e. no R-curve was present.

A range of methods were used to calculate the fracture energies of the adhesives. The fracture energies calculated using all the analysis methods investigated in the present work between tests conducted at all the test rates used have shown good agreement. At test rates of 1 m/s and below, any method of analysis may be used. However, the simplest analysis method to use is the force method, as only the force versus time data are required. The other methods require high-speed photography to obtain displacement, crack length or crack velocity data.

At test rates of more than 1 m/s, force-independent methods of analysis, using the test rate and average crack velocity may be required if the force data becomes very oscillatory due to dynamic effects. These force-independent data may be obtained using high-speed photography.

All the adhesives tested showed a reduction in fracture energy with increasing test rate. The magnitude of the reduction varied from only 8 % to over 35 % for the range of adhesives tested as the test rate increased from 10^{-5} to 1 m/s, i.e. as the crack velocity was increased from 10^{-4} to 20 m/s.

SEM of the fracture surfaces showed that as the test rate was increased the fracture surfaces showed less rubber particle cavitation and less deformation. The surfaces of adhesives that showed low fractures energies appeared smooth and almost featureless, indicating that little deformation had occurred.

Chapter Five

Three-Point Bend Tests

5.1 Introduction

The three-point bend (TPB) or Charpy test is a Standard method[57, 58] for determining the mode I fracture energy, G_c, of a range of materials, as discussed in Section 2.6.5.2. This test method will be used to compare the performance of bulk adhesive and joint specimens, using the 'AV119' adhesive. The results obtained using this method will be compared to those from the TDCB tests described in the previous Chapter. This will attempt to establish whether the initiation value of G_c is dependent predominantly on the test rate or the time to failure, t_f. The recently introduced European Structural Integrity Society (ESIS) protocol[58] will be used to analyse the results of the high rate TPB tests. The influence of dynamic effects will be considered, and their reduction using damping material will be discussed. SEM of the fracture surfaces will be used to investigate any differences in the fracture surfaces at different test rates, or between the bulk and joint specimens.

5.2 Experimental Procedure

5.2.1 Introduction

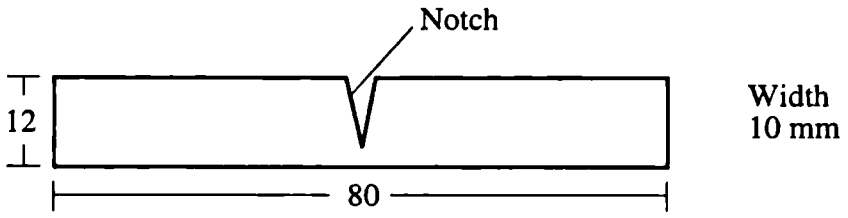
The TPB specimens were tested on two different machines at various test rates. An impact pendulum machine ('CEAST', Italy) and a high-speed servo-hydraulic machine ('Instron', UK) were used. Tests were conducted at test rates of 0.5 m/s on the pendulum machine, and at 0.3 and 2 m/s on the high-speed servo-hydraulic machine (HSSHM).

The current work used both bulk and joint specimens, 80 mm long with a 10 x 12 mm cross-section, as shown in Figure 5.1. These were notched to a depth of between 0.6 and 9 mm, as in previous work[49, 60, 125]. The specimens were placed centrally on a pair of supports, as shown in Figure 5.2. The supports are 48 mm apart, corresponding to the nodes of a beam of this length in free vibration. This reduces the magnitude of any oscillations when the specimen is struck.

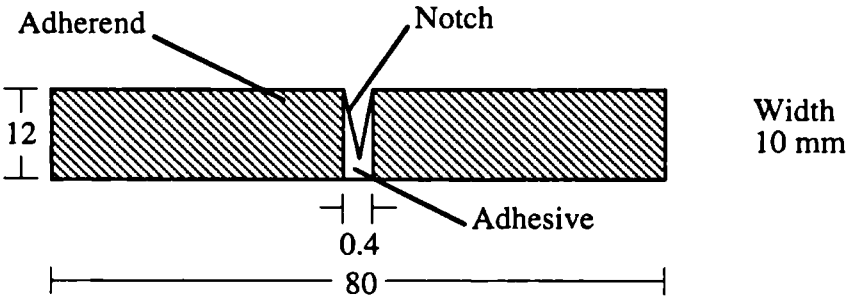
The adhesive fracture energy, G_c, is calculated by plotting the energy absorbed during the test versus a function of the notch depth. The notch tip should be sharp enough that a

true 'lower bound' value of the fracture energy is calculated. A blunt crack will give a fracture energy that is erroneously high.

When the time to failure is in the order of 1 ms or less, dynamic effects, as discussed in Chapter 2, can be expected to become significant. These effects will be considered in Section 5.4.



(a) Bulk adhesive specimen.



(b) Adhesive joint specimen.

Figure 5.1: Three-point bend specimens, showing dimensions used, (a) bulk adhesive specimen, (b) adhesive joint specimen. All dimensions in millimetres.

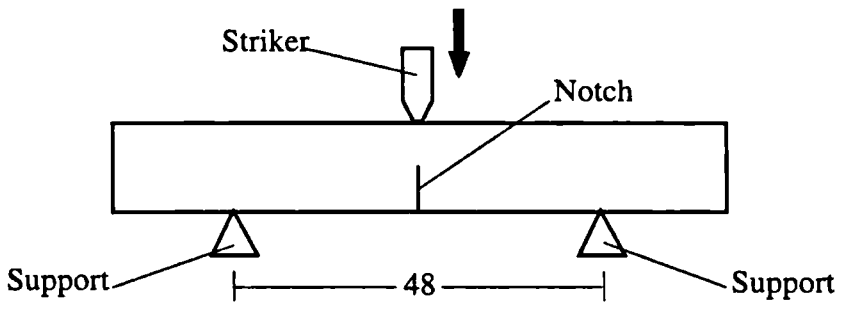


Figure 5.2: Three-point bend test arrangement. Dimensions are in millimetres.

5.2.2 Specimen Manufacture

5.2.2.1 Bulk Specimens

Bars of bulk 'AV119' adhesive were prepared by 'AEA Technology'. The 'AV119' adhesive was injected into an evacuated mould and cured for 8 hours at 80°C, followed by a post-cure of 2 hours at 120°C. This cure schedule prevented the heat produced by the exothermic reaction during cure from over-heating and damaging the adhesive[126]. Bars approximately 15 x 25 x 400 mm long were produced. The use of the vacuum ensured that air entrapment was kept to a minimum.

Approximately eight specimens of the required size were milled from each bar of bulk adhesive. These were notched with a single-point cutter, producing a V-shaped notch. Kinloch and various co-workers[60, 125] inserted a natural crack into their specimens by tapping a razor blade into the notch, causing a crack to jump ahead of the notch tip. This method was tried, but a natural crack could not be generated. Attempts to produce a natural crack required high forces, such that the razor blade became embedded in the specimen. Care must also be taken that the crack arrests after a short distance without fracture of the specimen. However, cracks could not be initiated using this technique.

Thus in the current work, the notches were sharpened by drawing a razor blade across the notch tip. This method is recommended for use with polymers by the European Structural Integrity Society (ESIS) protocol[58] when a natural crack cannot be produced. However, it should be noted that this method may produce a crack tip that is blunter than a natural crack, and hence an erroneously high fracture energy value may be obtained. The razor blade cannot simply be pressed into the notch tip as this can lead to residual stresses being imposed[58].

5.2.2.2 Joint Specimens

The joint specimens used steel adherends, prepared using a gritblast and degrease surface treatment, as described in Chapter 3. In common with the other tests in the current work, an adhesive layer thickness of 0.4 mm was used.

In previous work, three-point bend joint specimens have been made by moulding silicone rubber around a blank, the same size as the finished specimen[60, 125]. This blank is then removed, and the adherends, cut to length to give the required adhesive thickness, placed in the mould. The adhesive is poured into the gap between the adherends, and cured.

However, this method was found not to be practicable for the 'AV119' adhesive due to its high viscosity. The adhesive would not flow into the gap between the adherends, but bridged across it instead. This was the case both at room and elevated temperature, although raising the temperature of the adhesive does reduce its viscosity. Specimens were then made using longer silicone rubber moulds, allowing the adhesive to be injected into the gap between the adherends before they were pushed together. However, it was found that, due to the high coefficient of friction and the low stiffness of the rubber, the adherends tended to be misaligned in the finished specimen. A metal mould was designed, see Figure 5.3, which proved to be successful in eliminating these problems. However, the mould needs to be pre-heated and the cure time for the 'AV119' adhesive extended to 3 hours at 120°C due to the high thermal inertia of the mould. All the joint specimens used in the current work were produced using this metal mould, as described below.

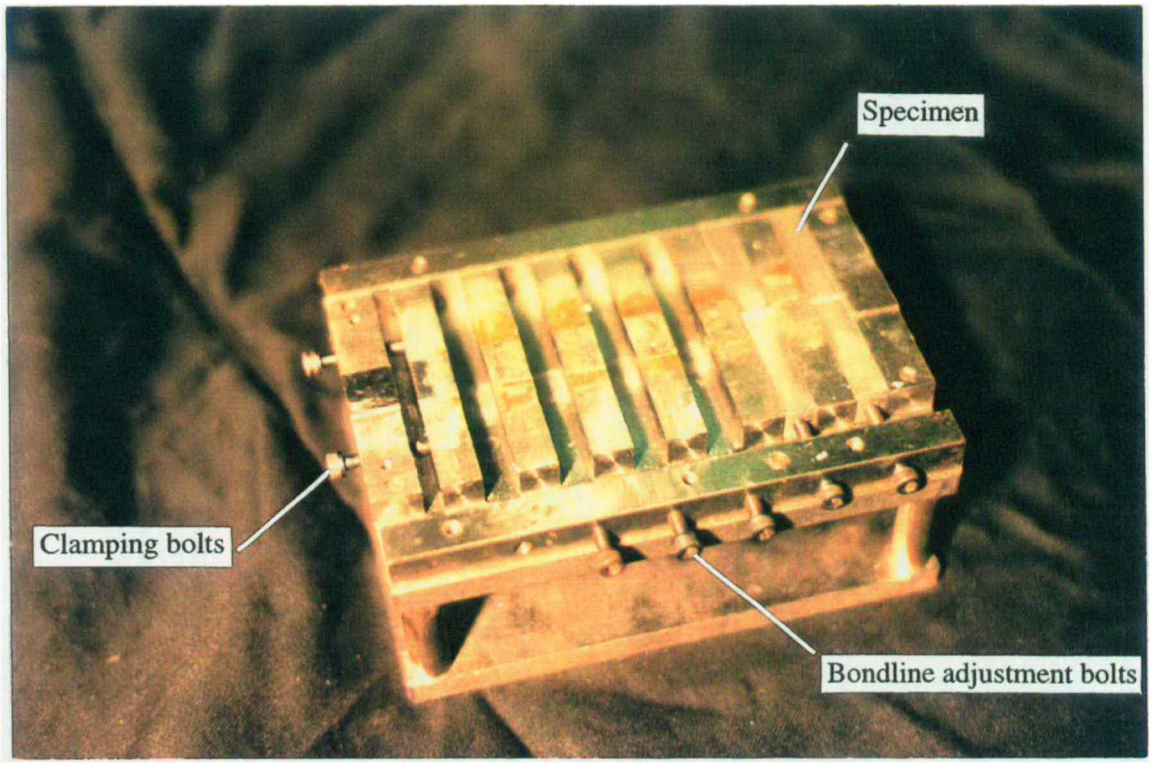


Figure 5.3: Metal mould for TPB joint specimens.

Prior to bonding, the adherends were sawn to length to give a finished specimen length of approximately 80 mm, including the adhesive. The saw marks were removed by grinding the surfaces to be bonded. A jig was used to ensure that the finished surface was perpendicular to the sides of the specimen. This kept a constant adhesive thickness across

the joint. The surfaces of the adherends to be bonded were gritblasted and degreased, as described in Section 3.4.2.

The adherends were placed in the metal mould, leaving a gap of approximately 8 mm between each pair. The clamping bolts were tightened, such that one of each pair of adherends was just able to slide in its slot. The adhesive was injected into the gap between the adherends, ensuring that the tip of the nozzle was kept below the surface of the dispensed adhesive to prevent air entrapment. The adhesive layer adjustment bolts were tightened to move each adherend towards its pair, a weight being used to prevent the adherends from tipping whilst being moved. The spacers between the specimens are stepped such that they come to the full height of the specimen at the adhesive layer, see Figure 5.3, preventing any leakage of adhesive, but allowing the weight to press down on the adherends for almost their full length.

A digital vernier calliper was used to measure the total length of the specimens. When all six specimens had a 0.5 mm adhesive layer thickness, the weight was removed and the excess adhesive removed. The weight was replaced, and the adhesive layer adjustment bolts tightened finally to give a 0.4 mm adhesive layer thickness. The slight excess of adhesive left in the adhesive layer allowed for the improved gap filling due to the reduction in the adhesive viscosity as the temperature is increased during cure. However, if a large excess of adhesive is left then the adhesive tends not to flow, and not fill the gaps. The clamping bolts were finally tightened, and the joints cured. After curing, any excess adhesive was removed using a file and emery paper.

The narrow adhesive layer of the joint specimens prevented the use of the V-shaped single point cutter, as used with the bulk specimens. Notches were initially machined by using a razor blade mounted as a cutter in a milling machine. The notch must be machined in small increments to prevent damage to the specimen or cutter. This also ensures that the notch is straight, as longer notches tend to become curved because the razor blade is relatively flexible compared to the single-point cutter. Thus this method is very time-consuming. Attempts were made to propagate a natural crack in the specimens by tapping a razor blade into the notch produced. However the narrowness of the notches made this impossible as the blade tended to stick part of the way down the notch without initiating a crack. Razor blades that were thin enough to reach the bottom of the crack either bent or fractured at the tip when tapped. Thus a natural crack could not be produced with these specimens.

To check whether the production of a sharper crack tip was necessary, some joint specimens were tested on the pendulum machine with the razor blade machined notch

alone. However, the force required to fracture these specimens was greater than the capacity of the load-cell, and the energies were considerably higher than for the bulk specimens. From this it must be concluded that this method does not give a sufficiently sharp notch tip.

To produce a wider notch a jeweller's saw was used. This allowed the razor blade to reach the bottom of the notch. However, there were still problems with trying to propagate a natural crack, and a natural crack could not be initiated. Thus the notch was sharpened by drawing a razor blade across the notch tip. This method was used to prepare all the joint specimens for which results are presented, as for the bulk specimens.

5.2.3 Pendulum Machine Tests

The pendulum testing machine used is shown in Figure 5.4. The striker is mounted on the pendulum, and allowed to impact the specimen. The velocity at impact can be altered by varying the angle from which the pendulum is dropped. The striker is instrumented, and is used to measure the force versus time response of the striker. The response is recorded by a transient recorder, and the data transferred to an 'Apple II' computer for analysis. The computer software displays the force versus time response of the striker, and calculates energy and displacement data using the mass of the pendulum and the test rate at impact.

Prior to testing a static calibration of the load-cell is performed using a dummy specimen placed on the specimen supports. A calibration frame is fitted to the machine, and the pendulum placed such that the striker is in contact with the dummy specimen. Weights are added to the frame, and the load-cell output is compared to the manufacturer's published data. The zero load and the load-cell gain are adjusted to achieve the best agreement between the measured output and the published data over the working range. The weights and calibration frame are then removed. The pendulum drop angle is adjusted to give the desired velocity at impact. The timebase of the transient recorder is set to give the maximum amount of data over the estimated time to failure of the specimen. The transient recorder can record 2016 data-points over a set interval of between 2 and 126 ms. The tests in the current work used the smallest timebase setting of 2 ms, giving approximately one datapoint every microsecond.

The test rate could be altered by varying the angle from which the pendulum was dropped, e.g. 10° corresponds to 0.3 m/s. It was not possible to alter the mass of the pendulum, and hence the energy available at a given velocity. The energy available is the

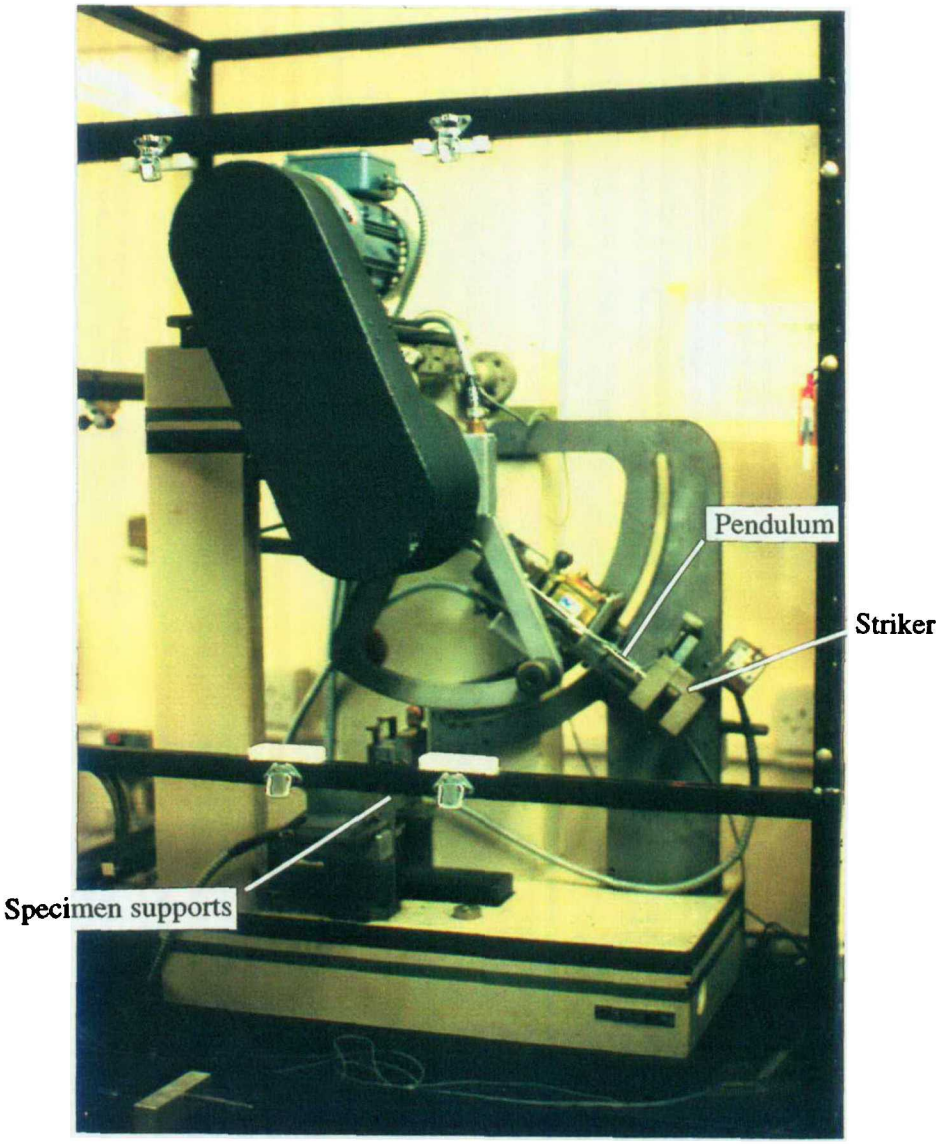


Figure 5.4: The pendulum three-point bend testing machine.

potential energy (m.g.δh), i.e. the pendulum mass multiplied by the acceleration due to gravity and the change in height. At 0.3 m/s the pendulum was dropped from an angle of 10° from the vertical. As the pendulum is 0.5 m long, the energy available was 0.075 J. This was insufficient to break many of the specimens, and thus the test rate was increased to 0.5 m/s, corresponding to an angle of 15°. In this case, the maximum energy available is.0.17 J. Thus all tests using the pendulum machine were performed at 0.5 m/s.

5.2.4 High-Speed Servo-Hydraulic Machine (HSSHM) Tests

A small piezo-electric load-cell and steel striker were attached to the ram of the high-speed servo-hydraulic machine (HSSHM), as used for the TDCB tests discussed in Chapter 4. The striker was made as small as possible, whilst retaining the same tip radius and included angle as the pendulum machine striker. This was to minimise the mass, and hence the inertia, of the system.

Tests were performed at 0.3 and 2 m/s, using a total travel of 100 mm. The 80 mm pre-travel used allows the ram to accelerate to the required velocity before striking the specimen. The extra travel means that the ram only starts to decelerate after the specimen has broken. Thus the specimen experiences a constant rate during the test. The extra travel is also important because the load-cell is mounted on the moving part of the testing machine, and can act as an accelerometer, producing an extraneous spike in the force signal when the ram velocity changes.

As for the tests described in Chapter 4, the force versus time response of the specimens was recorded using a transient recorder oscilloscope. The displacement versus time response of the machine ram was also recorded, enabling the test rate to be calculated. The data were then transferred to a computer for analysis. The maximum force, time to failure and the energy absorbed during the test were calculated.

5.3 Analysis

As discussed above, the TPB test uses a multi-specimen approach to enable the value of the material fracture energy to be found. A series of specimens with different notch depths are tested, and the energy required for fracture measured. The depth of the notch is varied in order to give a range of crack lengths, and hence a range of values of the geometry factor, ϕ. This enables a value of G_c to be calculated using the equation derived in Section 2.6.5.1,

$$G_c = \frac{U_c}{bd\phi}. \qquad (5.1)$$

where U_c is the energy absorbed in the test, b is the width and d is the depth of the specimen. Values of the geometry factor, ϕ, are available in tabular form[48, 58], and are shown in Appendix 3. Intermediate values are obtained by linear interpolation between the published values. Hence, from Equation 5.1, the fracture energy is the gradient of a linear fit to a plot of the energy absorbed in the test versus $bd\phi$, where the value of ϕ is dependent on the initial crack length.

5.4 Dynamic Effects

5.4.1 Introduction

For an epoxy three-point bend specimen at low rates of test, the force versus time response of the specimen is linear, see Figure 5.5. For the bulk and joint specimens tested in this work, failure occurs at the maximum load, P_c. The energy absorbed in the test is the area under this graph multiplied by the test rate.

When the test rate is increased, dynamic effects can become significant. Oscillations are superimposed on the linear response, see Figure 5.6. These are caused by the specimen flexing and losing contact with the supports and the striker, and hence with the load-cell, as shown in Figure 5.7. The measured load may even become negative. There can be large differences between the measured forces and those acting in the specimen[48, 49]. Thus the area under the curve, and hence the calculated energy, becomes meaningless, as described below.

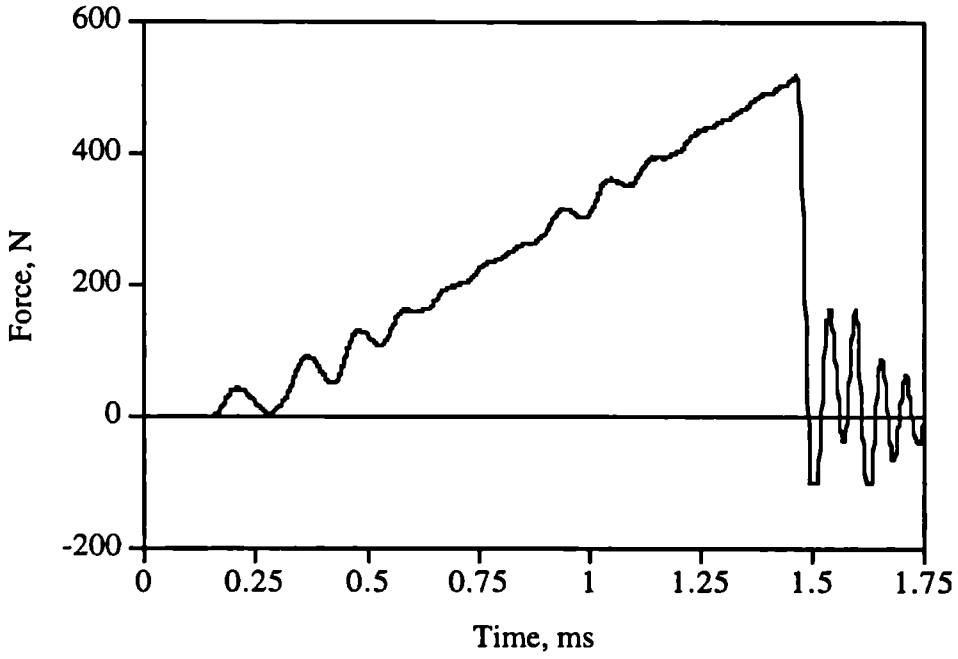


Figure 5.5: Force versus time response of bulk 'AV119' TPB specimen tested on high-speed servo-hydraulic machine at 0.3 m/s. Failure occurs at maximum load.

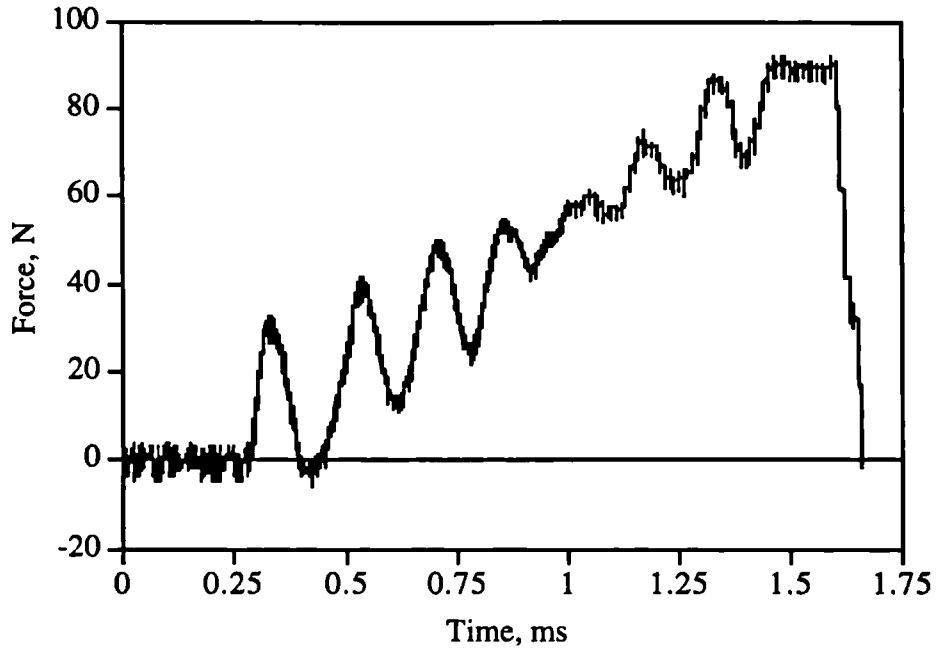


Figure 5.6: Force versus time response of bulk 'AV119' three-point bend specimen showing oscillations due to dynamic effects, tested on high-speed servo-hydraulic machine at 2 m/s. Compare with Figure 5.5.

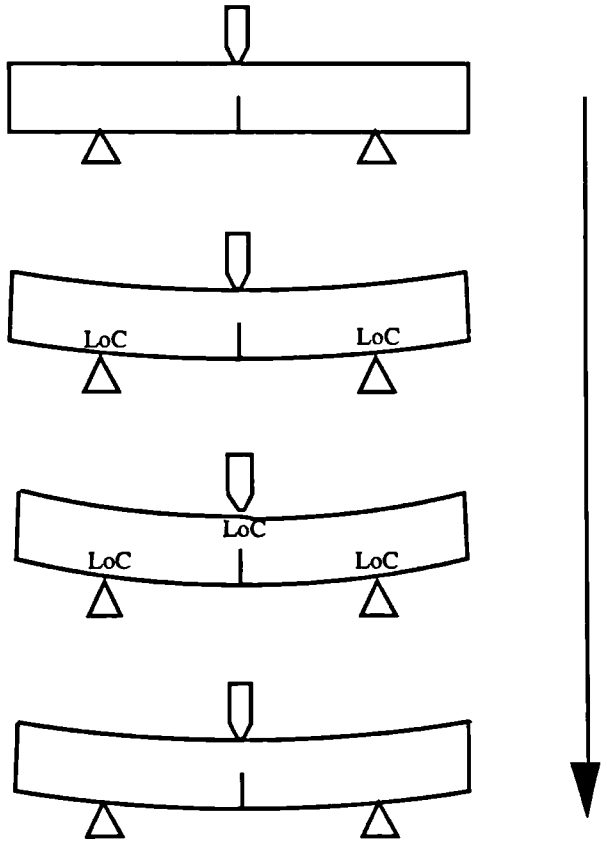


Figure 5.7: Loss of contact (LoC) in three-point bend test, which will cause oscillations in the measured force versus time response, after[127].

5.4.2 Mass/Spring Model of Dynamic Effects

A model of the dynamic effects in the TPB test has been proposed by Williams and Adams[48, 61, 62], as shown in Figure 5.8. This models the test as a mass and two springs. The specimen is modelled as an equivalent mass, m, and a spring of stiffness k_2. The other spring represents the contact stiffness, of magnitude k_1, between the pendulum and the specimen. Note that the stiffness k_2 is a function of the notch depth, a. The equivalent mass is 17/35 of the specimen mass[61]. Using this mass/spring model, Williams and Adams[61, 62] have predicted that oscillations will occur in the force versus time response if the load-cell is mounted on the striker, as described below.

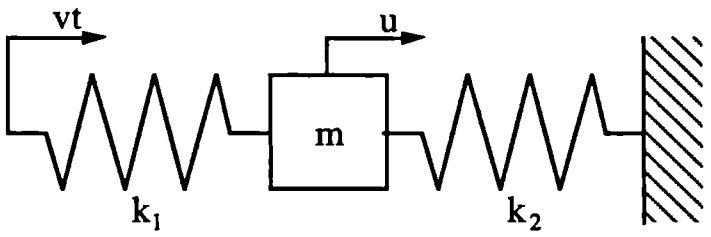


Figure 5.8: Mass/spring model of the three-point bend test, after Williams and Adams[62].

The equation of motion for the mass in the mass/spring system of Williams & Adams[48] is given by

$$m\ddot{u} = -k_2 u - k_1(u - vt) \tag{5.2}$$

where u is the displacement of the mass, and v is the striker velocity. This equation can be rewritten as

$$m\ddot{u} + (k_1 + k_2)u = k_1 vt \tag{5.3}$$

Integrating, using the initial conditions that $u = \dot{u} = 0$ at $t = 0$ gives

$$u = \left(\frac{k_1}{k_1 + k_2}\right)\left(\frac{v}{\omega}[\omega t - \sin(\omega t)]\right) \tag{5.4}$$

where ω is the natural frequency of the system, and

$$\omega = \sqrt{\frac{(k_1 + k_2)}{m}} \tag{5.5}$$

This model assumes that there are no energy losses in the contact zone, whereas energy will be absorbed by plastic deformation and friction, but these corrections increase the complexity of the analysis. It is also assumed that the contact stiffness is linear, which simplifies the analysis. In reality the striker tip is cylindrical, and hence the contact stiffness will be non-linear. However, the results are reported not to differ much from the non-linear form[62].

The predicted force on the striker, P_1, will be

$$P_1 = k_1(vt - u) = \left(\frac{\alpha}{\alpha+1}\right)k_2\frac{v}{\omega}[\omega t + \alpha\sin(\omega t)] \tag{5.6}$$

where

$$\alpha = \frac{k_1}{k_2} \tag{5.7}$$

This is <u>not</u> equal to the force in the specimen, which is given by

$$P_2 = k_2 u = \left(\frac{\alpha}{\alpha+1}\right)k_2\frac{v}{\omega}[\omega t - \sin(\omega t)] \tag{5.8}$$

The force required for the calculation of the energy absorbed during the test, and hence the calculation of G_c, is the force on the specimen, P_2. However, it is P_1, the force on the striker, that is measured during a TPB test.

A dimensionless force, P', can be defined as

$$P' = P\left(\frac{\alpha+1}{\alpha}\right)\left(\frac{1}{k_2}\right)\left(\frac{v}{\omega}\right) \tag{5.9}$$

This allows the predicted force on the striker to be compared to that on the specimen. Figure 5.9 shows graphs of P' versus ωt. These show that oscillations are superimposed on the linear force versus time response. However, the magnitude of the oscillations in P_2, the force in the specimen, is small compared to those in the striker, P_1. The oscillations are also out of phase. Thus it can be seen that the measured force is not equal to that experienced by the specimen. Hence the energy calculated from the force P_1 may not be equal to that required to fracture the specimen.

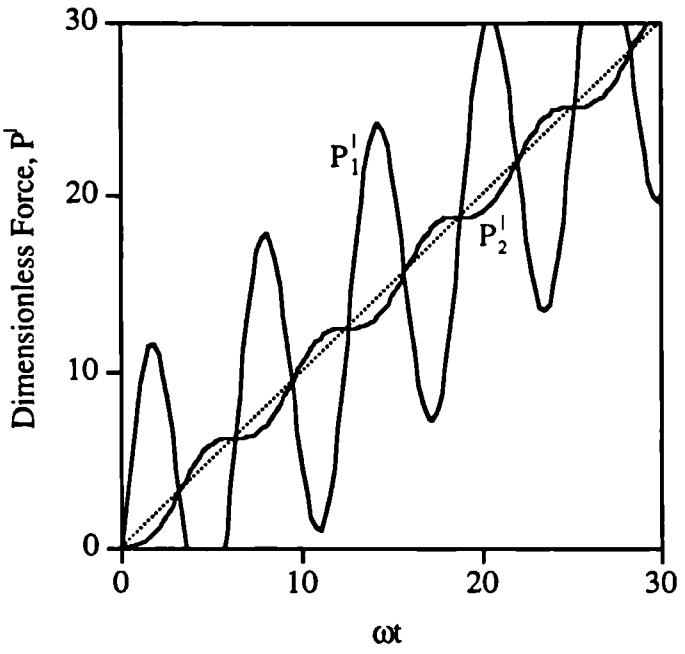


Figure 5.9: Theoretical graph of dimensionless force, P', versus ωt for three-point bend test with $k_1/k_2 = 10$, after Williams and Adams[62]. P'_1 is the force measured by the striker, and P'_2 that experienced by the specimen.

However, in reality there will be some damping in the system. This effect can be modelled by placing a dashpot in parallel with the spring k_2. Solving the equation of motion for the subsystem consisting of the mass m, spring k_2 and the damper gives the additional damping term[62].

$$e^{\frac{\omega t}{\pi}\ln(\varepsilon)} \tag{5.10}$$

where ε is the coefficient of restitution. The full derivation for this expression is given by Williams and Adams[62]. It has been shown[48] that for polymers $\varepsilon \sim 0.53$, hence the damping term becomes

$$e^{-\frac{\omega t}{5}} \tag{5.11}$$

This term is placed in front of the harmonic terms in Equations 5.6 and 5.8. The non-dimensional forces can be plotted against ωt, as shown in Figure 5.10. This shows that the oscillations in the force values tend to die out, and when $\omega t > 15$ they have virtually no effect. Thus when the time to failure of a specimen is large, the influence of dynamic effects will be small.

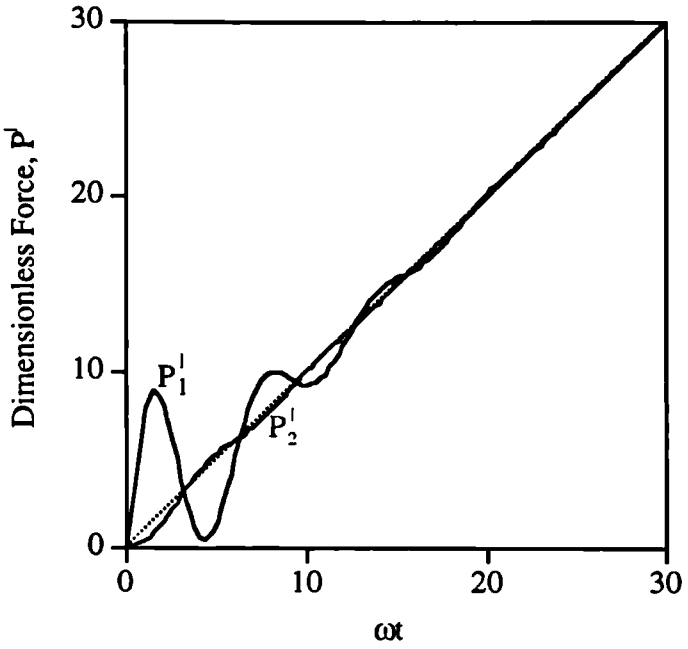


Figure 5.10: Theoretical graph of dimensionless force, P', versus ωt for mass/spring model of three-point bend test with $k_1/k_2 = 10$, after[62], with damping term $e^{-\omega t/5}$ applied to each harmonic term. P'_1 is the force measured by the striker and P'_2 that experienced by the specimen.

Returning to the undamped case, the effect of the oscillations can also be shown by subtracting Equation 5.8 from Equation 5.6,

$$P_1 - P_2 = k_1\left(\frac{v}{\omega}\right)\sin(\omega t) \qquad (5.12)$$

The mean value will occur when $\sin(\omega t) = 0$, and the maximum and minimum values when $\sin(\omega t) = \pm 1$. Hence, Equation 5.12 may also be written

$$P_1 = P_2 \pm k_1\left(\frac{v}{\omega}\right) \qquad (5.13)$$

This relationship indicates that the oscillations in the measured force are dependent on the test rate, v, and the contact stiffness, k_1. Thus, as the test rate increases, the magnitude of the oscillations would be expected to increase. However, reducing the contact stiffness will reduce the magnitude of the oscillations. This is the principle behind the ESIS protocol method discussed in the next Section, where reducing the contact stiffness allows specimens to be tested at higher velocities without significant dynamic effects.

5.4.3 ESIS Protocol Method for 'Allowable' Dynamic Effects

An Appendix to the ESIS protocol on the TPB testing of polymers[58] discusses the experimental aspects of testing specimens at high rate, and gives a method for calculation of 'valid' fracture energies. The problems caused by dynamic effects are avoided by reducing the oscillations to a level where they are considered not to be significant, and ignoring any tests with significant dynamic effects. The recommended method is to place some damping material on the specimen where the striker makes contact, as shown in Figure 5.11. This reduces the contact stiffness between the striker and the specimen. In terms of the mass/spring model discussed above, the contact stiffness, k_1, is reduced. The aim is to reduce the oscillations between $P_Q/2$ and P_Q to within a band of width ±5 % of P_Q, see Figure 5.12. Hence this will reduce the error between the force measured by the load-cell and that experienced by the specimen. The protocol[58] explains how to determine the value of P_Q, but as a first approximation $P_Q = P_c$, the maximum force.

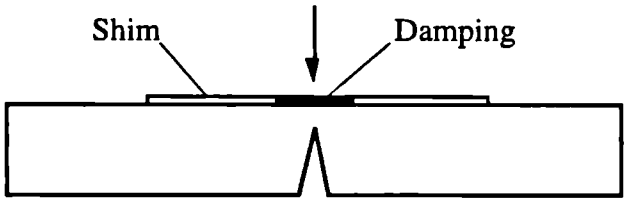


Figure 5.11: Damping material applied to three-point bend specimen.

The use of damping increases the time to failure of the specimen, but only increases the energy absorbed, U_c, slightly, see Figure 5.13. It is possible to correct the calculated value of G_c for effects such as indentation of the striker and supports into the specimen, by performing rebound tests on unnotched specimens with damping in place, see Figure 5.14. Tests must be performed for each specimen, damping and test rate combination. There is also a risk of damaging the testing machines and load-cells, especially with the present joint specimens, since these are very stiff. This method is more applicable for soft polymers where indentation may be significant. However, with the specimens used in the current work the effect of indentation will be limited, as the 'AV119' adhesive is relatively hard and brittle. The effect on the steel joint specimens is likely to be even less. Thus these rebound tests were not performed for the current work. It is likely that the kinetic energy of the specimen will have a more significant effect, especially for the joint specimens due to their relatively high mass, see Section 5.5.5.

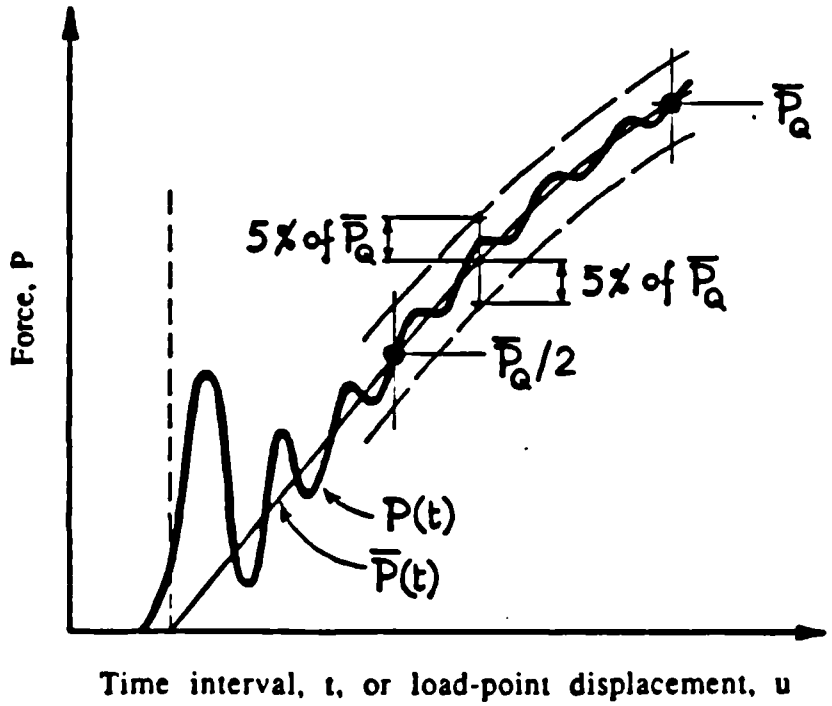


Figure 5.12: ESIS protocol method for allowable dynamic effects. Oscillations between $P_Q/2$ and P_Q must lie within a band of ±5 % of P_Q, after[58].

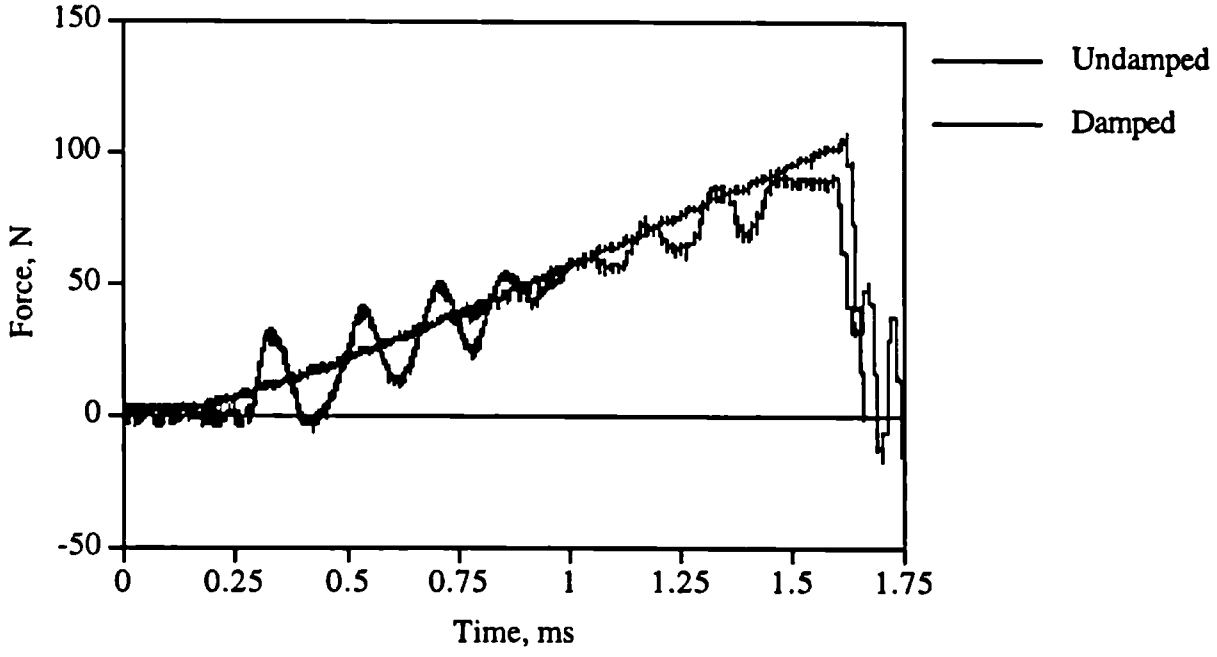


Figure 5.13: Damped and undamped response of bulk 'AV119' adhesive specimens tested at 0.3 m/s. Damped using 0.05 mm of grease, but note that the response is overdamped.

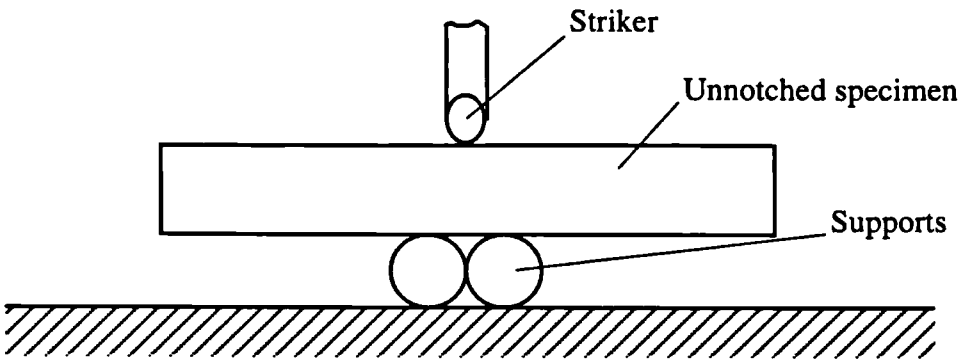


Figure 5.14: Experimental arrangement for compliance/indentation test.

Initially 'Blutak' ('Evode', UK) was used as the damping material. However, this is a solid and is not fully displaced after damping the initial contact. The latest work in this area favours the use of grease to reduce the contact stiffness[128]. As this is a liquid it will damp the initial contact, but be displaced easily by the striker. Thus, though it reduces the dynamic effects, it will only affect the contact stiffness at the beginning of the test, see Figure 5.13.

All the test data presented in the current work used Castrol 'Heavy' grease as the damping material. This was chosen as it is a relatively thick grease and so only a thin layer is required, thus the time to failure of the specimen is increased by as little as possible. The grease was applied as a bead and spread to the required thickness using a razor blade. The thickness was controlled by pieces of shim on either side, as shown in Figure 5.12. The bulk specimens required very little damping to reduce the dynamic effects to within the acceptable limits, even 0.05 mm of grease could cause the response to be overdamped, as shown in Figure 5.13. Damping material thicknesses of between 0.05 and 0.65 mm were used. However, there was little extra effect on the dynamic effects arising from increasing the thickness above 0.4 mm.

5.5 Results

5.5.1 Introduction

As discussed above, fracture mechanics tests using bulk and joint specimens were performed using the three-point bend test method. The 'AV119' adhesive was used, and tests were conducted at test rates of 0.3 and 2 m/s using the high-speed servo-hydraulic machine (HSSHM). Additionally, bulk specimens were tested at a test rate of 0.5 m/s on the pendulum machine. Prior to testing, the specimens were notched to various depths.

The tip of the notch was sharpened by drawing a new razor blade across it. Thus the radius of the notch tip is nominally the same in all tests.

This Section discusses the results of the bulk specimen TPB tests, then those using the joint TPB specimens. The results of scanning electron microscopy (SEM) on the fracture surfaces are also considered. It should be noted that the best linear fits to the test data do not pass through the origin. This effect is discussed further in Section 5.5.5, where the effect of the kinetic energy of the specimen on the test data is discussed. Finally, the values of the adhesive fracture energy, G_c, from the TPB tests are compared with those from the TDCB tests described in Chapter 4.

Confidence limits were calculated for each of the linear regressions performed in the present work, using the analysis shown in Appendix 4. A 90 % confidence interval was used throughout.

Previous workers in this area have found that the fracture energies from bulk adhesive and joint TPB tests were the same at equal test rates[59]. However, the tests used aluminium-alloy adherends. The use of stiffer, steel, adherends in the present work will indicate whether the use of the time to failure rather than the test rate is preferable when comparing bulk adhesive and joint data.

5.5.2 Bulk Specimen Results

Bulk specimens were tested at 0.5 m/s using the impact pendulum machine. Although dynamic effects were present, these specimens were tested without a layer of damping material because even a 0.05 mm thickness of grease caused the response to be overdamped. A G_c value of 640 J/m^2 was obtained, see Figure 5.15. Dynamic effects were found to be larger than using the servo-hydraulic machine. As the striker is falling freely rather than being driven, there is likely to be more bounce on contact, and this may cause the increased dynamic effects.

Bulk 'AV119' specimens were tested using the HSSHM at 0.3 m/s. These showed significant dynamic effects, the oscillations being greater than the ±5 % band specified by the ESIS protocol[58],. Further tests were carried out using a damping material, as discussed in Section 5.4.3. The dynamic effects were reduced, and the oscillations fell within the specified band of ±5 % of P_Q, see Figure 5.16. These tests gave a G_c value of 950 J/m^2, see Figure 5.17. Tests conducted at 2 m/s, using damping, gave a value of 520 J/m^2, as shown in Figure 5.18.

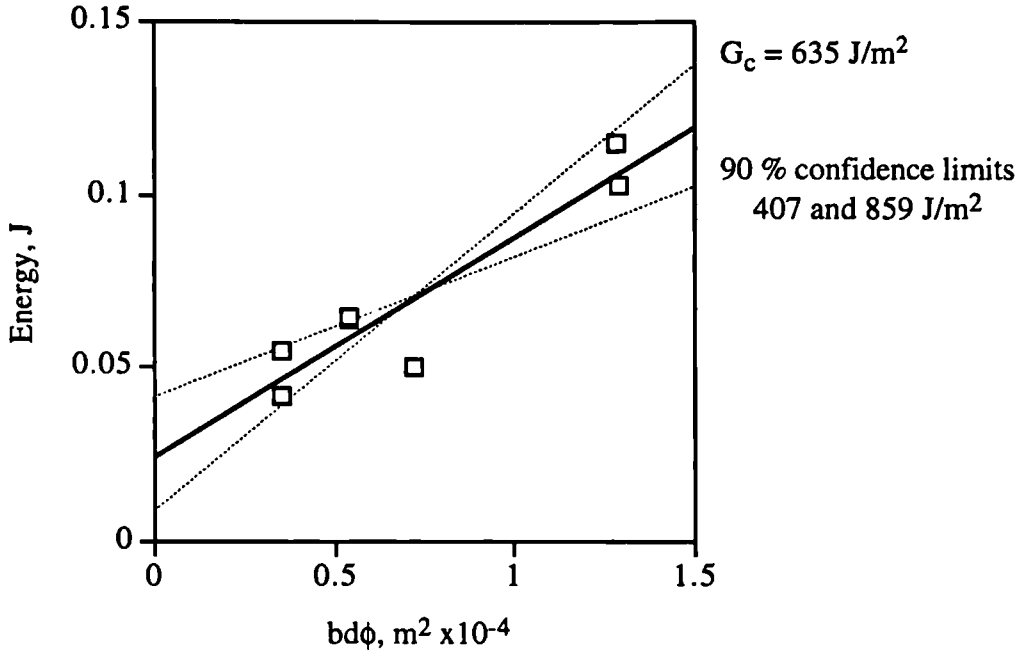


Figure 5.15: Energy versus bdϕ graph for bulk 'AV119' TPB tests using the impact pendulum machine at a test rate of 0.5 m/s, no damping material used. Best linear relationship to data, obtained using least squares regression, shown as solid line, and 90 % confidence limits are shown as dotted lines.

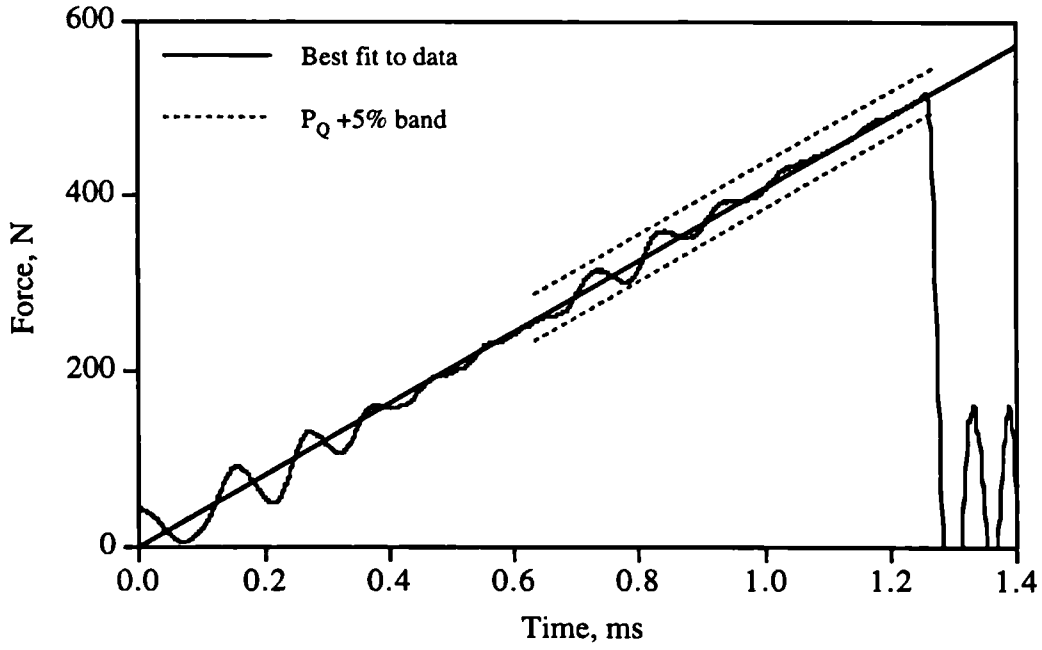


Figure 5.16: ESIS protocol method applied to TPB test on bulk specimen of 'AV119' adhesive, tested using the HSSHM at a test rate of 0.3 m/s, showing that the dynamic effects are less than the specified ±5 % of P_Q between $P_Q/2$ and P_Q.

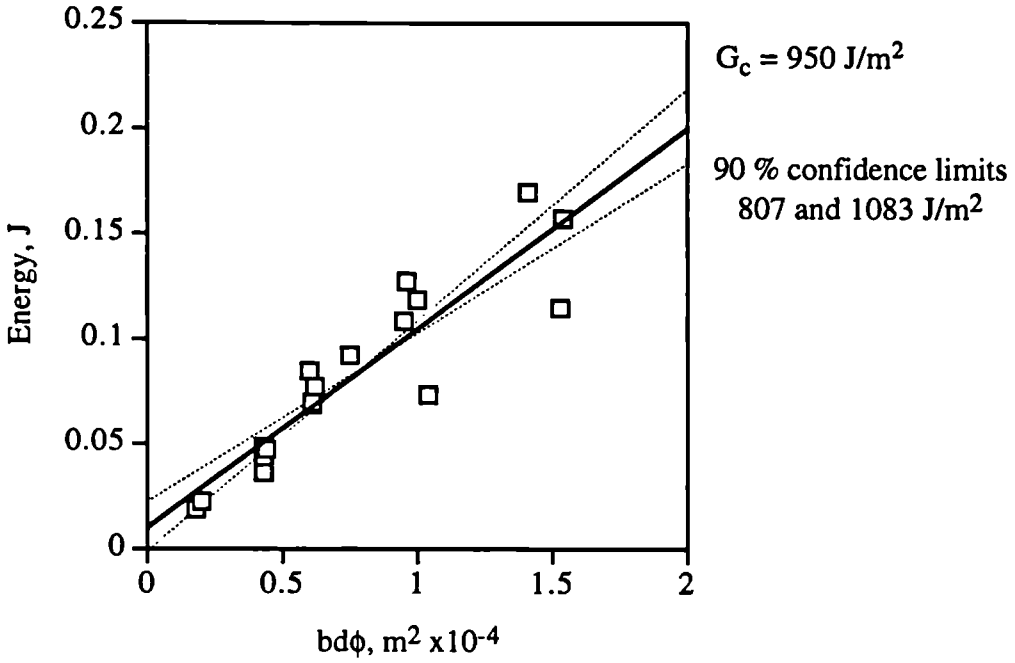


Figure 5.17: Energy versus bdϕ graph for bulk 'AV119' TPB tests. Tested using the HSSHM at a test rate of 0.3 m/s. Best linear relationship to data, obtained using least squares regression, shown as solid line, and 90 % confidence limits are shown as dotted lines.

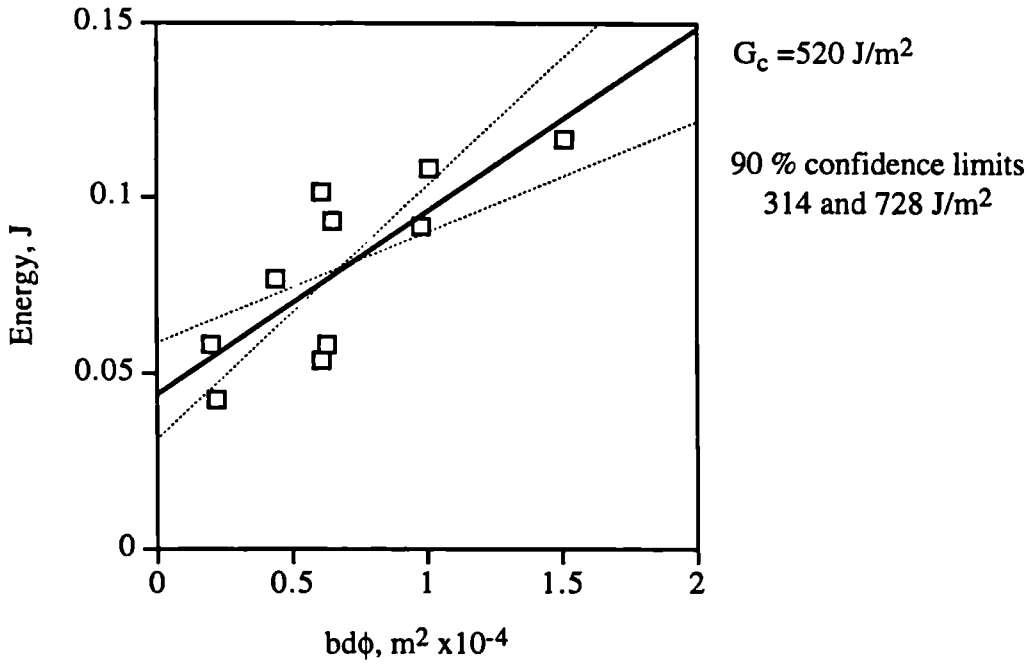


Figure 5.18: Energy versus bdϕ graph for bulk 'AV119' TPB tests. Tested using the HSSHM at a test rate of 2 m/s. Best linear relationship to data, obtained using least squares regression, shown as solid line, and 90 % confidence limits are shown as dotted lines.

5.5.3 Joint Specimen Results

The 'AV119'/steel joint specimens gave a G_c value of 690 J/m^2 when tested at 0.3 m/s, see Figure 5.19, and 260 J/m^2 at 2m/s, see Figure 5.20. Damping material was used for these tests.

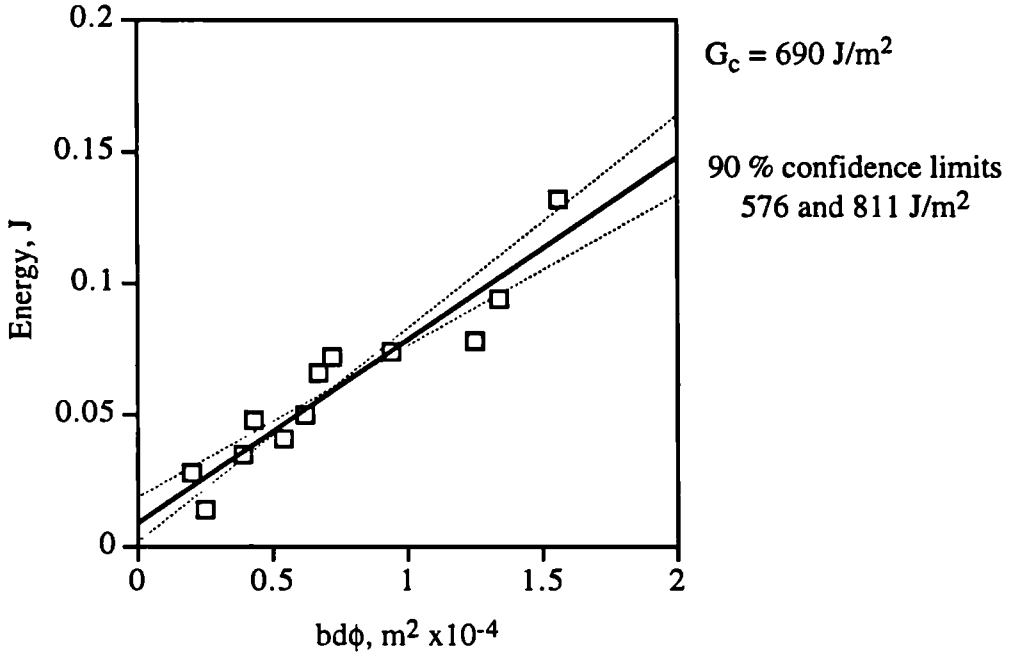


Figure 5.19: Energy versus bdϕ graph for 'AV119'/steel TPB joint specimens tested at 0.3 m/s using the HSSHM. Best linear relationship to data, obtained using least squares regression, shown as solid line, and 90 % confidence limits are shown as dotted lines.

5.5.4 Comparison of Bulk and Joint Specimen Results

The adhesive fracture energies obtained from the three-point bend tests are plotted versus test rate in Figure 5.21. The error bars shown on these data represent the 90 % confidence intervals discussed earlier. The agreement between the data obtained using the bulk and joint specimens, and using the two testing machines is good. Further, the adhesive fracture energy decreases as the test rate is increased.

However, for a given test rate, the adhesive fracture energies obtained using the joint specimens are lower than those using the bulk adhesive specimens, as shown in Figure 5.21 and Table 5.1. SEM of the joint specimen fracture surfaces showed that these exhibited cohesive-in-adhesive fracture (see Section 5.5.6), as, of course, did the bulk specimens. The probable explanation for the lower fracture energy obtained from the joint tests is that the joint specimens are stiffer, and hence the adhesive experiences a

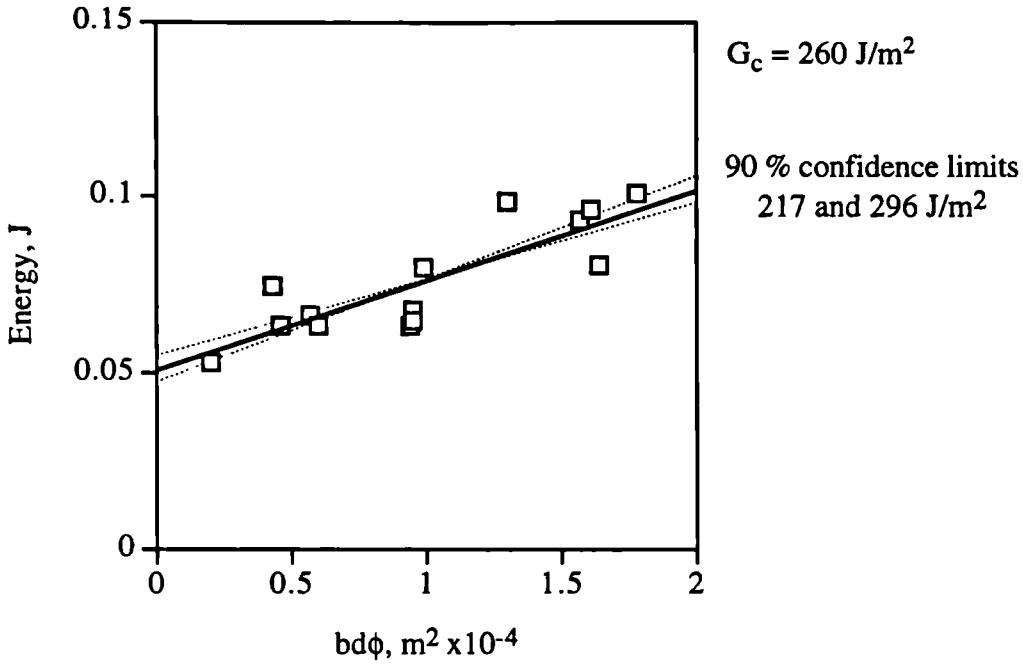


Figure 5.20: Energy versus bdϕ graph for 'AV119'/steel TPB joint specimens tested at 2 m/s using the HSSHM. Best linear relationship to data, obtained using least squares regression, shown as solid line, and 90 % confidence limits are shown as dotted lines.

relatively higher loading rate. For example, a bulk specimen with a 2 mm crack tested at 0.3 m/s had a time-to-failure, t_f, of 1.35 ms, while for a joint specimen for the same crack length it was 0.45 ms, see Table 5.1. The fracture energies obtained from the bulk and joint specimen TPB tests are shown plotted against time to failure in Figure 5.22. The agreement between the bulk and joint data is now very good when the fracture energies are plotted against the time to failure, t_f.

Table 5.1: Fracture energies (with 90 % confidence limits) obtained using three-point bend tests, showing test rate and average time to failure.

Specimen type	Testing machine	Test rate, m/s	Time to failure, ms	Fracture energy, J/m²	90 % Confidence	
					a + α	a - α
Bulk	HSSHM	0.3	1.47	**950**	1083	807
Joint	HSSHM	0.3	0.50	**690**	811	576
Bulk	Pendulum	0.5	0.81	**635**	859	407
Bulk	HSSHM	2	0.29	**520**	728	314
Joint	HSSHM	2	0.04	**260**	296	217

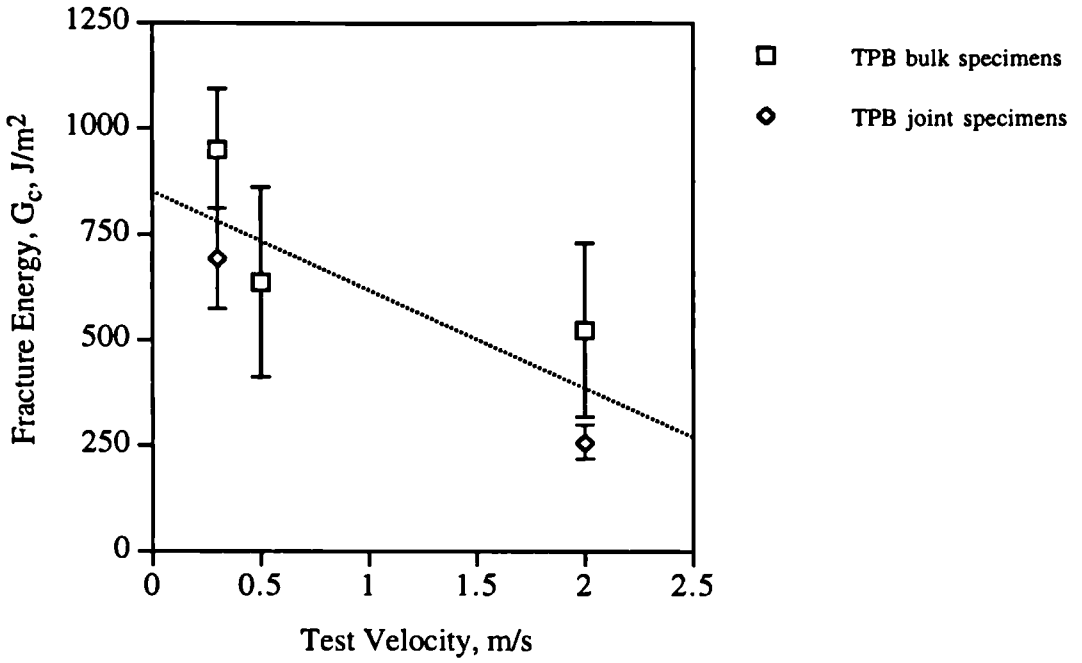


Figure 5.21: Fracture energy versus test rate for bulk and joint TPB tests, using the 'AV119' adhesive. Error bars show the 90 % confidence interval for the fracture energy values.

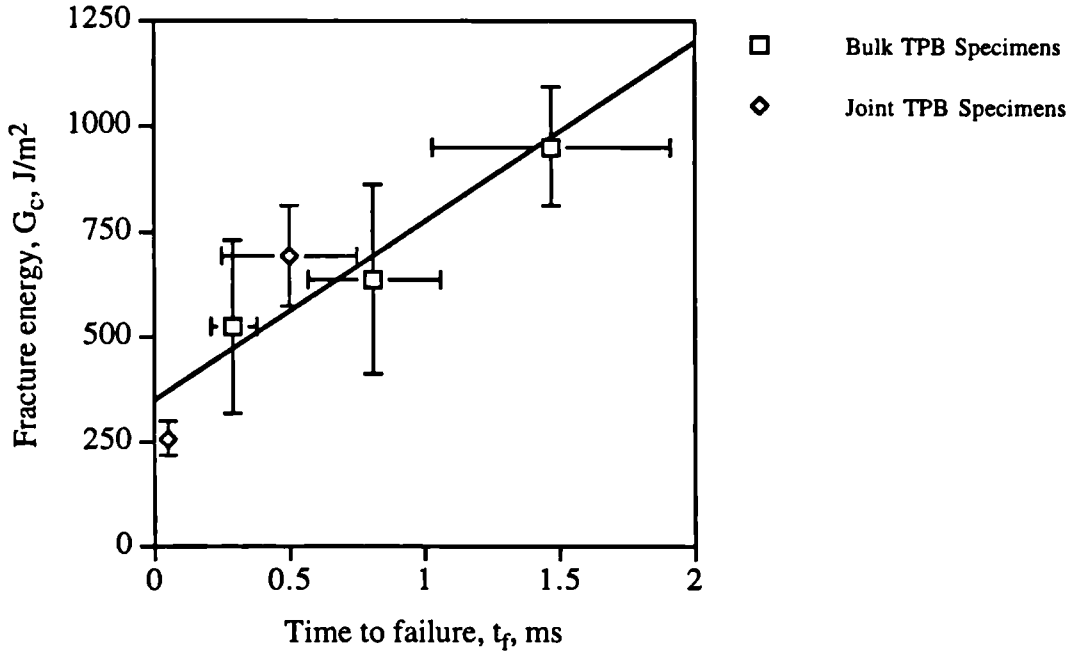


Figure 5.22: Graph of fracture energy versus average time to failure, i.e. time to crack initiation, for TPB specimens. Error bars are one standard deviation for the time to failure, and a 90 % confidence interval for the fracture energy values.

It may be concluded that both the testing machines used, the impact pendulum machine and the high-speed servo-hydraulic machine, give comparable results. Thus either may be used for three-point tests. However, it should be noted that the impact pendulum machine used in the present work was not able to be used at 0.3 m/s because insufficient energy was available to break the specimens. Further, the dynamic effects were more pronounced using the pendulum machine.

5.5.5 Kinetic Energy Correction

As can be seen from the graphs shown above, in Figures 5.15 and 5.17 to 5.20, the best linear fits to the energy versus $bd\phi$ data do not pass through the origin. One possible reason for this positive intercept is that not all the measured energy goes into specimen fracture, but that some is converted into kinetic energy of the specimen. This can be seen experimentally as the broken halves of the specimen fly through the specimen supports.

Marshall, Williams & Turner[129] have proposed an analytical solution for calculating the kinetic energy imparted to the specimen. This postulates that a fraction of the total energy lost by a pendulum striker of mass M is converted into kinetic energy of the specimen. The kinetic energy of the specimen is given by

$$U_k = \frac{mv^2(1-\varepsilon^2)}{(1+m/M)} \qquad (5.14)$$

where m is the specimen mass, v is the test rate, and ε is the coefficient of restitution. The masses of the bulk and joint specimens are 0.012 and 0.073 kg respectively. Table 5.2 shows the calculated values of the kinetic energy correction, in millijoules, compared with the y-axis intercept from Figures 5.15 and 5.17 to 5.20. Data are presented for coefficients of restitution, ε, of between zero and 0.5. These data show that this kinetic energy correction alone cannot account for the positive intercept.

When $\varepsilon = 0$, all the energy of the pendulum is converted to kinetic energy of the specimen. For perfect contact, i.e. when no kinetic energy is transferred to the specimen but all the energy goes into fracture of the specimen, $\varepsilon = 1$. Williams[48, 62] found that for a range of polymers, $\varepsilon = 0.53$. However, if this value is substituted into Equation 5.14, the kinetic energy correction does not reduce the energy-axis intercept for the pendulum machine tests considerably, as shown in Table 5.1. A kinetic energy correction can be calculate for the HSSHM tests by assuming that $m/M << 1$, i.e. $(1+m/M) = 1$. The choice of other values of ε rather than 0.5, e.g. 0 or 0.1, also do not account for the non-zero

Table 5.2: Kinetic energy correction for 'AV119' three-point bend tests, (a) bulk specimen tests, (b) joint specimen tests. Note HSSHM test correction data assume that M >> m, i.e. (1 + m/M) = 1. Kinetic energy values calculated from Equation 5.14.

(a) Kinetic energy correction for 'AV119' TPB bulk specimen tests.

Bulk specimens	Velocity, m/s	Time to failure, ms	Intercept, mJ	Kinetic energy, mJ		
				ε=0.5	ε=0.1	ε=0
Pendulum 0.5m/s	0.5	0.81	24.5	1.0	1.5	3
HSSHM 0.3m/s	0.3	1.47	9.3	0.4	0.5	1.1
HSSHM 2m/s	2	0.29	44.2	18	23.8	48.0

(b) Kinetic energy correction for 'AV119' joint specimen tests.

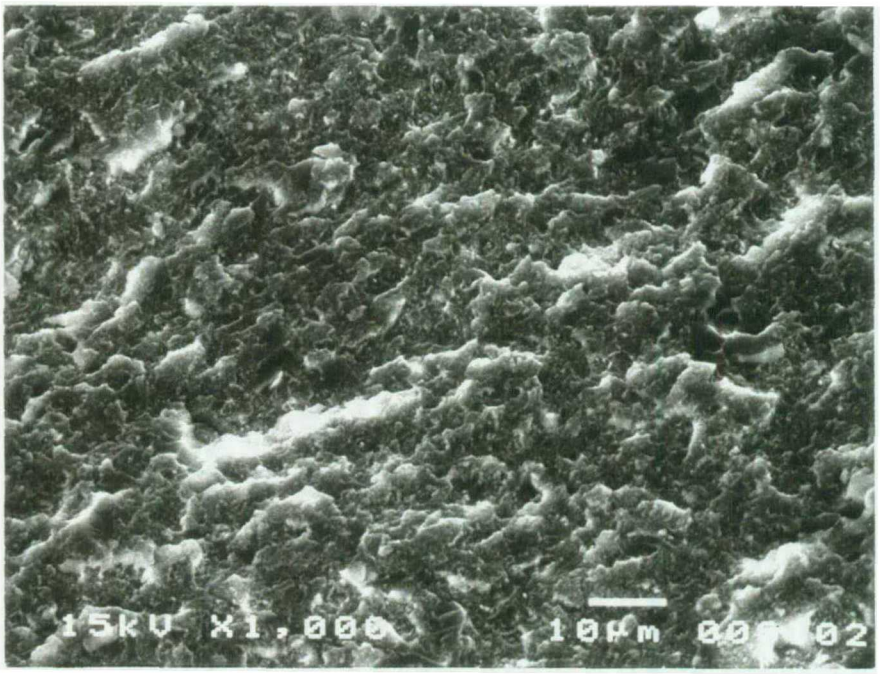
Joint specimens	Velocity, m/s	Time to failure, ms	Intercept, mJ	Kinetic energy, mJ		
				ε=0.5	ε=0.1	ε=0
HSSHM 0.3m/s	0.3	0.5	9.0	2.5	3.3	6.6
HSSHM 2m/s	2	0.043	50.6	113	149	292

axis intercept. Thus in the present work this kinetic energy correction does not accurately predict the differences in the intercept energy.

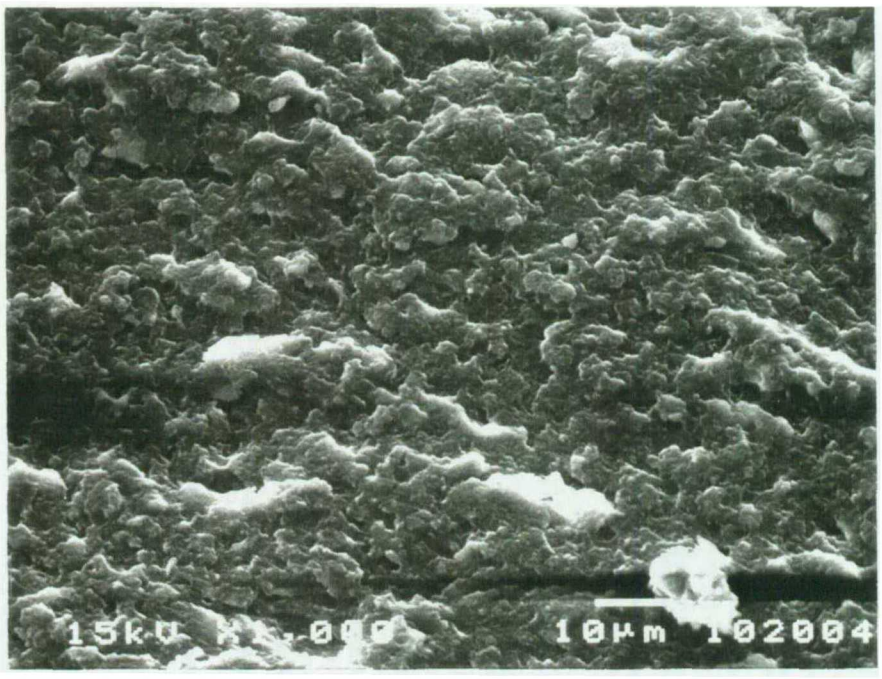
5.5.6 Fractography

SEM of the TPB specimen fracture surfaces showed that all the specimens exhibited cohesive-in-adhesive failure, see Figures 5.23 and 5.24.

The bulk specimen fracture surfaces showed a rougher appearance at 0.3 m/s than at 2 m/s, see Figure 5.23. This greater deformation at the lower test rate is consistent with the higher fracture energy obtained. A similar effect is seen with the fracture surfaces of the joint specimens, as shown in Figure 5.24. However, there is no evidence of cavitation of the rubber particles on either set of micrographs. The surfaces are similar to those shown in Chapter 4, from the TDCB tests. The lack of cavitation implies that the energy-absorbing mechanisms involved in the rubber toughening, i.e. the massive shear yielding, are not being initiated as effectively as at low test rates (as discussed in Chapter 4), and hence relatively low fracture energies are expected.

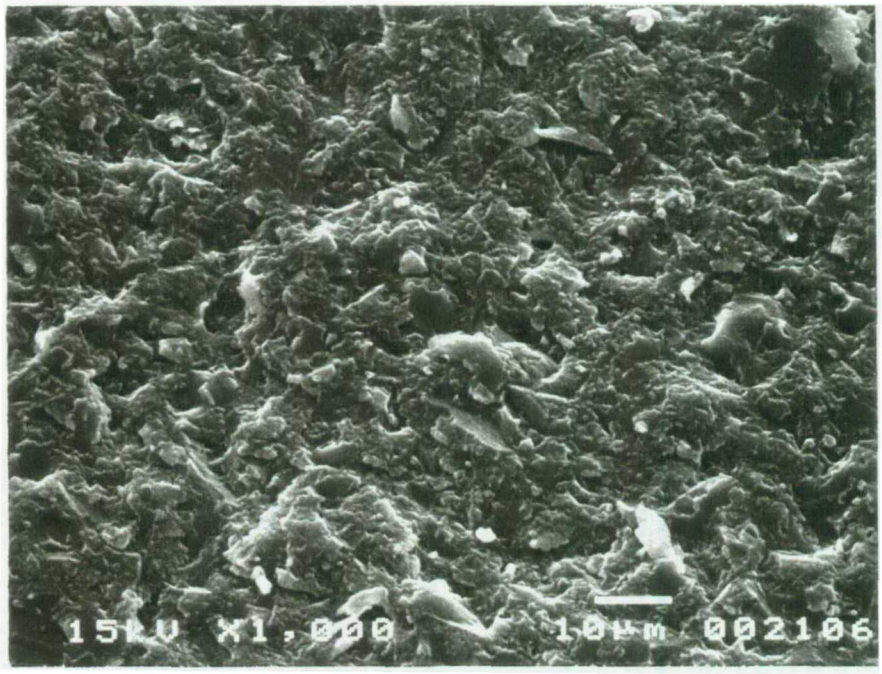


(a) Test rate 0.3 m/s.

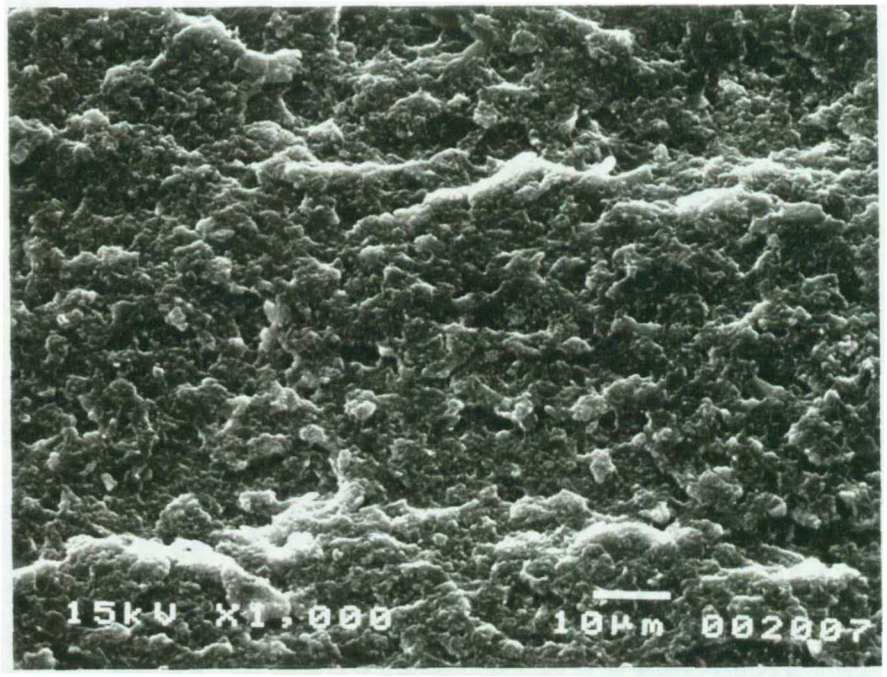


(b) Test rate 2 m/s.

Figure 5.23: Scanning electron micrographs of fracture surfaces of bulk 'AV119' TPB specimens, tested at (a) 0.3 m/s, and (b) 2 m/s. (Crack propagation is from left to right.)



(a) Test rate 0.3 m/s.



(b) Test rate 2 m/s.

Figure 5.24: Scanning electron micrographs of fracture surface of 'AV119' joint specimens, tested at (a) 0.3 m/s, and (b) 2 m/s showing cohesive-in-adhesive fracture. (Crack propagation is from left to right.)

5.5.7 Comparison with TDCB Results

The three-point bend tests described above showed a decrease in the adhesive fracture energy with decreasing time to failure, and increasing test rate. This effect was also observed using the TDCB tests discussed in Chapter 4. The data from the two test methods may be compared by plotting the measured fracture energies against the time to failure, i.e. the time to the initiation of crack growth, as shown in Figure 5.25, or the test rate, see Figure 5.26.

The agreement between the two test methods when the fracture energies are plotted against the time to failure is poor. This is to be expected due to the differences in test geometry, and hence the effective loading rates. The effective loading rate of the three-point bend test is much higher than that of the tapered double-cantilever beam test as the initial crack length is much shorter.

However, when the results are compared by plotting the measured fracture energies against the test rate, as shown in Figure 5.26, the agreement between the TPB and TDCB test methods is good.

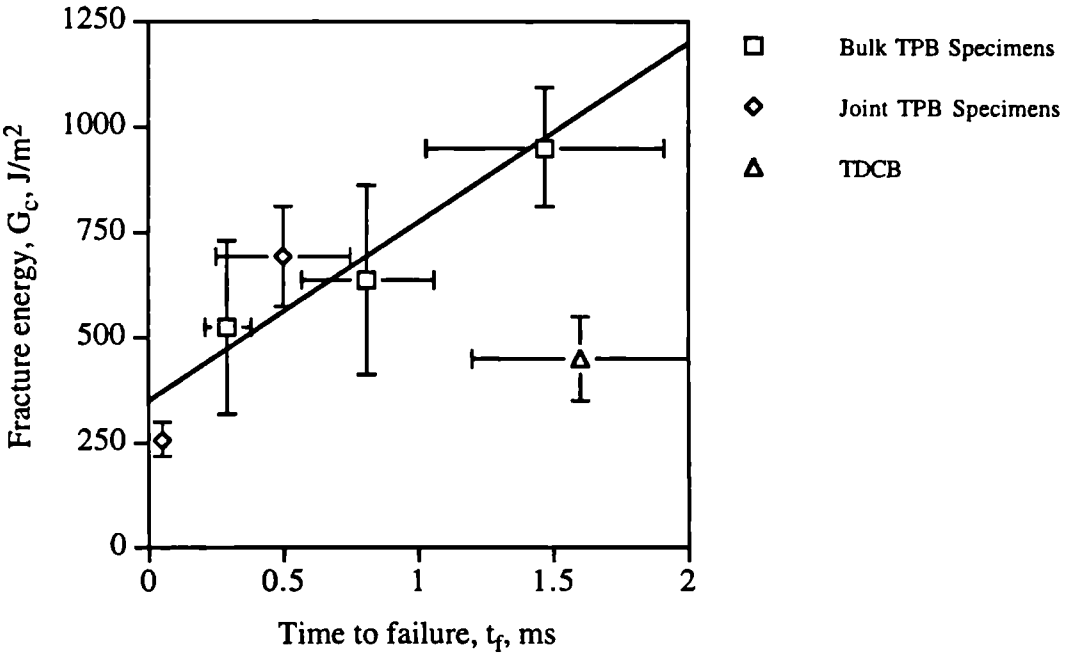
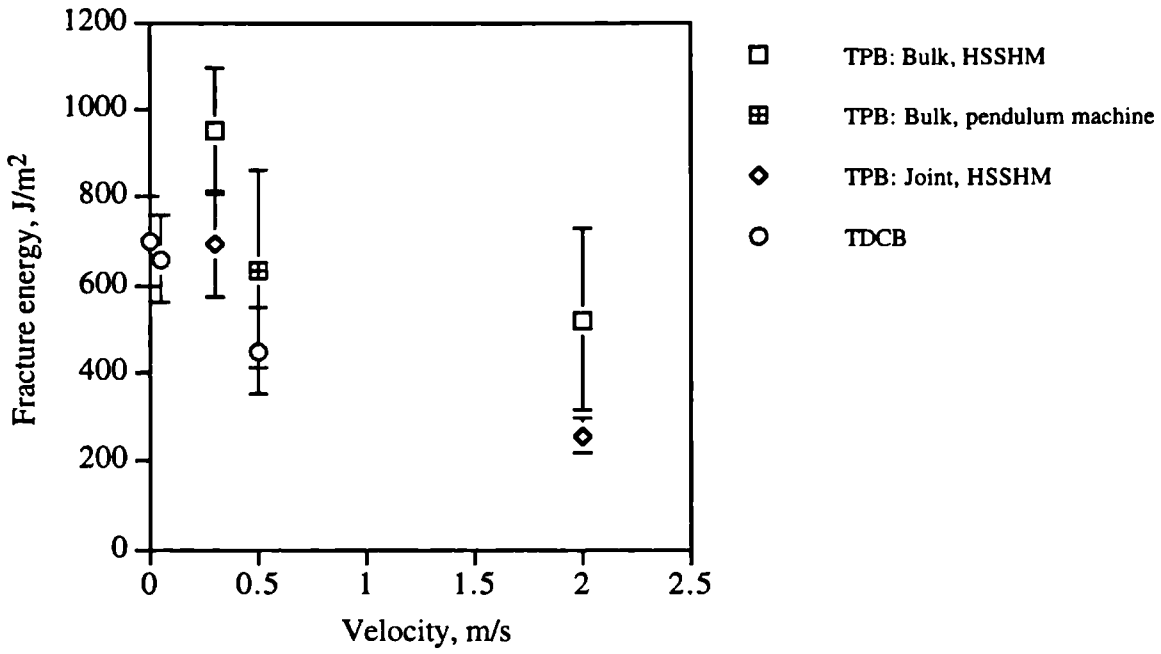
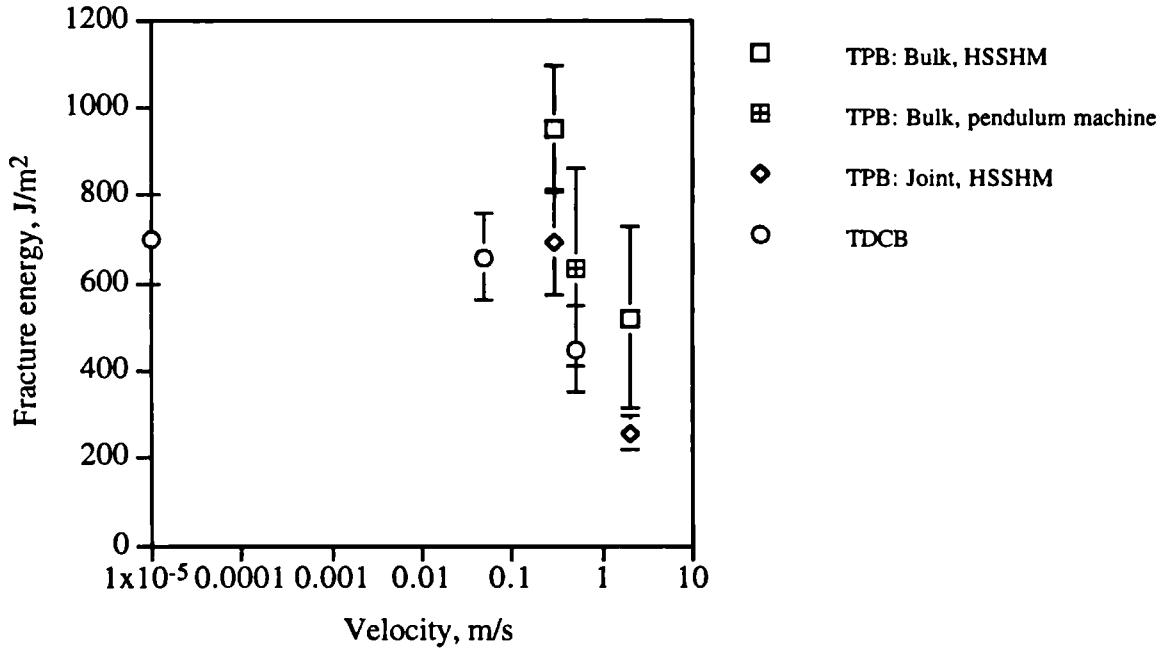


Figure 5.25: Graph of fracture energy versus average time to failure, i.e. time to crack initiation, for TPB and TDCB specimens. Error bars are one standard deviation for the time to failure, and a 90 % confidence interval for the fracture energy values.



(a) Linear axes.



(b) Linear-log axes.

Figure 5.26: Fracture energy versus test rate for bulk and joint TPB tests, plus TDCB results, using 'AV119' adhesive, (a) Linear axes, (b) Linear-log axes. Error bars indicate the 90 % confidence interval for the TPB fracture energy values.

5.6 Conclusions

The present work has described a method for the manufacture of adhesive joint three-point bend specimens that can be used for viscous adhesives. The use of the metal mould described in the text ensures that the specimens are parallel, and that the amount of air trapped in the adhesive is kept to a minimum.

The TPB test does not require such complicated equipment as the TDCB test, as an impact pendulum machine may be used. The TPB test also requires smaller specimens. However, the TPB test uses a multi-specimen approach to determine the adhesive fracture energy, G_c, and hence is more time-consuming. The dynamic effects are more pronounced, and become important at a lower test rate. Various corrections can be applied to the results, which add to the complexity of the testing procedure. The ESIS protocol provides a useful method of reducing the dynamic effects, and allows fracture energy values to be calculated at high test rates. However, the use of damping poses its own problems. The number of specimens required is increased as the correct thickness of damping material must be found to reduce the dynamic effects, but not to overdamp the response.

The results of the three-point bend testing show that the adhesive fracture energy, G_c, decreases with increasing test rate. Further, the agreement between the data obtained using the bulk and joint specimens, and using the two testing machines is good. However, for a given test rate, the fracture energies obtained using the joint specimens are lower than those using the bulk adhesive specimens, although SEM of the fracture surfaces showed that all the specimens exhibited cohesive-in-adhesive fracture. The explanation for the lower fracture energy obtained using the joint specimens is that the joint specimens are stiffer, and hence the adhesive experiences a relatively higher loading rate. This was confirmed by plotting the fracture energy against the time to failure, and there was excellent agreement between the bulk and joint specimen results.

The fracture energy values obtained using the TDCB tests discussed in Chapter 4 were compared to those obtained using the TPB tests. The agreement between the data when the fracture energies were plotted against the time to failure was poor. However, when the G_c values were plotted against the test rate, the agreement between the data was found to be very good. Thus the fracture energy of the adhesive is predominantly dependent on the test rate, and the agreement between the fracture mechanics data obtained using the methods investigated in the present work is very good.

Chapter Six

Impact Wedge-Peel Tests

6.1 Introduction

As discussed in Section 2.7.2, the impact wedge-peel (IWP) test is an International Standard method[1] which is used to measure the resistance to cleavage of adhesives at a high test rate. The work presented in this Chapter discusses the application of this method to a range of epoxy adhesives when used to bond either aluminium-alloy or steel adherends. These results will be compared with the adhesive fracture energies, G_c, obtained using the TDCB tests which were reported in Chapter 4. High-speed photography and thermal imaging will be used to investigate specimen failure. Additionally, a finite element model will be used to predict the IWP cleavage-force from the values of the adhesive fracture energy

6.2 Discussion of Published Work

The ISO Standard specifies that the IWP specimens should be 90 mm long by 20 mm wide, and made with sheet metal adherends between 0.6 and 1.7 mm thick. These are bonded over a length of 30 mm, the unbonded arms being formed to give a 'tuning fork' profile, see Figure 6.1. No starter crack or notch is used with these specimens. The free arms of the specimen are clamped, and a wedge is driven through the bonded portion, as shown in Figure 6.1. The wedge velocities specified by the Standard are 2 m/s for steel adherends, and 3 m/s for aluminium-alloy adherends.

Most of the work carried out on this test to date, for example by workers at Ford Research and Ciba Polymers, has been concerned with the evaluation of adhesives[26, 130]. However, very little information has been published[131, 132]. The information that is available discusses the usefulness of the test method, rather than presenting quantitative results.

The ISO Standard does not specify whether the profile of the adherends should be formed prior to or after bonding. Workers at Ciba Polymers[130] have shown that forming the adherends prior to bonding can result in a larger bead of adhesive in the 'V' formed by the adherends, and so they bend the adherends by hand after bonding. However, the work conducted by Davis and Fay[26] at Ford Research has shown

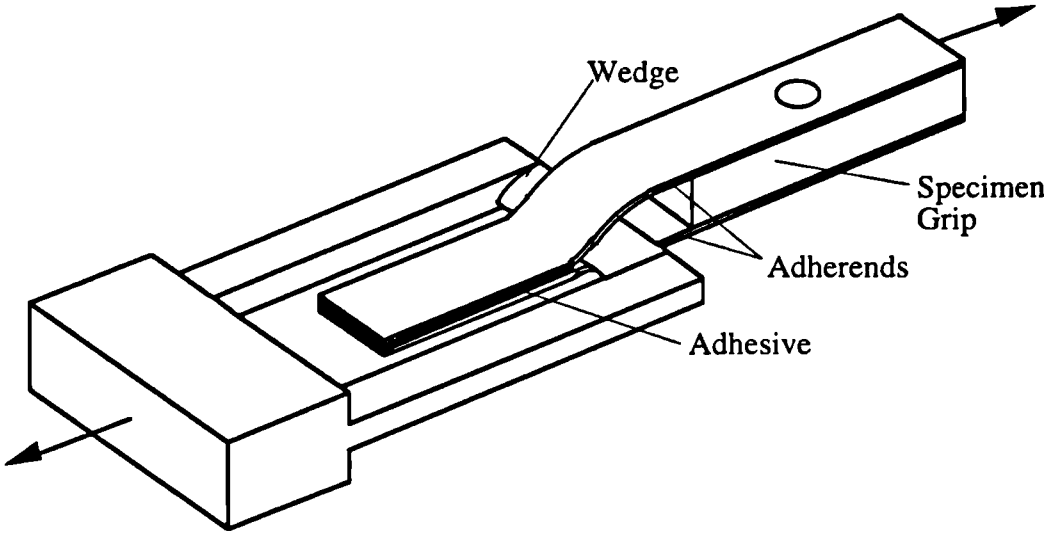


Figure 6.1: The impact wedge-peel (IWP) test.

that more consistent results may be achieved by forming the adherends prior to bonding, as forming the adherends after bonding may generate a crack in the adhesive, and the variability of the adherend profile produced may influence the results. In addition, it may be impossible to bend thicker adherends by hand. Thus the current work will form the adherends prior to bonding. The bead size will be minimised by removing as much as possible of the excess adhesive from the 'V' formed by the adherends before curing.

Work by Thouless et al [133] and Dickie & Ward[134] has used a similar test, where the specimen is placed on a stationary wedge and impacted with a falling weight, see Figure 6.2. In this version of the test the open ends of the specimen are free rather than clamped as with the IWP test shown in Figure 6.1. All tests reported by these authors, using both aluminium-alloy and steel adherends, were conducted using an impact velocity of 2 m/s.

Thouless et al[133] used an analytical method to estimate the adhesive fracture energy, G_c, from the final curvature of the adherends. The G_c values calculated were considerably lower than those measured experimentally using other methods, although all failures were cohesive-in-adhesive. For example, using the TDCB tests discussed in Chapter 4, the 'LMD1142' adhesive was found to have a G_c value of 4.25 kJ/m^2 at a crack velocity of 2 m/s. Thouless et al calculated a value of only 1.95 kJ/m^2 for this adhesive from tests with aluminium-alloy adherends, and the value from tests with steel adherends was even lower at 1.20 kJ/m^2. Similarly, the value calculated for the 'XD4600' adhesive was much lower

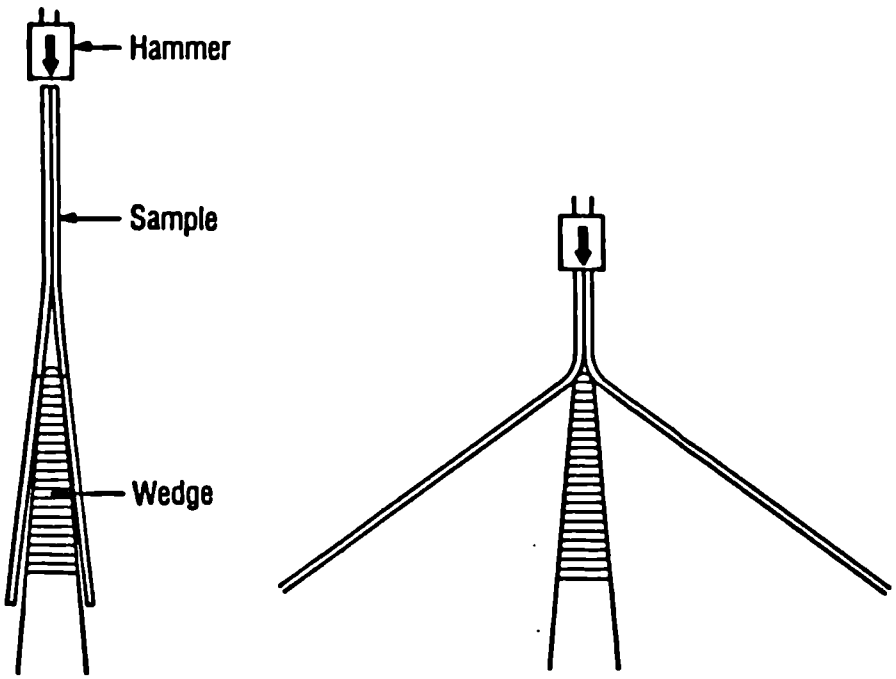


Figure 6.2: Thouless et al falling weight impact wedge test, from[133].

than published values[68].

Using this analytical solution Thouless et al attributed 7 % of the energy consumed in the test to adhesive fracture, 28 % to plastic deformation of the adherends and the remaining 65 % to frictional heating. However if the value of G_c is considered to be underestimated by a factor of 2.2, i.e. 4.25 kJ/m^2 instead of 1.95 kJ/m^2, then the adhesive fracture would account for 15 % of the energy. They estimated that the energy consumed by the plastic deformation was approximately four times the energy due to fracture of the adhesive, hence this term would contribute 62 %. Frictional heating would then only make up the remaining 23 %. Thus the plastic deformation of the adherends would be the dominant energy absorption mechanism, rather than the frictional heating as suggested by the authors. The use of thermal imaging to investigate the temperature increases due to frictional heating will be discussed in Section 6.4.

The large underestimation of the adhesive fracture energy may be due to the authors' use of simple beam theory to model the specimen. This type of analysis has been shown to be inadequate by other workers when used to analyse the DCB specimen[135, 136], a geometry that is similar in many respects to the test used by Thouless et al. The inaccuracy of the predictions limits the usefulness of this analytical solution. However, in the present work a finite element model of the IWP test will be used to calculate the wedge cleavage-force from the adhesive fracture energy. This will be discussed in Section 6.7.

6.3 Experimental Procedure

6.3.1 Specimen Manufacture

The IWP specimens in this work used 0.9 mm thick steel and aluminium-alloy adherends. Details of the adherends used are given in Chapter 3. These were guillotined to the required size, 20±0.25 mm wide by 90 mm long. They were pre-formed by clamping the ends to be bonded in a jig, and tapping a forming wedge between the free ends to separate and plastically deform them, see Figure 6.3. The clamping hole was drilled using the same jig, a spacer being clamped between the adherends to prevent bending whilst drilling.

Prior to bonding the surfaces of the adherends were gritblasted and degreased, as detailed in Section 3.3. Adhesive was applied to both adherends, with a loop of copper wire to ensure a constant adhesive layer thickness of 0.4 mm. Work by Holmes[130] and Davis[26] has shown that the presence of this wire has no effect on the results, but they used copper wire because its low stiffness should minimise any possible effect. Further tests by Davis and Fay[26] to investigate whether the use of a stiffer wire, e.g. stainless steel, has any effect have proved inconclusive. The adherends were brought together and clamped in individual bonding jigs, shown in Figure 6.4, the excess adhesive being removed prior to curing. Care was taken to remove all the adhesive from the 'V' formed by the adherends before curing.

Any excess adhesive present round the sides of the specimen after curing was removed with a knife or file. The small bead of cured adhesive in the 'V' formed by the adherends, if present, was not removed to prevent any possible notching effect.

6.3.2 High Rate Testing

The specimens were tested using a high-speed servo-hydraulic machine, as shown schematically in Figure 6.5. For consistency and ease of comparison, the present work used a test rate of 2 m/s for both the steel and the aluminium-alloy specimens, rather than the 2 and 3 m/s respectively as recommended by the Standard. The test apparatus used a lost-motion device (LMD), which allows the ram to accelerate for a short distance and reach the required velocity before it picks up the specimen, see Figure 6.5. The contact between the ram and the LMD was damped using rubber washers to reduce any oscillations when the LMD is picked up. The specimen grip and LMD were made from titanium to reduce the inertia of the system. The specimen grip, rather than the wedge shackle as recommended by the Standard, is attached to the moving part of the testing machine for the same reason. An oscilloscope was used to record the displacement versus time output from the testing machine and the force versus time signal, as shown

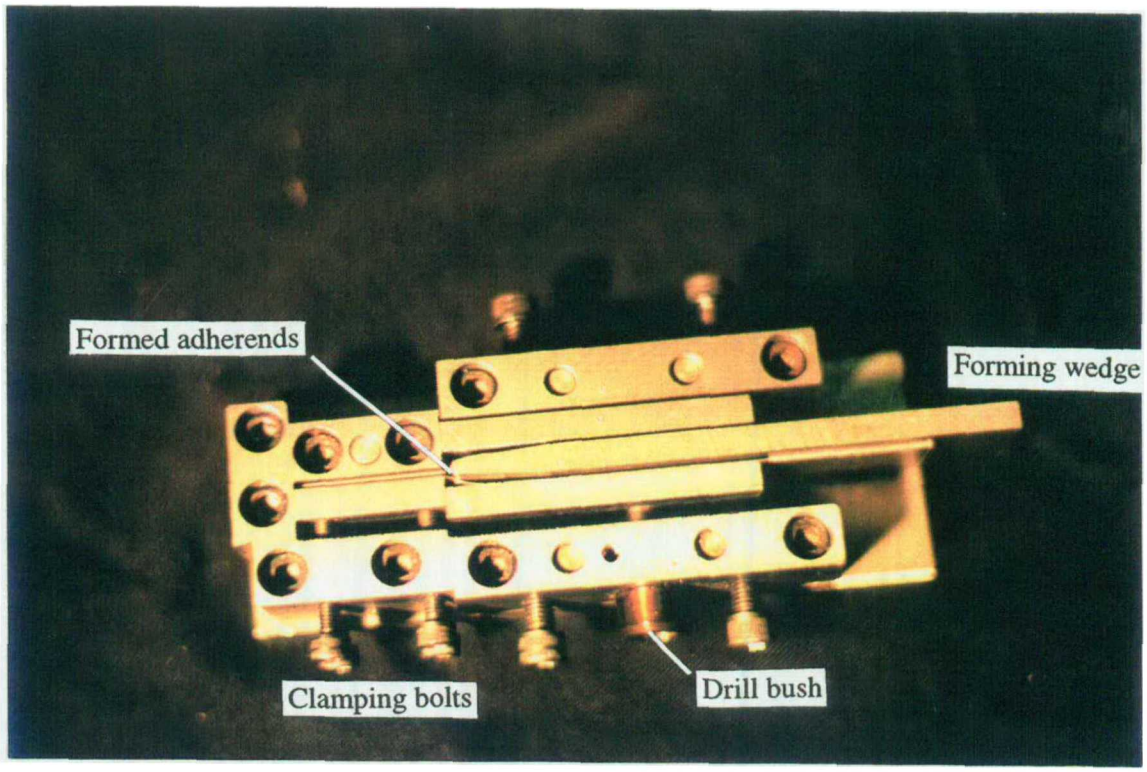


Figure 6.3: Pre-forming jig used for IWP adherends.

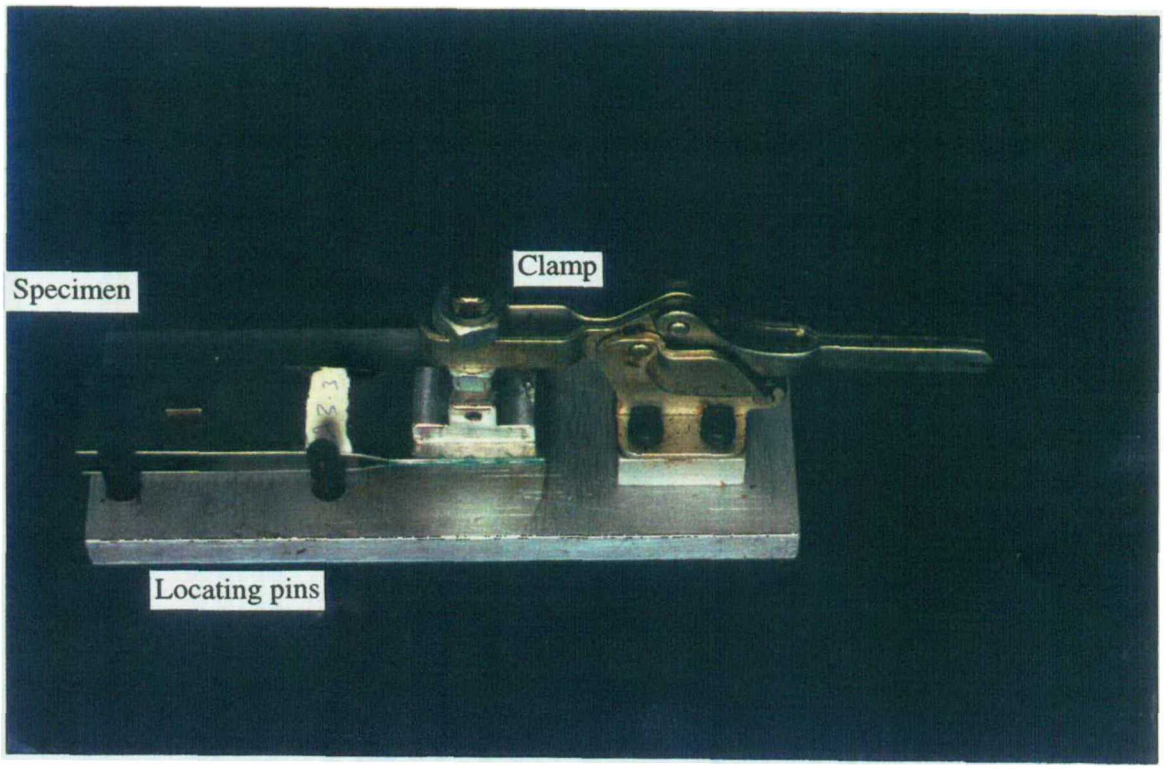


Figure 6.4: Bonding jig used for IWP specimens.

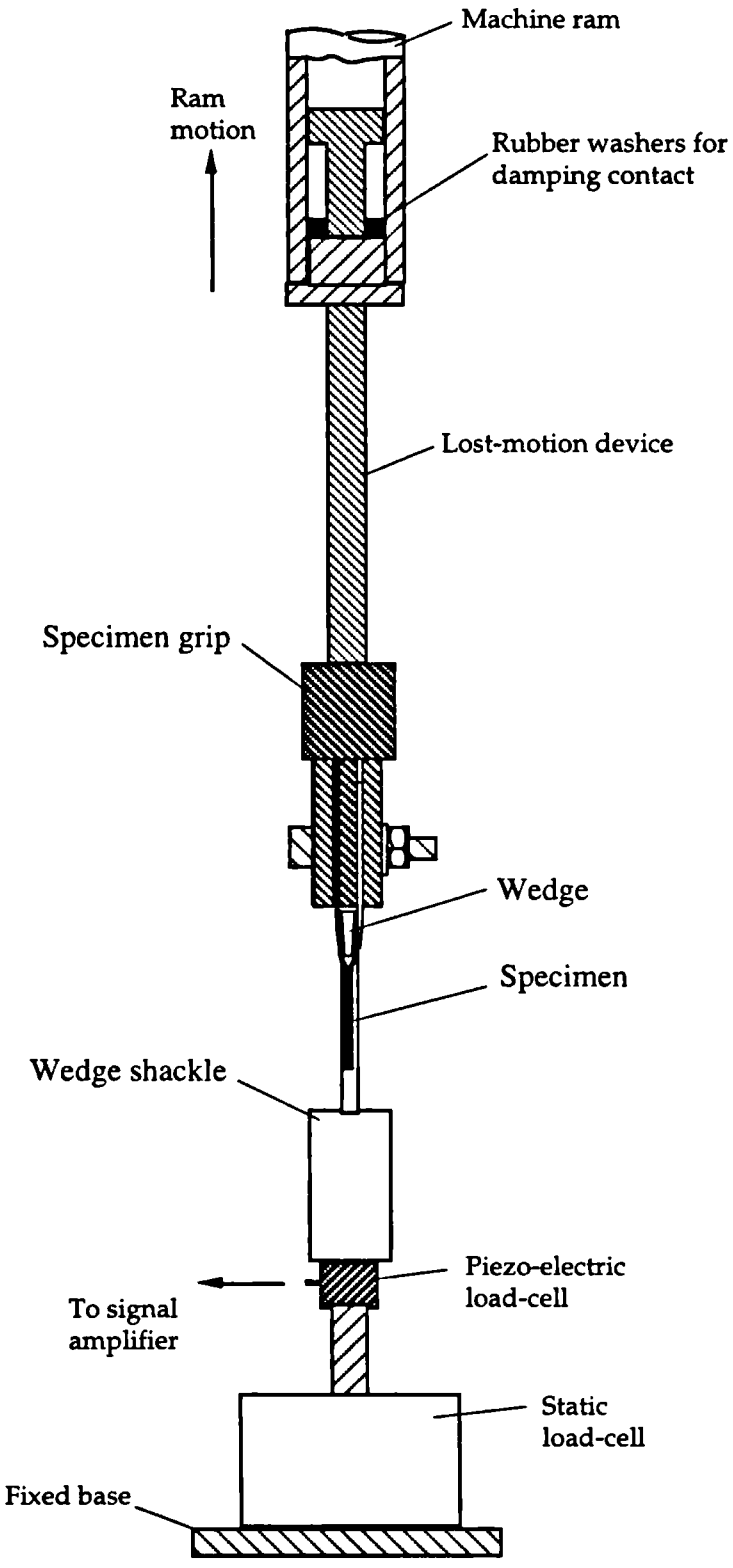


Figure 6.5: High rate test apparatus for IWP tests.

schematically in Figure 6.6. These traces were then transferred to a computer analysis package to calculate the results, as described in Section 6.5. High-speed photography was also used with some tests, see Section 6.3.3.

A small piezo-electric load-cell, as used in Chapter 4, was mounted below the wedge shackle and was initially used to measure the force on the specimen, as shown in Figure 6.5. However, this system was found to resonate at just over 2 kHz. The traces produced were unsuitable for the calculation of results due to the large oscillations superimposed on the specimen response, see Figure 6.7. Therefore strain gauges were bonded onto the arms of the wedge. Initially these were wired individually. The signals were recorded on two oscilloscopes, and then combined once the data had been transferred to the computer analysis package. This process was time-consuming because the oscilloscopes triggered at different times, with a variable interval between the triggers. However, the strain gauges produced a much clearer trace than the load-cell, see Figure 6.8. The response is also much closer to that reported by other workers in this field[26, 130].

The strain gauges were connected into a bridge circuit, producing a single signal and thus reducing the amount of post-processing required. The signals were not filtered, for the reasons discussed in Chapter 2. This arrangement was calibrated by placing a dummy specimen in the fixtures and applying a constant force. Calibrations were performed at forces up to 3 kN, and the response showed perfect linearity. In the calibration exercises, the static load-cell, as shown in Figure 6.5, was used to measure the force applied as the signal from the piezo-electric load-cell decays quickly. This static calibration was checked using specimens provided by Ford. Good agreement was found between the results[26] from these specimens and those tested by other laboratories. For example, the steel specimens bonded with the 'ESP110' adhesive gave an average total energy of 3.9±0.9 J. This compares with 3.4±0.8 J obtained by Ford[26]. The details of how typical force versus time traces, such as that shown in Figure 6.8, are analysed will be discussed later, in Section 6.5.

Analysis of the signals from individual strain gauges shows that the wedge exhibits bending in some tests. This puts pairs of gauges into tension and compression, so the effect cancels out when the gauges are combined in the bridge circuit.

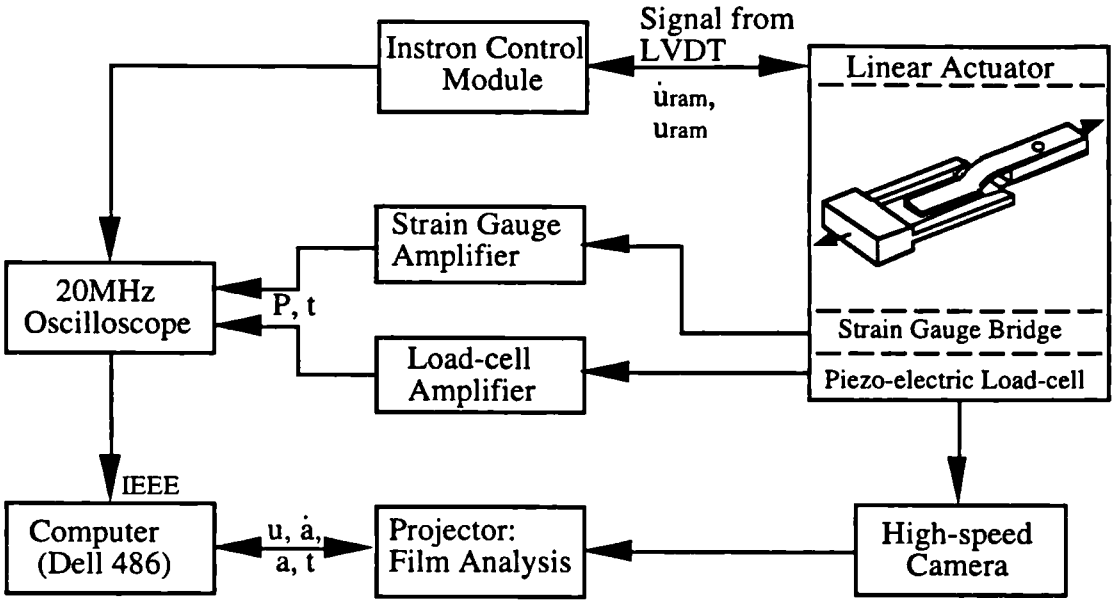


Figure 6.6: Schematic of testing arrangement for impact wedge-peel tests.

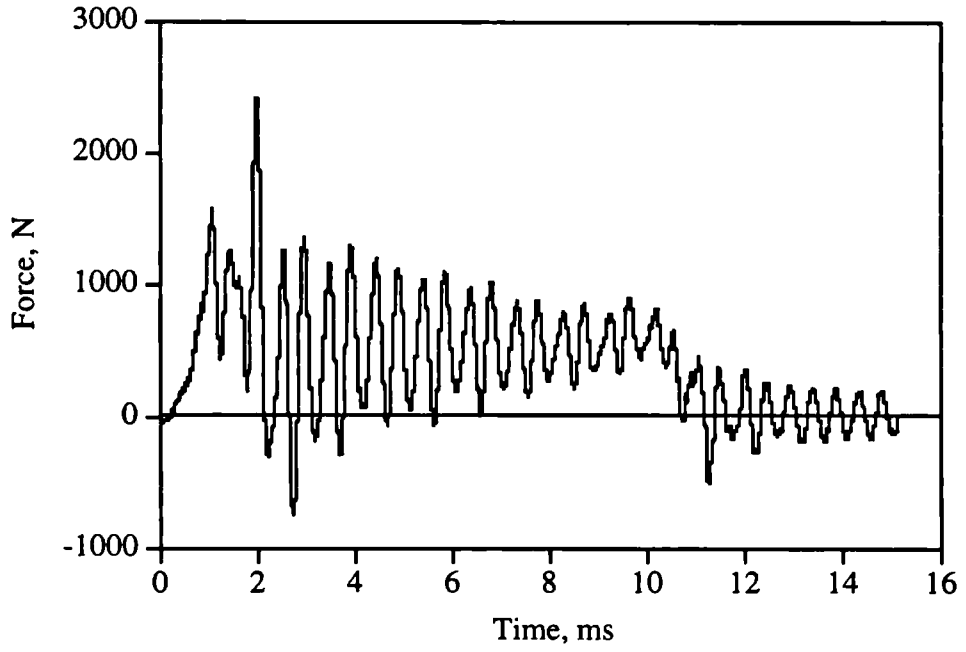


Figure 6.7: Force versus time trace from piezo-electric load-cell, showing oscillatory response. Steel specimen bonded with 'XB5315' adhesive, test rate of 2 m/s, stable crack growth.

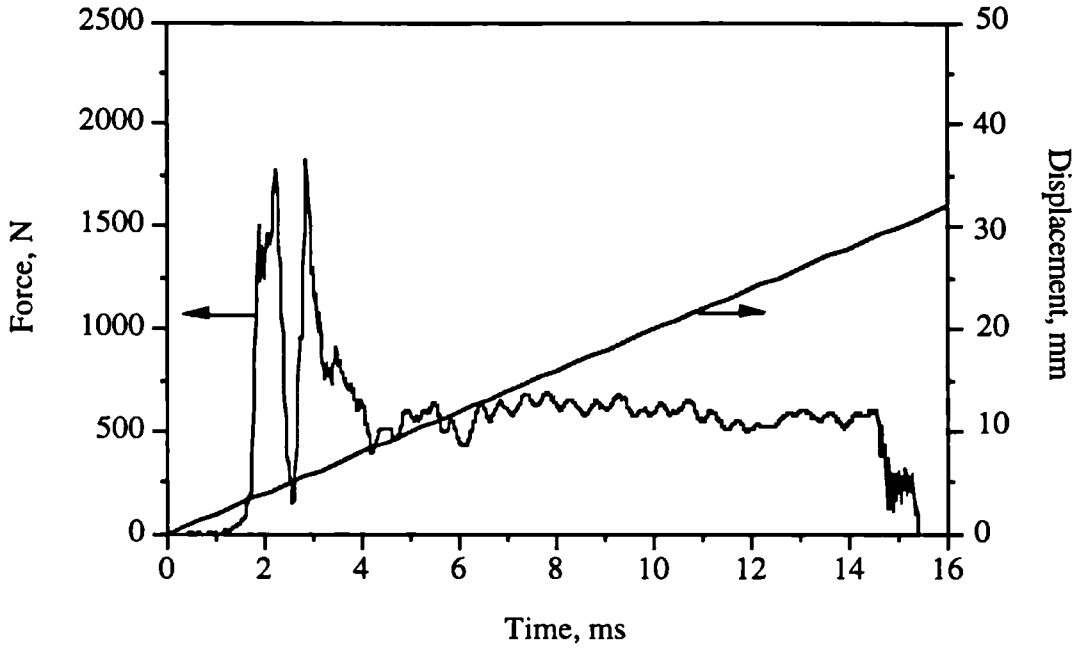


Figure 6.8: Force and displacement versus time response from instrumented wedge, steel specimen bonded with 'XB5315' adhesive tested at 2 m/s, stable crack growth. Compare with the response of the load-cell shown in Figure 6.7.

The signal from the strain gauge bridge and the displacement, taken from an LVDT on the machine ram, were recorded. The test rate was calculated from the gradient of the displacement versus time response. This response was linear, see Figure 6.8, and hence the test rate was constant. Room temperature (20°C) tests were conducted at 10^{-4} and 2 m/s. Additionally, 2 m/s tests were conducted at -40 and 60°C.

The -40 and 60°C tests were performed using an environmental chamber mounted on the testing machine. The time taken for the specimens to attain the test temperature was measured using a thermocouple embedded in the adhesive layer of a sample specimen. It was also necessary for the strain gauge bridge to reach the test temperature, and for the output to stabilise. Thus, after the specimen was placed in the testing fixture, it was allowed to acclimatise for 15 minutes before being tested. The broken specimen was removed and the chamber left for a further ten minutes before the next specimen was fitted.

The strain gauge bridge was calibrated at all the test temperatures used. This showed a linear relationship between the calibration factor and the test temperature, with a gradient of 320 mV/N°C. This corresponds to a change of 0.76 N per degree centigrade for a force of 1000 N.

6.3.3 High Speed Photography

A 16 mm 'Photec IV' rotating prism high-speed camera ('Hadland Photonics') was used to film some of the IWP tests to investigate how the specimens failed at the high test rate. The specimens were illuminated with floodlights and a focused tungsten spotlight. These were activated immediately before testing to prevent any heating of the specimen. Tungsten-balanced Eastman 7250 colour film was used.

A typical wedge-peel test at 2 m/s lasts about 15 ms. To enable sufficient data to be taken from the film to compare with the force versus time traces, the camera was run at its maximum speed of 5000 frames per second. The camera was fitted with a half-frame converter, enabling two pictures to be taken on each frame of film, giving a total of 10,000 pictures per second (pps). This would be expected to give about 150 pictures of the test in progress. Although the film used was 100 feet long, due to the time taken for the camera to accelerate to full speed, the film was still accelerating when the specimen was tested. Thus, the final framing rate was less than that specified. However, as the camera printed a timing mark on the film every millisecond, the actual framing rate could be calculated. These timing marks showed that a framing rate of approximately 6000 pps was obtained, giving about 90 pictures over the duration of the test.

The disadvantage with using such a high framing rate is that, as the film speed is increased, the picture quality deteriorates, which produces a grainy picture. The picture also becomes darker, as less light is absorbed by the film when it is travelling faster. Additionally, due to the geometry of the wedge-peel shackle, the camera could not be placed parallel to the plane of the crack, i.e. side-on to the specimen. Instead it was placed at an angle of approximately 45°, making the crack less clear. These effects combine to make the crack tip difficult to locate on the final image, and may lead to errors in the subsequent analysis of the films.

To analyse the high speed films, they were projected onto a screen, allowing measurements to be taken. The distance from the wedge tip to the crack tip was measured from the image, as was the distance from the wedge to the end of the specimen. Thus, the crack length, and hence the crack velocity, and the specimen velocity could be calculated. The magnification factor of the image was calculated from the projected size of the wedge shackle.

6.4 Thermography

Some of the IWP tests were filmed using an 'Agema TIC 8000' thermal imaging camera, using the maximum frame capture rate of 25 frames per second. A metal plate, cooled to 0°C, was placed behind the test apparatus so that it was distinguishable from the background signal. This also allows the camera to be focused on the specimen. The specified temperature range is divided into sixteen levels, with a minimum of 0.2°C between each level[137].

Room temperature tests were performed on steel IWP specimens bonded with the 'XW1044' adhesive at a test rate of 2 m/s. The maximum temperature observed was about 55°C on the adhesive material removed from the adhesive layer by the wedge, see Figure 6.9, compared with an ambient 20°C. This is a temperature rise of 35°C. The maximum temperature seen on the fracture surface of the adhesive was 41°C, a rise of 21°C, as shown in Figure 6.10.

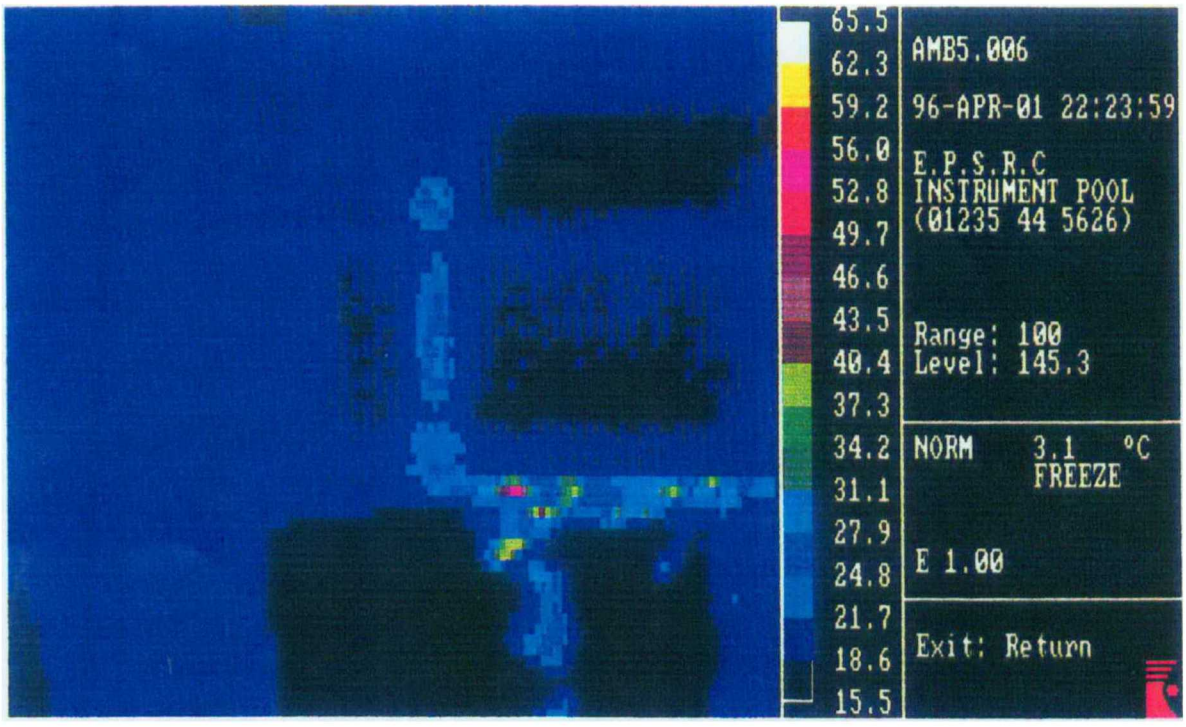
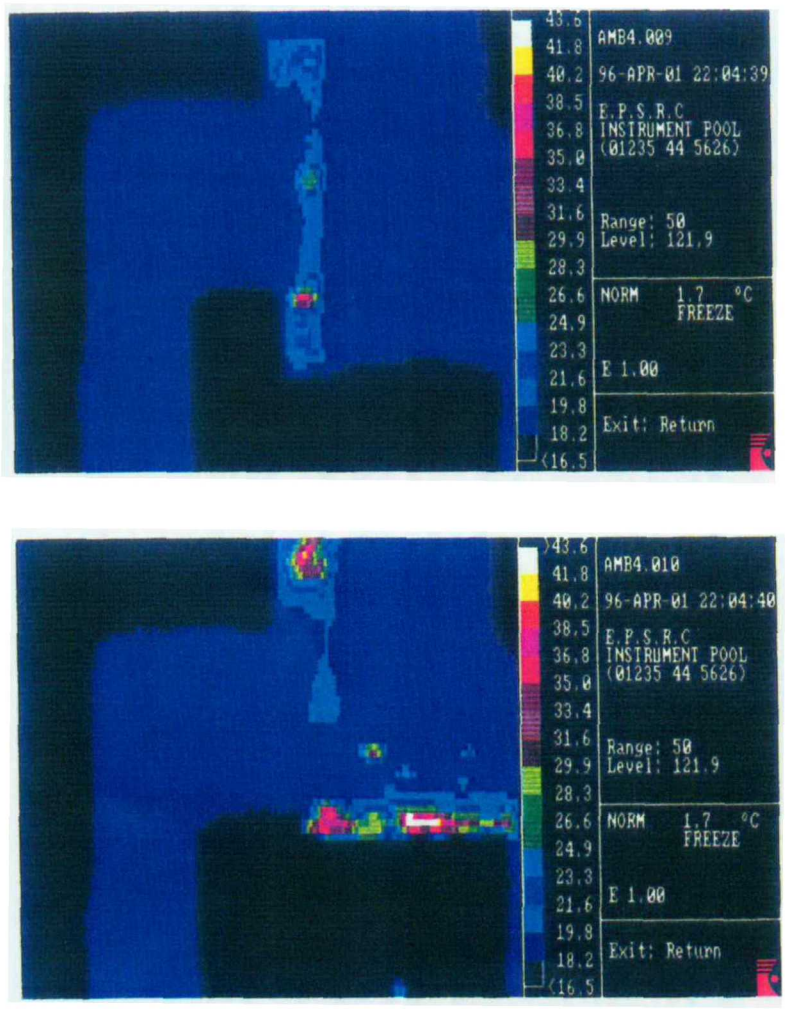


Figure 6.9: Thermal image of impact wedge-peel test showing a maximum temperature of 55°C on the material removed from the adhesive layer by the wedge, for a steel specimen bonded with 'XW1044' adhesive, tested at 2 m/s and 20°C.



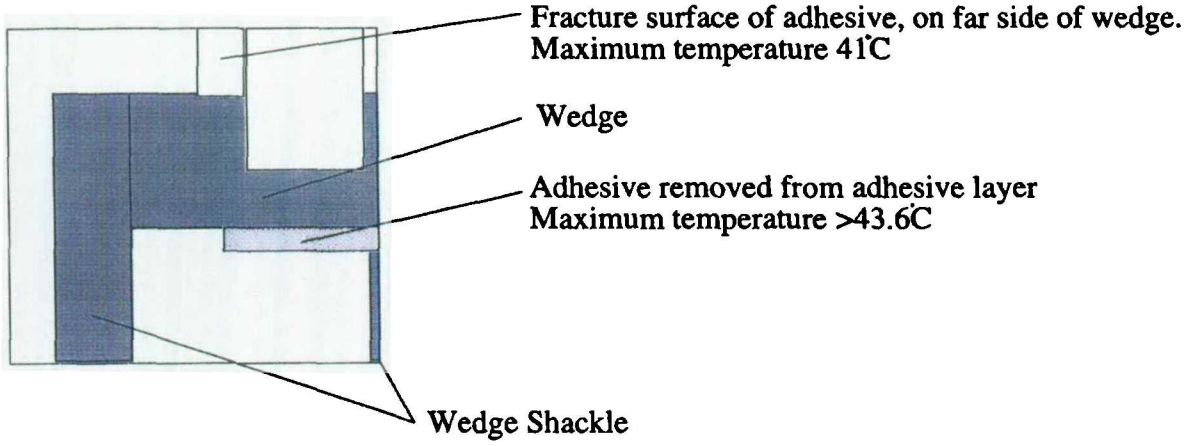


Figure 6.10: Thermal images of IWP test, showing a maximum temperature of greater than 43.6°C on the material removed from the adhesive layer, for a steel specimen, bonded with 'XW1044' adhesive, tested at 2 m/s and 20°C.

For comparison, T-peel tests were performed on steel specimens bonded with the 'XW1044' adhesive, see Figure 6.11. The specimens were made from IWP specimens by bending the unbonded arms to an angle of 90° from the bonded region. The unbonded arms were also shortened to allow them to be fitted into the grips used. These tests allowed the temperature rise due to the fracture to be measured, without the frictional heating due to the wedge. These tests showed an ambient temperature of 17°C and a maximum of 20°C at the crack tip and on the final fracture surface, as shown in Figure 6.12. The recorded temperature rise of only 3°C shows that little heat is generated by the fracture and deformation of the adherends. Thus the temperature rises observed during the IWP test must result mostly from frictional heating of the adhesive due to the wedge passing over the fracture surface.

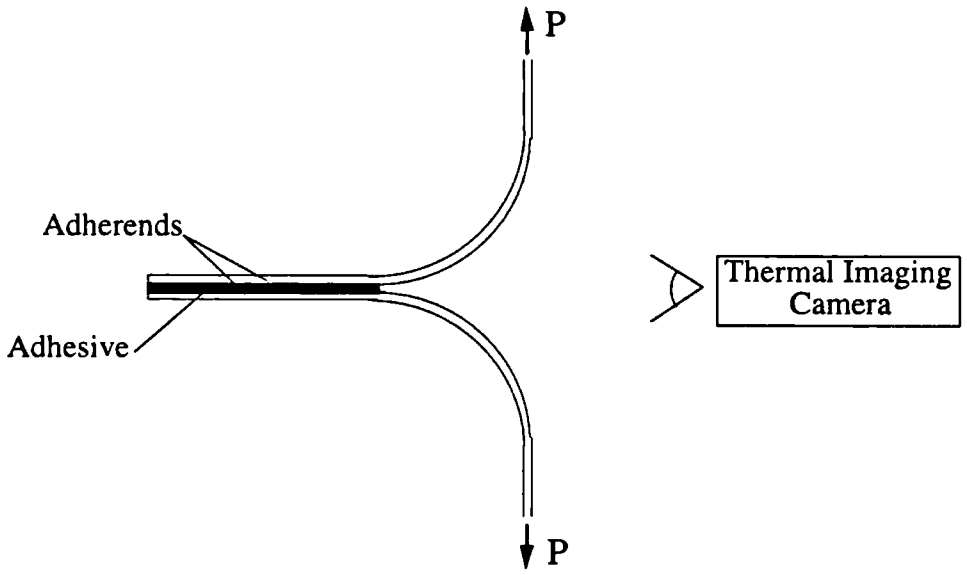


Figure 6.11: The T-peel test geometry, showing position of thermal imaging camera.

Work reported by Dickie & Ward[134], using the test configuration shown in Figure 6.2, observed that temperature increases of up to 125°C can occur at the wedge due to friction. The corresponding temperature rise at the crack tip was only about 10°C. The authors do not mention where their thermal imaging equipment was placed, and so it is not possible to determine at what points they were measuring the temperature. However, their equipment used a faster frame capture rate than the camera used in the current work, and hence the peak temperatures measured may be more accurate than those in the current work. However, it should be noted that the total energies measured by the previous workers and those from the IWP tests in the current work are comparable.

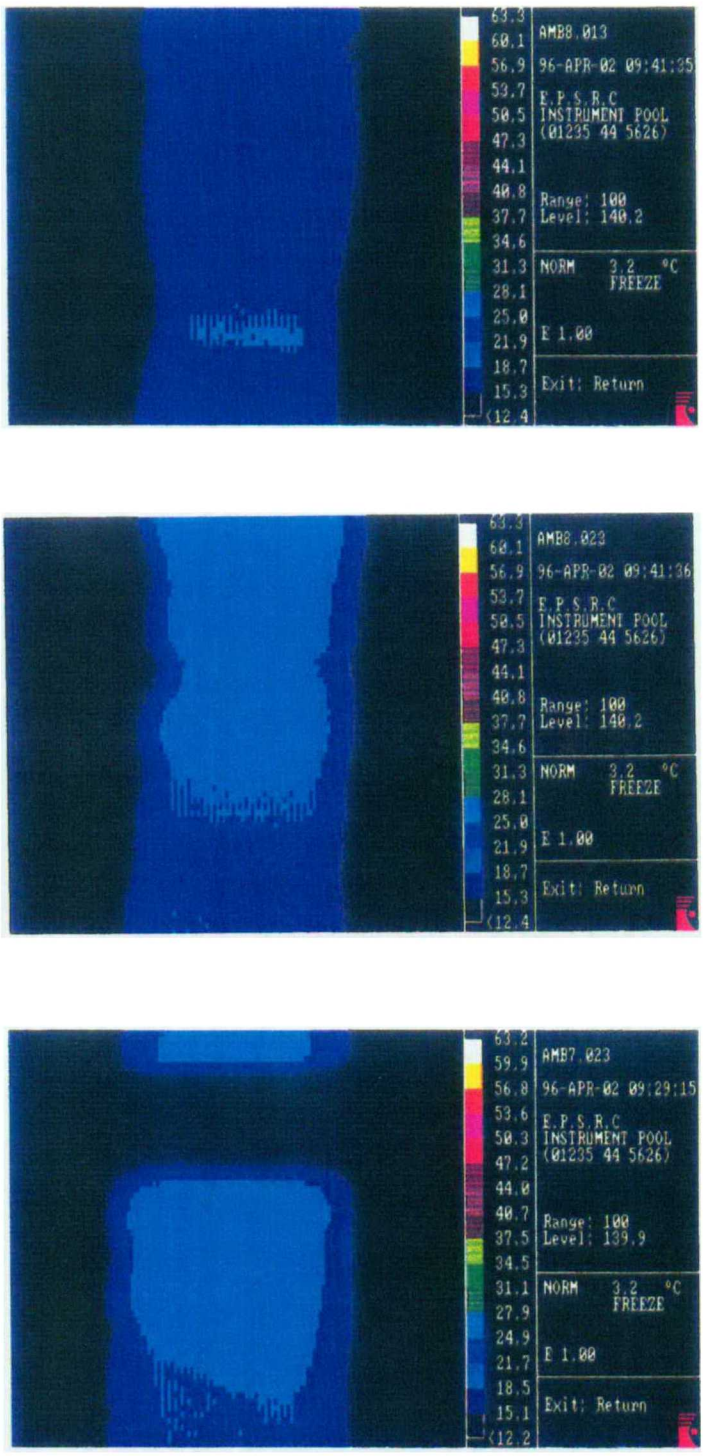


Figure 6.12: Thermal images of T-peel test, showing a temperature rise of 3°C at crack tip. Images from two tests have been combined, looking down the throat of the specimen. Steel specimens, bonded with 'XW1044' adhesive, tested at 2 m/s and 20°C.

Nevertheless, it is difficult to make a direct comparison as few experimental details are given.

The observations of the IWP test reported in the current work show lower peak temperatures and a very localised heating effect. This would indicate that little energy is consumed by the frictional heating. The differences in the results may be explained by the difference in the test geometries, as shown in Figures 6.1 and 6.2. It is not possible to estimate the amount of energy absorbed by the frictional heating as the volume of adhesive affected cannot be determined, due to the limited resolution of the camera. If it is restricted to the surface of the adhesive, little energy will be absorbed. However, if the entire thickness of the adhesive is heated much larger amounts of energy than those measured in the test can be absorbed. For example, an adhesive layer 0.4 mm thick would require 0.4 J to raise its temperature by only 1°C. (This assumes a density of 1200 kg/m^3, and a specific heat capacity of 1.4 kJ/kgK. The latter value is quoted for unfilled epoxy resin[138].) Note that a steel specimen bonded with the 'XW1044' adhesive typically absorbed a total of 7.3 J during the IWP test. Thus the observed temperature rises of 25°C would require 10 J to heat the entire thickness of the adhesive, more energy than is absorbed during the test.

To obtain an accurate picture of the thermal response of the specimen a faster camera system is required. Improved resolution is also required to determine the thickness of the adhesive affected by the temperature rise. Given this information, it should be possible to estimate the amount of energy that is absorbed by the frictional heating. However, the current work has shown that friction between the wedge and the fractured surface of the adhesive does play a part in the IWP test. Thus it will be necessary to include the effect of friction in the finite element model discussed in Section 6.7.

6.5 Analysis of the IWP Test Data

6.5.1 Introduction

This Section discusses how the IWP test data are analysed. The method of analysis recommended by the ISO Standard will be considered, and the problems associated with it will be discussed. Other possible methods of analysis will also be considered. Finally the best method of analysis will be identified. However, first the shape of a typical IWP force versus time curve will be considered by looking at how a crack grows through the specimen.

6.5.2 Types of Crack Growth in the IWP Specimen

6.5.2.1 Stable Crack Growth

Stable crack growth was observed for all the adhesives used at 60°C, and for most of the adhesives at 20°C, using a test rate of 2 m/s. A typical IWP force versus time trace, when stable crack growth occurs, consists of one or two peaks followed by a 'plateau' region, as shown in Figure 6.13. The initial rise occurs when the wedge makes contact with the specimen. Rapid crack growth occurs when a crack initiates, typically after approximately 1 ms, and the measured force drops. The crack then runs for about 5 mm and arrests. This forms the first peak, and the process is repeated for the second peak, after which the crack growth is stable through the rest of the specimen. This stable 'plateau' region typically lasts for approximately 10 ms for a test at 2 m/s. Analysis of the high-speed films shows that the crack velocity is equal to the test rate over this region, and there is about 20 mm of stable crack growth in the 'plateau' region.

At both the test rates used, of 10^{-4} and 2 m/s, the crack velocity is constant and equal to the test rate over the 'plateau' region. Observations at 10^{-4} m/s indicate that the crack tip is a constant distance ahead of the wedge over this portion of the test. The smaller this distance, the higher the recorded 'plateau' force. Analysis of the high-speed films confirms that this is also the case at 2 m/s.

Towards the end of the test, the distance from the crack tip to the wedge increases, causing a decrease in the recorded force. This can be seen on Figure 6.13 after 14.5 ms. This is observed both by visual observation at 10^{-4} m/s and by analysis of the high speed films of the 2 m/s tests. This effect is probably caused by changes in the specimen compliance as the crack tip approaches the end of the specimen.

Specimens that exhibit a 'plateau' region in their force versus time trace, as shown in Figure 6.13, exhibit considerable plastic deformation of the adherends, see Figure 6.14a. Thus a large amount of energy is absorbed in comparison with specimens that exhibit no stable crack growth.

6.5.2.2 Unstable Crack Growth

All the steel specimens tested at -40°C exhibited unstable crack growth. Specimens which exhibit unstable crack growth typically show a force versus time response similar to that shown in Figure 6.13. The response in the peak region is similar to that seen in stable failure, namely the crack initiates then arrests, and initiates again. However, the crack does not arrest a second time or settle into the stable crack growth state described above. Instead the crack propagates completely through the specimen. For example, a crack

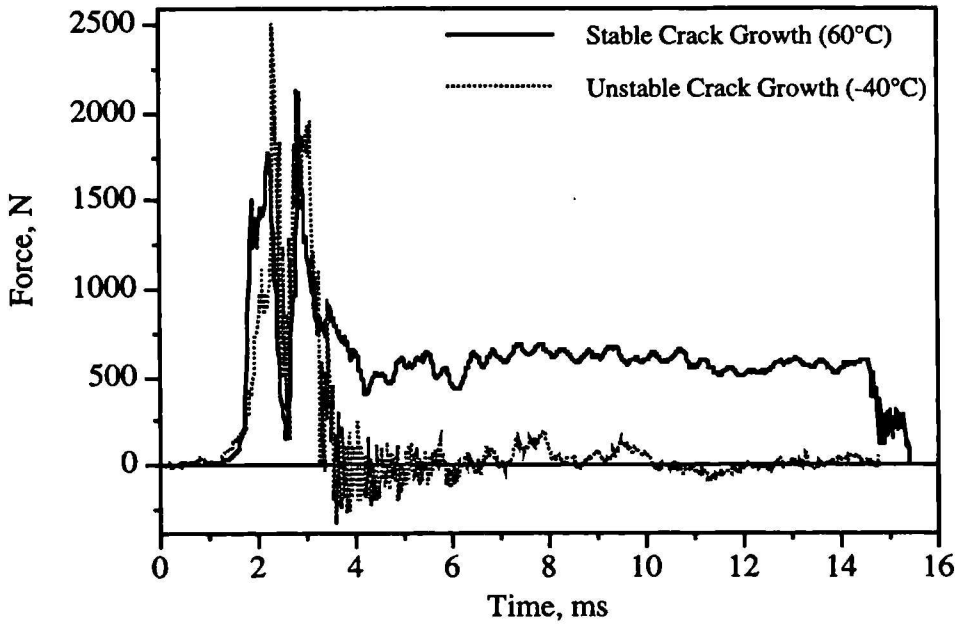
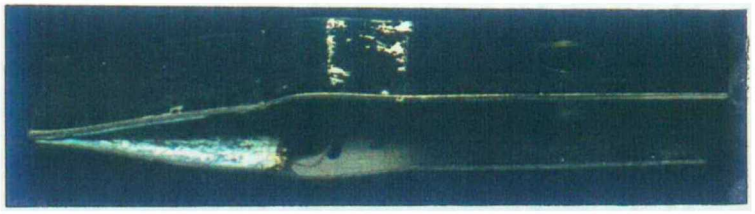
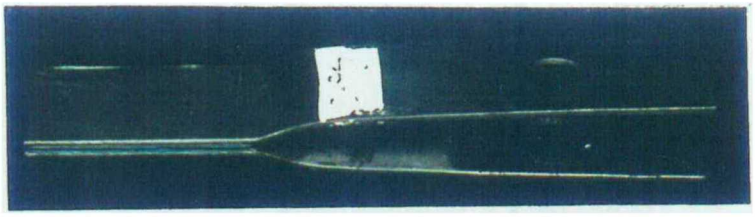


Figure 6.13: Force versus time responses from impact wedge-peel specimens shown in Figure 6.14. Steel substrates bonded with 'XB5315' adhesive, tested at 2 m/s and at 60 and -40°C.



(a) Stable crack growth showing plastic deformation of substrates. 'XB5315' adhesive with steel substrates, tested at 60°C.



(b) Unstable crack growth showing no plastic deformation of substrates. 'XB5315' adhesive with steel substrates, tested at -40°C.

Figure 6.14: Fractured impact wedge-peel specimens tested at a rate of 2 m/s showing the extent of plastic deformation, (a) stable crack growth (60°C), and (b) unstable crack growth (-40°C).

velocity of 30 m/s was measured, using the high-speed photography, for the unstable failure of a steel specimen bonded with the 'AV119' adhesive, tested at 2m/s and 20°C. In this case there was only one initiation, and the crack never arrested. The high crack velocities observed result in a very short time to failure, in the order of 1 to 2 ms compared with about 15 ms for stable failure. Little energy is absorbed by the specimen during unstable failure, and no plastic deformation of the adherends occurs, see Figure 6.14b.

6.5.3 Methods of Analysis

6.5.3.1 The ISO Standard Method

The ISO Standard specifies that the average cleavage-force is calculated from the force versus time data, disregarding the first 25 % and the last 10 % of the curve, see Figure 6.15. The energy is also calculated, by integrating over the same part of the curve, and multiplying by the test rate. The trace shown in Figure 6.15 displays initial peaks, followed by a 'plateau' region where stable crack growth occurs. Thus for a test which exhibits stable crack growth the ISO Standard analysis method calculates the force and energy values from within the 'plateau' region.

6.5.3.2 Criticisms of the ISO Standard Method

However, some test results do not show this stable 'plateau' region, but fail in an unstable manner, as shown in Figure 6.16. Here the ISO Standard analysis method calculates a large cleavage force indicative of a 'tough' adhesive when the joint is actually exhibiting very 'brittle' behaviour, as shown in Figure 6.17 and Table 6.1. The wedge-cleavage force values calculated using the ISO Standard method apparently indicates that the specimen which exhibits unstable failure performs better than that which exhibits stable failure. This is obviously not the case, as can be seen if the total energies absorbed are compared, see Table 6.1. The energy values calculated using the ISO Standard method (as a proportion of the total energy absorbed) are significantly higher for the 'unstable' failure than that from the 'stable' failure. Thus this ISO Standard analysis method fails to give a true measure of the specimen performance.

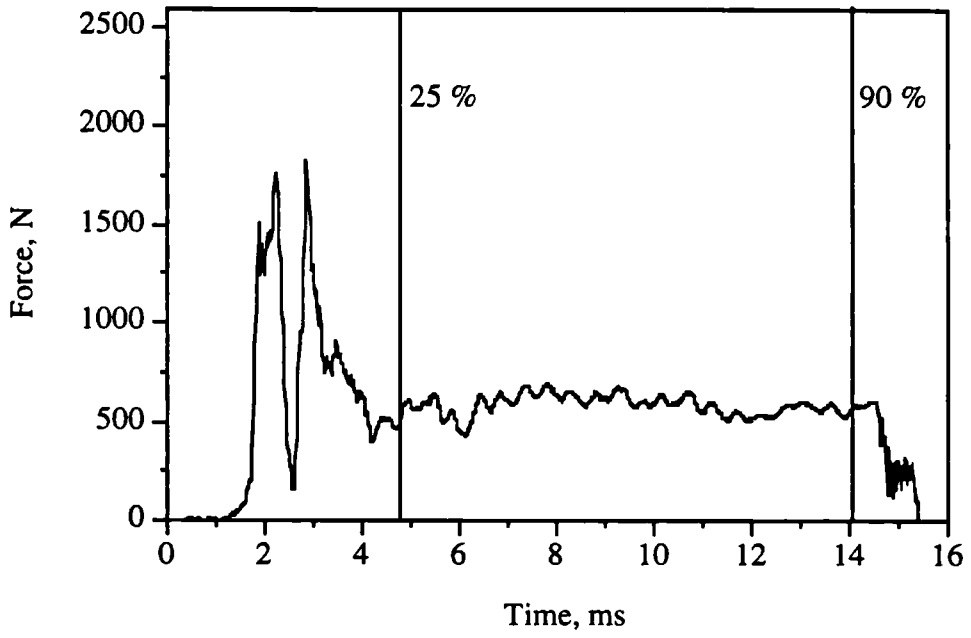


Figure 6.15: ISO Standard method of calculating wedge cleavage-force, stable crack growth. Steel specimen bonded with 'XB5315' adhesive tested at 2 m/s and 20°C.

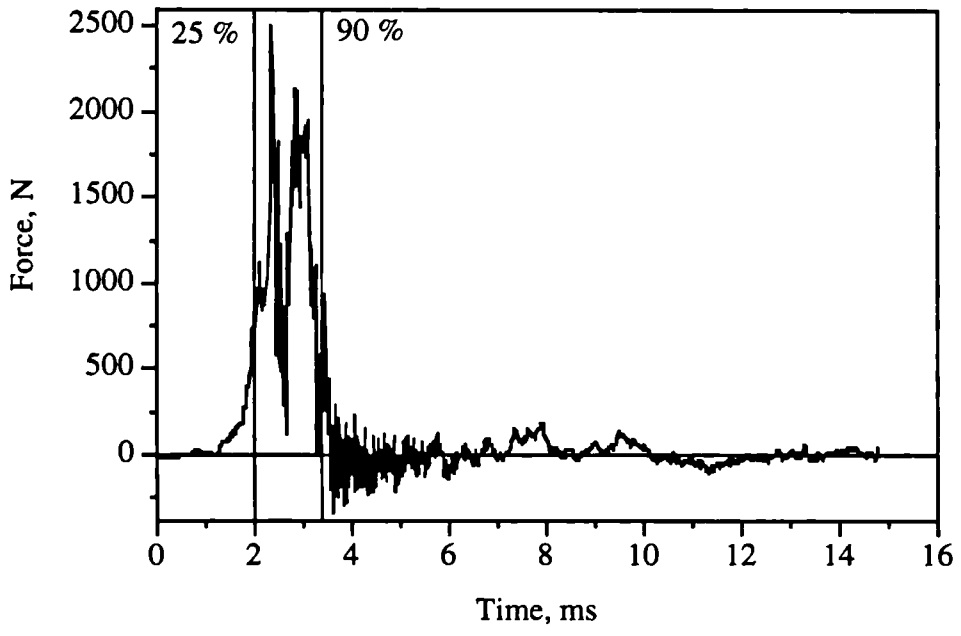


Figure 6.16: Impact wedge-peel test, unstable crack growth, showing the ISO Standard force interval. Steel specimen bonded with 'XB5315' adhesive, tested at 2 m/s and -40°C. (Compare with Figure 6.15.)

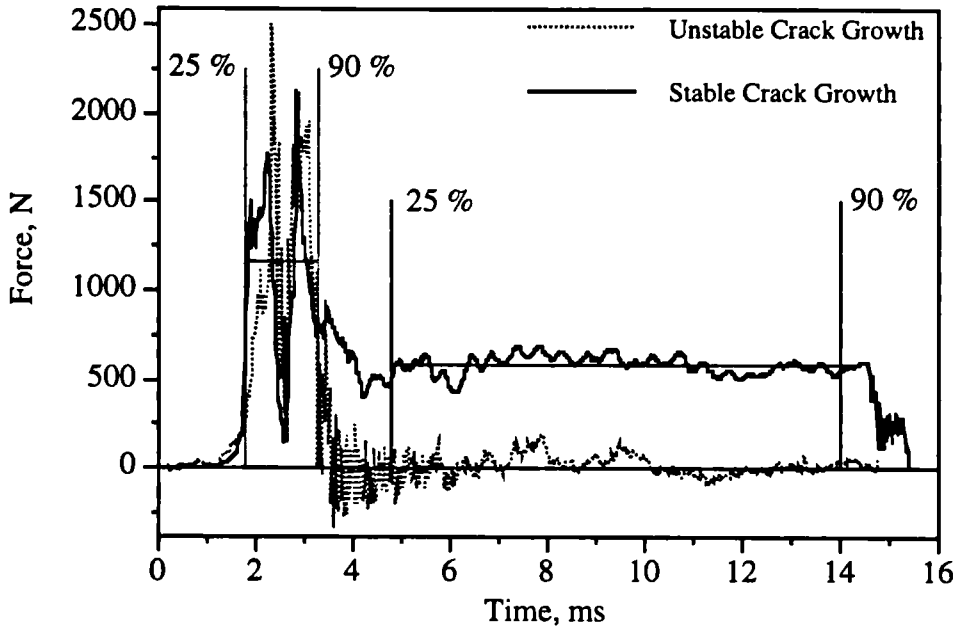


Figure 6.17: ISO Standard method of analysis applied to stable and unstable crack growth, steel specimens bonded with 'XB5315' adhesive tested at 2 m/s, showing average IWP cleavage-forces calculated using ISO Standard method.

Table 6.1: Impact wedge-cleavage force and energy values calculated by the ISO Standard method, stable and unstable crack growth, for steel specimens bonded with 'XB5315' adhesive tested at 2 m/s. (Force versus time responses shown in Figures 6.15 and 6.16.)

Crack growth	ISO Standard method		Total energy, J	Standard energy / total energy
	Cleavage-force, N	Energy, J		
Stable	590	10.2	16.8	0.61
Unstable	1170	3.5	3.8	0.92

6.5.3.3 Other Methods of Analysis

As the ISO Standard method of analysis has its disadvantages, hence it is useful to consider whether another method is preferable. The test data can be analysed by calculating the force and/or the energy over a number of intervals, as shown in Figure 6.18. Force and energy data have therefore been obtained using these intervals, see Appendix 5. The data presented in Appendix 5 are summarised in Table 6.2.

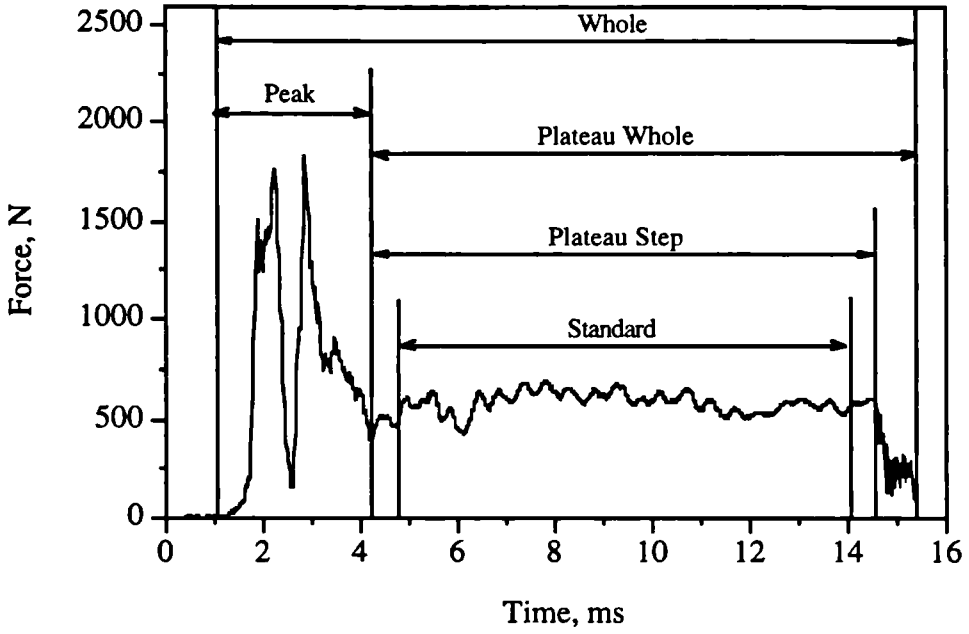


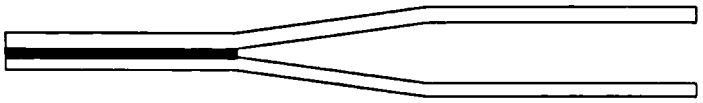
Figure 6.18: Analysis methods for impact wedge-peel test evaluated in current work. Also see Appendix 5.

Table 6.2: Average force and energy calculated over intervals identified in Figure 6.18, steel adherends bonded with 'XB5315' adhesive, tested at rate of 2 m/s and 20°C (summary of data shown in Appendix 5).

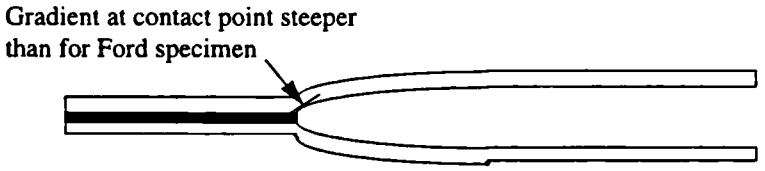
	Whole	Peak	Plateau whole	Plateau step	Standard
Force, N	535	732	532	547	553
Energy, J	14.4	3.9	10.4	10.2	8.9

6.5.3.4 Effect of IWP Specimen Geometry

Any analysis method that includes the initial peaks in the calculations is sensitive to the profile of the adherends, although the ISO Standard does not specify what profiles may or may not be used. For example, test specimens manufactured by Ford Research, and tested by the author, tapered at a shallow angle from the open end to the adhesive layer, see Figure 6.19, while those produced by the author follow more closely the profile drawn in the ISO Standard. The author's specimens possess a higher effective stiffness, so the initial gradient of the force versus time response is steeper, see Figure 6.20. Thus less energy is absorbed in the peak part of the response. The length of unstable crack propagation in a specimen with a shallow profile is also greater, thus there is a shorter



(a) Ford specimen design, shallow taper.



(b) Author's specimen design, steep taper.

Figure 6.19: IWP specimen designs used by Ford and by the author, showing differences in geometry at the wedge contact point, (a) Ford specimen design, (b) author's specimen design.

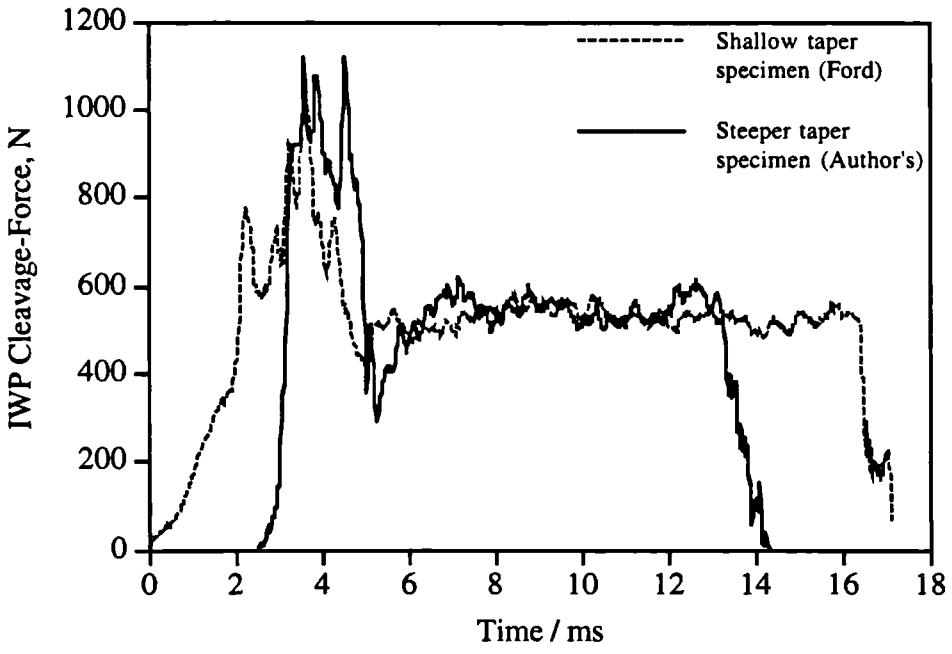


Figure 6.20: Force versus time responses of IWP specimens using Ford and author's own specimen design. Specimen designs are shown in Figure 6.19. Steel specimens bonded with 'XB5315' adhesive, tested at 2 m/s.

length of adhesive remaining when the transition to stable crack growth occurs, and hence the 'plateau' region is shorter, and less energy is absorbed in this portion of the test, as shown in Figure 6.19 and Table 6.3. Note that the average cleavage-force calculated using the ISO Standard method is the same for both types of specimen, but the energies calculated using the ISO Standard method differ considerably.

Table 6.3: Impact wedge-cleavage force and energy values calculated by ISO Standard method, and total energy, Ford and author's own specimens. Data shown are mean (±standard deviation). The data shows that the best measure of comparison is the Standard cleavage-force. Steel specimens bonded with 'XB5315' adhesive, force versus time responses shown in Figure 6.20.

	ISO Standard method		Whole method
Specimen Type	Cleavage-force,N	Energy, J	Total energy, J
Ford	**585** (±40)	**11.9** (±0.6)	**17.6** (±0.5)
Author	**555** (±25)	**8.9** (±0.9)	**12.5** (±1.1)

Note: Data for author's specimens shown in full in Table 6.2 and Appendix 3.

Thus the energy calculated using any of the methods of analysis shown in Figure 6.18 is affected by the adherend profile. This is confirmed if the energy is calculated from the whole data, see Table 6.3. As the ISO Standard allows any profile to be used, an analysis based on comparison of energies should not be used.

However, it is possible to compare the average force values in the 'plateau' region, as these are unaffected by the adherend profile. As it is simpler to locate the start and end of the test than the start and end of the 'plateau' region, the interval suggested by the ISO Standard analysis is the simplest. Thus for stable failure, the average wedge cleavage-force should be calculated from the force versus time data, disregarding the first 25 % and the last 10 % of the curve.

6.5.3.5 Analysing Unstable Failure

The problem of analysing unstable failure must also be addressed. It is suggested that when unstable failure occurs, i.e. there is no 'plateau' region, a zero force value should be quoted. This new method overcomes the problem that the Standard method indicates 'excellent' joint performance when unstable failure occurs, i.e. when the joint performance is poor. Example results are given in Table 6.4 for the data presented in Figure 6.17, i.e. the stable and unstable failure using steel adherends bonded with the 'XB5315' adhesive.

Table 6.4: Average cleavage force calculated from the force versus time data presented in Figure 6.17, disregarding the first 25 % and the last 10 % of the curve. ISO Standard and author's methods are used to analyse both stable and unstable failure. Data shows that Standard method does not give sensible result, erroneously indicating that the specimen which performs very poorly (i.e. unstable failure) is better. Author's method provides better measure of joint performance.

Crack growth	ISO Standard method Cleavage-force, N	**Author's method Cleavage-force, N**
Stable	590	**590**
Unstable	1170	**0**

6.5.3.6 Preferred Method of Analysis

In summary, it is proposed that the best method of analysis is to calculate the average cleavage-force calculated by the Standard method, providing that this section is contained within the 'plateau' region, i.e. for stable failure. Where no 'plateau' region exists, a zero value should be quoted, i.e. for unstable failure. This method provides the greatest differentiation, allows for differences in specimen design, and also clearly identifies when unstable failure occurs.

6.6 Correlation of IWP Results and Adhesive Fracture Energies

6.6.1 Introduction

As discussed above, IWP tests were conducted at 2 m/s at room temperature (20°C), as specified by the Standard. Additional tests were performed at -40 and 60°C (both at a test rate of 2 m/s). These are considered to be the upper and lower 'in service' temperatures for these adhesives in automotive applications[26]. Tests were also conducted at a test rate of 10^{-4} m/s, at 20°C.

This Section discusses the effect of changing these variables, and compares the results obtained with the adhesive fracture energies measured using the TDCB tests described in Chapter 4. Note that the locus of failure of the IWP specimens was always cohesive-in-adhesive, as with the TDCB tests.

The test data are analysed by calculating the average force between 25 and 90 % of the time-to-failure if stable failure occurred. If unstable failure occurred, a zero force value is quoted.

6.6.2 High Rate Tests

The IWP cleavage-forces measured at 2 m/s were plotted against the adhesive fracture energies measured using the fracture mechanics (TDCB) tests described in Chapter 4, as shown in Figure 6.21; and also see Table 6.5. The G_c values shown are taken from the TDCB tests at crack velocities approximately equal to the stable crack velocities seen in the IWP tests. As mentioned above, an IWP test gives a crack velocity of 2 m/s using a test rate of 2 m/s. However, a crack velocity of 2 m/s is obtained from a TDCB test at applied constant displacement rates of between 0.05 to 0.1 m/s, depending on the toughness of the adhesive, as discussed in Chapter 4. The results show a correlation between the measured cleavage-force and the adhesive fracture energy, G_c, which is approximately linear. These data are summarised in Table 6.5.

However, the correlation between the IWP cleavage force and the adhesive fracture energy does not pass through the origin. Instead there is a limiting value of the fracture energy, i.e. one where unstable failure occurs, see Figure 6.21, for each combination of test conditions. For the specimens made with steel adherends this value is approximately equal to the fracture energy of the 'AV119' adhesive, as some of these specimens failed in an unstable manner. This gives a limiting adhesive fracture energy value of around 660 J/m^2, for tests using steel adherends at a test rate of 2 m/s, and at 20°C. This is the point where the transition from stable to unstable crack growth occurs as the adhesive fracture energy is reduced. Below this value, the toughness of the adhesive is insufficient to allow the adherends to deform plastically.

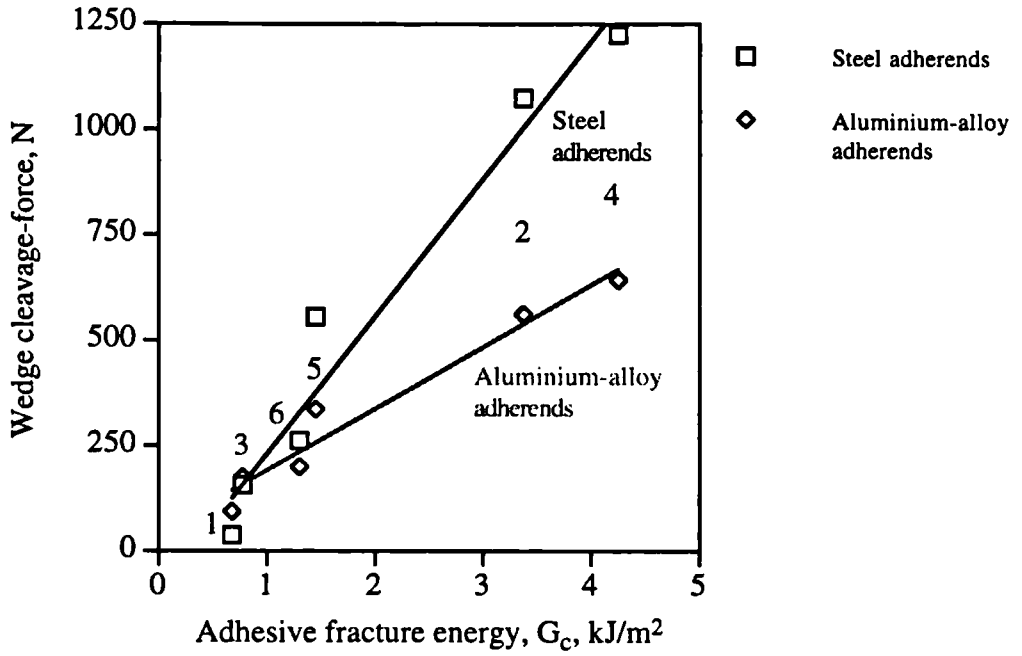


Figure 6.21: Impact wedge cleavage-force, at 2 m/s and 20°C, versus adhesive fracture energy from TDCB tests. Data are plotted for similar crack velocities, i.e. 2 m/s. See Table 6.5 for identification of adhesives.

6.6.3 Effect of Adherend Material

The gradient of the IWP cleavage-force versus fracture energy relationship is steeper for steel adherends than for aluminium-alloy adherends, see Figure 6.21. The difference may be explained as the higher modulus of the steel means that more energy, and hence a larger force is required to separate the adherends sufficiently for the wedge to pass between them. The limiting adhesive fracture energy, i.e. the fracture energy for zero cleavage force, is greater for steel adherends than for the aluminium alloy. This is probably due to the higher yield stress of the steel adherends. The yield stresses of the steel and aluminium-alloy adherends are 180 N/m^2 and 140 N/m^2 respectively. The material properties of the adherends are listed in Appendix 1.

Thus in general, higher forces were recorded from the tests with steel adherends than with aluminium-alloy. The exceptions are the adhesives with the lowest fracture energies, below 1 kJ/m^2, see Table 6.5. All specimens exhibited stable crack growth, except for some of the steel specimens bonded with the 'AV119' adhesive, which exhibited unstable failure.

Table 6.5: Room temperature impact wedge-peel results for test rates (and crack velocities) of 2 and 10^{-4} m/s, using aluminium-alloy and steel adherends. The G_c values are measured using the TDCB tests described in Chapter 4 at the given crack velocities. Note that in the IWP test the crack velocity is equal to the test rate. The test rates of the TDCB tests are approximately 0.1 and 10^{-5} m/s respectively.

Adhesive & number		2 m/s, 20°C Cleavage-force, N		10^{-4} m/s, 20°C Cleavage-force, N		Adhesive G_c, from TDCB tests, kJ/m^2	
		Steel	Alumin.	Steel	Alumin.	2 m/s	10^{-4} m/s
'AV119'	Mean	**32**	**91**	**257**	**259**	**0.66**	**0.70**
(1)	S.D.	(64)	(12)	(128)	(54)		
'ESP110'	Mean	**155**	**174**	**613**	**512**	**0.9**	**1.06**
(3)	S.D.	(20)	(16)	(266)	(88)		
'XW1044'	Mean	**261**	**197**	**529**	**270**	**1.1**	**1.05**
(6)	S.D.	(18)	(32)	(138)	(53)		
'XB5315'	Mean	**553**	**334**	**604**	**346**	**1.45**	**1.55**
(5)	S.D.	(26)	(47)	(44)	(70)		
'EA9309'	Mean	**1069**	**503**	**1000**	**1164**	**3.36**	**3.76**
(2)	S.D.	(115)	(12)	(150)	(175)		
'LMD1142'	Mean	**1223**	**640**	**1585**	**1161**	**4.25**	**4.59**
(4)	S.D.	(29)	(48)	(85)	(75)		

6.6.4 Effect of Test Temperature

Impact wedge-peel tests were performed at -40, 20 and 60°C, at a test rate of 2 m/s. At the higher temperatures, the measured cleavage-forces were generally higher, see Table 6.6. All the tests at -40°C using steel adherends exhibited unstable crack propagation, thus zero force values are quoted.

The reasons for these differences are more readily identified if the IWP data are plotted against the adhesive fracture energy, see Figure 6.22. This Figure shows the -40 and 20°C data, adhesive fracture energy data were not available at 60°C. The adhesive fracture energies were measured using TDCB tests at the relevant temperature, and at a crack

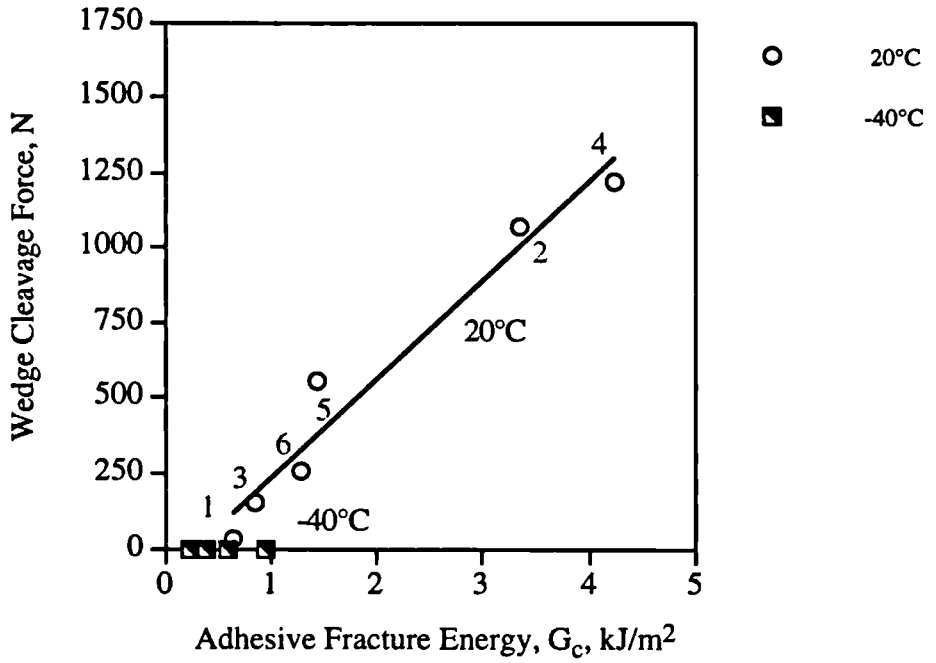
velocity of 2 m/s, which is equal to the stable crack velocity during an IWP test. Figure 6.22b shows that the relationship between the cleavage-force and the adhesive fracture energy for the tests using aluminium-alloy adherends appears to be unaffected as the temperature is decreased. This is probably because the modulus and yield stress of aluminium-alloy is not affected by the change in temperature[119, 139-141].

However, the limiting adhesive fracture energy using the steel IWP adherends is increased at the lower temperature. This effect is probably due to the increased yield stress, σ_y, of the steel adherends at lower temperatures. The available data suggest that σ_y increases by about 10 % as the temperature is reduced from 20°C to -40°C. (The modulus of the steel adherends will be unaffected by the temperature changes[140, 142, 143].) The increased yield stress of the adherends results in a larger force being required to plastically deform the adherends, and thus a tougher adhesive is required to withstand the higher forces.

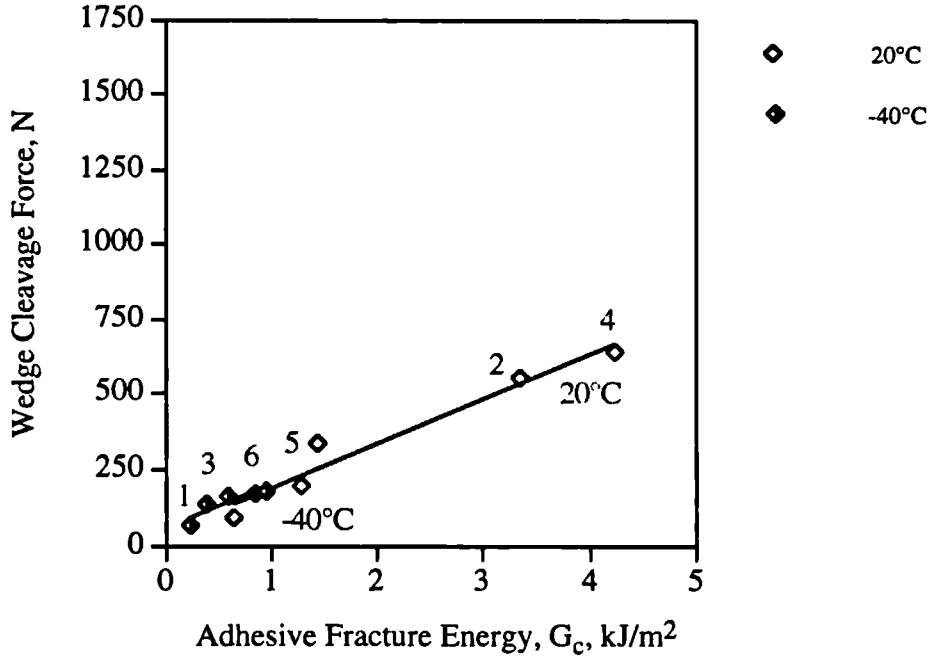
Table 6.6: Variation of IWP cleavage-force with temperature. All tests conducted at a test rate of 2 m/s.

Adhesive & number		2m/s, -40°C Cleavage-force, N		2m/s, 20°C Cleavage-force, N		2m/s, 60°C Cleavage-force, N	
		Steel	Alumin.	Steel	Alumin.	Steel	Alumin.
'AV119'	Mean	**0**	**66**	**32**	**91**	**319**	**315**
(1)	S.D.	(0)	(78)	(64)	(12)	(72)	(50)
'ESP110'	Mean	**0**	**136**	**155**	**174**	-	-
(3)	S.D.	(0)	(24)	(20)	(16)	()	()
'XW1044'	Mean	**0**	**183**	**261**	**197**	-	-
(6)	S.D.	(0)	(50)	(18)	(32)	()	()
'XB5315'	Mean	**0**	**165**	**553**	**334**	**1008**	**694**
(5)	S.D.	(0)	(42)	(26)	(47)	(90)	(19)

Note: - denotes combination not tested.



(a) Steel adherends.



(b) Aluminium-alloy adherends.

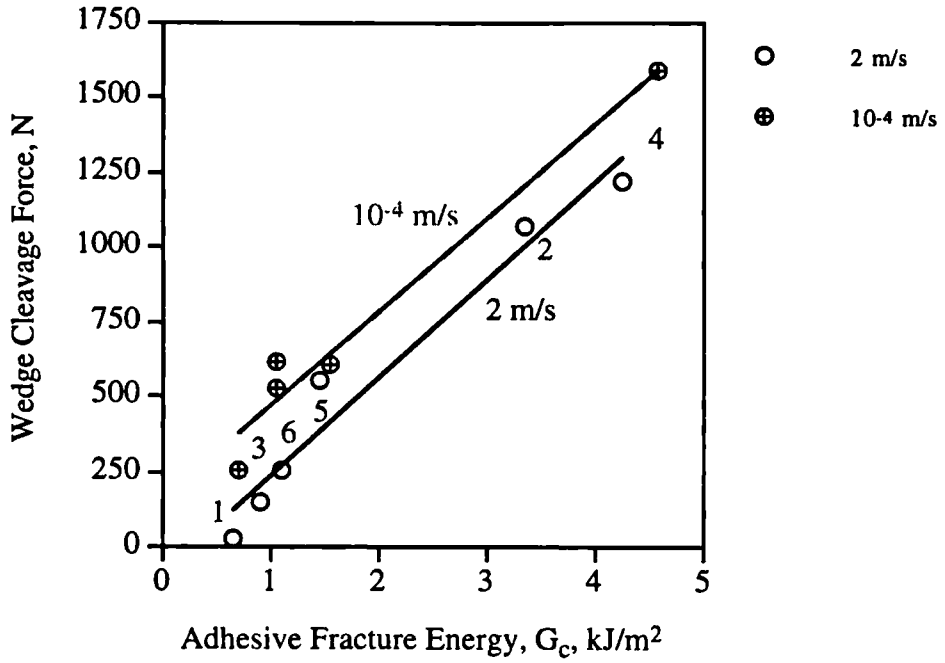
Figure 6.22: IWP cleavage-force versus adhesive fracture energy, G_c, measured from TDCB tests at -40 and 20°C, (a) steel adherends and (b) aluminium-alloy adherends. Crack velocities were 2 m/s; test rate for IWP was 2 m/s, and was about 0.1 m/s for the TDCB tests. See Table 6.6 for identification of adhesives.

6.6.5 Effect of Test Rate

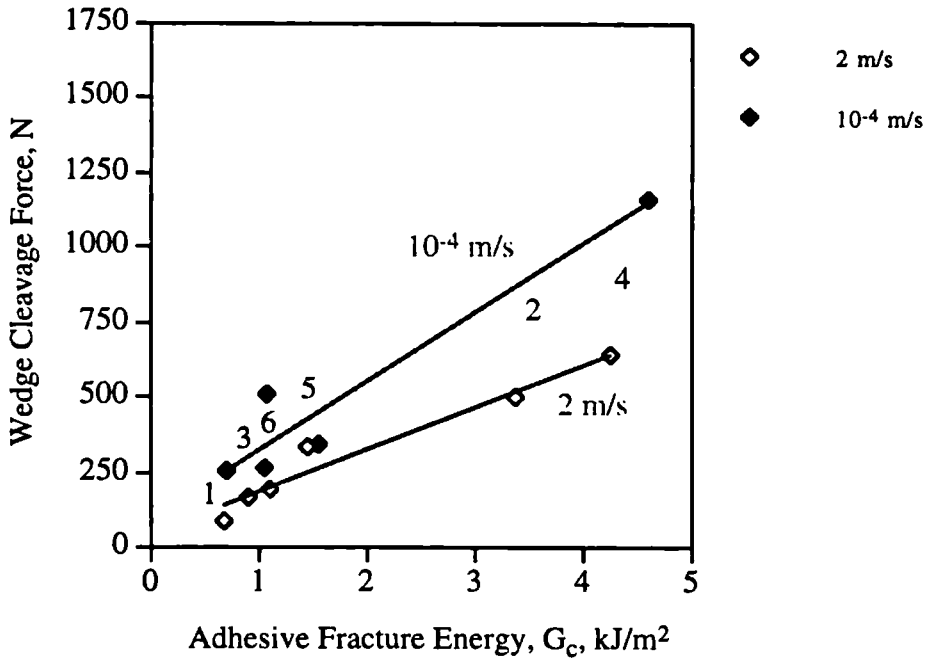
At the lower test rate of 10^{-4} m/s, the measured wedge cleavage-forces are higher than those at 2 m/s for both the steel and the aluminium-alloy adherends, as was shown in Table 6.5. However, it should be noted that as both the adhesive fracture energy and the IWP cleavage-force change with rate, the correlation between cleavage-force and G_c also changes. The relationship between these variables is still approximately linear, as shown in Figure 6.23. As before, these data have been plotted for equivalent crack velocities of 2 and 10^{-4} m/s for the high and low test rates respectively.

The gradient of the relationship between cleavage-force and G_c remains approximately the same at the lower rate, probably because the modulus of both the steel and aluminium-alloy adherends will be unaffected by the test rate, over this range[140]. The limiting adhesive fracture energy is also reduced, thus it is possible to obtain stable crack propagation in the IWP test with a less tough adhesive at the lower test rate. Increasing the test rate will increase the yield stress of the steel adherends, thus a smaller force will be measured. However it would be expected that the yield stress of the aluminium-alloy would not be affected by test rate[140], although the measured force was also reduced at the higher rate.

To confirm these trends, tensile test data would be required for these specific adherends. It would also be useful to perform some IWP tests with aluminium-alloy or steel adherends which possessed different yield stresses to those used in the present work. These aspects are discussed in Chapter 12, where suggestions for further work are considered.



(a) Steel adherends.



(b) Aluminium-alloy adherends.

Figure 6.23: IWP cleavage-force versus adhesive fracture energy from TDCB tests, at crack velocities of 10^{-4} and 2 m/s at 20°C, (a) steel adherends, (b) aluminium-alloy adherends. See Table 6.6 for identification of adhesives. Test rate equal to crack velocity for IWP tests, test rates 10^{-5} and 0.1 m/s respectively for TDCB data.

6.7 Finite Element Modelling

6.7.1 Modelling the IWP Test

A finite element (FE) model of the impact wedge-peel test, as shown in Figure 6.1, was set up using the 'ABAQUS' commercial FE package[144]. This modelled the unbonded region of the specimen and the 30 mm bonded length. A two-dimensional model was used, composed of eight noded quadratic elements. Due to symmetry it was only necessary to model half the specimen. The mesh used is comprised of 1400 elements, and is shown in Figure 6.24. Contact elements were used along the fractured surface of the adhesive, and contact between the wedge and the surface was assumed to be rigid/elastic.

The steel and aluminium-alloy adherends were modelled as elastic/plastic materials. Tensile tests were performed using the adherend materials at 10^{-5} m/s, to provide modulus and yield data. These data are listed in Appendix 1. The measured modulii, 207 and 69 GPa respectively, agree well with values quoted in the literature[141, 142, 145]. The adhesive was modelled as purely elastic, using published data[146] which are also given in Appendix 1. No high rate data were available, so all modelling will assume an IWP test rate of 10^{-4} m/s. This velocity was applied to the wedge, which is assumed to be rigid.

The nodes along the centre of the adhesive layer were released in turn, as shown in Figure 6.24, as the applied strain-energy release rate, G, at the crack tip (see below) reached the G_c value for the adhesive, which was measured experimentally using the TDCB tests described in Chapter 4. A time step was applied to the model, allowing the wedge to advance a fixed distance, and the value of G at the crack tip was calculated. Each step of the model took approximately two hours to run. If the model could not reach a solution, or the value of G was higher than the value of G_c measured using the TDCB tests, the time step was reduced, and the model run again using the same crack length. Similarly if $G < G_c$, the time step was increased until the calculated fracture energy agreed with G_c to within 5%. Once the fracture energies agreed within the tolerance, a further set of nodes was released, and the process repeated. Approximately fifty increments of crack length were used between initial contact and final failure.

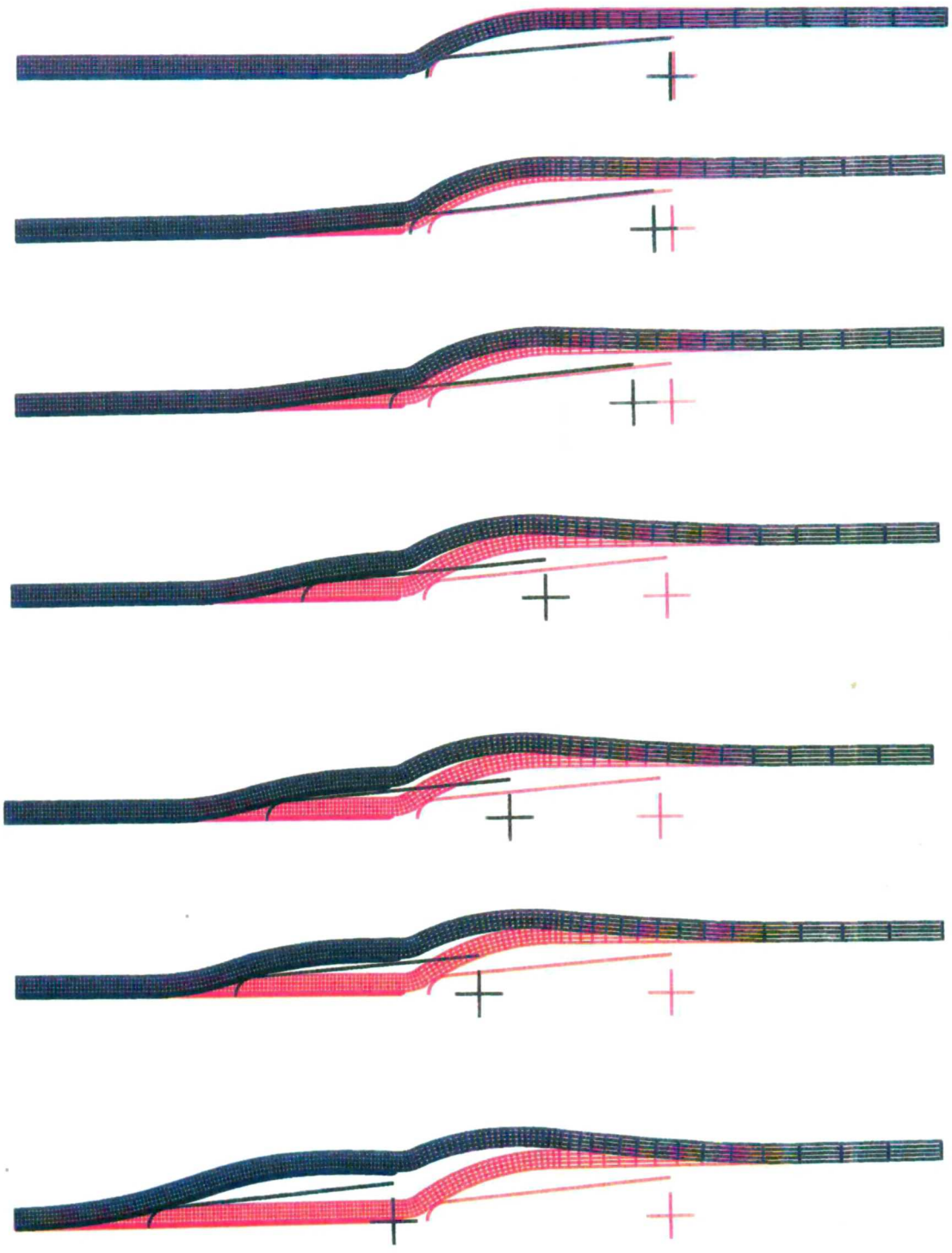


Figure 6.24: Series of finite element models, from initial contact to final failure, of an aluminium-alloy impact wedge-peel specimen bonded with the 'XB5315' adhesive being tested at 10^{-4} m/s. The initial, undeformed, mesh is shown in red, and the displaced mesh is shown in black. The elapsed times are 1, 6, 15, 35, 45, 60 and 85 s respectively, from top to bottom. The '+' symbol indicates a reference point on the wedge.

6.7.2 Universal Crack Closure Method

The universal crack closure method was used to calculate values of the adhesive fracture energy as a crack propagated through the specimen. This method, developed by Rybicki & Kanninen[147] uses the nodal forces at the crack tip and the nodal displacements at the next node (towards the crack mouth), see Figure 6.25. The strain-energy release rate is calculated from the relation

$$G = \frac{1}{2\beta}\left(P_x u_x + P_y u_y\right) \qquad (6.1)$$

where β is the element width, i.e. the distance between nodes, and P_x, P_y, u_x and u_y are the nodal forces and displacements in the x and y directions respectively.

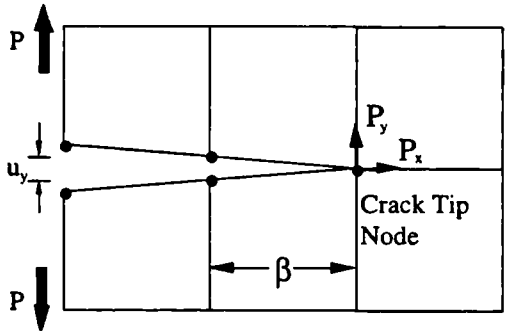


Figure 6.25: General finite element mesh around crack tip, showing parameters for use with universal crack closure method to calculate fracture energy, see Equation 6.1.

6.7.3 Effect of Friction

The contact between the wedge and the fractured surface of the adhesive was initially assumed to be frictionless. However the model predicted lower force values in the 'plateau' region than those measured experimentally, see Table 6.7. Thus friction between the wedge and the fractured surface of the adhesive was included in the model, confirming the observation made from the thermography work that friction indeed has some effect. The literature gives values of 0.4 to 0.5 for the coefficient of friction, μ, for the unlubricated contact between steel and a hard, rigid polymer, namely poly(methylmethacrylate)[148], the properties of which are similar to those of an epoxy adhesive. Both 0.4 and 0.5 give good agreement between the FE prediction and the experimental results, with the value of 0.5 giving the closest fit to this experimental data; using the 'XB5315' adhesive and steel adherends, as shown in Table 6.7.

Table 6.7: The effect of friction on the cleavage-force predicted by finite element modelling. Adhesive fracture energy, G_c, from TDCB tests for a crack velocity equal to that measured in IWP tests. Steel adherends bonded with 'XB5315' adhesive, 10^{-4} m/s test rate.

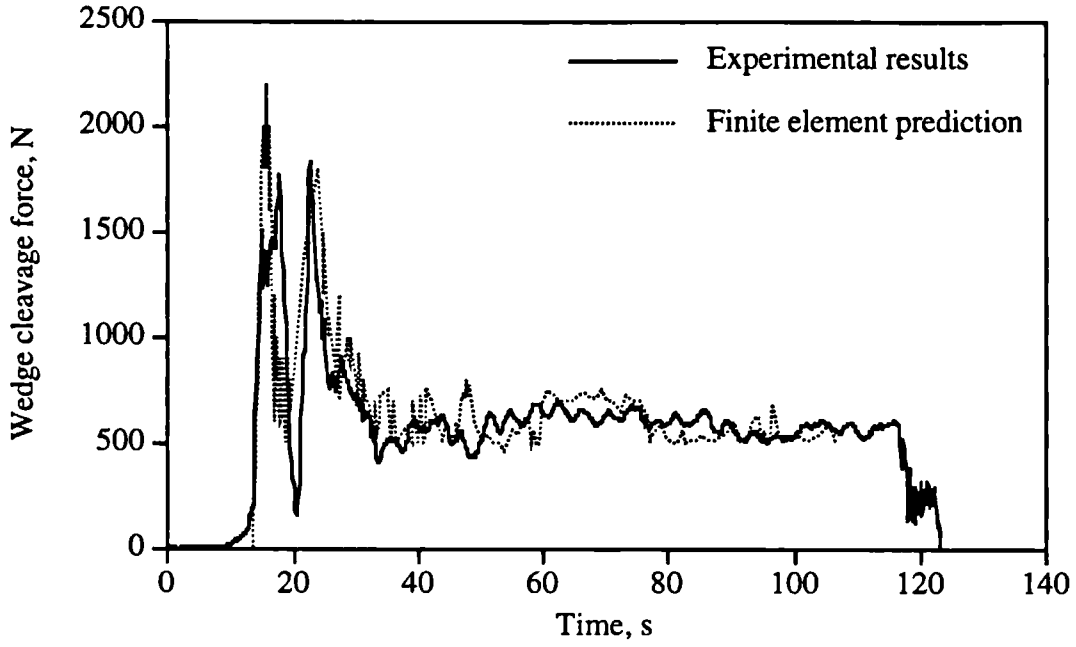
Coefficient of friction, μ	Adhesive fracture energy, G_c, kJ/m^2	Predicted IWP cleavage-force, N
Experimental	**1.5**	**600**
0	1.5	500
0	1.3	300
0.4	1.5	550
0.5	**1.5**	**600**

The use of a coefficient of friction lower than 0.5, for the same adhesive fracture energy, will give a lower predicted cleavage-force, see Table 6.7. However, the effect of friction is relatively small, as a zero coefficient of friction still gives a predicted cleavage-force of 500 N, while $\mu = 0.5$ gives a force of 600 N. By comparison, the use of an adhesive fracture energy of 1.3 kJ/m^2, rather than 1.5 kJ/m^2, gives a force of 300 N rather than 500 N. Thus neglecting friction only has a small effect compared with changing the value of the adhesive fracture energy. The predictions discussed below assume that the coefficient of friction between the wedge and the adhesive fracture surface equals 0.5.

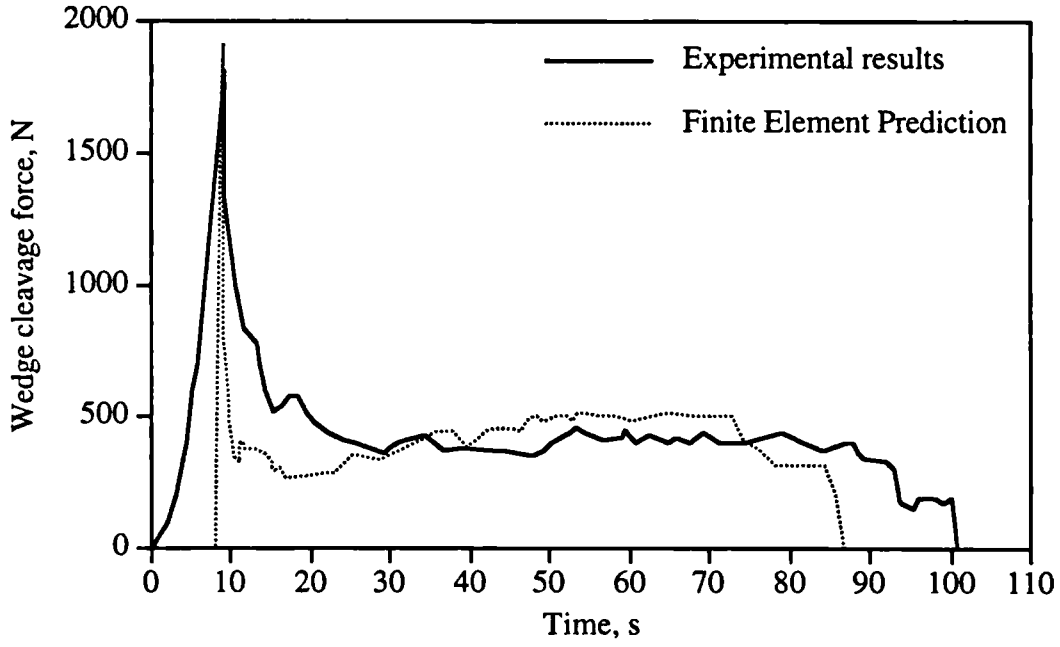
6.7.4 Comparison of Predictions and Experimental Results

To predict the IWP cleavage force requires the material properties of the adherends and the adhesive, i.e. the stress versus strain data plus the Poisson's ratio (see Appendix 1), and the fracture energy of the adhesive, determined as described in Chapter 4. A coefficient of friction of 0.5 is assumed.

Examples of the predicted force versus time response are shown in Figure 6.26, for the steel and aluminium-alloy adherends, using the 'XB5315' adhesive. The assumption of purely elastic contact between the rigid wedge and the specimen means that the predicted 'peak' response increases more steeply than is seen experimentally, especially using the aluminium-alloy adherends. The use of the universal crack closure method also requires that a small crack is present in the adhesive initially, whereas in reality there is none.



(a) Steel adherends.



(b) Aluminium-alloy adherends.

Figure 6.26: Finite element predictions and experimental force versus time data for IWP specimens bonded with 'XB5315', (a) steel adherends, (b) aluminium-alloy adherends. Test rate 10^{-4} m/s.

However, the agreement between the finite element predictions and the experimental results is extremely good.

6.7.5 Effect of Adherends

The predicted IWP cleavage-forces (in the plateau region) for a range of adhesives used with both aluminium-alloy and steel adherends are given in Table 6.8. Agreement between the predicted values and the forces measured experimentally is good for tests with both the steel and aluminium-alloy adherends. The FE modelling also predicts a smaller IWP cleavage-force for the aluminium-alloy adherends than for the steel, for a given adhesive fracture energy, as was observed experimentally, see Figure 6.26.

6.7.6 Conclusions from the Modelling Work

The present work has described the novel use of a finite element method to predict the wedge-cleavage force measured using the IWP test. The modelling work has shown that a smaller cleavage force would be expected when aluminium-alloy adherends are used compared with steel adherends, as is seen experimentally. The modelling work has also shown that the effect of friction is relatively small, although the accuracy of the predictions is improved if it is included. However, the effect of changing the coefficient of friction is much less than that of the adhesive fracture energy.

Most significantly, the modelling work has shown that it is possible to predict the impact wedge-peel cleavage-force from only the adhesive fracture energy and the material properties of the adherend and the adhesive. Further, there is excellent agreement between the FE predictions and the experimental results.

Table 6.8: Finite element predictions of wedge cleavage-force from adhesive fracture energy, and experimental data. IWP test rate 10^{-4} m/s. Adhesive fracture energy from TDCB tests at 10^{-5} m/s. All tests conducted at 20°C.

Adhesive	Adhesive G_c, kJ/m^2	IWP cleavage-force, N			
		Aluminium-alloy adherends		Steel adherends	
		FE prediction	Experimental	FE prediction	Experimental
'AV119'	0.7	220	260	-	-
'XB5315'	1.55	450	350	600	600
'LMD1142'	4.59	-	-	1290	1580

6.8 Conclusions

The method of analysing the impact wedge-peel test results proposed by the ISO Standard has been found to give misleading results in some cases, for example when the specimen fails entirely by unstable crack propagation. The ISO Standard requires that the energy absorbed and the average force are calculated over an interval of 25 to 90 % of the time to failure. Several alternative methods of analysis were proposed, and a preferred method has been identified. This work concludes that only the average force calculated by the Standard method should be quoted, and only if the Standard interval lies within an interval of stable crack propagation, i.e. the 'plateau' region of the response. If the failure is unstable, a zero value should be quoted. The values calculated using this method are independent of the specimen profile used, which is important because the Standard does not specify a preferred profile. The use of this new method has shown that the impact wedge-peel test can provide good discrimination between different adhesives.

The present work has shown that the measured cleavage-force depends on both the adhesive and the adherends used. (Note that all failure was cohesive-in-adhesive throughout). Thus the IWP test evaluates the energy-absorbing capabilities of the system, not the adhesive alone. However, a linear correlation between the IWP cleavage-force and the adhesive fracture energy, G_c, measured using the TDCB tests, has been identified. The gradient of this correlation is dependent on the adherend material used; the use of steel adherends results in a steeper gradient than using aluminium-alloy adherends due to the higher modulus of the steel.

The concept of a limiting value of the adhesive fracture energy in order to obtain stable crack propagation has been identified. This value is dependent on the test conditions. The limiting value increases with increasing test rate and decreasing temperature. It is also dependent on the adherend properties, the limiting value increasing with the yield stress of the adherend. This limiting value of the adhesive fracture energy has the potential to be used as a design criterion.

Almost all the room temperature and 60°C tests gave stable failure. Failure at -40°C was mostly stable for the aluminium-alloy joints, but unstable for steel. In general at higher temperatures, and also at the lower test rate, the recorded cleavage-forces were higher for the steel adherends, compared to aluminium-alloy adherends. This is consistent with the expected decrease in yield stress. The relationship between IWP cleavage-force and the adhesive fracture energy using aluminium-alloy adherends is unaffected by the change from 20°C to -40°C, at 2 m/s. The yield stress of aluminium-alloy is also unaffected over this temperature range.

Thermal imaging has shown temperature rises of up to 35°C on the adhesive surface. This heating is mostly the result of friction, as the specimen passes over the wedge, rather than the result of the fracture and deformation of the specimen. Evidence for this was provided by T-peel tests, where temperature increases will only be due to deformation and fracture, which showed a temperature rise of only 3°C.

A finite element model was used to predict the IWP cleavage-force from values of the adhesive fracture energy, G_c, measured using the TDCB tests. The effect of friction between the wedge and the fractured surface of the specimen was found to be small, although its inclusion improved the predictions somewhat. The IWP cleavage forces were predicted for several adhesives, using both steel and aluminium-alloy adherends. The agreement between the finite element predictions and the experimental results was found to be very good.

Chapter Seven

Impact Performance: Summary

7.1 Introduction

The impact testing presented in the current work investigated the effect of increasing the loading rate on the performance of a range of structural epoxy adhesives. Three test methods were used, the tapered double-cantilever beam (TDCB) test, the three-point bend (TPB) test and the impact wedge-peel (IWP) test. The first two of these are fracture mechanics methods, allowing the values of the adhesive fracture energies, G_c, obtained to be compared. The three-point bend test was additionally used to compare the performance of bulk adhesive and joint specimens. The values obtained from the fracture mechanics tests were compared to the IWP cleavage-force values, measured using the IWP test specimens, to investigate whether any correlations could be drawn between the methods. All failures in the present work were cohesive-in-adhesive, i.e. approximately through the centre of the adhesive layer.

7.2 Fracture Mechanics Tests

7.2.1 Tapered Double-Cantilever Beam (TDCB) Tests

The adhesive fracture energies, G_c, of a range of structural epoxy adhesives were measured at test rates between 10^{-5} and 1 m/s. A range of analysis methods were used to calculate the adhesive fracture energy, and good agreement was found between all the analysis methods used. Thus at test rates of 1 m/s and below, any of the methods of analysis described in Chapter 4 may be used to calculate G_c for the TDCB test. However, the simplest analysis method to use is the force method, as only the force versus time data are required to calculate G_c. The other methods require high-speed photography to obtain displacement, crack length or crack velocity data.

All the adhesives tested showed a reduction in G_c with increasing test rate. A reduction of up to 36 % was measured as the test rate was increased from 10^{-5} to 1 m/s, i.e. as the crack velocity was increased from approximately 10^{-4} to 20 m/s. Scanning electron microscopy (SEM) of the fracture surfaces showed a reduction in the amount of rubber particle cavitation with increasing test rate. Thus the energy absorbing mechanisms are less effective at higher test rates, which leads to less energy being absorbed during fracture and hence a reduction in the measured adhesive fracture energy.

7.2.2 Three-Point Bend (TPB) Tests

The present work has described a new method for the manufacture of adhesive joint specimens for three-point bend testing that may be used with viscous adhesives. The use of a metal mould and the method described in Chapter 5 ensures that the specimens are parallel, and that the amount of air trapped in the adhesive is kept to a minimum.

Three-point bend (TPB) tests were performed using bulk adhesive and joint specimens, using the 'AV119' adhesive. At the high test rates used (0.3 to 2 m/s), large oscillations in the force versus time response of the specimens were recorded, due to dynamic effects. These were found to be more significant when using the pendulum testing machine than when using the servo-hydraulic machine, probably because with the former the striker is falling freely rather than being driven. These oscillations were reduced by damping the contact between the striker and the specimen using grease.

The results of the three-point bend testing showed that the adhesive fracture energy, G_c, decreases with increasing test rate. An approximately linear correlation between fracture energy and average time to failure was also identified, the fracture energy decreasing with decreasing time to failure. Further, the agreement between the values of the fracture energies obtained using the bulk and joint specimens, and using the two testing machines, was excellent for a given time to failure.

Little rubber particle cavitation was observed on the fracture surfaces of the 'AV119' adhesive using SEM, and thus the energy absorbing mechanisms that are initiated by rubber particle cavitation are limited, which explains the relatively low fracture energy of the 'AV119' adhesive.

7.2.3 Comparison of Test Methods

The adhesive fracture energies obtained using the TDCB tests were compared to those obtained using the TPB tests. The agreement between the data when the G_c values obtained from these two test methods were plotted against the test rate was found to be very good. Thus the fracture energy of the adhesive is indeed a material property, independent of the test geometry, but which is dependent on the test rate.

The TDCB test is the easier and more reliable method of measuring the adhesive fracture energy. However, the TPB test does not require such complicated equipment as the TDCB test, as an impact pendulum machine may be used. The TPB test also requires smaller specimens. However, the TPB test uses a multi-specimen approach to determine the adhesive fracture energy, and hence is more time-consuming. Further, the dynamic

effects are more pronounced, and become significant at a lower test rate than is observed when using the TDCB test.

7.3 Impact Wedge-Peel (IWP) Tests

The current work has presented the first detailed data using this new ISO Standard test method, a test which is becoming popular in industry. This work has shown that the ISO Standard method for the analysis of the data from IWP tests can give misleading results in some cases. An improved method for analysing the experimental data has been identified. This improved method calculates the average cleavage-force over an interval of 25 to 90% of the test, if only stable crack growth occurs during this period. If unstable failure occurs, it is strongly suggested that a zero value should be quoted. Further, this improved method of analysis gives results that are independent of the specimen profile used, whilst the ISO Standard method may give large differences in the results due to specimen variations. Thus the precision of the results is also improved.

7.4 Correlations Between IWP Cleavage-Force and Adhesive Fracture Energy

A linear correlation between the IWP cleavage-force and the adhesive fracture energy, G_c, measured using the TDCB tests was identified, for equal crack velocities of 2 m/s. Further, this novel work has shown that this relationship is unique for each set of test conditions, e.g. test temperature, test rate and adherend material. The gradient of this correlation is dependent on the adherend material used; the use of steel adherends results in a steeper gradient than using aluminium-alloy adherends due to the higher modulus of the steel.

The novel concept of a limiting value of the adhesive fracture energy, G_c, in order to obtain stable crack propagation in the IWP test has been identified in the present work. This value is dependent on the test conditions. The limiting value (i) increases with increasing test rate and decreasing temperature, and (ii) is dependent on the adherend properties; the limiting fracture energy value increasing with the yield stress of the adherend. This property has the potential to be used as a design criterion.

7.5 Modelling the Behaviour of the Impact Wedge-Peel Test

A finite element model was developed and used to predict the IWP cleavage-force from the measured value of the adhesive fracture energy, G_c, at equal crack velocities of 10^{-4} m/s. The agreement between the values predicted by this novel work and the experimental results for the IWP test was very good; for both the steel and the aluminium-alloy adherends using several adhesives.

The impact wedge peel (IWP) test gives an indication of the performance of the adhesive/adherend combination, data which cannot be obtained from the fracture mechanics test methods. Thus it is particularly useful that the impact wedge-peel performance may be quantitatively modelled from a knowledge of the adhesive fracture energy, assuming that failure is cohesive-in-adhesive, as was seen experimentally.

7.6 Concluding Remarks

The impact testing presented in the current work has shown that the performance of a range of structural epoxy adhesives decreases with increasing test velocity. This reduction is due to a decrease in the extent of the toughening mechanisms around the crack tip in the adhesive. Further, the fracture mechanics data can be used to quantitatively predict the joint performance as assessed using an impact wedge-peel (IWP) test.

The following Chapters investigate the effect of cyclic fatigue and a 'wet' environment on two adhesives, which have been identified as possessing 'good' and 'poor' impact performance. A fracture mechanics approach is used to obtain quantitative data, which are then used to predict the performance of typical bonded joint geometries.

Chapter Eight

Durability of Adhesive Joints: A Fracture Mechanics Approach

8.1 Introduction

The following two Chapters discuss the work that was performed to evaluate the durability performance of two structural epoxy adhesives, and the use of the data obtained to predict the lifetime of bonded joints and components. These predictions will be discussed in Chapter 9, and comparisons with experimental results will be made. This Chapter describes the fracture mechanics approach used to investigate the effect of cyclic fatigue and water immersion on the adhesive joint performance.

The tapered double-cantilever beam geometry, as shown in Figure 8.1, was used for these tests. The 'AV119' and the 'LMD1142' adhesives were chosen, as the high rate testing described in Chapters 4 and 6 had identified these as possessing poor and good impact performance respectively. Aluminium-alloy and steel adherends were used. A gritblast and degrease (GB&DG) or chromic-acid etch (CAE) treatment was used for the aluminium-alloy adherends. Steel adherends were prepared using a gritblast and degrease treatment.

Firstly the fracture energy, G_c, of the adhesives at a constant displacement rate was measured for each adhesive/adherend combination to evaluate any differences caused by the surface treatments. However, in cyclic fatigue, crack growth can occur at values of the applied fracture energy that are less than G_c. Here the maximum applied fracture energy, or strain energy release rate, in a fatigue cycle is the controlling factor. Thus secondly, cyclic fatigue tests were performed using the tapered double-cantilever beam (TDCB) geometry. The rate of crack growth per cycle, da/dN, was measured as a function of the maximum applied fracture energy, G_{max}. As discussed in Chapter 2, this method has been successfully used to describe fatigue crack propagation, and has been previously validated[67, 122, 149, 150]. Joints were tested at a frequency of 5 Hz both 'dry', at 23°C and 55 % relative humidity, and 'wet', i.e. immersed in distilled water at 28°C.

Thirdly, scanning electron microscopy and surface chemical analysis techniques (X-ray Photoelectron Spectroscopy and Auger Electron Spectroscopy) were used to investigate the loci of joint failure, and to study the failure mechanisms.

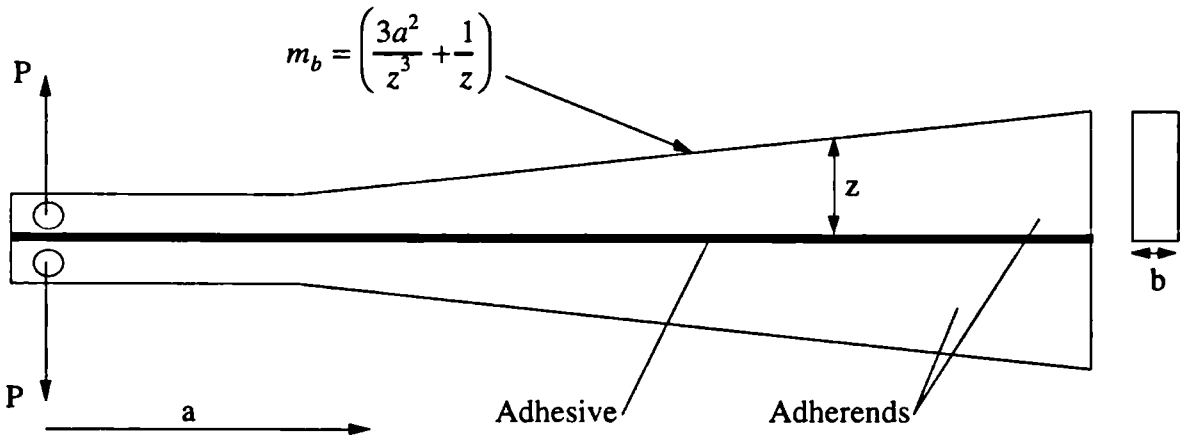


Figure 8.1: The tapered double-cantilever beam (TDCB) specimen.

8.2 Experimental Procedure

The steel and aluminium-alloy TDCB specimens were prepared as described in Section 4.3. A gritblast and degrease (GB&DG) or chromic-acid etch (CAE) treatment was used with the aluminium-alloy adherends. Steel adherends were prepared with a gritblast and degrease treatment. These surface treatments are described in Chapter 3.

Constant displacement rate tests were performed at 1 mm/min (10^{-5} m/s) as described in Section 4.4. The fracture energy, G_c, for each adhesive/adherend combination was calculated using the analysis given in Section 8.4.

Cyclic fatigue tests were performed both 'dry' and 'wet'. 'Dry' tests were conducted in air at 23±1°C and approximately 55 % relative humidity. 'Wet' tests were performed in a tank of distilled water, kept at a constant temperature of 28±1°C using a water circulator/heater. Steel specimens for 'wet' testing were sprayed with paint to reduce corrosion, and hence prevent discoloration of the water which would obscure the crack. The adhesive was left exposed (except for the thin layer of white paint on one side that enables the crack to be seen during testing) so as not to reduce the rate of water uptake. The 'wet' specimens were not aged, the fatigue testing was commenced within a few minutes of the specimen being placed in the water tank.

The beams were tested in fatigue at a frequency of 5 Hz using a servo-hydraulic machine, under displacement control. A sinusoidal waveform, with a constant displacement ratio (u_{min}/u_{max}) of 0.5 was used. The number of cycles, the maximum applied load, and the crack length were recorded at intervals. The crack length was monitored optically using a travelling microscope, and additionally for the 'dry' tests using a potential drop technique,

as described in Section 8.3. Both methods allowed the crack length to be measured to an accuracy of ± 0.01 mm.

To investigate whether the immersion time affected the measured relationship between da/dN and G_{max}, load control tests were also performed on steel beams bonded with the 'AV119' adhesive. These were tested 'wet'. The crack was grown a few millimetres from the starter foil in displacement control, to provide a naturally sharp crack tip. This was necessary because otherwise the crack tip was too blunt for crack growth to occur at the low applied fracture energies used. The testing machine was then switched to load control, and used to apply a value of the fracture energy equal to the threshold fracture energy, G_{th}, observed from the displacement control tests. The rate of crack growth, da/dN, was measured until there was no further change was recorded. The load, and hence G_{max}, was increased in steps until failure of the specimen occurred. The load control tests are discussed in more detail in Section 8.6.5.

8.3 Crack Length Measurement Using Crack Propagation Gauges

8.3.1 Introduction

The crack growth in the 'dry' tests was monitored with a crack propagation gauge system, which used a potential drop technique. This was the 'Fractomat' system from Rumul, Switzerland. A foil gauge is bonded to the side of the specimen, see Figure 8.2, through which a constant current is passed. As the crack grows the gauge breaks, increasing its resistance. The resultant change in potential (voltage) is converted to a crack length and logged at intervals on computer, as shown schematically in Figure 8.3. This potential drop technique has been evaluated and used successfully for fatigue testing on bulk adhesive and joint specimens, as well as other specimen types[65, 151, 152]

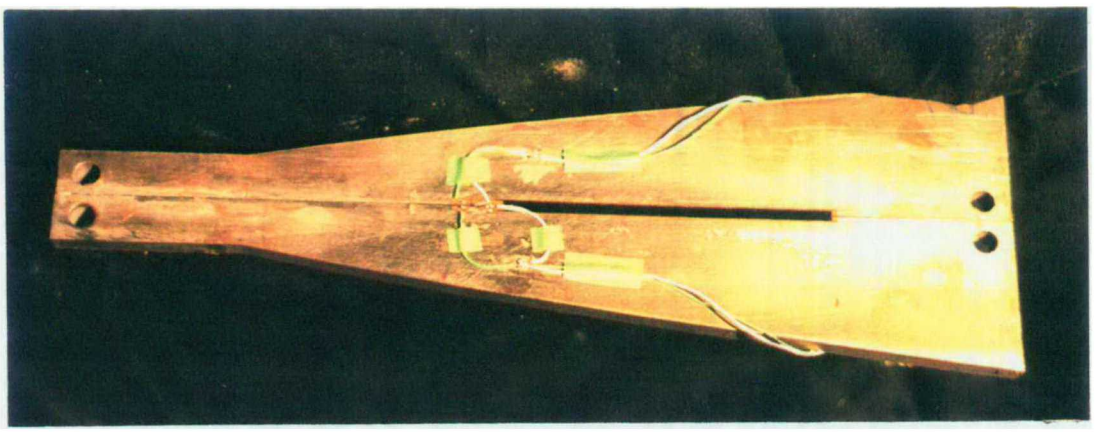


Figure 8.2: The Rumul 'S100' crack gauge bonded to a TDCB specimen.

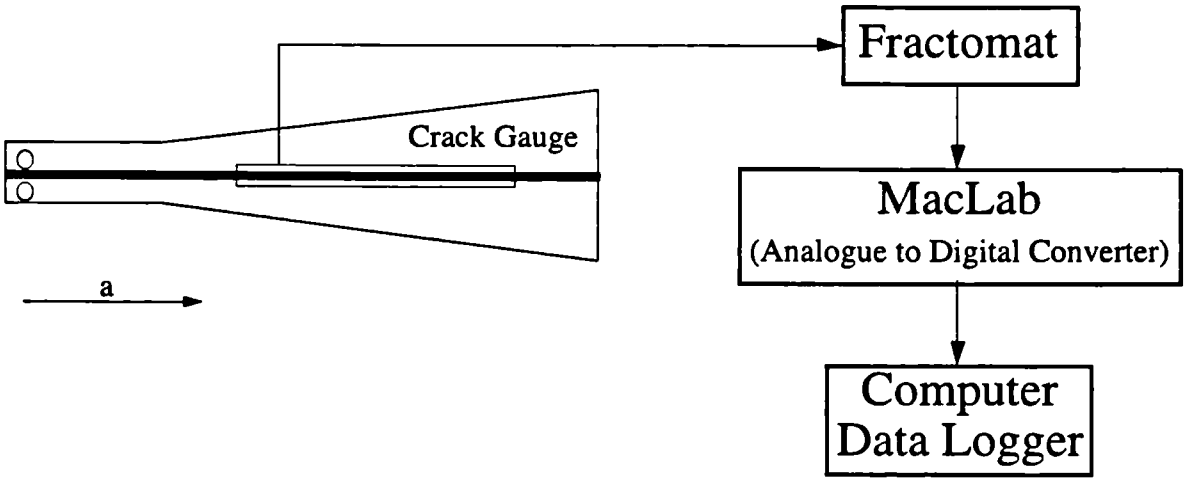


Figure 8.3: Crack gauge system schematic.

8.3.2 Gauge Application

A line was scribed on the TDCB specimen about 100 mm from the loading point, to locate the end of the gauge. The areas of the specimen where the gauge and the soldering terminals would be bonded were degreased, and etched by wiping with a surface conditioner, followed by a neutraliser. The gauge was laid on a clean surface and picked up with pressure-sensitive tape. It was placed in position on the specimen using the alignment marks on the gauge to ensure it was central over the adhesive layer. The tape was secured at one end, and peeled back to expose the underside of the gauge. This process was repeated for the two pairs of soldering terminals. The adhesive used was a two-part epoxy. This was mixed according to the manufacturer's instructions and applied to the gauge and the relevant areas of the specimen. The gauge and terminals were smoothed onto the surface of the specimen. The pressure-sensitive tape holds the gauge in position until the adhesive cures. A strip of PTFE was placed over the specimen, and covered with a sheet of silicone rubber and a metal backing plate. Pressure was applied using two spring clamps. The adhesive was cured for 2 hours at 70°C. After curing the pressure-sensitive tape was removed, and wires soldered to the terminals, as shown in Figure 8.2.

Crack gauges were not used for the 'wet' fatigue testing as their presence has been shown to affect the measured relationship between da/dN and G_{max}. Jethwa[65] showed that the presence of the gauge reduced the rate of water uptake compared with a non-gauged specimen, as the gauge prevented water from gaining access to one side of the adhesive layer.

8.3.3 Experimental Procedure

The gauge was connected to the 'Fractomat', see Figure 8.3. This provides the constant current supply to the gauge, and displays the distance that the crack has propagated into the gauge. The constant current supply was adjusted using the potentiometer on the front panel of the 'Fractomat' until the crack length display read zero. The distance from the loading point to the active part of the gauge was measured using a vernier calliper. Although the 'Fractomat' displays the crack length in millimetres, the output to the 'MacLab' is in volts, and so a conversion must be set on the computer so that the software gives a reading in millimetres. The voltage output from the 'Fractomat' was sampled from the computer software. The measured crack length was set to be equivalent to the measured voltage. However, two values are required to convert from voltage to crack length, so the potentiometer on the front panel of the 'Fractomat' was adjusted until the display read 90 mm, and the output sampled again. This sets the conversion from voltage to crack length, and the 'Fractomat' was zeroed again.

The load values must be converted in a similar manner. The specimen was placed in the testing machine and the slack in the pins taken up. The output voltage from the load-cell was sampled from the computer software, providing one conversion value. The mean displacement was applied to the specimen, and the cyclic loading superimposed. The load was sampled again, and the maximum value used as the second conversion value. Thus the computer gives the load in Newtons and crack length in millimetres as a function of the number of cycles. One second samples were taken at intervals of between 1 minute and 2 hours. Samples were taken more frequently at the beginning of the test when the crack growth rate was higher. The data were analysed to give the maximum load and crack length in each data sample. Values of G_{max} and da/dN were calculated using the equations in Section 8.4.

8.3.4 Comparison of Potential Drop and Optical Methods

The crack lengths measured via the optical and potential drop methods were in excellent agreement, as shown in Figure 8.4. However problems were encountered at longer crack lengths on some of the 'AV119'/steel specimens. Figure 8.5 shows a plot of compliance (u_{max}/P_{max}) versus crack length for one of these specimens. The TDCB specimen is designed such that this relationship is linear, but the increase in crack length indicated by the increase in compliance, and seen optically, is not recorded accurately by the potential drop method. This problem was only encountered on the 'AV119'/steel specimens, the stiffest specimens used, at small maximum displacement values. Thus it is suggested that the problems are due to the gauge not breaking, or the broken halves of the gauge remaining in contact, due to the small displacement. However, in most cases no problems

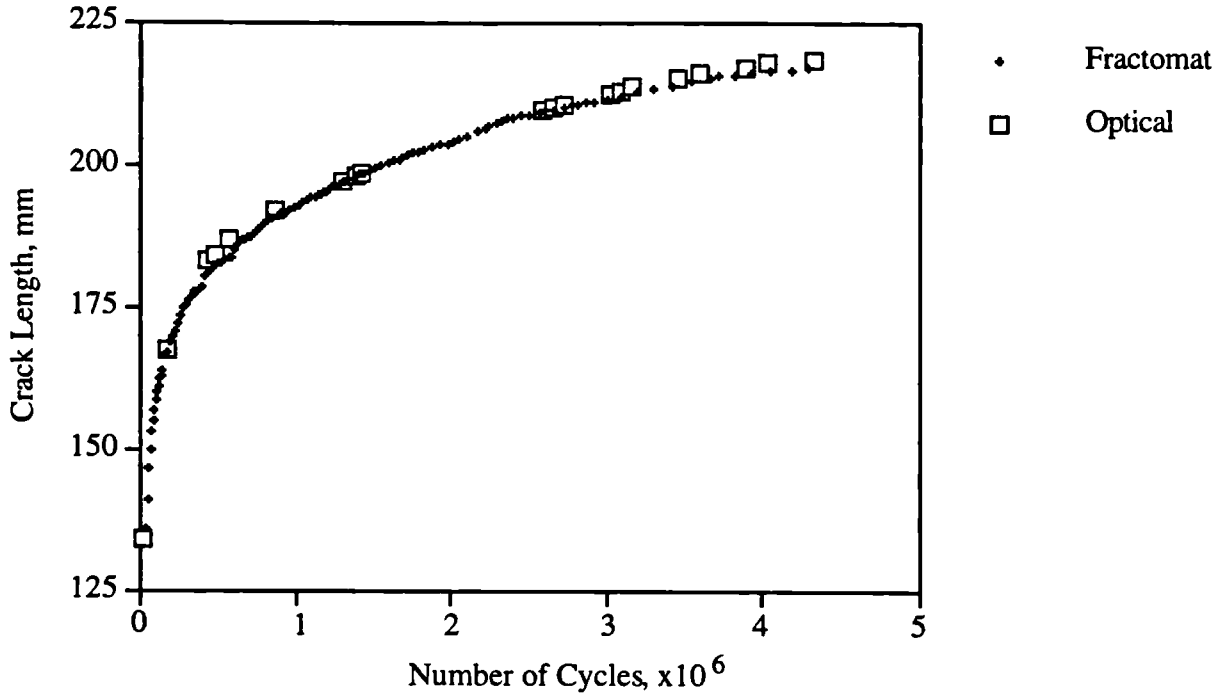


Figure 8.4: Comparison of crack length measurements by optical and potential drop ('Fractomat') methods. Note the excellent agreement between the two methods.

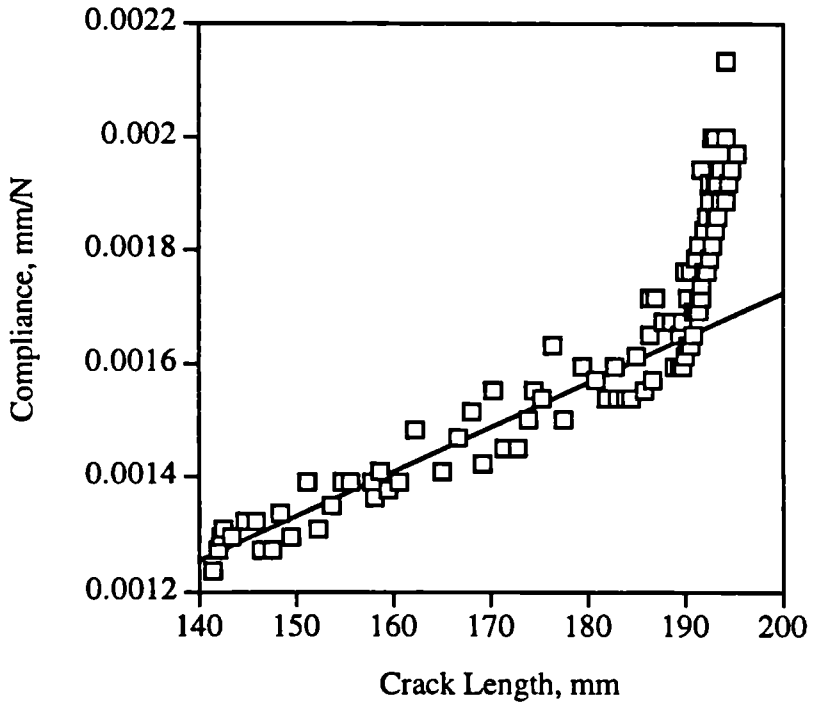


Figure 8.5: Compliance versus crack length from crack gauge showing the deviation from linear response caused by the gauge failing to register increase in specimen crack length.

were observed with the crack gauges. Problems with the gauges can be identified by the deviation from the linear response, as shown in Figure 8.5, or from comparisons with the optical measurements of the crack length taken using the travelling microscope. In these cases, the results from the gauges were ignored.

8.4 Analysis

As was shown in Chapter 2, the adhesive fracture energy, G_c, can be calculated from the crack propagation load, P_c, for a constant displacement rate test using

$$G_c = \frac{4P_c^2 m_b}{E_s b^2} \qquad (2.18)$$

where

$$m_b = \left(\frac{3a^2}{z^3} + \frac{1}{z}\right) = \text{Constant} \qquad (2.17)$$

where z is the height of the adherend, see Figure 8.1, and $m_b = 2\ mm^{-1}$.

Similarly in fatigue loading, the maximum applied fracture energy, G_{max}, can be found from

$$G_{max} = \frac{4P_{max}^2 m_b}{E_s b^2} \qquad (8.1)$$

The calculated value of G_{max} can be plotted against the rate of crack growth per cycle, da/dN, on logarithmic axes. The general form of the relationship is shown in Figure 8.6.

The central linear portion of the curve (II) can be described by a simple Paris law relationship

$$\frac{da}{dN} = D(G_{max})^n \qquad (8.2)$$

where D and n are found by fitting the relationship to the experimental data and may be considered as material parameters.

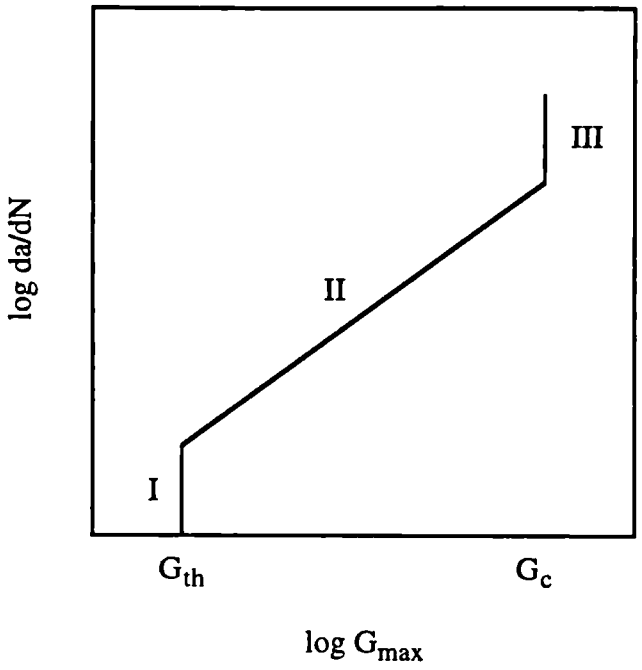


Figure 8.6: Typical plot of crack growth rate per cycle, da/dN, versus maximum applied fracture energy, G_{max}, (logarithmic axes).

It is possible to use ΔG, the applied range of fracture energy, in place of G_{max},[67] where

$$\Delta G = G_{max} - G_{min} \tag{8.3}$$

This leads to a similar relationship with the rate of crack growth per cycle to that seen above,

$$\frac{da}{dN} = A_f(\Delta G)^q \tag{8.4}$$

where A_f and q are constants.

However, during the unloading part of the fatigue cycle the fracture surfaces can come into contact. This interference, due to corrosion and the generation of debris on the fracture surface, may prevent the crack from closing, and hence produce a G_{min} value that is artificially high. Thus it has been suggested that the use of G_{max} is preferable[106, 108]. Thus the present work will use G_{max}, calculated using Equation 8.1. The use of G_{max} rather than ΔG has no effect on the overall trend of the results.

Returning to Figure 8.6, the complete curve is of a sigmoidal form, and can be described by a modified Paris law relationship,

$$\frac{da}{dN} = DG_{max}^{n}\left\{\frac{1-\left(\frac{G_{th}}{G_{max}}\right)^{n_1}}{1-\left(\frac{G_{max}}{G_c}\right)^{n_2}}\right\} \qquad (8.5)$$

where n_1 and n_2 are material parameters which are calculated by fitting Equation 8.5 to the experimental data, the values of D and n having been found using Equation 8.2. The threshold value, G_{th}, is the minimum value of the fracture energy (I), and G_c is the constant displacement rate value (III). The threshold value, G_{th}, can be used as a conservative design parameter, as below this value a crack will not propagate.

The simple and modified Paris law relationships will be used in Chapter 9 to model the fracture mechanics data discussed in this Chapter. The relationship between da/dN and fracture energy tends to be steeper for adhesives than for metals, i.e. the value of n is larger. A typical value[65] of n for a structural epoxy adhesive is n = 3, while for steel n = 1. Thus once a crack in an adhesively-bonded component becomes sufficiently large to be detectable using non-destructive evaluation, the remaining life of the component will be short, whereas a metal component may be allowed to continue to operate until the crack reaches a specified length, as the crack growth rate is much slower. Thus as n is large for adhesives, the main parameter of interest is G_{th}, as below this value of the applied strain energy release rate a crack will not grow.

8.5 Results - Constant Displacement Rate Tests

8.5.1 Introduction

Values of the fracture energy, G_c, were calculated using Equation 2.18. Many specimens failed by stable crack growth at a constant load, and hence the calculated fracture energy is constant as the crack grows through the specimen, as shown in Figure 8.7. The results obtained for the combinations of adhesives and adherends tested are shown in Table 8.1.

As G_c is considered to be a material property, it would be expected that its value would be independent of the adherend used if failure was purely cohesive-in-adhesive. However, cohesive-in-adhesive failure only occurred when CAE treated aluminium-alloy adherends were used.

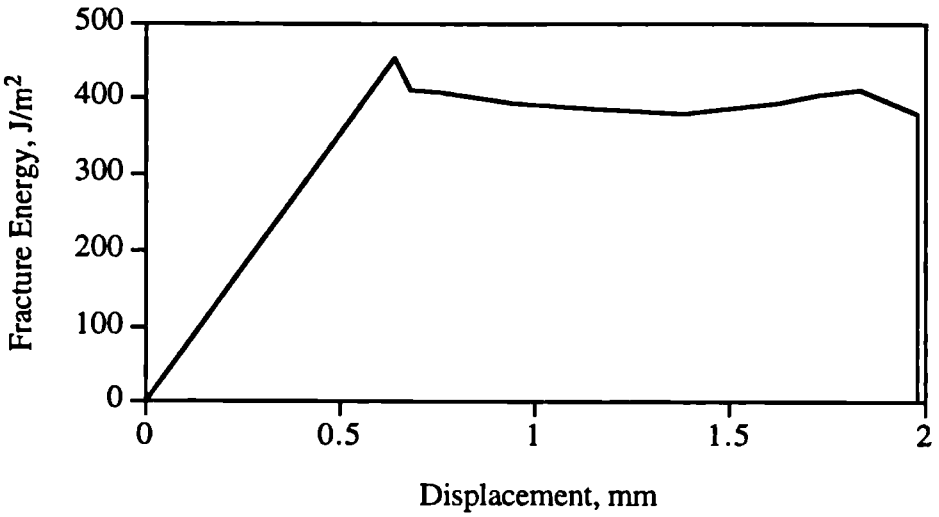


Figure 8.7: Fracture energy versus displacement for constant displacement rate 'AV119'/steel TDCB test, showing stable crack growth and a somewhat higher initiation value.

Table 8.1: Fracture energy values from constant displacement rate TDCB tests, (a) 'AV119' adhesive, (b) 'LMD1142' adhesive.

(a) 'AV119' adhesive.

Adherend	Failure Locus	Fracture Energy, G_c, J/m^2	Standard Deviation, J/m^2
CAE Aluminium	Cohesive	700	70
GB&DG Aluminium	Interfacial	520 / 200	70
GB&DG Steel	Interfacial	450 / 190	75

(b) 'LMD1142' adhesive.

Adherend	Failure Locus	Fracture Energy, G_c, J/m^2	Standard Deviation, J/m^2
CAE Aluminium	Cohesive	4590	50

Note: Where two values are shown these represent the initiation and arrest values respectively for stick/slip crack propagation.

The initial crack propagation was often from a somewhat higher load value, and hence at a higher fracture energy, than might be expected from the rest of the test, as shown in Figure 8.7. This is because propagation is from the end of the foil insert, which is not as sharp as a natural crack, and thus does not give a true 'lower-bound' value. Such artificially high values were ignored.

Stick/slip failure occurred in some tests, the crack tending to initiate and propagate for a distance of 80 to 100 mm before arresting. In these cases the force versus displacement response has a saw-tooth appearance, see Figure 8.8, and an initiation and an arrest value of the fracture energy are quoted in Table 8.1.

8.5.2 'AV119' Adhesive

The chromic-acid etch (CAE) treated aluminium-alloy specimens bonded with the 'AV119' adhesive exhibited stable crack growth with a cohesive-in-adhesive locus of failure when tested at a constant displacement rate. The average value of G_c measured was 700 J/m^2.

The 'AV119' specimens which used the gritblasted and degreased (GB&DG) aluminium-alloy adherends did not exhibit the stable cohesive crack propagation seen in the 'AV119'/CAE aluminium-alloy tests. Instead crack propagation was in a stick/slip manner, see Figure 8.8. Here the crack propagated a short distance, typically between 80 and 100 mm, and arrested. The speed of crack propagation was much greater than the crosshead speed. The specimens failed by several of these crack propagation and arrest events. Hence initiation and arrest values of fracture energy are quoted in Table 8.1. The first initiation was often from a higher value of fracture energy than the subsequent initiation events, as shown in Figure 8.8. This is because this first initiation occurs from the starter foil, when the crack tip is blunter than the natural crack that is present when the crack has propagated further down the length of the specimen. Hence the G_c value obtained would be expected to be erroneously high. These first initiation values were ignored.

The steel specimens bonded with the 'AV119' adhesive exhibited both types of failure. Firstly, where stable crack growth occurred, see Figure 8.7, the failure was apparently interfacial, and the G_c value was reduced. Secondly, stick/slip propagation was also observed, as shown in Figure 8.8, and a G_c value of 450 J/m^2 was measured. In this case failure was cohesive-in-adhesive, with small areas of apparently interfacial failure at the crack arrest/initiation points, see Figure 8.9. Some steel specimens exhibited both types of failure.

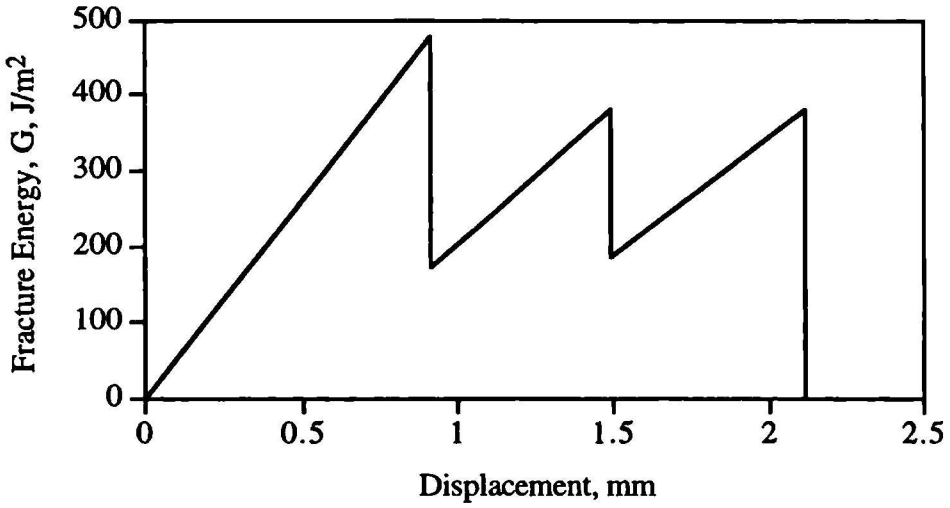


Figure 8.8: Fracture energy versus displacement graph from 'AV119'/steel TDCB specimen tested at a constant displacement rate, showing stick/slip crack growth.

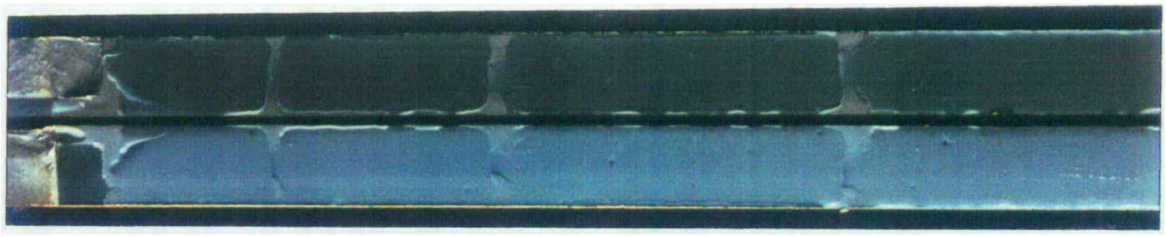


Figure 8.9: Fracture surface of constant displacement rate 'AV119'/steel test specimen showing cohesive failure, plus areas of apparently interfacial failure between arrest and initiation points from stick/slip crack growth. (Crack propagation is from left to right.)

8.5.3 'LMD1142' Adhesive

An average G_c value of 4590 J/m^2 was measured from the tests using the 'LMD1142' adhesive when used to bond CAE aluminium-alloy adherends, as shown in Table 8.1. Failure was cohesive-in-adhesive, and in a stable manner.

8.6 Results - Fatigue Tests

8.6.1 Introduction

The results from the fatigue fracture mechanics, i.e. TDCB, tests were plotted as graphs of the rate of crack growth, da/dN, versus the maximum applied fracture energy, G_{max}, using

logarithmic axes, see Figures 8.11, 8.16, 8.20 and 8.33. All the tests showed evidence of a threshold fracture energy, G_{th}, below which crack growth does not occur. These values, and the loci of joint failure, are given in Tables 8.2 & 8.7 for the 'AV119' and 'LMD1142' adhesives respectively.

The fracture surfaces were analysed using Auger Electron Spectroscopy (AES) and X-ray Photoelectron Spectroscopy (XPS), to identify their elemental composition[118, 153, 154]. The first technique is more suited to the aluminium-alloy specimens, and provides good spatial resolution as the analysis area is 100 μm in diameter. The XPS data is taken over an area which is 5 mm in diameter, but this technique is more suitable for the analysis of the steel specimens than AES[121]. Depth profiling was also used with the above techniques. The surface is eroded to a known depth by ion bombardment, and then analysed. Thus any changes in the composition with depth can be identified[153]. The depth profile of the AES could be calibrated, and so the depth at which analyses were carried out is known. However, the XPS data could not be calibrated and so only an etch time is quoted[121]. Contamination of the fracture surfaces by silicon was observed using both AES and XPS with some 'wet' specimens. This is probably due to decomposition of the silicone sealant used to seal the joints in the water tanks.

The results obtained using the fracture mechanics durability tests are presented in Section 8.6.3, which considers each combination of adhesive, adherend and surface treatment in turn. However, before the durability results are discussed it is useful to consider how far water will have diffused into the joints during the 'wet' tests.

8.6.2 Diffusion of Water into Adhesive Joints

Water can enter a joint by diffusion through the bulk of the adhesive or by permeating along the interface, as described in Section 2.7. The first of these processes can be modelled using Fick's second law of diffusion. This allows the concentration of water at any point in a joint to be found after a time, t, using[75]

$$\frac{C_t}{C_\infty} = 1 - \frac{4}{\pi}\sum_{n=0}^{\infty}\frac{(-1)^n}{(2n+1)}\exp\left[\frac{-D(2n+1)^2\pi^2 t}{4l^2}\right]\cos\left[\frac{(2n+1)\pi x}{2l}\right] \qquad (2.21)$$

where C is the water concentration, D is the diffusion coefficient, and 2l is the joint thickness.

Diffusion data was available in the literature for the 'AV119' adhesive[77, 92]. The authors used samples of bulk adhesive which were immersed in water, held at a constant

30°C[92]. The samples were removed at intervals and weighed. Measurement of the mass of water absorbed enabled the diffusion coefficient of the adhesive to be calculated and gave a value of the diffusion coefficient, D, of 3.18×10^{-14} m^2/s. Hence, the concentration of water at a given point in any joint can be found[75, 96] , using Equation 2.23. At saturation, the adhesive was found to have absorbed approximately 5 % of its own weight of water[92].

A typical 'wet' test lasted for about 10×10^6 cycles, equivalent to 3 weeks of water immersion. Using the data above, it is possible to calculate the water concentration profile within the joint after this time, as shown in Figure 8.10. The concentration of water at the edge of the joint will be 100 %. After 10×10^6 cycles, points at a distance of less than 0.25 mm in from the edge of the joint (i.e. 4.75 mm from the centre of the joint) would have a water concentration of more than 50 % of saturation. After 16×10^6 cycles, the longest test time used, water would have reached about 1.5 mm in from the edge of the joint, with only about 3 % of saturation being present at 1 mm in from the edge of the joint.

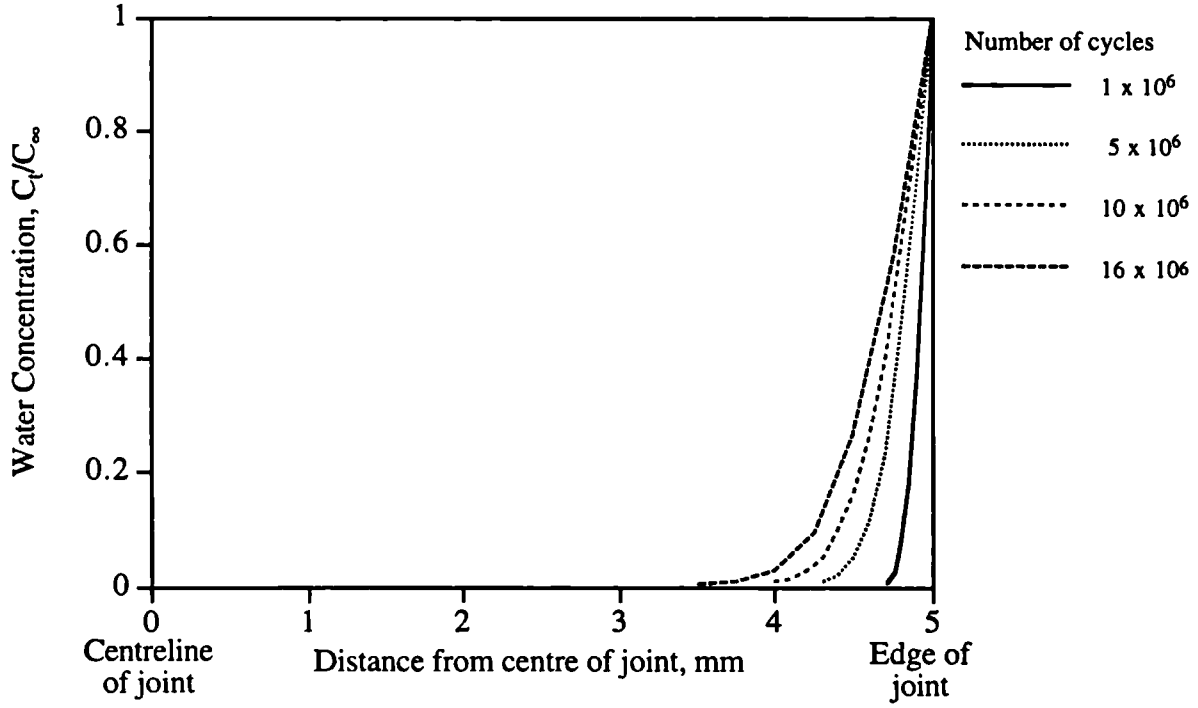


Figure 8.10: Water concentration distributions for 'AV119' adhesive at various water immersion times, (expressed as a number of cycles, tests were conducted at 5 Hz), calculated using 30°C diffusion data from[92], after[75, 96]. At saturation, the adhesive absorbs 5 % of water by weight[92]. Note that 10×10^6 cycles is approximately equivalent to three weeks.

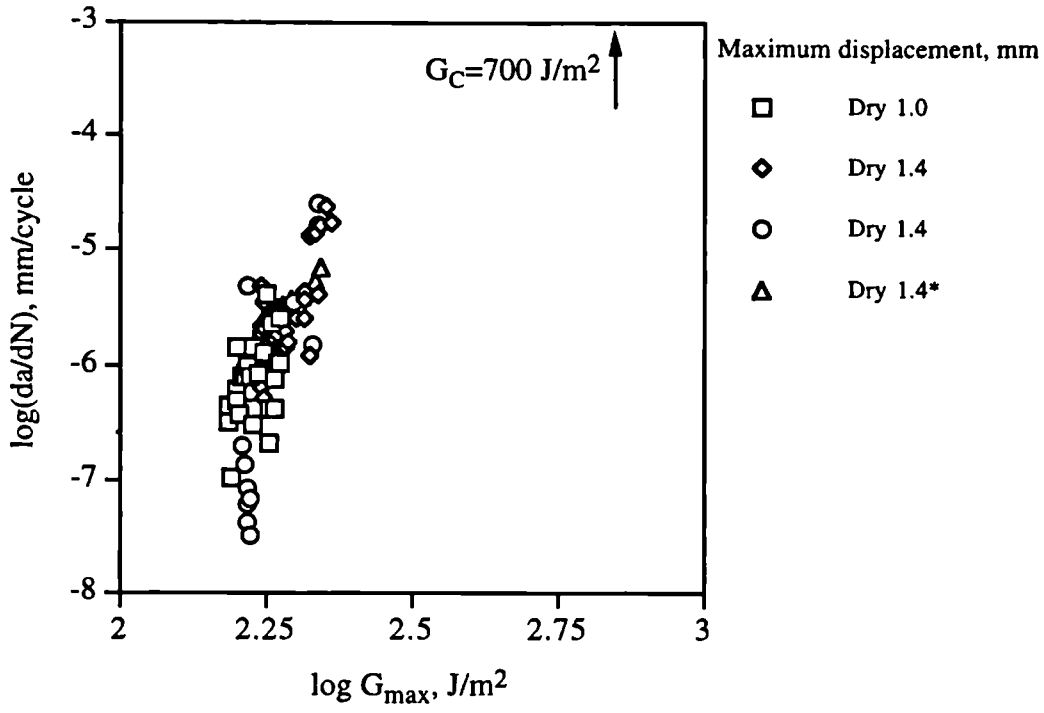
Thus the water diffusion data shows that bulk diffusion from the edges of the joint is unlikely to have a major effect on the durability performance of the 'AV119' adhesive during the short-term tests used in the present work. However, as discussed in Chapter 2, water may also diffuse into the bulk from the crack tip, or along the interface, and these processes can lead to significant reductions in the durability of the joint.

8.6.3 'AV119' Adhesive Fatigue Test Results

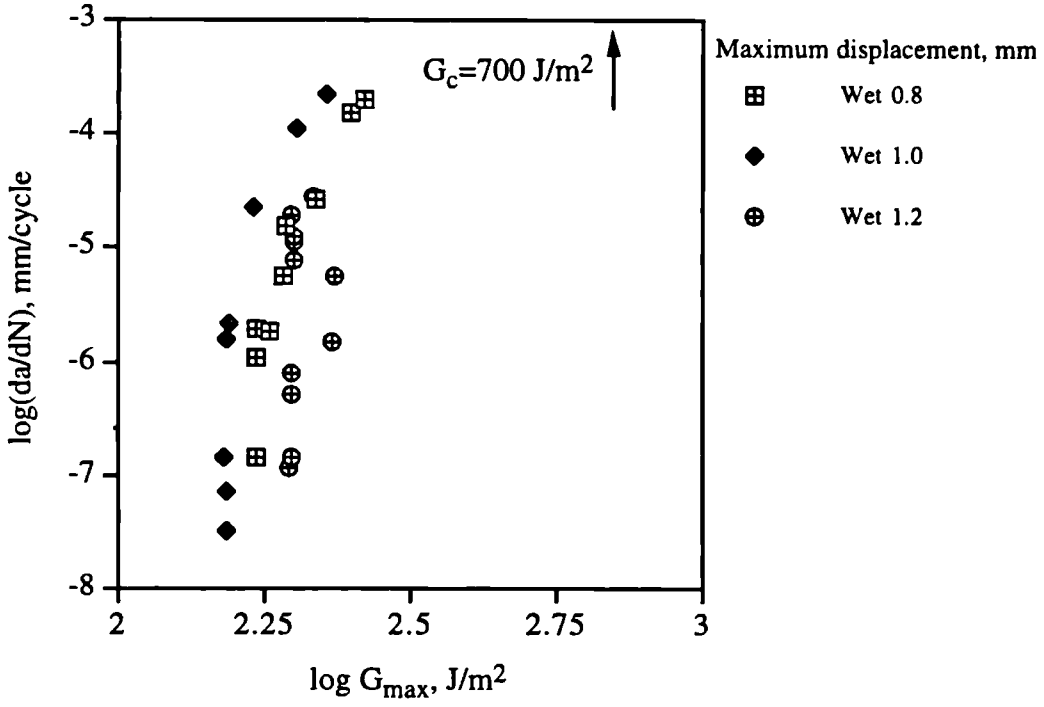
8.6.3.1 Chromic-Acid Etched Aluminium-Alloy

The fatigue tests conducted in the 'dry' environment using aluminium-alloy TDCB specimens bonded with the 'AV119' adhesive, with the CAE surface treatment, gave a threshold fracture energy value, G_{th}, of 160 J/m^2, see Figure 8.11 and Table 8.2. Failure was in a cohesive-in-adhesive manner, as shown in Figure 8.12. These data compare with a G_c value of 700 J/m^2 obtained using the constant displacement rate tests. Thus the cyclic loading has reduced the fracture energy by a factor of about four. Observations of the fracture surfaces using scanning electron microscopy confirmed that the fracture was cohesive-in-adhesive, as shown in Figure 8.13. Rubber particle cavitation is visible, indicating that the toughening mechanisms discussed in Chapter 2 are occurring, However, less cavitation is visible than was observed from the constant displacement rate (10^{-5} m/s) tests, as shown in Figures 4.10 and 4.12. Thus a reduction in fracture energy between the constant displacement rate and the fatigue tests may be expected, and is indeed observed.

For the 'wet' tests, apparently interfacial failure was observed visually, see Figure 8.12, and a threshold value of 175 J/m^2 was recorded, as shown in Figure 8.11. The surface analyses performed using AES showed aluminium oxide on both surfaces, see Table 8.3. These data indicate that failure was through the oxide. Residual adhesive is also present, indicated by the presence of carbon, which was not seen on the 'as treated' (control) samples, discussed in Chapter 3. Table 8.3 also shows that some corrosion and thickening of the oxide has occurred, as there is a relatively thick layer of aluminium oxide present. No elemental aluminium is detected at a depth of 40 nm on the metal side, compared with a depth of 10 nm on the 'as treated' samples, as discussed in Chapter 3. SEM of the fracture surfaces shows oxide and adhesive present on both surfaces, as shown in Figure 8.14.



(a) 'Dry', (* denotes crack gauge data, otherwise from travelling microscope measurements).



(b) 'Wet'

Figure 8.11: Rate of crack growth versus applied maximum fracture energy for 'AV119' adhesive with chromic-acid etched aluminium-alloy adherends, (a) 'dry', and (b) 'wet'.

Table 8.2: Apparent locus of failure and threshold fracture energy, G_{th}, values (±range) from TDCB cyclic fatigue tests using the 'AV119' adhesive.

Adherend & surface treatment	'Dry'			'Wet'		
	Failure locus	G_{th}, J/m²	Range, J/m²	Failure locus	G_{th}, J/m²	Range, J/m²
CAE Aluminium	C	**160**	±10	O	**175**	±20
GB&DG Aluminium	I	**85**	±5	O	**25**	±5
GB&DG Steel	I	**85**	±10	O	**20**	±5

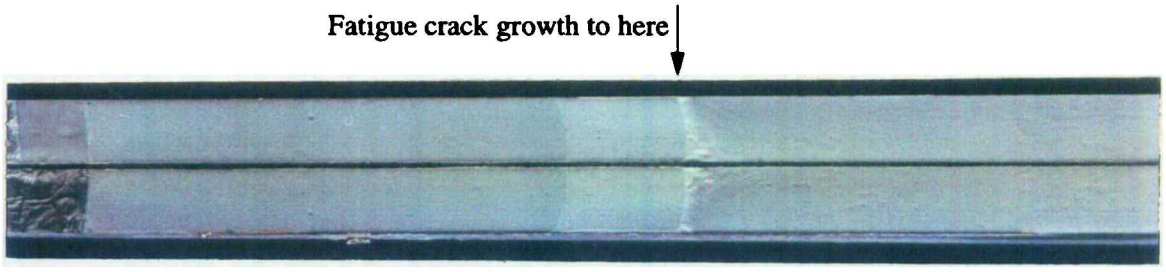
Failure loci:

C Cohesive in the adhesive.

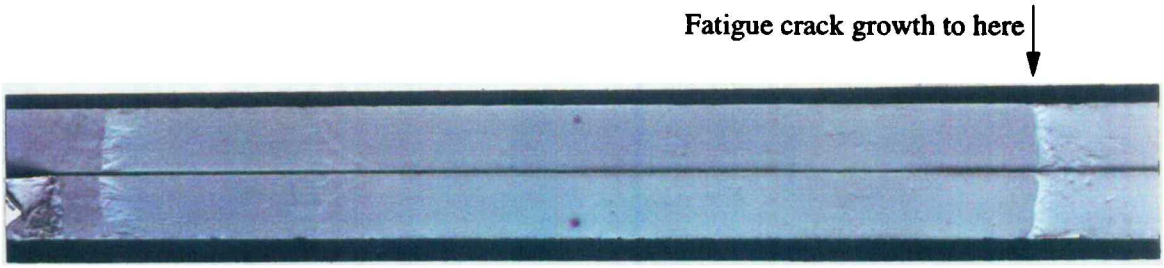
I Close to the interface.

O Oxide.

(Note that some residual adhesive may be present on surfaces where the failure appears to be through the oxide or close to the interface.)

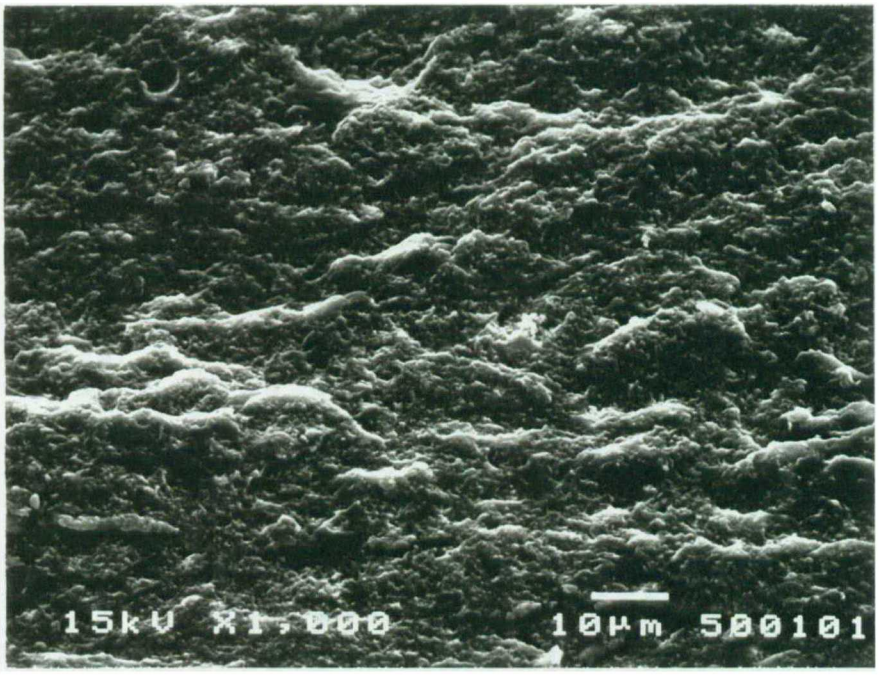


(a) 'Dry'.

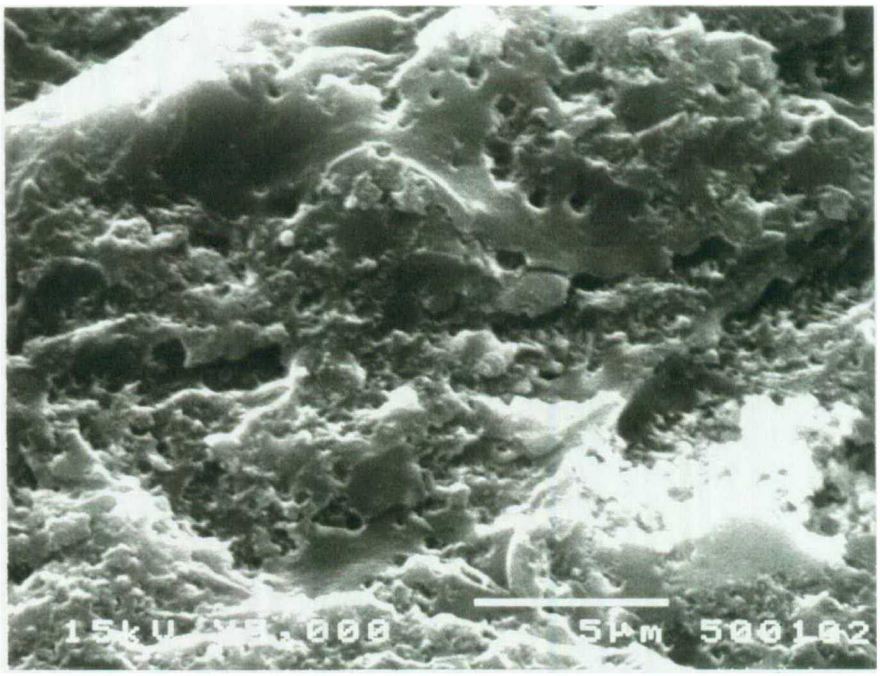


(b) 'Wet'.

Figure 8.12: Fracture surfaces of CAE aluminium-alloy specimens bonded with 'AV119' tested in fatigue, (a) 'dry', showing cohesive-in-adhesive failure, and (b) 'wet', showing apparent interfacial failure. (Crack propagation is from left to right.)



(a) Magnification x1,000.



(b) Magnification x5,000.

Figure 8.13: Micrographs of fracture surface of CAE aluminium-alloy bonded with 'AV119' adhesive, tested 'dry', showing cohesive-in-adhesive failure with some cavitated rubber particles present, (a) magnification x1,000, and (b) magnification x5,000. (Crack propagation is from left to right.)

Table 8.3: AES results for 'wet' 'AV119'/CAE aluminium-alloy fatigue specimens, showing elemental composition by atomic percentage.

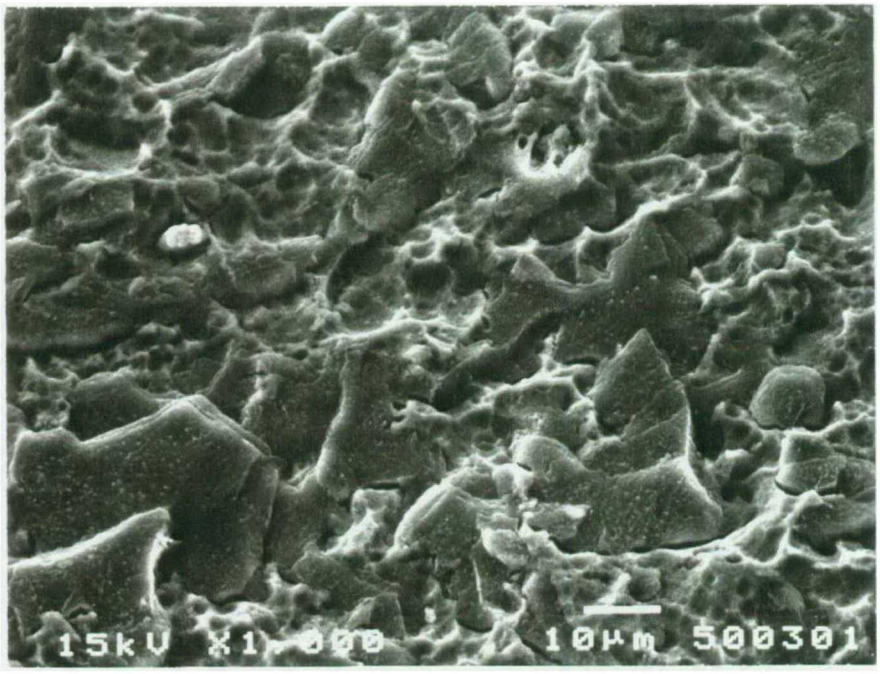
	Area	Depth, nm	Al(o)	Al(e)	C	N	O
'Metal'	A	0	16.5	0	25.0	0	57.4
Side	A	14	23.9	0	31.8	0	44.3
	A	43	23.5	0	36.2	0	40.2
	B	0	2.9	0	58.3	2.7	35.5
	B	13	23.2	0	31.8	0	44.0
	B	42	25.2	0	30.0	0	44.9
'Adhesive'	A	0	4.1	0	63.8	0	30.5
Side	A	14	21.5	0	38.1	0	40.0
	A	41	8.4	0	60.6	0	31.1
	A	75	4.4	0	77.3	0	18.3
	B1	0	3.9	0	56.0	2.0	36.2
	B2	0	31.5	0	13.7	0	53.5

Note:

1. Al(o) is the percentage of aluminium in the form of oxide, Al(e) is the percentage of aluminium in the elemental form.
2. The results for areas 'A' and 'B' are from replicate analyses on visually similar areas of the fracture surfaces. The area 'A' on one fracture surface is approximately opposite 'A' on the other. Similarly, the areas 'B1' and 'B2' are approximately opposite area 'B'.
3. Si, S < 1.0 %, Cl <2.0 %.



(a) 'Adhesive' side.



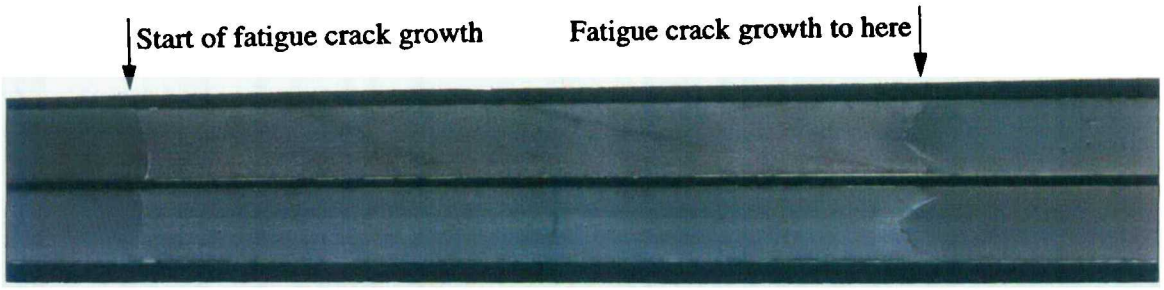
(b) 'Metal' side.

Figure 8.14: Micrographs of fracture surfaces of CAE aluminium-alloy TDCB specimens bonded with 'AV119' adhesive, tested 'wet', (a) 'adhesive' side, and (b) 'metal' side. (Crack propagation is from left to right.)

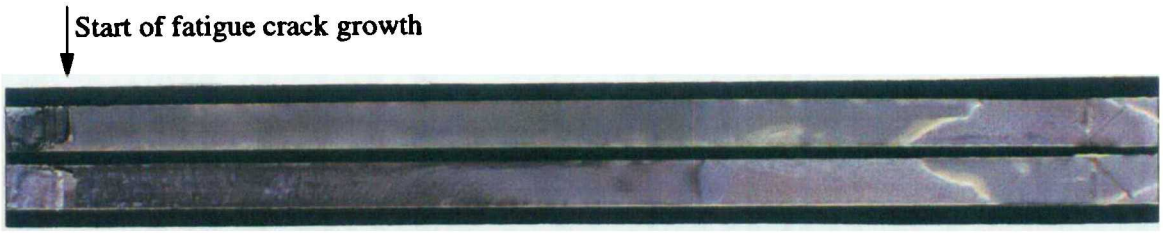
8.6.3.2 Gritblasted & Degreased Aluminium-Alloy

Specimens manufactured using the GB&DG treated aluminium-alloy adherends failed apparently interfacially when tested 'dry', as shown in Figure 8.15. The threshold fracture energy obtained was 85 J/m^2, see Figure 8.16.

The surface chemical analyses performed using AES on one of the specimens after 'dry' testing indicated that interfacial failure occurred, see Table 8.4. However, the AES results, shown in Table 8.4, at zero depth on the adhesive side could come from surface contamination, as 100 % carbon was detected. In this case the failure may be through the oxide. However, Table 8.4 also shows that elemental aluminium is detected at a depth of 16 nm on the metal side (area A). This shows that the oxide layer is the same thickness as that observed on the 'as treated' aluminium-alloy, discussed in Chapter 3. The high percentage of magnesium close to the surface, again as observed with the data presented in Chapter 3, would also indicate that failure has occurred close to the interface.



(a) 'Dry'.



(b) 'Wet'.

Figure 8.15: Fracture surfaces of aluminium-alloy specimen bonded with the 'AV119' adhesive, gritblast & degrease surface treatment, (a) 'dry' and (b) 'wet'. (Crack propagation is from left to right.)

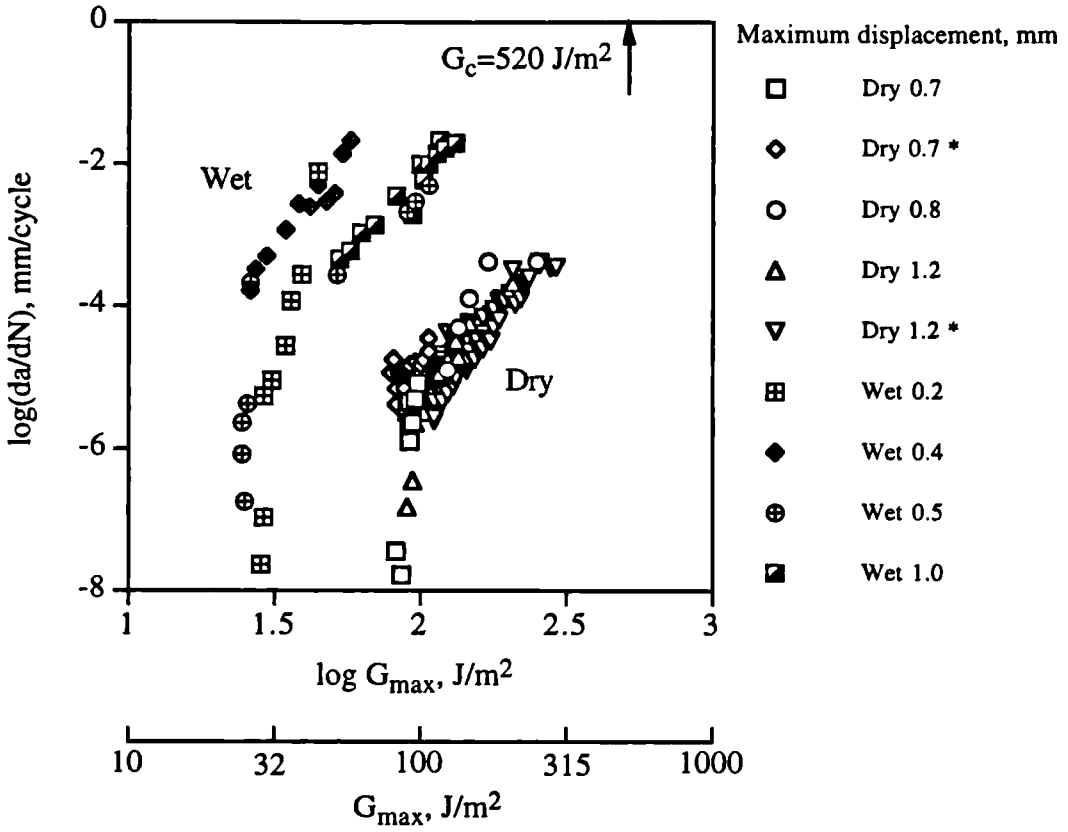


Figure 8.16: Rate of crack growth versus applied maximum fracture energy for 'AV119' adhesive with gritblasted and degreased aluminium-alloy adherends, (* denotes crack gauge data).

Table 8.4: AES results for GB/DG aluminium-alloy specimen bonded with 'AV119' adhesive, fatigue tested 'dry'.

	Area	Depth, nm	Al(o)	Al(e)	Mg	C	N	O
'Metal'	A	0	7.2	0	21.4	30.0	1.2	38.4
Side	A	16	7.5	64.4	6.9	6.9	0	14.3
	A	48	3.4	82.1	0	6.1	0	8.4
	B	0	12.5	0	20.6	19.9	0	45.1
'Adhesive'	A	0	0	0	0	100	0	0
Side	C	0	0	0	0	100	0	0

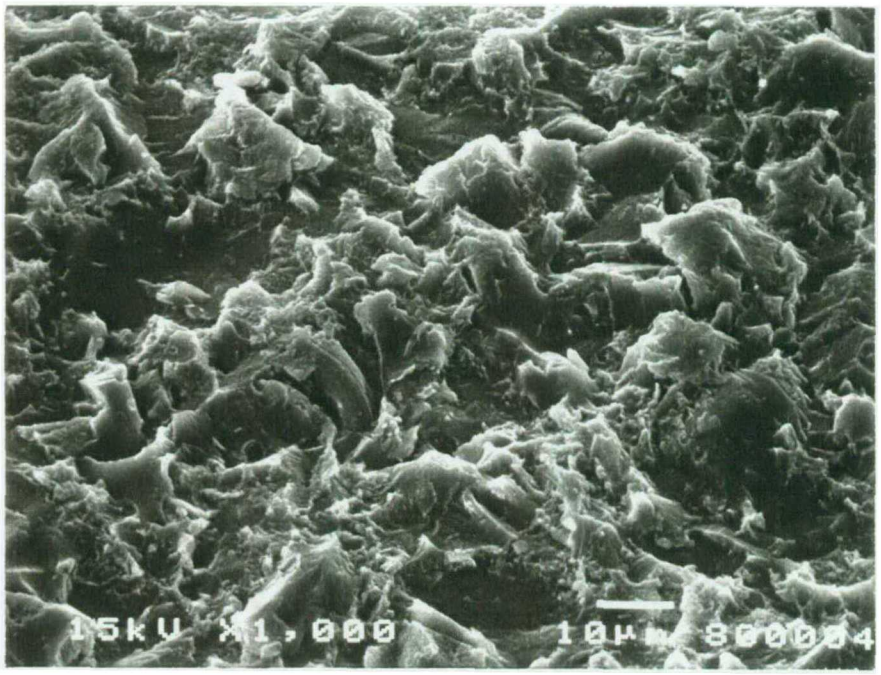
Note:

1. Al(o) and Al(e) are the percentages of aluminium in the oxide and elemental forms respectively.
2. Si & S < 1.1 %.

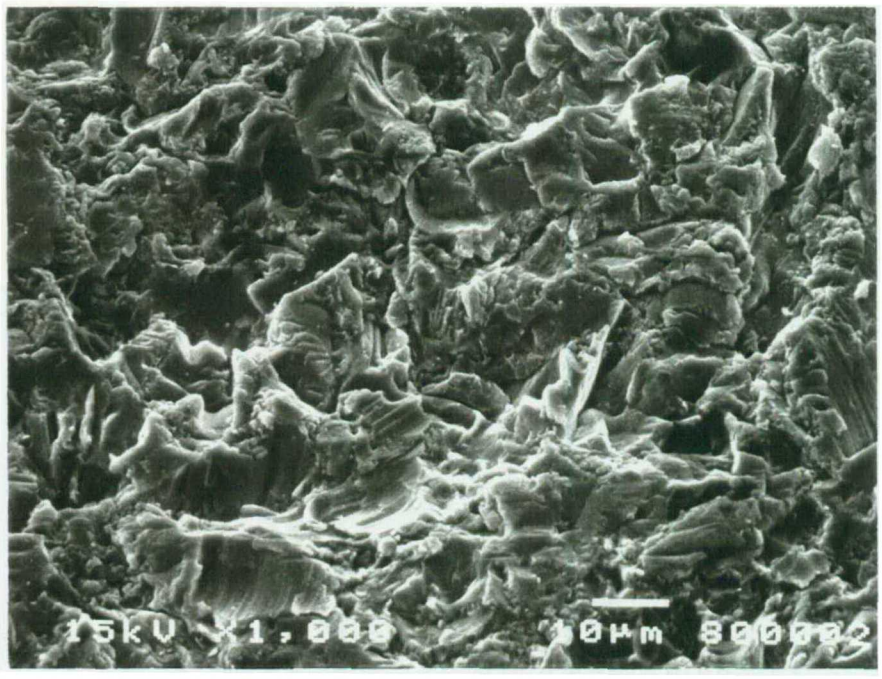
The scanning electron micrographs of the fracture surfaces are shown in Figure 8.17. These show that fully cohesive-in-adhesive failure does not occur, as can be seen if Figure 8.17 is compared to Figure 8.13. This indicates that failure occurs close to the interface.

Note that if failure occurs close to the interface, the plastic zone will be smaller than that for failure through the centre of the adhesive layer, as the full plastic zone cannot form due to the presence of the adherend. Thus a reduction in the measured threshold fracture energy may be expected. Further, the reduction in the measured value of G_{th} from 160 J/m^2 using the CAE treated aluminium-alloy adherends to 85 J/m^2 using the GB&DG aluminium-alloy adherends is consistent with the loss of half the plastic zone due to failure close to the interface.

The 'wet' tests gave a G_{th} value of 25 J/m^2 using the 'AV119' adhesive and GB&DG aluminium-alloy adherends, see Figure 8.16. An example of the fracture surfaces is shown in Figure 8.15. The AES results for one of the 'wet' specimens, shown in Table 8.5, indicate that failure occurs through the aluminium oxide, with some residual adhesive present. This is indicated by the persistent presence of aluminium oxide on the 'adhesive' side of the fractured specimen as the analysis depth is increased. This locus of failure is confirmed by the SEM images which show that both fracture surfaces have a similar appearance, see Figure 8.18. A large amount of corrosion is seen on the fracture surfaces further from the crack tip, as shown in Figure 8.19. However, comparing Figures 8.18 and 8.19 indicates that this corrosion occurs after the joint has failed.



(a) 'Adhesive' side.



(b) 'Metal' side.

Figure 8.17: Micrographs of GB/DG aluminium-alloy specimens bonded with the 'AV119' adhesive, tested 'dry', showing failure occurs close to the interface, (a) 'adhesive' side, and (b) 'metal' side. (Crack propagation is from left to right.)

Table 8.5: Surface analysis results from AES of GB/DG aluminium-alloy specimens bonded with 'AV119' adhesive, fatigue tested in 'wet' environment.

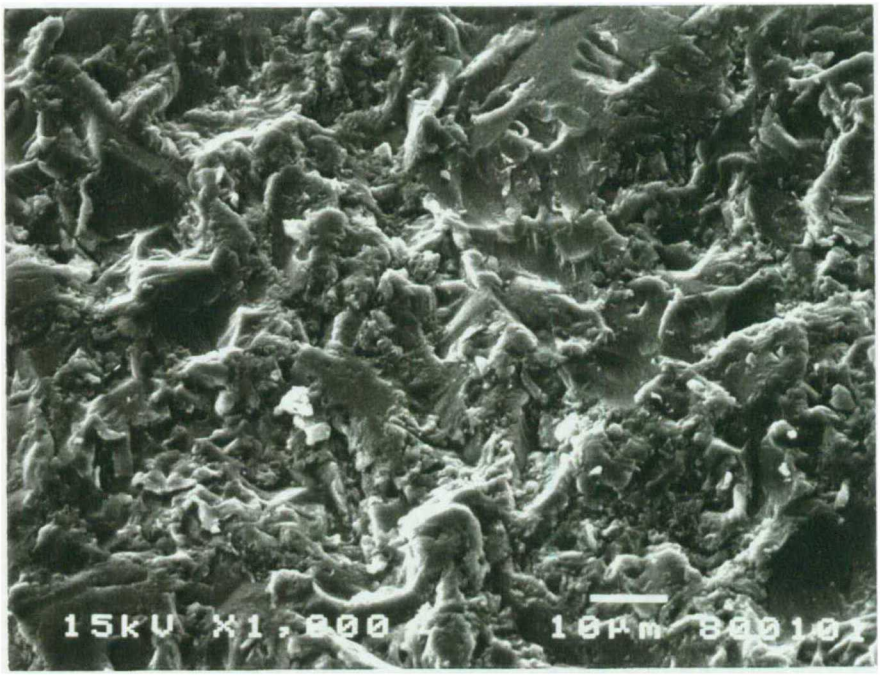
	Area	Depth, nm	Al(o)	Al(e)	Si	C	O
'Metal'	A	0	29.3	0	0	10.1	59.0
Side	B	0	31.7	0	1.1	9.5	57.1
	C	0	34.5	0	0.6	7.2	56.9
	C	8	38.0	0	1.0	3.1	57.2
	C	32	29.9	15.7	0.5	3.7	49.2
	C	64	21.0	44.1	0	2.9	32.1
	C	96	16.2	56.8	0	3.3	23.7
	C	160	12.0	67.9	0	2.7	17.4
'Adhesive'	A	0	31.4	0	0	9.8	58.4
Side	B	0	25.9	0	1.1	17.2	55.3
	B	16	31.7	0	0	9.5	58.8
	B	48	31.9	0	0	9.0	59.2
	B	112	30.5	0	0	10.5	59.0

Note:

1. Al(o) and Al(e) are the percentages of aluminium in the oxide and elemental forms respectively.
2. S < 1 %, Cl < 0.7 %.



(a) 'Adhesive' side.



(b) 'Metal' side.

Figure 8.18: Micrograph of GB&DG aluminium-alloy specimens bonded with the 'AV119' adhesive, tested 'wet', showing failure occurs through the oxide layer, (a) 'adhesive' side, and (b) 'metal' side. (Crack propagation is from left to right.)

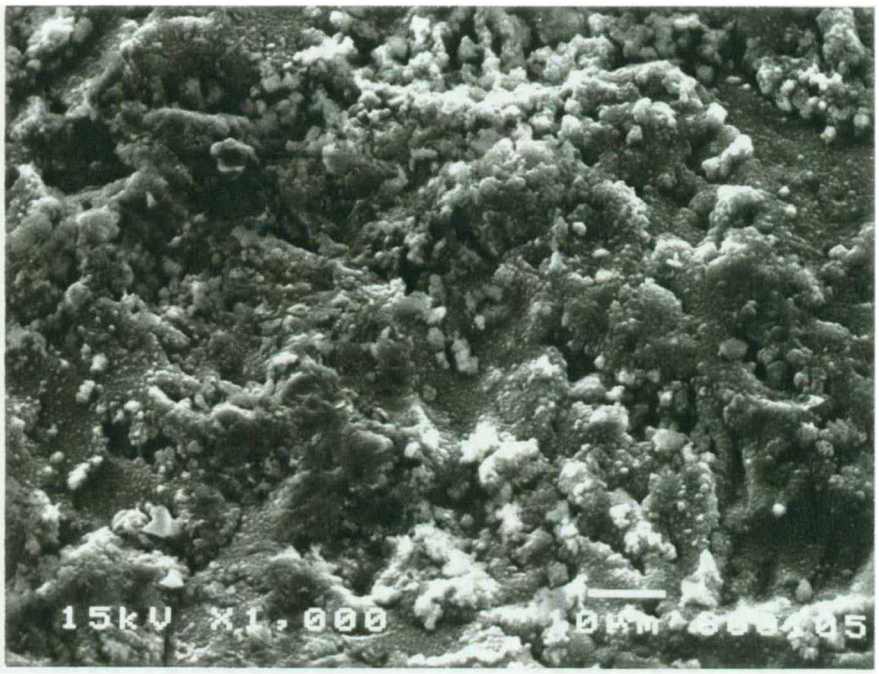
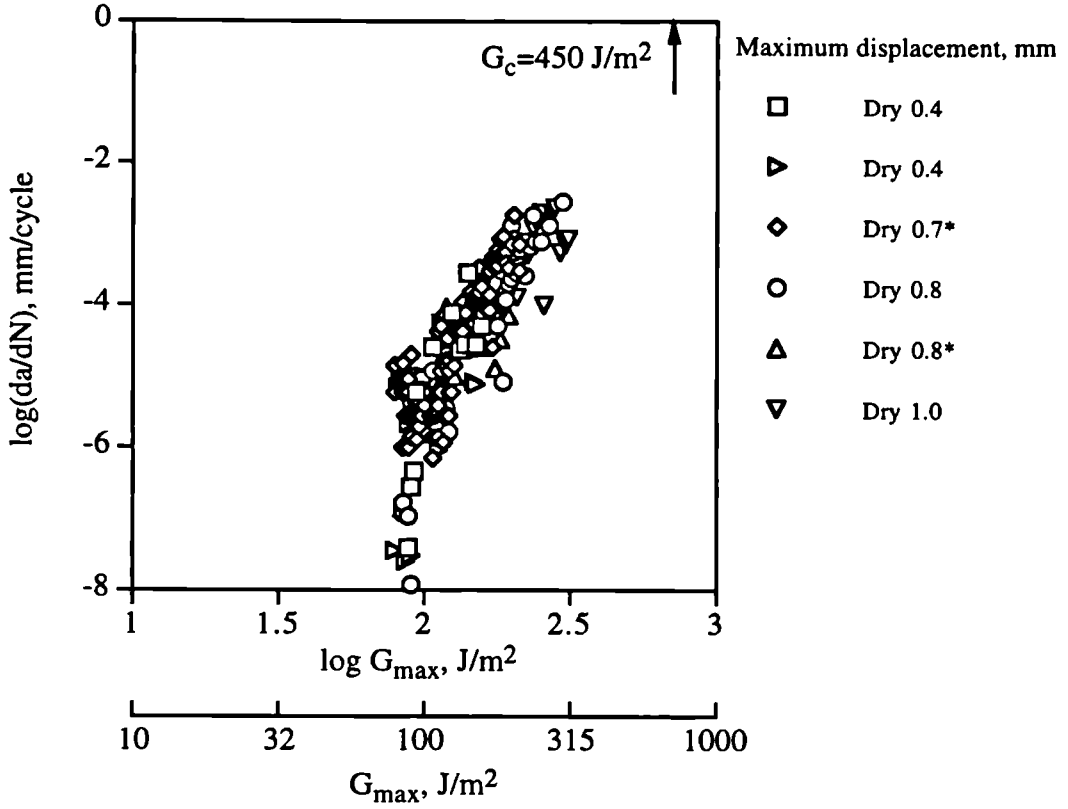


Figure 8.19: Micrograph of GB&DG aluminium-alloy specimen bonded with the 'AV119' adhesive, tested 'wet', showing post-failure corrosion, compare with Figure 8.18(b).

8.6.3.3 Steel

'Dry' fatigue testing of the 'AV119'/steel specimens gave a threshold value, G_{th}, of 85 J/m^2, see Figure 8.20. The visual failure locus was apparently interfacial, as shown in Figure 8.21. Surface analyses were performed on one of the 'dry' specimens using XPS, and the results are shown in Table 8.6. These indicate that failure is cohesive-in-adhesive, but close to the interface. The SEM images obtained, see Figure 8.22, show residual adhesive on both sides of the specimen, with cavitated rubber particles visible. However, the fracture surfaces are not the same as those seen for fully cohesive-in-adhesive failure, as may be seen if Figure 8.22 is compared to Figure 8.13.

This failure locus accounts for the reduction in the measured value of G_{th}, due to the reduced size of the plastic zone. as failure occurs close to one adherend, a plastic zone only half the size of that for fully cohesive-in-adhesive failure can form. Further, the value of G_{th} is half that measured for fully cohesive-in-adhesive failure, as was measured using the GB&DG aluminium-alloy adherends.



(a) 'Dry', (* denotes crack gauge data, otherwise from travelling microscope).

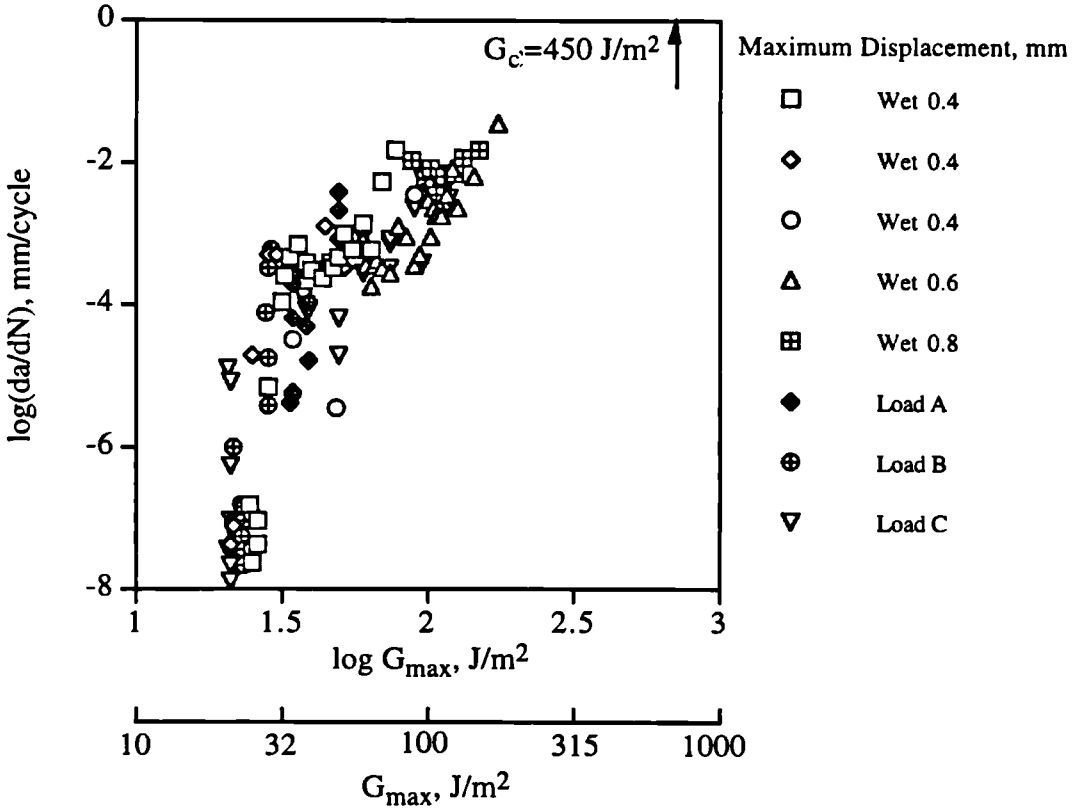


Figure 8.20: Rate of crack growth versus applied maximum fracture energy for steel adherends bonded with 'AV119' adhesive, (a) 'Dry', (b) 'Wet'.

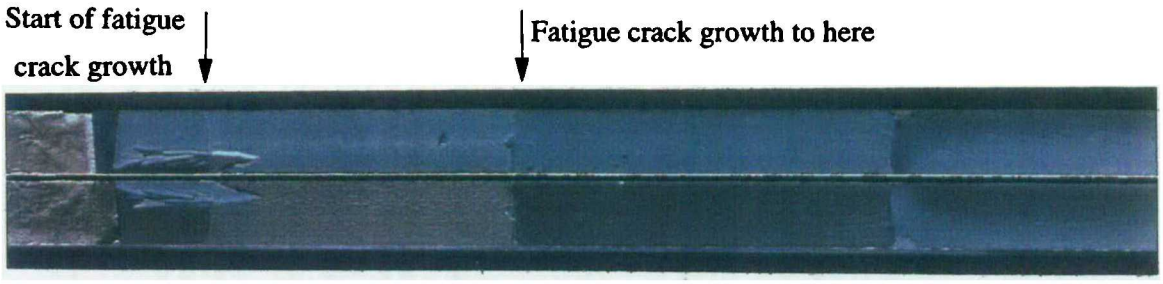


Figure 8.21: Fracture surface of 'dry' steel TDCB fatigue specimen bonded with 'AV119' adhesive showing apparently interfacial failure. (Crack propagation is from left to right.)

Table 8.6: XPS results for 'dry' steel specimen bonded with 'AV119' adhesive, showing elemental composition by atomic percentage.

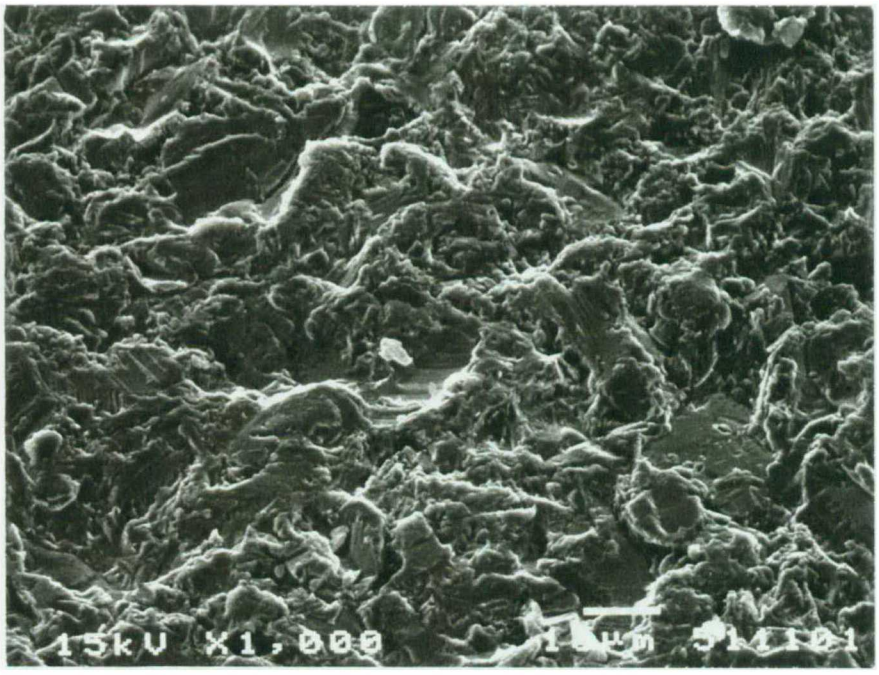
	Etch Time, s	Fe	Si	C	N	O
'Adhesive'	0	0	3.7	73.7	2.8	19.3
Side	60	0	2.6	82.7	2.9	10.2
	130	0	2.0	75.0	2.8	8.8
	300	0	2.3	87.6	2.3	6.8
	1500	0	1.9	87.7	3.1	6.2
'Metal'	0	0	4.5	65.5	2.0	28.0
Side	1500	19.7	0	58.7	5.0	16.6

Note:

The etch times could not be calibrated, and so the depth at which the analyses were conducted cannot be quoted, however a rough estimate of the etch rate would be 1 nm/min. At this rate an etch time of 1500 s would give a depth of 25 nm.



(a) 'Adhesive' side.



(b) 'Metal' side.

Figure 8.22: Micrographs of fracture surfaces of steel specimen bonded with 'AV119' adhesive, tested in 'dry' fatigue, showing failure occurs close to the interface, with residual adhesive on both surfaces, (a) 'adhesive' side, and (b) 'metal' side. (Crack propagation is from left to right.)

The 'wet' fatigue tests gave a threshold fracture energy value of 20 J/m^2, see Figure 8.20b. These 'wet' specimens exhibited a considerable amount of corrosion on both of the fracture surfaces, see Figure 8.23. This would seem to indicate that the failure was within the oxide layer on the surface of the steel. However, some specimens did not show uniform corrosion, as shown in Figure 8.24. The cream areas amongst the brown/black corrosion appear to be residual adhesive. Hence these specimens have failed partly cohesively, although the measured value of G_{th} is unaffected by the locus of failure. The gross corrosion seemed to be a post-failure effect, as areas at the crack tip show less corrosion. The fracture surfaces were examined using SEM, and were seen to be heavily corroded, see Figure 8.25. However, no other conclusions can be drawn from the microscopy.

The photograph of the fracture surfaces, Figure 8.24, also shows that there is some discoloration in the area directly in front of the crack tip. This is probably due to corrosion of the surface oxide beneath the adhesive. It was shown in Section 8.6.2 that the rate of water diffusion through the bulk adhesive was insufficient for water to penetrate across the full width of the joint in the time available. Thus if this area is corrosion, water is diffusing along the interface faster than through the bulk adhesive. However, areas well ahead of the crack tip showed no discoloration. This would indicate that water is permeating from the crack tip rather than from the sides of the specimen.

The presence of the heavy corrosion is either due to failure occurring through the oxide, which subsequently corrodes heavily or due to oxide transfer. The latter case involves particles of oxide that are carried in the water being attracted to the fracture surface due to its high surface energy. Alternatively the fracture surfaces may come into contact during the closing part of the fatigue cycle, and the oxide is transferred from a corroded surface to an uncorroded one. However, this oxide transfer mechanism does not explain the 'two-tone' nature of some of the fracture surfaces. Thus it must be concluded that failure occurs through the oxide, with some areas of cohesive-in-adhesive failure on some specimens. However, the value of G_{th} is unaffected by the locus of failure.

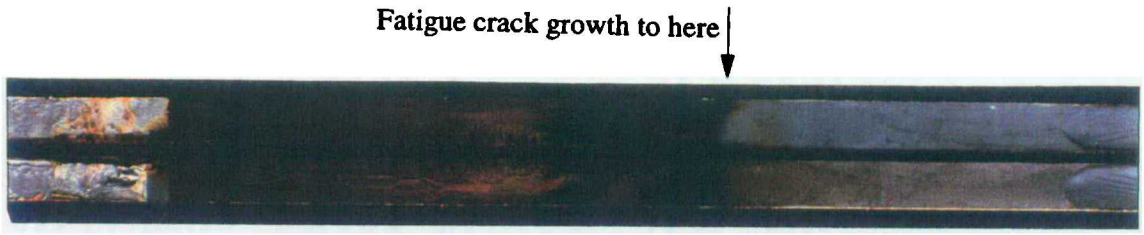


Figure 8.23: Fracture surface of 'wet' steel specimen bonded with the 'AV119' adhesive, showing failure occurs through the oxide, which subsequently corrodes, on both fracture surfaces. (Crack propagation is from left to right.)

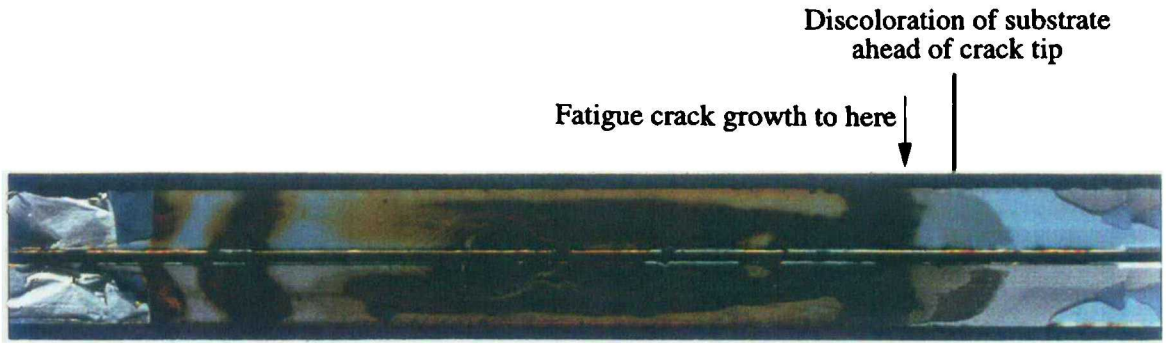


Figure 8.24: Fracture surface of steel specimen bonded with the 'AV119' adhesive, tested 'wet', showing that failure occurs through the surface oxide, with areas of cohesive-in-adhesive failure (cream), and discoloration ahead of crack tip. (Crack propagation is from left to right.)

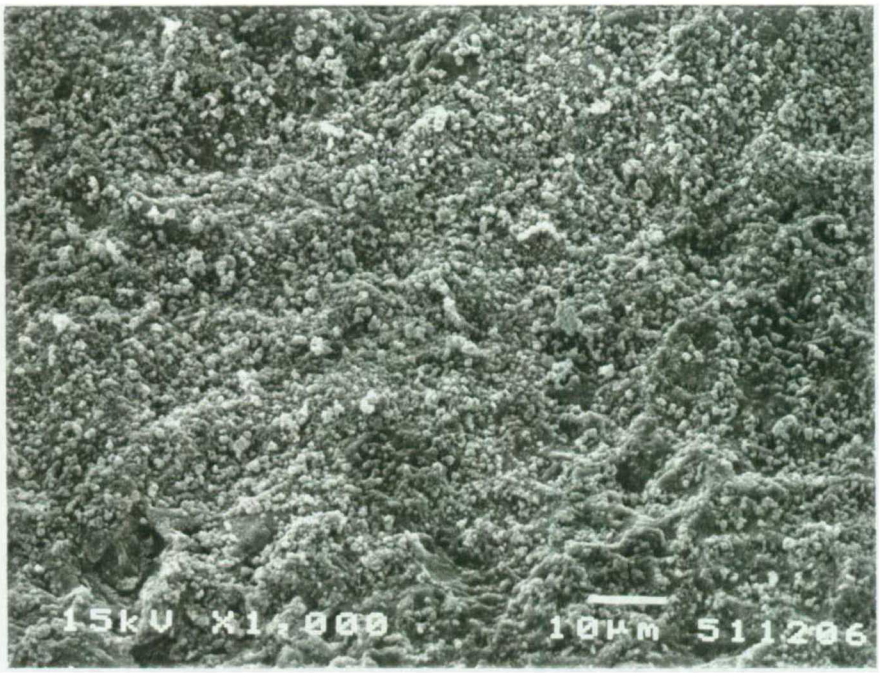


Figure 8.25: Micrograph of fracture surface of 'wet' steel specimen bonded with 'AV119', showing corrosion after failure through oxide.

8.6.3.4 'AV119' Fatigue Data Summary

All the data obtained from the fatigue TDCB tests using the 'AV119' adhesive are collected together in Table 8.2 and Figure 8.26. These show that the fatigue performance of the CAE aluminium-alloy specimens is relatively unaffected by the water immersion, compared with the GB&DG treatment. The 'dry' threshold for the GB&DG treatment is half that for the CAE, the values being 85 and 160 J/m^2 respectively. The water immersion reduces the threshold value for the GB&DG treatment, from 85 to 25 J/m^2. The steel specimens gave a G_{th} value of 85 J/m^2 when tested 'dry', and 20 J/m^2 in the 'wet' environment. In general, testing in the 'wet' environment led to failure through the metal oxide. When tested 'dry' the specimens failed in a cohesive-in-adhesive manner for the CAE treatment or close to the interface when the GB&DG treatment was used.

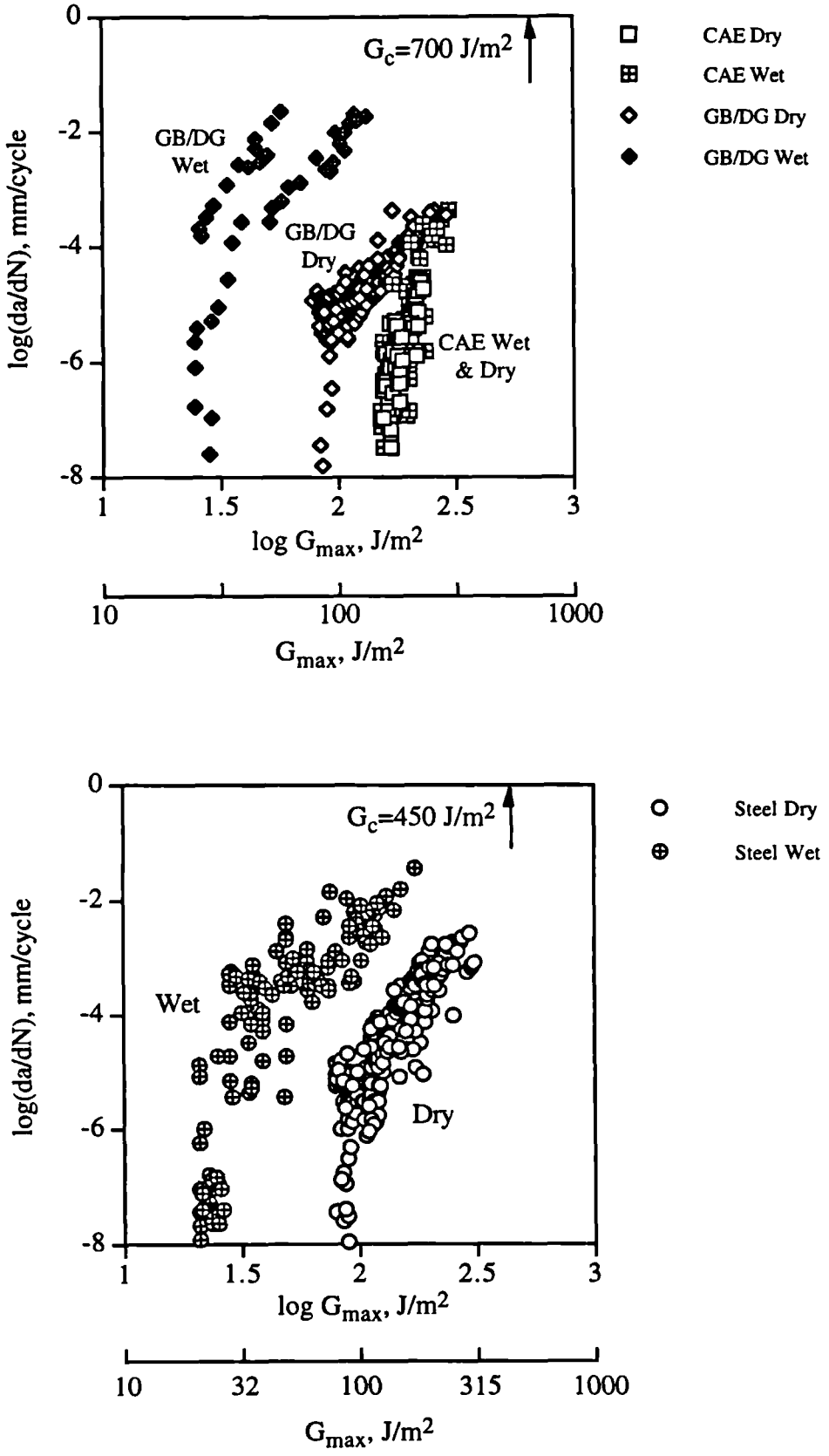


Figure 8.26: Rate of crack growth versus maximum applied fracture energy for the 'AV119' adhesive, (a) aluminium-alloy adherends, using chromic-acid etch and gritblast and degrease surface treatments, (b) steel adherends.

8.6.4 'LMD1142' Adhesive Fatigue Test Results

8.6.4.1 Chromic-Acid Etched Aluminium-Alloy

The 'dry' fatigue tests using the 'LMD1142' adhesive gave a cohesive-in-adhesive failure, with a threshold fracture energy of 510 J/m^2, see Table 8.7 and Figure 8.27. The threshold is less well-defined than that for the 'AV119' adhesive, which may be due to the lower modulus of the 'LMD1142' adhesive[124]. However, the data do meet the American Society for Testing and Materials (ASTM) requirement[64] that the crack growth rate should be less than 10^{-7} mm/cycle, when the crack growth rate is considered to be negligible. Photographs of the fracture surfaces after 'dry' fatigue testing are shown in Figure 8.28. The cohesive-in-adhesive locus of failure was confirmed by SEM, but there are few cavitated rubber particles present on the fracture surfaces, see Figure 8.29. The fracture surfaces of the specimens tested at a constant displacement rate of 10^{-5} m/s, as discussed in Chapter 4, showed large numbers of cavitated rubber particles, see Figures 4.9 and 4.11. Thus the reduction in fracture energy, from 4590 J/m^2 at a constant displacement rate to a threshold value of 510 J/m^2 in fatigue, is due to the reduction of rubber particle cavitation, and hence the energy absorbed during fracture, under fatigue loading.

'Wet' fatigue of the 'LMD1142' adhesive gave a threshold fracture energy of 290 J/m^2, as shown in Figure 8.30 The failure was apparently interfacial optically, see Figure 8.31. However, although failure occurred very close to the interface, SEM showed that adhesive was present on both fracture surfaces, as shown in Figure 8.32. As with the 'dry' tests discussed above, few cavitated rubber particles were present, but these may be seen on both fracture surfaces. The reduction in the threshold fracture energy occurs as a full plastic zone is unable to form due to the presence of the adherend.

Table 8.7: Apparent locus of failure and threshold fracture energy, G_{th}, values (±range) from TDCB cyclic fatigue tests using the 'LMD1142' adhesive.

Adherend & surface treatment	'Dry'			'Wet'		
	Failure locus	G_{th}, J/m^2	Range, J/m^2	Failure locus	G_{th}, J/m^2	Range, J/m^2
CAE Aluminium	C	**510**	±40	I	**290**	±30

Failure loci:

C Cohesive in the adhesive.

I Close to the interface.

Note that some residual adhesive may be present although failure is close to the interface.

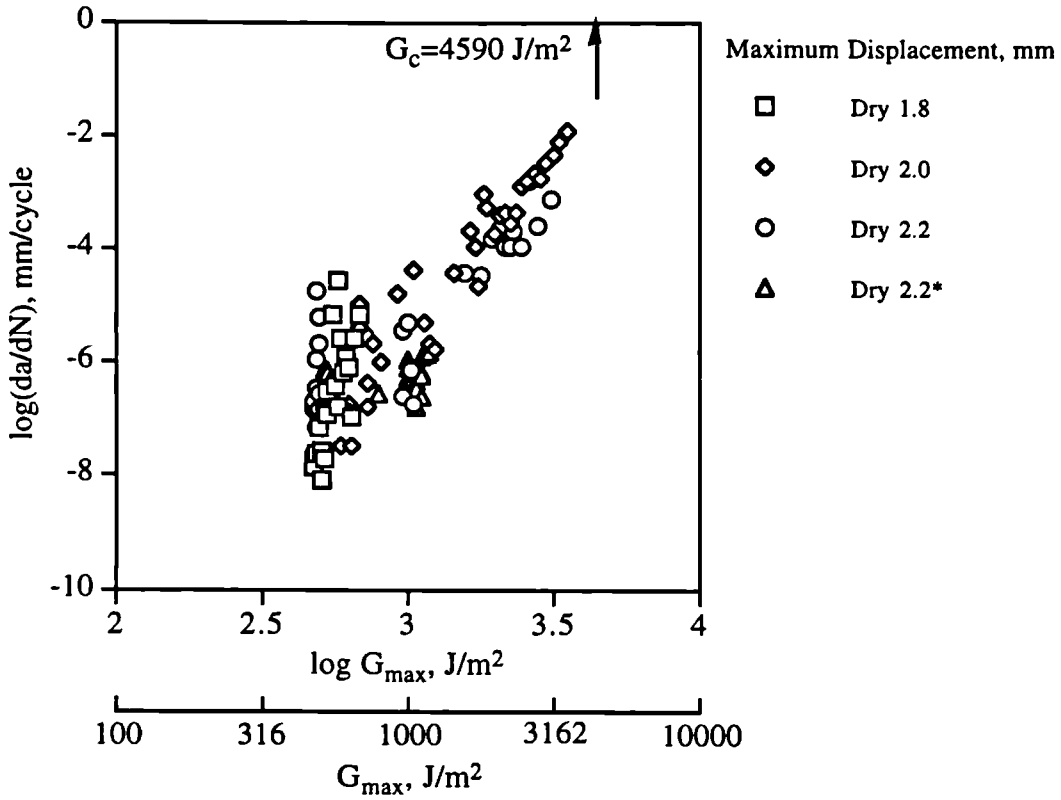


Figure 8.27: Rate of crack growth versus maximum applied fracture energy for CAE treated aluminium-alloy specimens bonded with 'LMD1142' adhesive, tested 'dry', (* denotes crack gauge data).

The rate of crack growth versus fracture energy data for both 'dry' and 'wet' tests are gathered together in Figure 8.33. The threshold fracture energies and loci of failure are also listed in Table 8.7.

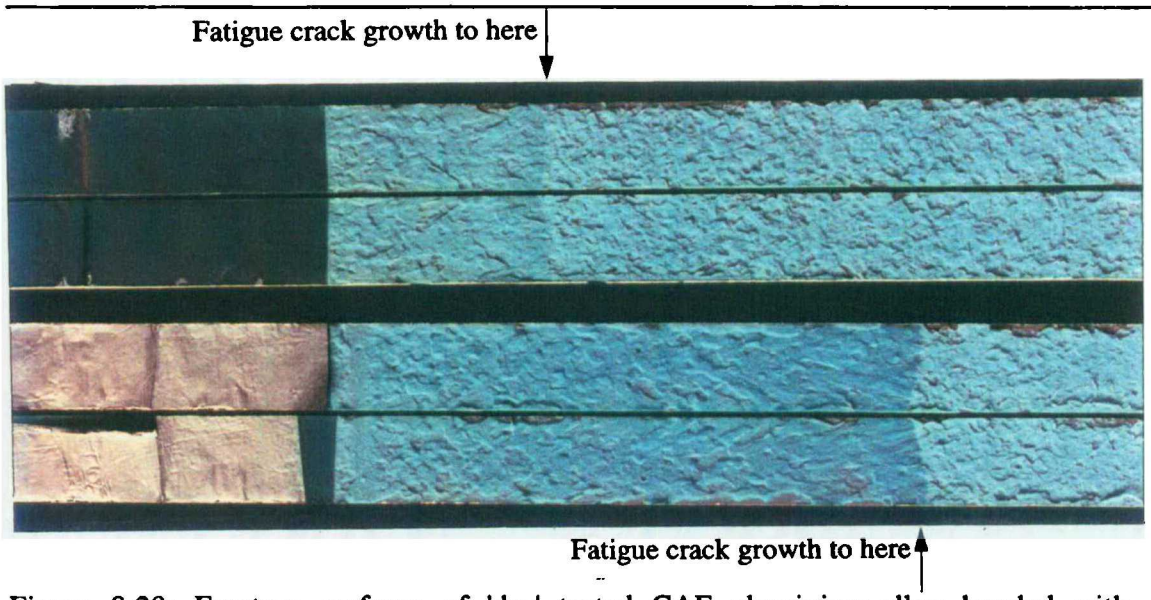


Figure 8.28: Fracture surfaces of 'dry' tested CAE aluminium-alloy bonded with 'LMD1142' adhesive. (Crack propagation is from left to right.)

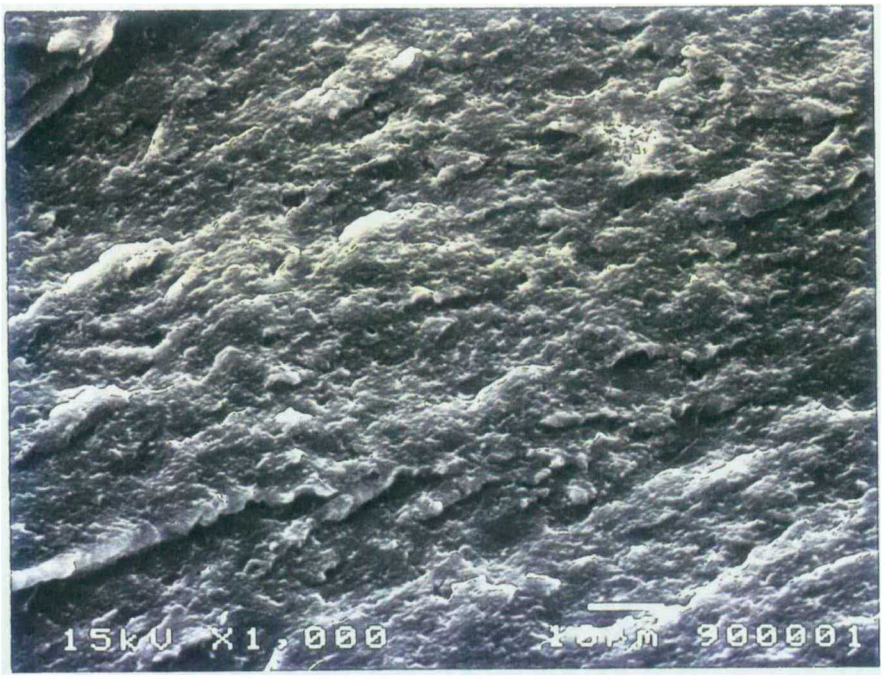


Figure 8.29: SEM image of fracture surface of CAE treated aluminium-alloy specimen bonded with 'LMD1142' adhesive, tested 'dry'. Failure is cohesive-in-adhesive, but there is little evidence of rubber particle cavitation. (Crack propagation is from left to right.)

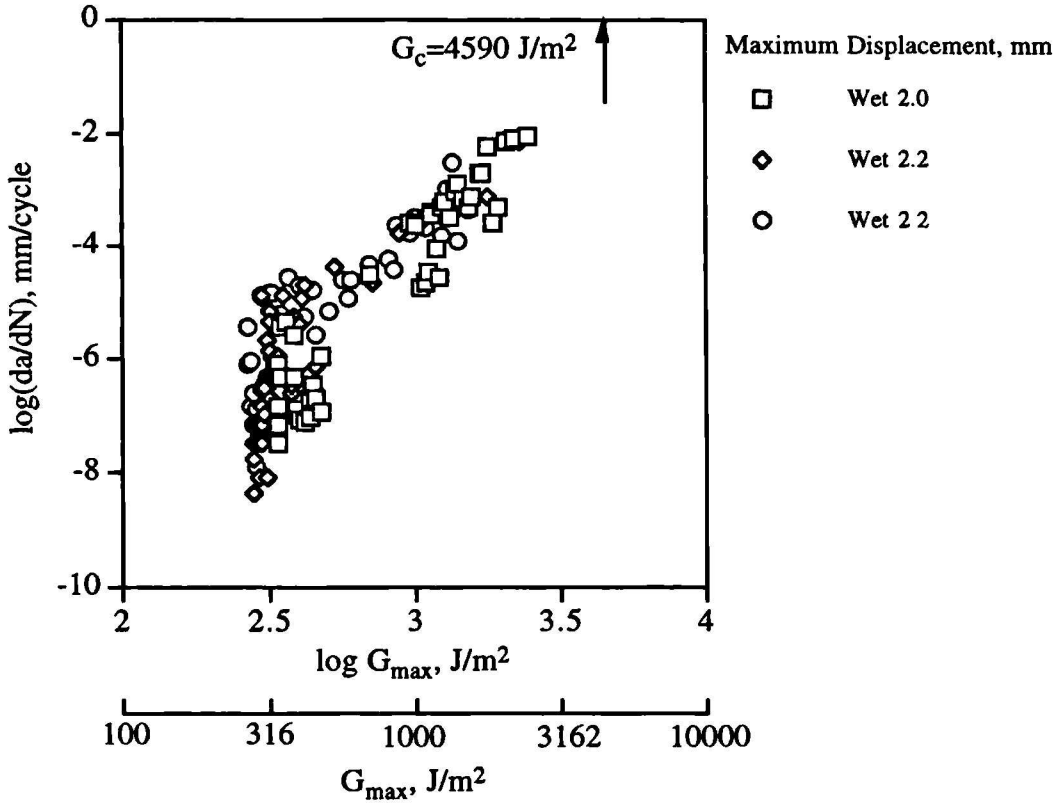


Figure 8.30: Rate of crack growth versus maximum applied fracture energy for CAE treated aluminium-alloy specimens bonded with 'LMD1142' adhesive, tested 'wet'.

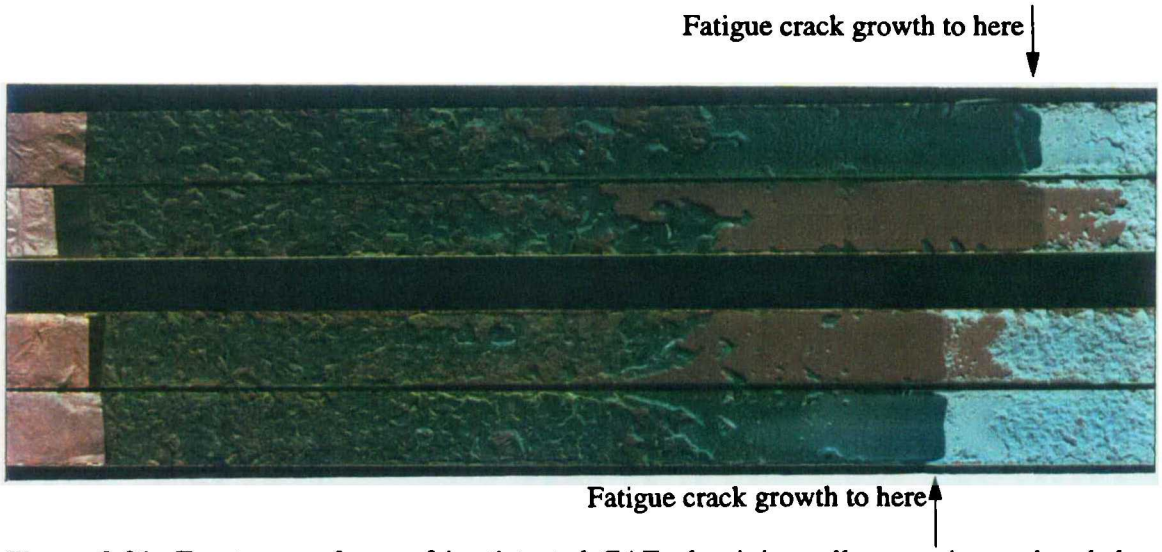
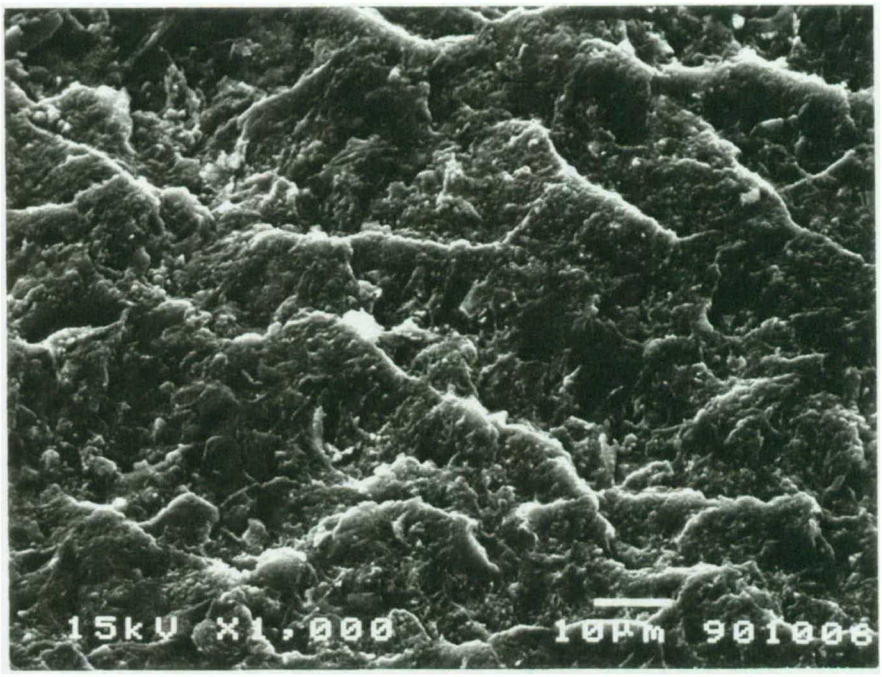
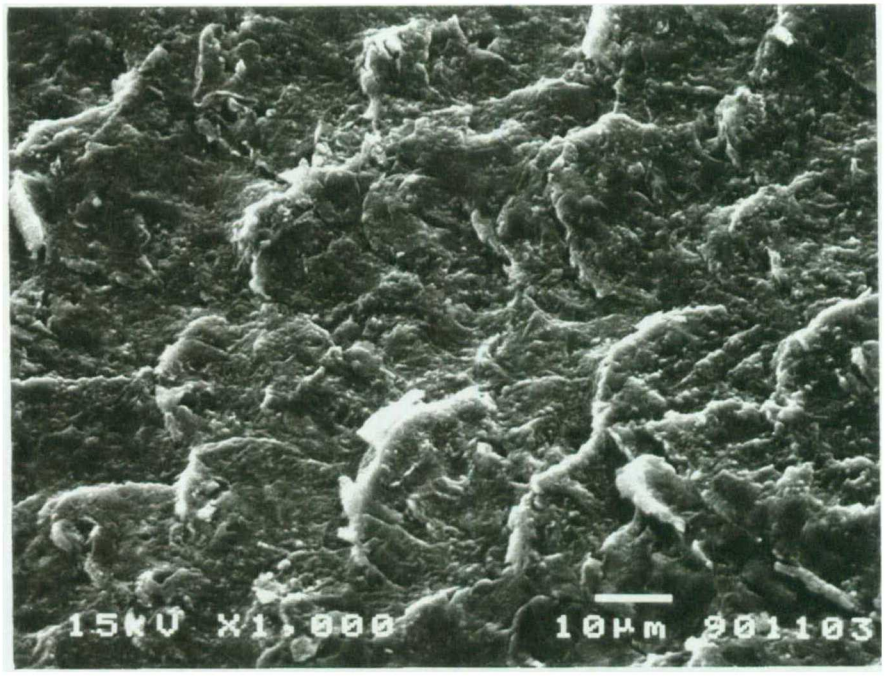


Figure 8.31: Fracture surfaces of 'wet' tested CAE aluminium-alloy specimens bonded with 'LMD1142' adhesive, showing apparently interfacial failure. (Crack propagation is from left to right.)



(a) 'Adhesive' side.



(b) 'Metal' side.

Figure 8.32: Micrographs of fracture surface of CAE aluminium-alloy specimen bonded with 'LMD1142' adhesive, tested 'wet', indicating that failure has occurred close to the interface, (a) 'adhesive' side, and (b) 'metal' side. (Crack propagation is from left to right.)

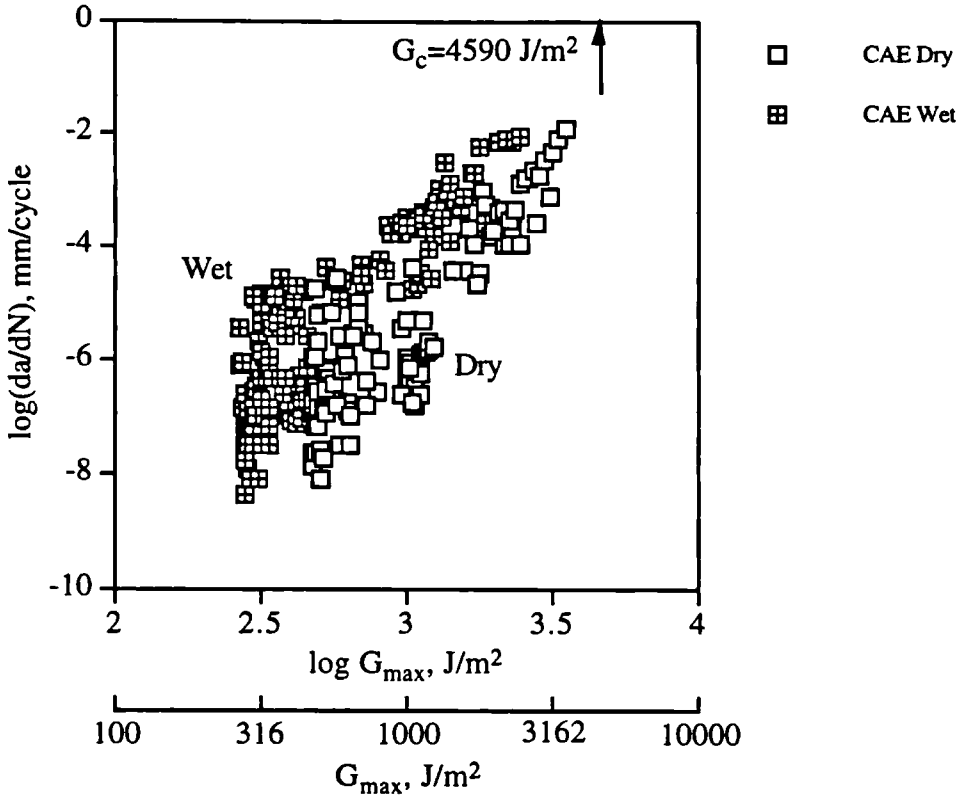


Figure 8.33: Graph of crack growth rate versus maximum applied fracture energy for 'LMD1142' adhesive, on logarithmic axes. Data from 'dry' and 'wet' tests is presented.

8.6.5 Load Control Tests

In order to determine whether the results obtained using the 'wet' fatigue tests were independent of the immersion time, load control tests were performed to investigate the effect of increasing G_{max} during a 'wet' test. In these tests the specimens that were tested at a low applied G_{max} would experience a short immersion time, and those at a high G_{max} would have a long immersion time. These conditions are the opposite of those seen in the displacement control tests, discussed in Sections 8.6.3 and 8.6.4. Steel specimens bonded with the 'AV119' adhesive were used for these tests. The specimens were placed in water and cycled at the threshold value of G_{max} found from the displacement control tests, i.e. G_{th}. The measured rate of crack growth was plotted against the number of cycles on log-log axes, as shown in Figure 8.34. This shows that the crack growth rate approaches that seen in the displacement control tests, less than $10^{-4.5}$ mm/cycle, after approximately 5×10^3 cycles, equivalent to about 15 minutes.

Prior to commencing the load control tests, the specimens were pre-cracked in displacement control. As the starter foil is blunt compared to a natural crack, if the specimen is not pre-cracked then a crack will not propagate at the low values of applied fracture energy used for these tests. Note that pre-cracking the specimen in displacement control only required a few hundred cycles. As the pre-cracking is performed at a higher value of G_{max} than the subsequent load control test, this creates a larger damage zone than that for the subsequent load control test. Thus the crack growth rate starts off higher than may be expected from the displacement control test data, and decreases towards the value seen from the displacement control tests at G_{th}. This crack growth behaviour is consistent with the crack growing out of the damage zone.

After approximately 10×10^6 cycles (equivalent to 3 weeks), the load, and hence the value of G_{max}, was increased. The rate of crack growth was measured. The load was increased in steps until failure of the specimen occurred.

The log da/dN versus log G_{max} data for the load control tests are presented in Figure 8.35. This Figure shows that the load control points fall within the scatter band from the displacement control tests, though G_{max} is increasing with time whereas G_{max} decreases with time for displacement control. This test lasted for 10×10^6 cycles, which is equivalent to 3 weeks immersion in water. The timescale of this test was similar to that seen in the displacement control tests. Thus there is no effect of water immersion time on the relationship between rate of crack growth and the maximum applied fracture energy, over the timescale of the tests in the current work. The value of the threshold fracture energy obtained is also unaffected.

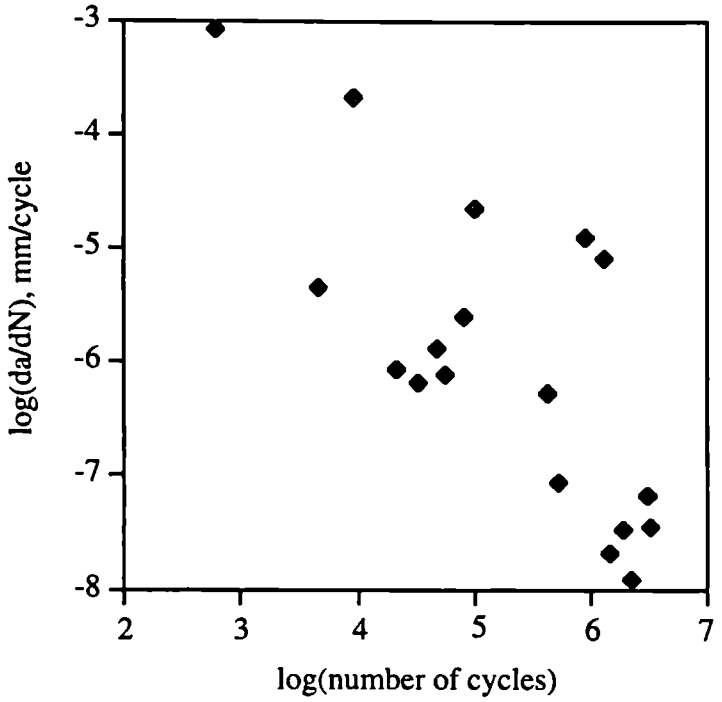


Figure 8.34: Rate of crack growth versus number of cycles for load control test on 'wet' 'AV119'/steel specimen, logarithmic axes. Maximum load 240 N, G_{max} = 21 J/m^2.

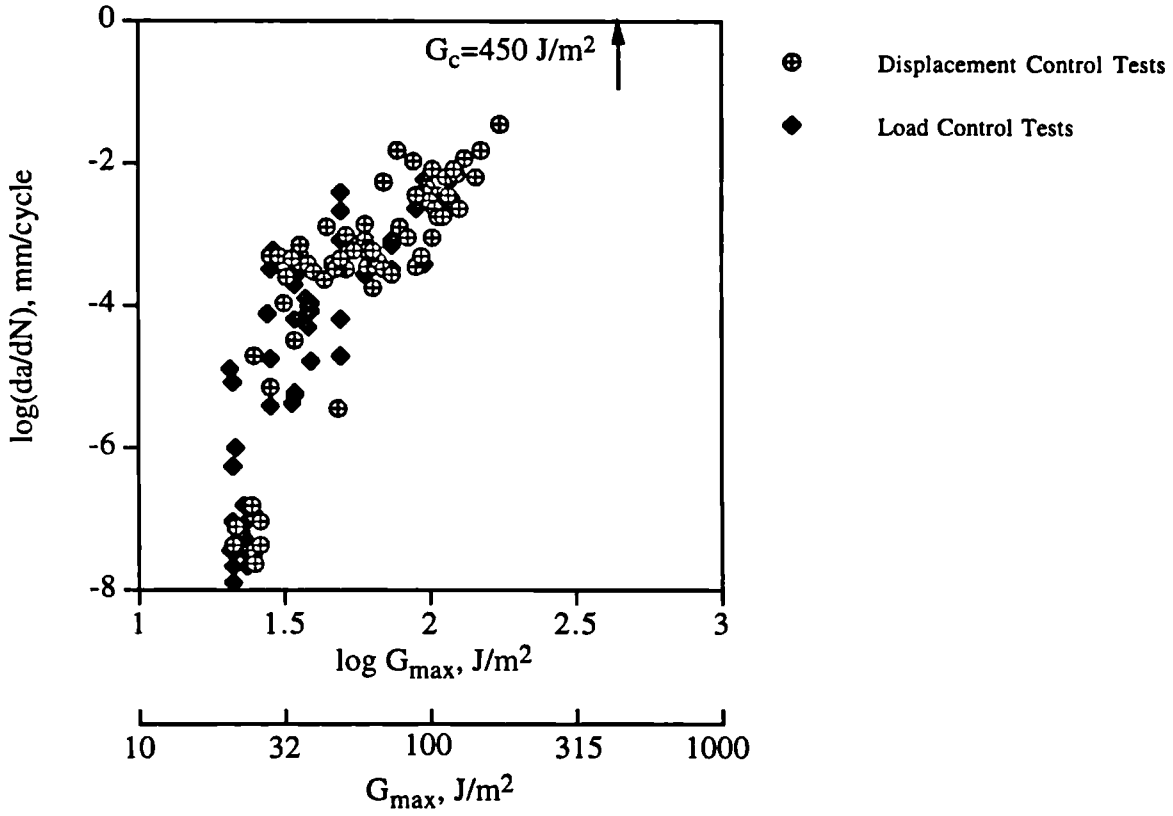


Figure 8.35: Rate of crack growth versus maximum applied fracture energy (logarithmic axes) for steel TDCB specimens bonded with the 'AV119' adhesive, tested 'wet'. Data show the same relationship from using either displacement or load control.

8.6.6 Discussion

The fatigue tests using the TDCB specimens have shown that there is a threshold value of the fracture energy, G_{th}, in fatigue below which the crack growth rate is negligible. This value is much lower than the constant displacement rate, G_c, value. This effect has been observed by other authors, see Table 8.8, for a range of structural epoxy adhesives. The data presented in the present work has confirmed that the magnitude of this reduction is dependent on the adhesive used, and that a high G_c value does not necessarily imply a high G_{th} value, as shown in Table 8.8. Note that failure is cohesive-in-adhesive using both constant displacement rate and 'dry' fatigue loading.

Table 8.8: Fracture mechanics data showing constant displacement rate adhesive fracture energy, G_c, and 'dry' fatigue threshold fracture energy, G_{th}. All failure was cohesive-in-adhesive. Data from present work except where shown.

Adhesive & manufacturer	Adherend	G_c, J/m^2	G_{th}, J/m^2	G_{th}/G_c	Reference
'EA9309', Hysol Dexter	1	5700	150	0.03	[106]
'LMD1142', Ciba Polymers	2	4590	510	0.11	-
'XD4600' Ciba Polymers	2	3500	355	0.10	[65]
'FM73M', American Cyanamid	1	2930	280	0.10	[106]
'AF-163-2M', 3M	2	1720	560	0.33	[150]
'EA9628(NW)', Hysol Dexter	2	1700	178	0.10	[155]
'Terokal 4520-34', Teroson	3	740	240	0.32	[65]
'AV119', Ciba Polymers	2	700	160	0.23	-

Note:

Adherends used:

1. Carbon-fibre reinforced plastic (CFRP).
2. Aluminium-alloy (CAE surface treatment).
3. Electrogalvanised steel.

Table 8.8 shows that the threshold fracture energy in 'dry' fatigue is between 3 % and 33 % of the constant displacement rate fracture energy for these adhesives. Further, the magnitude of the reduction from G_c to G_{th} is dependent upon the individual adhesive. Osiyemi[106] suggested that the performance of the 'FM73M' adhesive was better than that of the 'EA9309' adhesive due to the presence of the polymeric fibre carrier mat. SEM showed that the carrier fibres were broken under fatigue loading, while they remained

intact during the constant displacement rate tests[106]. However, most of the adhesives shown in Table 8.8 do not use a carrier, and thus this explanation cannot be proposed as a general explanation of the relative fatigue performance. Indeed, information describing why one adhesive performs better in fatigue than another is scarce. Jethwa[65] does not present micrographs of the 'dry' fatigue fracture surfaces, and the micrographs presented by Osiyemi[106] are of a low magnification. Thus no conclusions may be drawn as to the relative amounts of rubber particle cavitation, or other toughening mechanisms, occurring around the crack tip with these adhesives. However, the present work has shown that there is significantly less rubber particle cavitation under fatigue loading than at a constant displacement rate for the 'LMD1142' and the 'AV119' adhesives. Thus the toughening mechanisms, as discussed in Chapter 2, are less effective under fatigue loading. Hence a large reduction in the measured fracture energy would be expected, as is indeed observed, the value of G_{th} being significantly smaller than G_c.

The specimens bonded using the 'AV119' adhesive tested under 'wet' conditions did not fail in a cohesive-in-adhesive manner. Surface analyses showed the presence of metal oxide on both of the fracture surfaces. Two explanations have been postulated for the mechanism of failure. The first is that failure occurred through the metal oxide, which is weakened by the ingress of water, and the second is that failure occurred at the interface, but oxide transfer has taken place. These two mechanisms will be considered in turn.

Weakening and failure of the metal oxide has been observed, or postulated as the mechanism of failure, by various authors[84, 87, 91]. Jethwa[65] observed failure through the oxide layer using CAE aluminium-alloy adherends bonded using a rubber-toughened epoxy adhesive ('XD4600') after 'wet' fatigue testing. This locus of failure was confirmed using TEM, AFM and XPS. TEM was also used to investigate the thickness of the oxide layer at and just ahead of the crack tip. This concluded that a subtle process of hydration/corrosion was possibly occurring, which was sufficient to weaken the oxide, but not to show up as gross hydration, and hence thickening of the layer[65].

The alternative explanation for the presence of metal oxide on both fracture surfaces is oxide transfer after interfacial failure. As discussed in Chapter 2, the work of adhesion for an epoxy/metal interface in water is negative. Hence there is driving force for debonding at the interface. Thus interfacial failure may occur between the adhesive and the metal oxide, as observed experimentally in some cases[156]. The exposed oxide will corrode and the oxide may be transferred to the adhesive surface, due to facial interference or deposition. This thermodynamic approach assumes that only secondary bonding is occurring. The joint strength does not decrease to zero as it is unlikely that

water would fully displace the adhesive as there are likely to be interfacial primary forces present.

However, in the present work, the ratio of minimum to maximum displacement is 0.5, and the fracture surfaces do not fully close during the fatigue tests. Hence facial interference should be limited. Further, Kinloch, Welch and Bishop[23] considered the problem of oxide transfer. They placed a sheet of cured adhesive against a sheet of aluminium-alloy and exposed them to water at 60°C for seven hours. The surface of the adhesive was then examined using XPS, but no aluminium was detected. Thus the authors[23] concluded that oxide transfer was not occurring, and that failure occurred through the oxide. In the present work, the use of XPS, AES and SEM close to the final crack tip would seem to indicate that all failures during 'wet' testing occurred through the oxide rather than the oxide being present on the fracture surfaces due to oxide transfer. Thus failure probably occurred through the metal oxide in the present work.

However, it should be noted that significant corrosion of the metal adherend surface occurs after joint failure. This effect has been observed by various authors[21, 65, 69]. In the present work the thickness of the oxide was observed using SEM, and was seen to increase as the point of interest was moved away from the final crack tip. The surface pretreatment may greatly effect the stability of the oxide on exposure to water[69]. In the present work, the surface analyses were performed close to the final crack tip, where little or no post-failure corrosion is present. These analyses indicated that all failures during 'wet' testing occurred through the oxide, for the 'AV119' adhesive.

Water has been shown to reduce the fatigue resistance of the 'AV119' adhesive when used on steel or GB&DG aluminium-alloy adherends, i.e. the threshold fracture energies are lower under 'wet' fatigue loading than under 'dry' conditions, as shown in Table 8.9. The threshold values obtained from the specimens using the chromic-acid etched (CAE) aluminium-alloy adherends were largely unaffected by the presence of water, see Table 8.9. Note that the loci of failure were through the oxide for all the 'wet' tests using the 'AV119' adhesive. It has not been established whether the oxide generated by the CAE treatment is intrinsically stronger, or whether there is improved wetting and intrinsic adhesion[6]. However, the durability of specimens using the CAE treatment is certainly better, i.e. the value of G_{th} is larger than using the GB&DG treatment. It may be that the adhesive is able to establish bonds that are more stable than the van der Waals forces, and hence are more resistant to environmental attack, as with some primers[6], or to establish more of them. Alternatively, the oxide layer formed after GB&DG treatment may be less stable, and thus failure can occur more easily through the oxide formed after the GB&DG treatment, resulting in a reduction in the measured value of G_{th}.

The steel specimens bonded using the 'AV119' adhesive do not exhibit corrosion in areas well ahead of the crack tip, thus indicating that water entering from the edge of the joint is not the governing factor. The action of opening and closing the joint may pump water into the crack tip. Thus the water is initially only a short distance from the interface. Once water has access to the interface here it can permeate along the interface, and weaken this region just ahead of the crack tip. This may account for the discoloration seen ahead of the crack tip on some 'AV119'/steel specimens.

8.7 Conclusions

A fracture mechanics approach has been used successfully to evaluate the durability performance of two adhesives, using both aluminium-alloy and steel adherends. This approach was a quantitative one, and hence the data obtained may be used to predict the lifetime of bonded joints, as discussed in Chapter 9. The tapered double-cantilever beam (TDCB) specimen geometry was used for these tests.

The constant displacement rate tests using the 'AV119' adhesive to bond the chromic-acid etched (CAE) aluminium-alloy adherends gave an adhesive fracture energy, G_c, value of 700 J/m^2. Here failure was stable and cohesive-in-adhesive. Stick/slip failure was observed for the 'AV119' adhesive using steel and gritblasted and degreased (GB&DG) aluminium-alloy adherends. Fracture energies of 450 and 520 J/m^2 respectively were measured. In these cases failure was apparently interfacial. A fracture energy of 4590 J/m^2 was measured for the 'LMD1142' using CAE aluminium-alloy adherends. Failure was stable and cohesive-in-adhesive These data are summarised in Table 8.9.

The results of fatigue tests using the TDCB specimens are also summarised in Table 8.9. These fatigue tests have shown that for both adhesives, and all the surface treatments, there is a threshold value of the fracture energy, G_{th}. This is where the crack growth rate becomes vanishingly small, of the order of 0.01 mm in a million cycles. The value of this threshold depends on both the adhesive and the adherend/surface treatment combination used, as apparently interfacial failure can occur, especially under 'wet' conditions, i.e. water immersion at 28°C.

Fatigue testing of the 'AV119' adhesive under 'dry' conditions, 23°C and approximately 55 % relative humidity, gave a threshold fracture energy, G_{th}, of 160 J/m^2 using CAE aluminium-alloy adherends. Here failure was in a cohesive-in-adhesive manner and through the centre of the adhesive layer. The specimens that used the steel or GB&DG aluminium-alloy adherends gave a G_{th} value of 85 J/m^2, and failure occurred close to the interface. The lower fracture energy associated with this locus of failure is expected as the

plastic zone size is restricted by the presence of the adherend. Further, the value is approximately half that measured when cohesive-in-adhesive failure occurs, as would be expected if the plastic zone was approximately half the size due to the presence of the adherend.

Scanning electron microscopy of the fracture surfaces of the 'LMD1142' adhesive after constant displacement rate and 'dry' fatigue testing showed that the locus of failure was cohesive-in-adhesive in both cases. The fracture surfaces of the specimens tested at a constant displacement rate of 10^{-5} m/s showed large numbers of cavitated rubber particles. However, there were few cavitated rubber particles present on the fracture surfaces after fatigue testing. Thus the reduction in fracture energy, from 4590 J/m^2 at a constant displacement rate to a threshold value of 510 J/m^2 in 'dry' fatigue, is due to the reduction in the amount of rubber particle cavitation, and hence of the energy absorbed during fracture, under fatigue loading. Similarly, a reduction in the amount of rubber particle cavitation under fatigue loading was observed using the 'AV119' adhesive, compared with tests at a constant displacement rate.

The 'wet' fatigue testing caused a reduction in the measured threshold fracture energy value in most cases. The exception was the specimens using the 'AV119' adhesive to bond chromic-acid etched aluminium-alloy adherends, where the value of G_{th} was unaffected, and actually increased slightly from 160 to 175 J/m^2, see Table 8.9. The locus of failure for all the 'wet' tests using the 'AV119' adhesive was through the metal oxide, although some residual adhesive was present on the fracture surfaces. The threshold value for the GB&DG surface treatment using both the aluminium-alloy and steel adherends was also reduced, from 85 J/m^2 in both cases under 'dry' conditions to 25 and 20 J/m^2 respectively under 'wet' conditions. It is thought that a combination of adhesive displacement from the interface and weakening of the oxide by the presence of water causes the reductions in performance.

The value of G_{th} for the 'LMD1142' adhesive was reduced from 510 J/m^2 to 290 J/m^2 by the 'wet' environment, as shown in Table 8.9. However, these values are both considerably lower than the G_c value measured at a constant displacement rate of 4590 J/m^2.

The 'AV119' adhesive shows better durability than the 'LMD1142' adhesive (using the CAE treated aluminium-alloy adherends) if the G_{th} values are expressed as a proportion of the constant displacement rate, G_c, value. For 'AV119' both the 'dry' and 'wet' G_{th} values are approximately 0.25 of G_c. However, the G_{th} values for the 'LMD1142' are 0.11 and 0.06 of G_c respectively. Thus, on this comparative basis, the adhesive with the lower G_c value, and the poor impact performance exhibits the better durability. The specimens

using the CAE surface treatment exhibited better durability than those using the GB&DG treatment. This may be due to improved wetting or the greater stability of the oxide produced by the CAE treatment.

Table 8.9: Summary of constant displacement rate and fatigue test data from TDCB tests, with apparent locus of failure from microscopy and surface chemical analysis, (a) 'AV119' adhesive, and (b) 'LMD1142' adhesive.

a) 'AV119' adhesive.

Adherend & surface treatment	Constant rate fracture energy, G_c, J/m^2	Threshold fracture energy, G_{th}, J/m^2		G_{th} / G_c,	
		'Dry'	'Wet'	'Dry'	'Wet'
CAE aluminium-alloy	700 C	160 C	175 O	0.23	0.25
GB&DG aluminium-alloy	520 I	85 I	25 O	0.16	0.05
GB&DG steel	450 I	85 I	20 O	0.19	0.04

b) 'LMD1142' adhesive.

Adherend & surface treatment	Constant rate fracture energy, G_c, J/m^2	Threshold fracture energy, G_{th}, J/m^2		G_{th} / G_c,	
		'Dry'	'Wet'	'Dry'	'Wet'
CAE aluminium-alloy	4590 C	510 C	290 I	0.11	0.06

Note:

Failure loci:

C Cohesive-in-adhesive.

I Close to interface.

O Oxide.

Chapter Nine

Lifetime Prediction Studies of Bonded Joints and Components

9.1 Introduction

The aim of any durability testing is to define a safe working envelope of conditions within which the performance of a component is predictable. The durability data obtained in the previous Chapter provides a 'fail-safe' limit, i.e. the value of G_{th}, below which fatigue crack growth does not occur. However, to keep below this limit requires that the joint is only lightly loaded. It is more efficient to operate at higher applied loads, but to do so requires that the joint will not fail during its working life. Thus it would be beneficial to be able to predict the lifetime of an adhesive joint at any given load. This would allow a safe working load to be specified, to obtain the required working life without failure occurring. The present Chapter uses the fracture mechanics durability data obtained in Chapter 8 to estimate the lifetimes of simple, though realistic, bonded joints and components. These predictions are compared with experimental results.

9.2 Bonded Joints

9.2.1 Introduction

The single lap joint, as shown in Figure 9.1, is a very common joint design. It is the simplest way to bond two thin sheet adherends, and the most frequently used joint design in industry. Hence, as discussed in Section 2.9, this test geometry is often used to compare the performance of adhesive joints under fatigue loading[65, 105, 157]. This Section describes constant displacement rate and fatigue tests using single lap joints which consisted of steel adherends bonded using the 'AV119' adhesive. The fatigue tests were performed 'wet', with the joints immersed in water at 28°C. A backface strain technique was also used to investigate whether the fatigue life of the lap joints was dominated by the initiation or the propagation of cracks.

An analytical and a finite element model were used to describe the variation of the maximum applied fracture energy, G_{max}, with crack length in the lap joint. This information, combined with the fracture mechanics data obtained in Chapter 8, allowed a prediction of the joint life to be made. These lifetime prediction models will be discussed in Section 9.2.5. Comparisons will be made between the predicted values and the

experimental results. The sensitivity of the predictions to the boundary conditions used, for example the initial flaw size, will also be discussed.

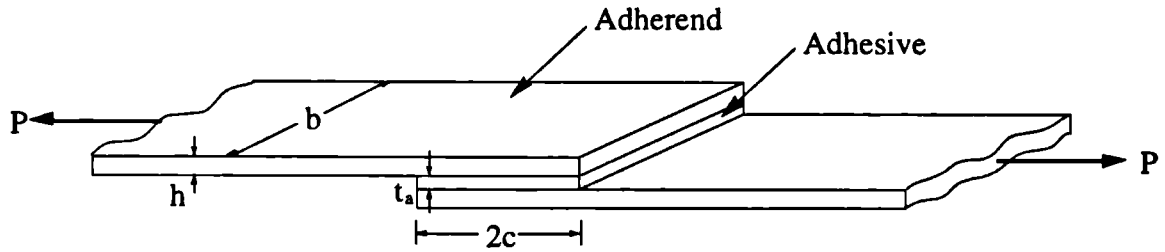


Figure 9.1: The single lap joint geometry used for the lifetime prediction studies.

9.2.2 Experimental Procedure

9.2.2.1 Specimen Manufacture

The lap joint specimens were made according to the method laid down in the ASTM Standard[158]. Sheets of 2 mm thick steel were milled to size, approximately 250 by 100 mm. The areas to be bonded were gritblasted and degreased, as described in Section 3.4. The adhesive was applied and spread to approximately 15 mm from one edge of each sheet. Short lengths of stainless steel wire, 0.4 mm in diameter, were placed at either end and in the middle of this strip to give a constant adhesive layer thickness. Pairs of sheets were placed in a jig to ensure that they were parallel, with an overlap length of 12.7 mm. Pressure was applied using an aluminium bar and 2 kg masses. The excess adhesive that squeezed out of the adhesive layer was allowed to form a natural fillet at the end of the overlap. The joints were cured at 120°C for 2 hours.

After curing, the sheets were cut into 25.4 mm wide specimens, discarding the edge and centre sections containing the wire spacers. Eight specimens were cut from each sheet. The width of the bonded region and the overlap length of each lap joint specimen were measured, and the bonded area calculated.

9.2.2.2 Constant Displacement Rate Tests

Specimens were tested in tension using a screw-driven 'Instron' testing machine. The grips were attached to the testing machine using universal joints to eliminate any misalignment. A grip separation of 140 mm was used, as recommended by the ASTM Standard[158]. Spacers, 2.4 mm thick, were used in the grips to ensure that the arms of the joint were parallel to the loading direction. The tests were conducted at a constant crosshead rate of

0.5 mm/min (10^{-5} m/s). The maximum load was recorded, and the nominal failure stress calculated by dividing the load by the bonded area. Two specimens were tested from each sheet.

9.2.2.3 Fatigue Tests

Joints were tested using a 'Mand' servo-hydraulic testing machine, using the same grips as for the constant displacement rate testing. Tests were conducted under load control using a load ratio (P_{min}/P_{max}) of 0.5, with a sinusoidal loading waveform. Maximum nominal stresses from 30 to 90 % of the average value obtained from the constant displacement rate tests were applied. The numbers of cycles to failure were recorded.

Tests were conducted 'wet', with the joint immersed in distilled water. A small tank was used, see Figure 9.2, with a tapered silicone rubber bung which, when compressed, sealed around one arm of the specimen. The tank rested on the lower grip of the testing machine. The water circulator heaters used for the TDCB tests gave too high a flow rate for this tank, so a peristaltic pump was used to circulate water into the tank, with a gravity-fed return to the reservoir, as shown in Figure 9.3. This enabled a constant 28°C water temperature to be maintained around the lap joint.

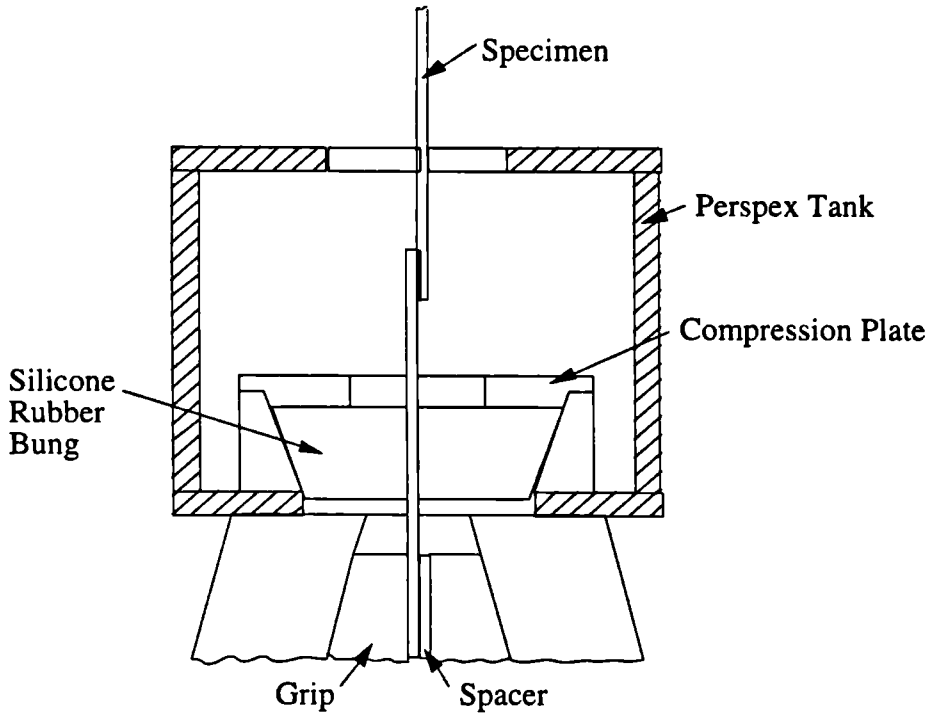


Figure 9.2: Water tank used for lap joint tests.

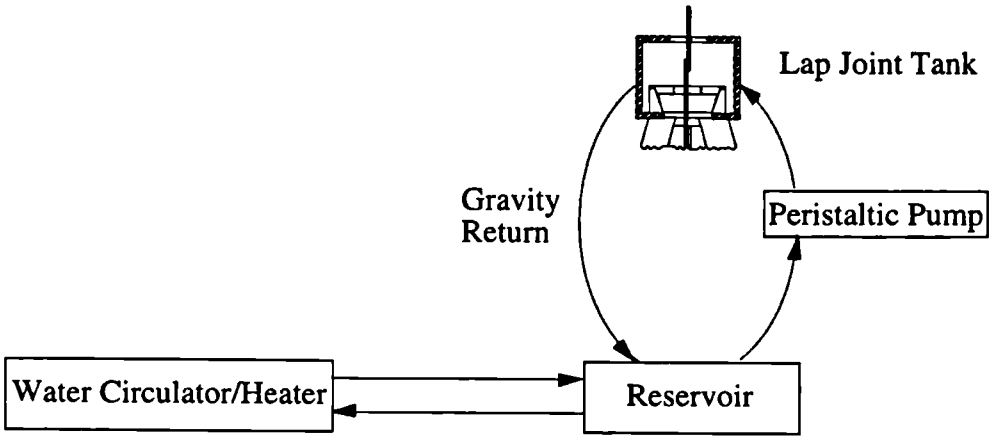


Figure 9.3: Schematic of water circulation system for lap joint tests.

9.2.3 Experimental Results

9.2.3.1 Constant Displacement Rate Tests

The force versus displacement response of a typical lap joint specimen is shown in Figure 9.4. The response was approximately linear, with 'pop-ins' towards the end of the test when the adhesive fillet began to crack. The deviation from linearity prior to failure was caused by plastic deformation of the specimen. The tests gave a mean nominal failure stress of 24 MN/m^2, with a standard deviation of 2.3 MN/m^2. Failure loads were in the order of 7700 N, equivalent to a load per unit width of 305 kN/m. These data are given in full in Appendix 6.

When examined visually, the locus of failure was apparently interfacial, see Figure 9.5. In general, the adhesive remained on the joint overlap. Areas of adhesive that had failed close to both interfaces were present, i.e. leaving a flap of adhesive that was detached from both adherends, as shown in Figure 9.5 as area '4' on the 'metal' side of the joint. This indicates that failure was by the growth of cracks from both ends of the overlap.

However, SEM of the fracture surfaces showed that fracture occurs close to the interface. Some residual adhesive is visible on the areas of apparently interfacial failure, with cavitated rubber particles present, see Figure 9.6a. Where a thick layer of adhesive is visible optically, the SEM also identifies adhesive and cavitated rubber particles, as shown in Figure 9.6b.

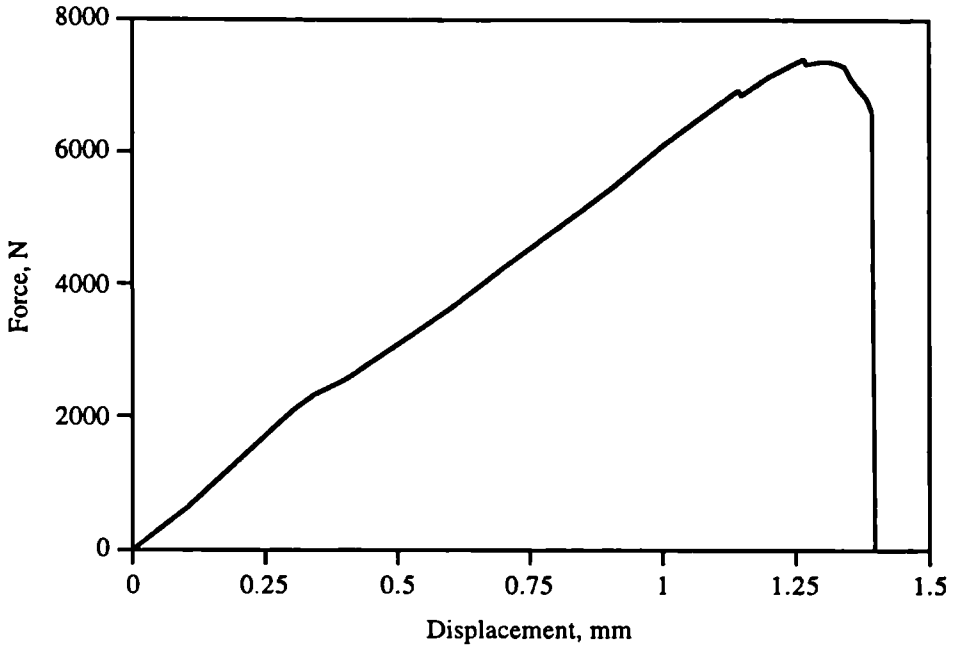
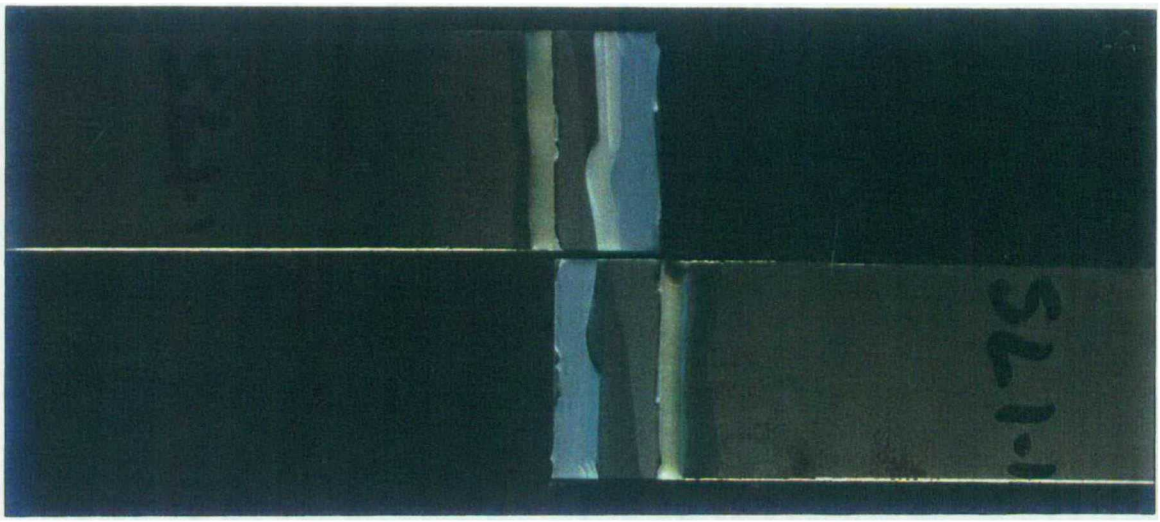
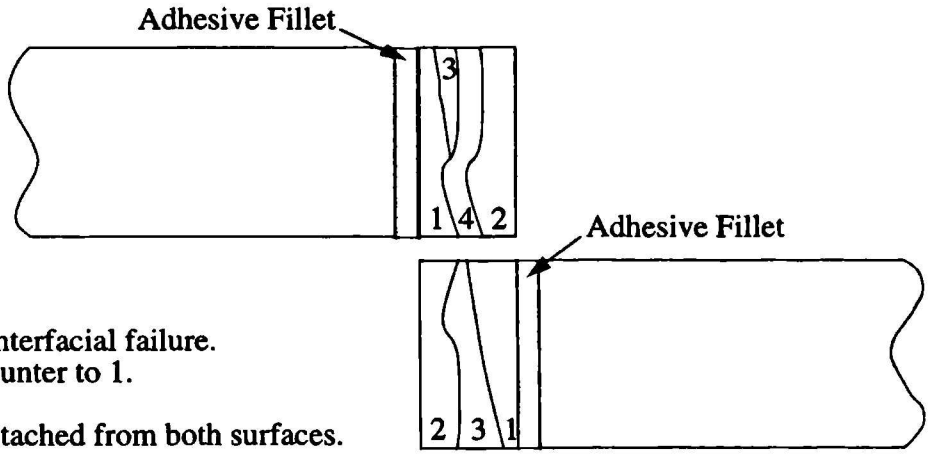


Figure 9.4: Force versus displacement response of steel lap joint specimen bonded with 'AV119' adhesive, constant displacement rate test at 0.5 mm/min. Response is approximately linear until onset of plastic deformation.



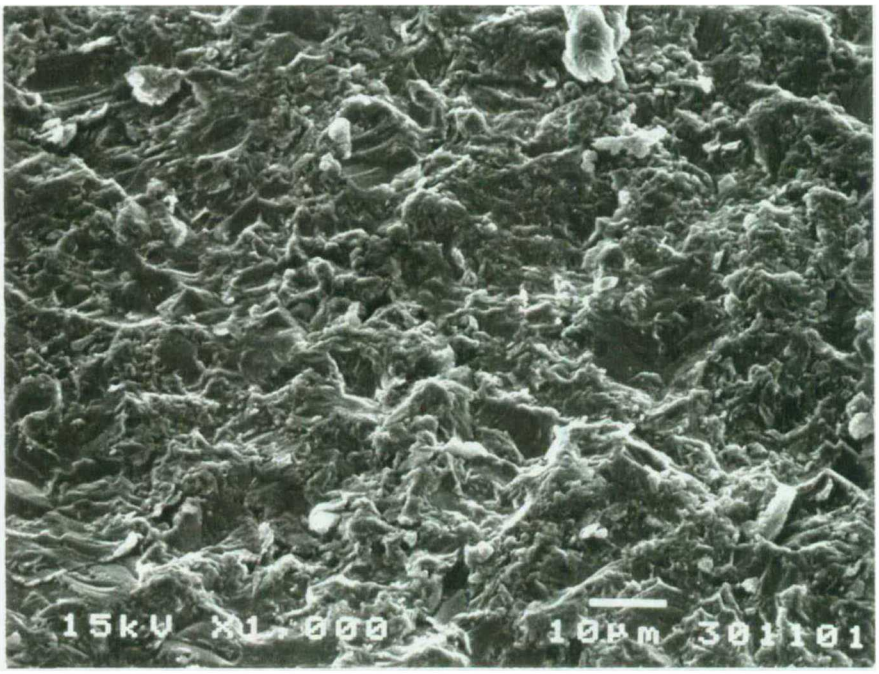
(a) Photograph of fracture surfaces.



Key:
1. Apparently interfacial failure.
2. Adhesive, counter to 1.
3. Adhesive.
4. Adhesive, detached from both surfaces.

(b) Schematic identification of areas of fracture surface.

Figure 9.5: Fracture surfaces of 'AV119'/steel lap joint specimen after constant displacement rate testing, (a) photograph of fracture surfaces, (b) schematic identification of areas of fracture surface.



(a) Apparently interfacial failure.



(b) Adhesive, counterface to (a).

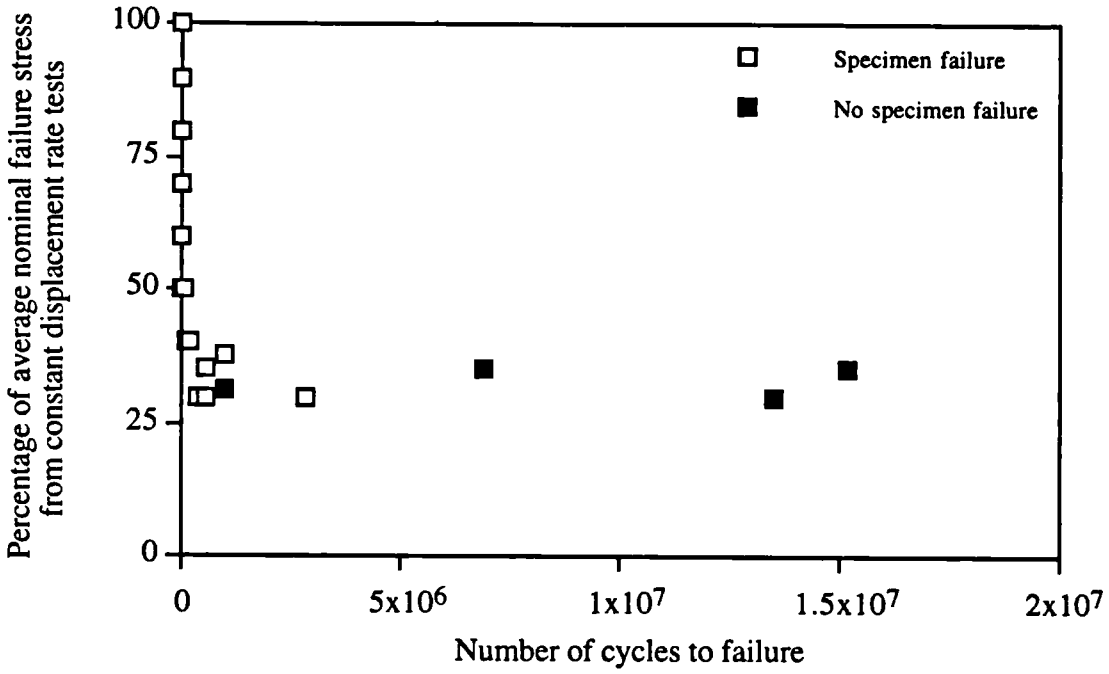
Figure 9.6: Scanning electron micrographs of fracture surface of lap joint tested at constant displacement rate, (a) apparently interfacial failure, (b) adhesive, counterface to (a).

9.2.3.2 Fatigue Tests

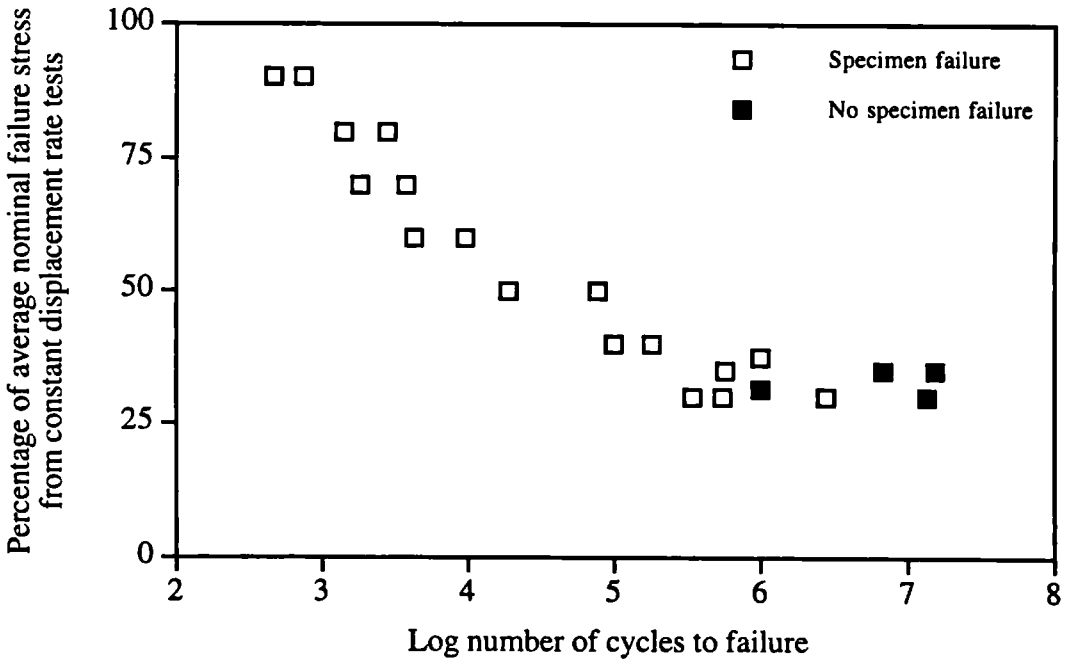
The results from the single lap joint 'wet' fatigue tests are shown in Figure 9.7. The nominal stress applied to the joint, expressed as a percentage of that measured using the constant displacement rate tests, is plotted against the measured number of cycles to failure. These data are listed in full in Appendix 6. At high stress levels the joint life is short. Even at 60 % of the nominal failure stress measured using the constant displacement rate tests, the joint life is less than 10000 cycles. This is equivalent to half an hour of testing at a frequency of 5 Hz. Joint lives of longer than 24 hours are seen at below 35 % of the nominal failure stress. Joint life increases rapidly at around 30 % of the nominal failure stress, where it could exceed 1.5×10^7 cycles, equivalent to a month at 5 Hz, without failure occurring. This is evidence of an effective fatigue threshold, below which failure does not occur, as indicated by previous work[65, 159].

The joints exhibited apparently interfacial failure, see Figure 9.8. Note that the joint shown in this Figure experienced a relatively short immersion time, and hence corrosion is limited. Surface analyses were performed using Auger Electron Spectroscopy (AES) and X-ray Photoelectron Spectroscopy (XPS), the results of which are shown in Table 9.1, and the analysed areas are identified in Figure 9.8. Depth profiling was used, the surface being eroded using ion bombardment to a known depth, allowing analyses to be performed at various depths below the surface. These data show surface contamination by silicon, probably due to decomposition of the silicone rubber bung used to seal around the specimen, as shown in Figure 9.2. Although no iron was detected at zero depth on the fracture surfaces, iron is detected at depths of 10 nm or less on both the 'adhesive' and 'metal' sides of the joint. This indicates that failure has occurred through the iron oxide, and it is assumed that surface contamination obscures any iron present. The same locus of failure, through the oxide, was seen using the TDCB specimens discussed in Section 8.6.3.3. As the same locus of failure is seen with both types of specimen, the TDCB fatigue data can be used to predict the lifetime of the lap joint specimens in fatigue.

The AES of the 'metal' side of the joint shows both iron and carbon at a depth of 10 nm, as does the counterface on the 'adhesive' side using both the AES and the XPS techniques. However, the more persistent presence of carbon in the depth profile of the 'dark' area shows that there is a thicker layer of residual adhesive than in the 'light' area. The increasing ratio of iron to oxygen with depth shows that the proportion of elemental iron is increasing with depth. At a depth of 20 nm there is a significant amount of elemental iron plus some oxide present.

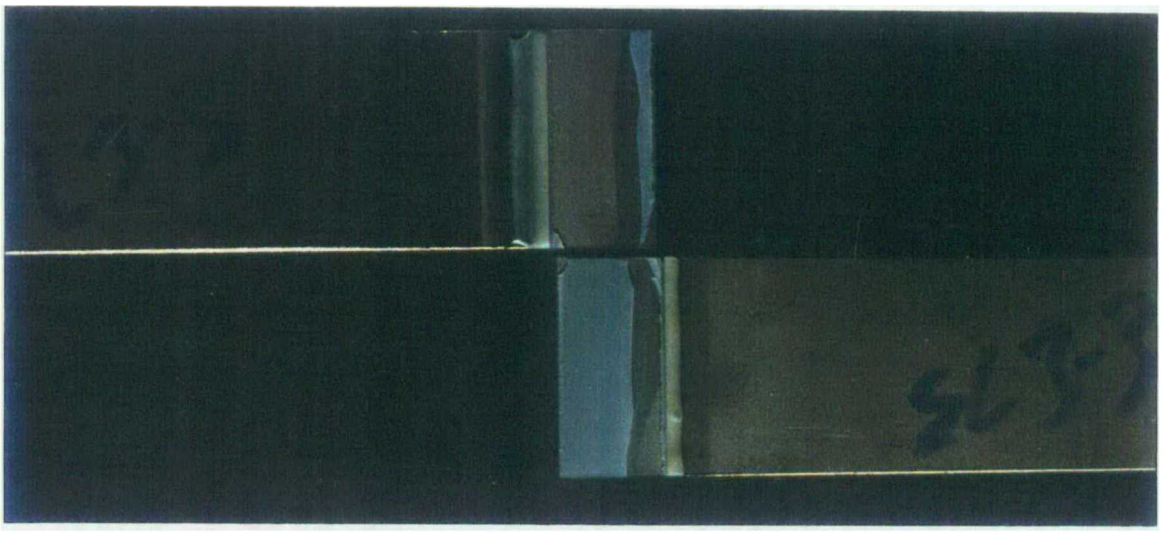


(a) Linear axis.

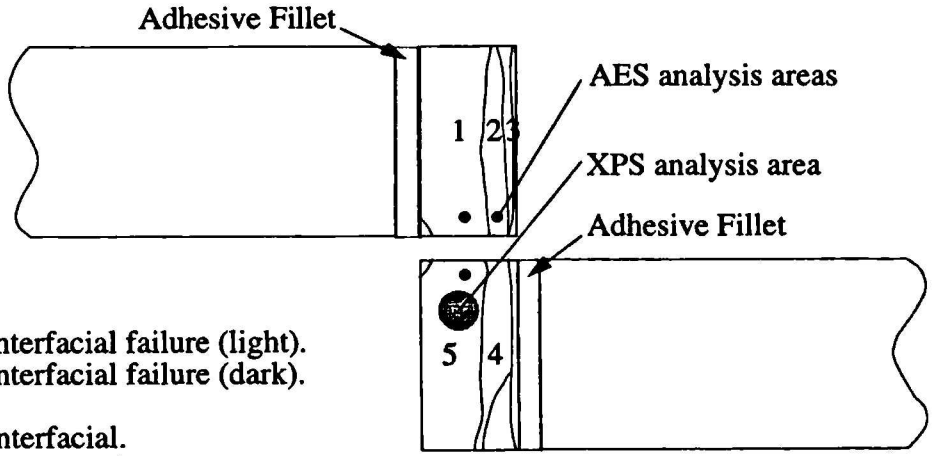


(b) Logarithmic axis.

Figure 9.7: Percentage of nominal failure stress from constant displacement rate tests versus fatigue life for 'AV119'/steel lap joints tested 'wet', (a) linear axis, (b) logarithmic axis.



(a) Photograph of fracture surfaces.



Key:
1. Apparently interfacial failure (light).
2. Apparently interfacial failure (dark).
3. Adhesive.
4. Apparently interfacial.
5. Adhesive, counter to 1.

(b) Schematic identification of areas of fracture surface.

Figure 9.8: Fracture surface of lap joint after fatigue testing, showing apparently interfacial failure, (a) photograph of fracture surfaces, (b) schematic identification of areas of fracture surface. Maximum applied stress 70 % of constant displacement rate test results. See Table 9.1 for surface chemical analysis results.

Table 9.1: Surface analysis results for 'AV119'/steel lap joint specimen tested in 'wet' fatigue at 70 % of nominal failure stress from constant displacement rate tests. See Figure 9.8 for identification of analysis areas.

a) AES analysis.

	Area	Depth, nm	Fe	Si	C	O
'Metal'	(Light)	0	0	50.1	25.4	24.5
Side	1	5	10.8	42.8	18.1	28.2
		10	26.9	31.0	12.7	29.4
		20	63.6	0	11.2	25.1
'Metal'	(Dark)	0	0	35.4	21.5	43.0
Side	2	5	0	24.5	34.6	40.9
		10	32.8	14.9	27.5	24.8
		20	35.6	3.4	40.2	20.8
		30	37.7	0	45.0	17.3
		50	44.6	0	40.0	15.4
		100	49.8	0	38.8	11.4
'Adhesive'	(Adhesive)	0	0	37.7	32.8	29.5
Side	5	10	26.7	3.1	21.6	48.6
		20	24.5	0	30.4	45.1

b) XPS analysis.

	Depth, nm	Fe	Si	C	N	O
'Adhesive'	0	0	13.7	62.2	2.5	21.6

SEM of the fracture surfaces showed some residual adhesive on area 1 of the 'metal' side, which was also detected by the AES analysis. The images obtained are shown in Figure 9.9. Adhesive was seen on the counterface to this area (area 5 on the 'adhesive' side), with cavitated rubber particles visible.

Corrosion was present on the fracture surfaces of the joints tested at lower applied stress levels, these experiencing a longer water immersion, see Figure 9.10. It is unlikely that all the corrosion occurred post-failure as the upper half of the joint was automatically removed from the water at failure by the testing machine. The lower half of the joint remained immersed. Thus any corrosion on the upper half of the joint probably occurred prior to failure. This can be seen as evidence of crack growth for a significant proportion of the fatigue life. The most severe corrosion is evident at the ends of the overlap, see Figure 9.10. This pattern of corrosion would seem to indicate that crack growth occurred from both ends of the overlap, until failure occurred when the area of adhesive remaining was insufficient to support the applied load. To investigate the pattern of crack growth further, a backface strain technique was used. This is described in Section 9.2.4 below.

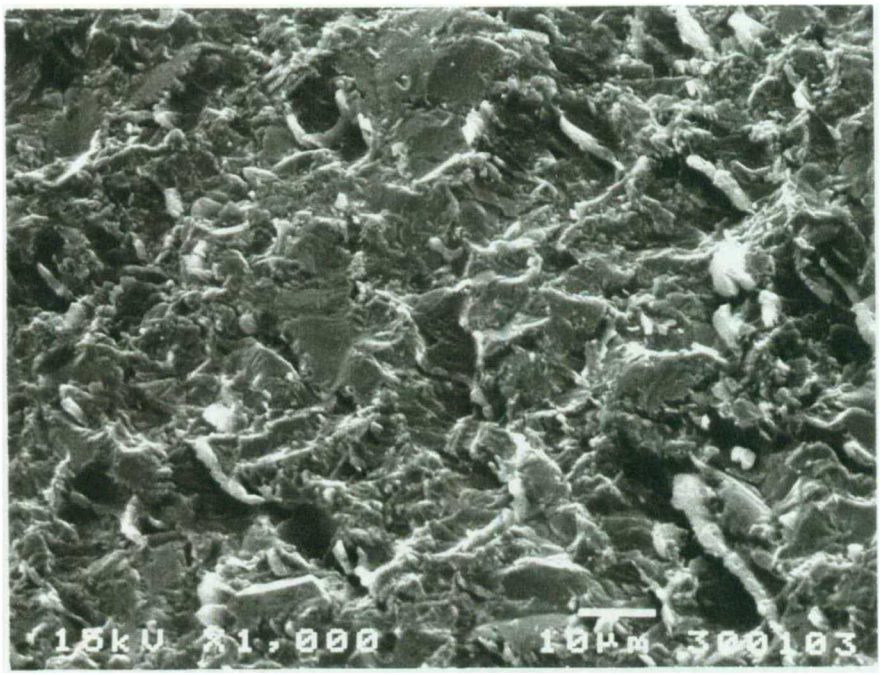
SEM showed that joints tested at lower stress levels also exhibited fracture surfaces similar to those seen in the 'wet' TDCB tests, see Figure 9.11. Again, the failure occurred through the oxide layer.

9.2.3.3 Summary of Experimental Results

Constant displacement rate testing of the single lap joints gave an average nominal failure stress of 24 MN/m^2, equivalent to 305 kN/m for an overlap length of 12.7 mm. Cyclic fatigue tests, conducted in water at 28°C showed an increasing joint life with lower applied stress levels. A threshold was identified at 30 to 35 % of the nominal failure stress measured using the constant displacement rate tests. At 30 % of the nominal failure stress, failure was not observed in some tests after 1.5×10^7 cycles. The failure locus was observed to be apparently interfacial visually, but detailed surface analysis indicated that failure occurred through the surface oxide. It is noteworthy that the same failure locus was observed using the TDCB specimens under the same conditions, as discussed in Chapter 8.



(a) 'Adhesive', area 5.



(b) 'Apparently interfacial', area 1.

Figure 9.9: Micrographs of fatigue tested single lap joint fracture surfaces, tested using a maximum applied stress of 70 % of the nominal failure stress, (a) 'adhesive', area 5, (b) 'apparently interfacial', area 1. Areas correspond to those identified in Figure 9.8.

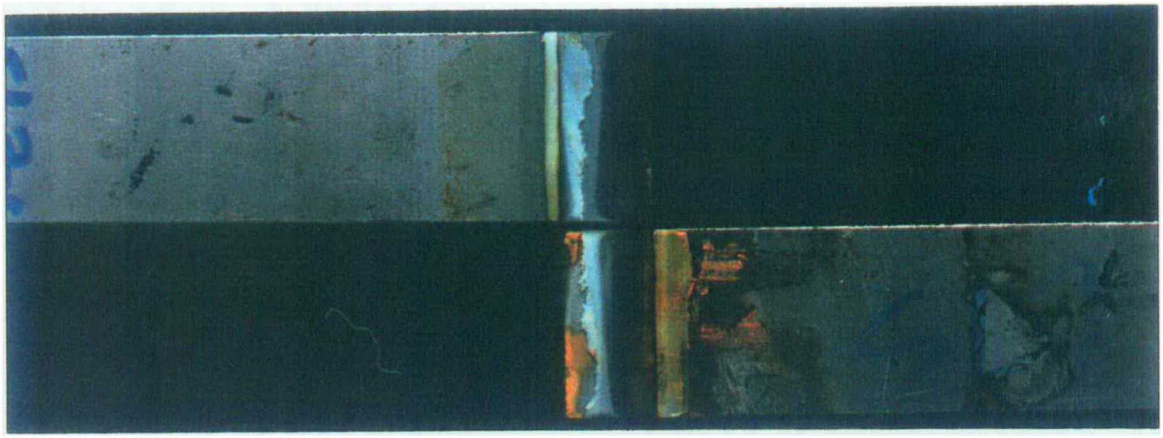


Figure 9.10: Fracture surfaces of single lap joint tested in 'wet' fatigue at 30 % of nominal failure stress. Note corrosion is more severe at ends of overlap, indicating that relatively slow crack growth occurred from both ends of the overlap.

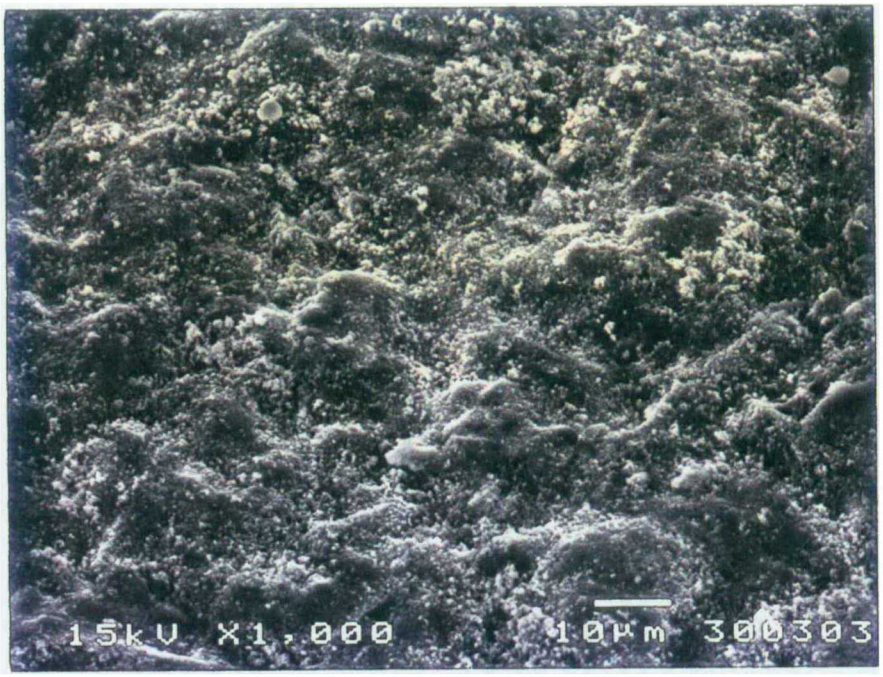


Figure 9.11: Micrograph of single lap joint subjected to 'wet' fatigue loading at 30 % of nominal failure stress. Time to failure 2.8 x 10^6 cycles, equivalent to 6.5 days.

9.2.4 Crack Detection Using a Backface Strain Technique

9.2.4.1 Introduction

Several authors have investigated the crack growth in single lap joints, and some results indicate that the fatigue life is dominated by the propagation of cracks[107, 157, 160], but other work has suggested that the time taken for crack initiation is dominant[159]. Thus it is useful to investigate which mechanism is dominant in the joints used in the present work, especially as the fracture mechanics approach used for the lifetime prediction assumes that crack propagation is dominant.

Fernando and Kinloch[107, 157] have used an ultrasonic method to investigate the crack growth. This showed that crack propagation accounts for much of the fatigue life of single lap joints. However, this method has its drawbacks as the fatigue test must be stopped, and the joint removed, to allow the ultrasonics to be used. An alternative method is the 'backface strain' technique. This technique uses strain gauges bonded to the backface of the specimen, opposite the ends of the overlap. Work by Zhang et al[160] using this method on single lap joints has shown that crack growth accounts for between 40 and 70 % of the fatigue life. This method allows crack propagation to be monitored continuously, and thus the fatigue test does not need to be interrupted. Further, the onset of crack growth may be identified more readily than by using an ultrasonic method, due to the poor resolution at the edges of the sample using the ultrasonic method. Thus the present work will use the backface strain technique to investigate the crack growth in the lap joint specimens.

The backface strain work by Zhang et al[160] and Imanaka et al[161] has used strain gauges bonded on the backface of the specimen, opposite the ends of the overlap, as shown in Figure 9.12a. Loading the specimen puts both gauges into compression, see Figure 9.12b, although softening of the adhesive may cause the backface strain to become less compressive. When a crack starts to grow from one end of the overlap the local deformation relaxes, and the compression on one gauge is decreased, but increased on the other, see Figure 9.12c. Crack growth from the other end of the overlap will cause a compression decrease in both gauges, as shown in Figure 9.12d.

Imanaka et al[161] and Zhang et al[160] positioned the gauges centrally above the end of the overlap. The authors reported that the best results are obtained when the gauges are as small as possible, as a crack can be detected when it is half as long as the gauge. The gauges used in the current work had a grid size of 1.57 mm square. Thus, according to Zhang et al[160] the crack will be detected when it is approximately 0.8 mm long.

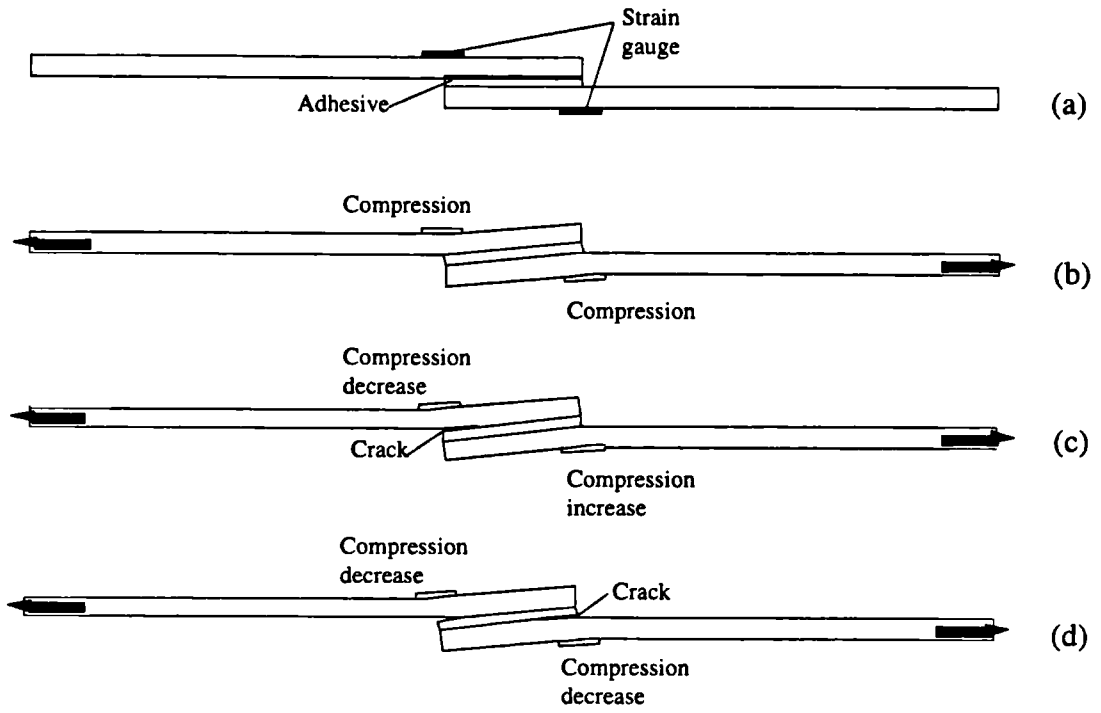


Figure 9.12: The backface strain technique for the detection of crack growth in bonded single lap joints, showing the effect of crack growth on the measured strain, (a) original arrangement, (b) loading applied, (c) crack growth from one end, and (d) crack growth from other end.

9.2.4.2 Experimental Procedure

Strain gauges were attached to the specimens using the same bonding procedure as used for the crack propagation gauges, see Section 8.4.2 above. They were positioned centrally over the ends of the overlap. The gauges were connected to an amplifier, and all the wires and connections sealed with polyurethane varnish or silicone rubber, to prevent the water immersion from causing a short circuit. However, even though the electrical components were thoroughly waterproofed, water frequently short-circuited the connections. In some cases re-coating the connections with varnish cured the short-circuit. However, this was often unsuccessful, and backface strain data could not be obtained from both gauges for the full lifetime of some of the specimens.

The signal from the gauges was sampled by computer, via the 'MacLab' data acquisition system described in Chapter 8. The load and displacement outputs from the testing machine were also recorded. A one second sample of data was taken every minute. This produced large amounts of data, but the high sampling frequency was required as the measured strain could increase rapidly near final failure.

The data were analysed to provide values of maximum load and maximum compressive strain against the number of cycles.

9.2.4.3 Backface Strain Results

The backface strain technique has shown crack growth for much of the fatigue life of the single lap joints, see Table 9.2. These data show that in many cases crack growth was first detected at less than 1 % of the joint lifetime. In all the tests, crack growth from at least one end of the joint was detected at less than 25 % of the joint lifetime. Thus at least 75 % of the joint life is associated with the propagation of cracks, rather than their initiation.

Some typical results are shown in Figures 9.13 and 9.14. Some gaps occur between the groups of data points in Figure 9.13 when the data acquisition system stopped recording and had to be re-started.

The test data shown in Figure 9.13 illustrates the effect of crack growth on the measured backface strain. Initially the strain is compressive, but decreases, i.e. becomes more tensile, as plasticisation due to water uptake softens the adhesive. A crack is detected at one end of the joint after about 3.5×10^6 cycles, when the compressive strain from gauge B increases. Further crack growth is indicated by the continued increase in the compressive strain measured by gauge B while the strain in gauge A decreases. Thus, there has been crack growth for over 75 % of the joint life, perhaps more as the joint had not failed when the test was stopped after 1.4×10^7 cycles.

The data from another test are shown in Figure 9.14. Here crack growth is detected at one end of the joint by backface gauge B after only 3×10^3 cycles. Crack growth from the other end of the joint is detected after 5×10^4 cycles, when the compressive strain decreases. Crack growth continues until joint failure occurs after approximately 3.5×10^5 cycles. Hence crack growth is detected from one end of the joint for over 99 % of the joint lifetime, and from both ends for over 85 % of the lifetime.

It is possible to detect crack growth from both ends of the joint even if one backface strain gauge fails, see Figure 9.15. Crack growth from one end of the joint is detected after 2.5×10^3 cycles, as indicated by the sharp increase in compressive strain. A crack is detected at the other end of the overlap after 7.5×10^4 cycles, when the strain decreases.

Table 9.2: Summary of backface strain results, showing percentages of joint life after which cracks were detected in the joints. 'Wet' fatigue of steel lap joints bonded with 'AV119' adhesive.

Joint number	Figure	Nominal stress, %	Cycles to failure	Crack growth detected after One crack Cycles	One crack %	Two cracks Cycles	Two cracks %
SL1-3	9.14	30	$3.5x10^5$	$3.0x10^3$	**1.0**	$5.0x10^4$	**14**
SL1-6		40	$1.0x10^5$	$5.0x10^2$	**0.5**	$5.8x10^3$	**6**
SL2-5	9.15	35	$5.8x10^5$	$2.5x10^3$	**0.5**	$7.5x10^4$	**13**
SL3-6		30	$2.8x10^6$	$1.0x10^4$	**0.5**	$3.7x10^4$	**1**
SL4-3	9.13	30	$>1.4x10^7$	$3.5x10^6$	**<25**	N/A	**-**

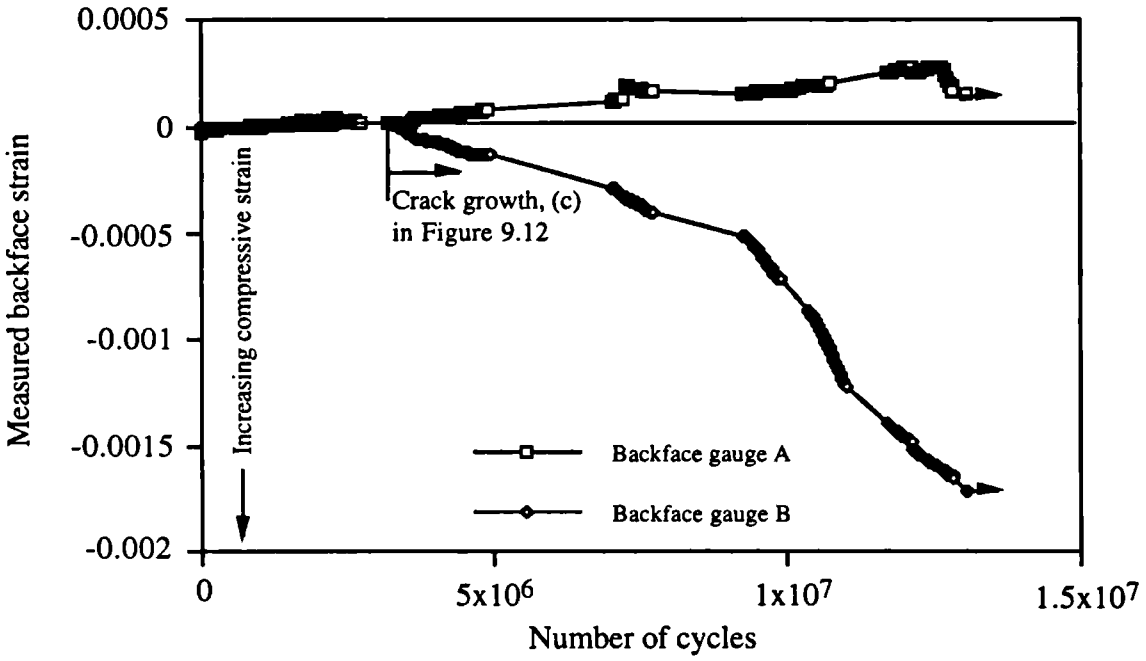


Figure 9.13: Backface strain versus number of cycles for lap joint. Crack growth is identified after 3.5 x 10^6 cycles, but at 1.4 x 10^7 cycles joint failure has not yet occurred. Steel lap joint bonded with 'AV119' adhesive, tested at 30 % of average nominal failure stress from constant displacement rate tests.

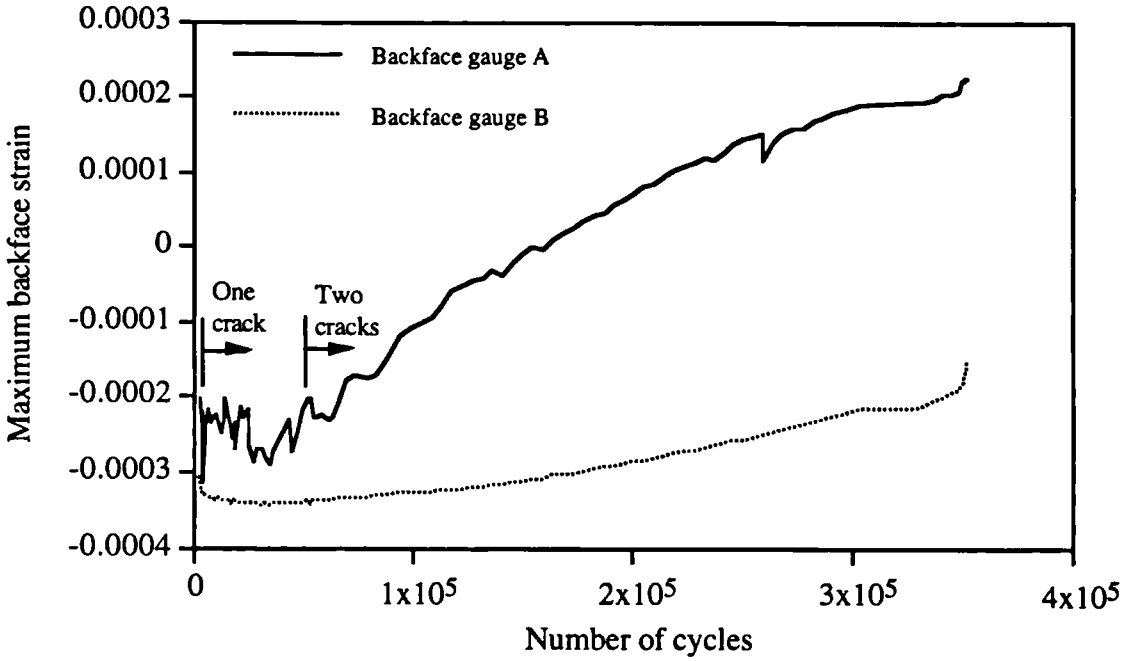


Figure 9.14: Backface strain versus number of cycles, specimen SL1-3. Steel single lap joint bonded with 'AV119' adhesive, tested at 30 % of average nominal failure stress from constant displacement rate tests. Joint failure occurred after 3.5×10^5 cycles.

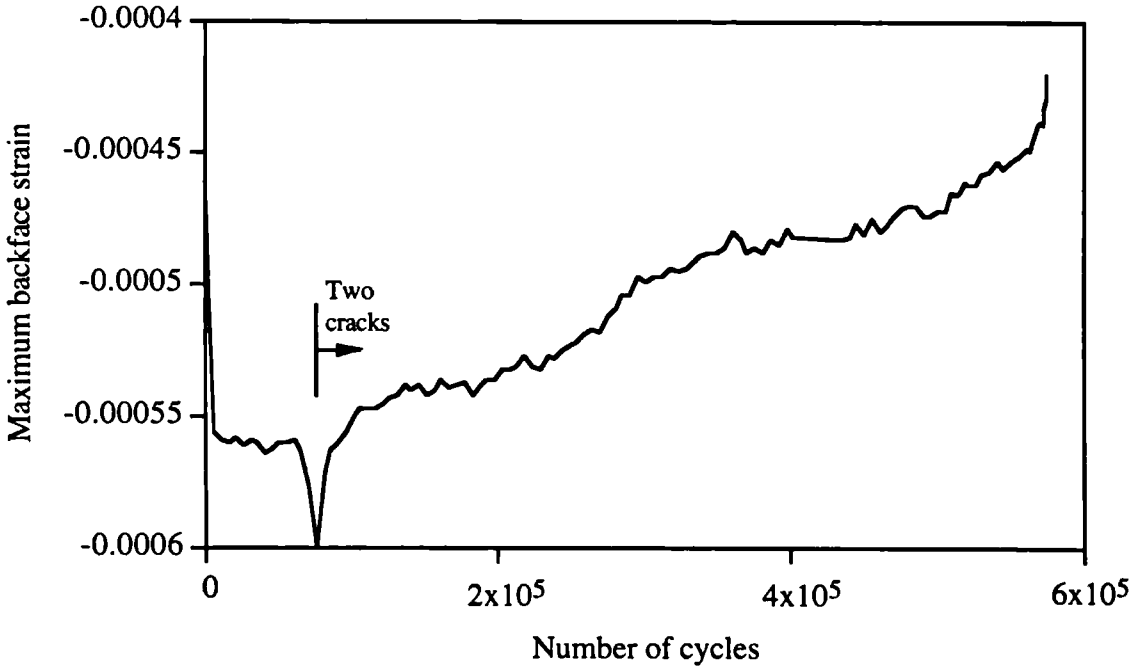


Figure 9.15: Backface strain versus number of cycles, specimen SL2-5. Steel single lap joint bonded with 'AV119' adhesive, tested at 35 % of average nominal failure stress from constant displacement rate tests. Joint failure occurred after 5.8×10^5 cycles.

In summary, the backface strain results from the 'AV119'/steel lap joints discussed in the current work have shown that crack growth occurs for at least 75 % of the joint lifetime in 'wet' fatigue. In many cases crack growth was detected for almost the entire life of the joints. These data are summarised in Table 9.2. Thus the fatigue life is dominated by the propagation, rather than the initiation, of cracks.

9.2.5 Lifetime Prediction Modelling

9.2.5.1 Introduction

Published work by Kinloch & Osiyemi[107] has shown that it is possible to predict the lifetime of adhesively-bonded composite single lap joints using data from double-cantilever beam (DCB) tests. Both sets of tests were conducted 'dry' under fatigue loading by the authors. They used an analytical approach to model the variation of maximum applied fracture energy, G_{max}, with crack length in the lap joint. Thus with a knowledge of the relationship between the rate of crack growth and G_{max} from the fracture mechanics tests, the lifetime of the lap joints could be predicted. This work has subsequently been extended to adhesively-bonded aluminium specimens using data generated from 'dry' fracture mechanics tests[65, 157].

The current work will consider the lifetime prediction of adhesively-bonded steel single lap joints when tested in a 'wet' environment. In addition to the analytical method described above, a finite element method will also be used to model the variation of G_{max} with crack length in the single lap joint. These data, when combined with the crack growth rate data from the fracture mechanics (TDCB) tests discussed in Chapter 8, will allow the joint lifetimes to be predicted. The predictions will be compared with the experimental data discussed in Section 9.2.3.

9.2.5.2 Analytical Approach

The analysis used by Kinloch & Osiyemi[107] describes the variation of G_{max}, the maximum applied strain energy release rate, with crack length in a single lap joint. The TDCB fatigue data discussed in Chapter 8 gives the relationship between the crack growth rate, da/dN, and G_{max}. Hence, by substitution and integration, the lifetime of the single lap joints can be predicted.

The first step is to model how G_{max} varies with crack length for a single lap joint. It has been shown analytically that these joints fail due to transverse tensile (σ_{11}) stresses, i.e. a mode I failure[54]. The maximum value of this cleavage stress can be found using analyses by Hart-Smith[54] and Zhao et al[162]

$$\sigma_{11} = M_e\left(\frac{E_a}{2t_aX}\right)^{1/2} \tag{9.1}$$

where E_a and t_a are the modulus and thickness of the adhesive respectively. The bending stiffness, X, is given by

$$X = \frac{E_s h^3}{12(1-\upsilon^2)} \tag{9.2}$$

where E_s, h and υ are the modulus, thickness and Poisson's ratio of the adherend. The bending moment per unit width, M_e, can be found from

$$M_e = \frac{KT(h+t_a)}{2} \tag{9.3}$$

where K, the bending moment factor, is given by

$$K = \frac{1}{1+ec} \tag{9.4}$$

where c is the overlap length of the joint, and

$$e = \left(\frac{T}{X}\right)^{1/2} \tag{9.5}$$

Here T is the load per unit width applied to the joint.

The fracture energy in a cracked beam can be found from work by Williams[163], given a knowledge of the bending moments at the crack tip. For mode I this analysis gives

$$G = \frac{12M_e^2}{E_s h^3} \tag{9.6}$$

This assumes symmetrical loading of the joint.

Substituting Equation 9.3 into Equation 9.6, using Equations 9.4 and 9.5, gives an expression for G_{max}

$$G_{max} = \frac{12}{E_s h^3}\left(\frac{T_{max}(h + t_a)}{2}\right)^2\left(\frac{1}{(1+ec)^2}\right) \tag{9.7}$$

where T_{max} is the maximum load per unit width applied to the lap joint in a fatigue cycle.

Assuming that a crack will grow through the adhesive layer parallel to the loading direction, then if it grows by a length, a, from both ends of the lap joint, the effective overlap length will be reduced from 2c to (2c-2a). Substituting this into Equation 9.7 gives

$$G_{max} = \frac{12}{E_s h^3}\left(\frac{T_{max}(h + t_a)}{2}\right)^2\left(\frac{1}{(1+e[c-a])^2}\right) \tag{9.8}$$

This describes the relationship between the applied fracture energy, G_{max}, and the crack length in the lap joint.

The TDCB tests discussed in Chapter 8 give the relationship between the crack growth rate per cycle, da/dN, and G_{max}. The full sigmoidal relationship can be modelled using a modified Paris law, i.e.

$$\frac{da}{dN} = DG_{max}^{n}\left\{\frac{1-\left(\frac{G_{th}}{G_{max}}\right)^{n_1}}{1-\left(\frac{G_{max}}{G_c}\right)^{n_2}}\right\} \tag{9.9}$$

where G_{th} and G_c are the fatigue threshold and constant displacement rate fracture energies respectively. The constants D, n, n_1, and n_2 are obtained by fitting the model to the experimental data.

Combining Equations 9.8 and 9.9, eliminating G_{max}, gives an integral expression for the expected number of cycles to failure of the lap joint,

$$N_f = \int_{a_o}^{a_f} \frac{\left[E_s h^3[1+e(c-a)]^2\right]^{n-n_2}}{DG_c^{n_2}\left[3\left[T_{max}(h+t_a)\right]^2\right]^{n-n_1}} \cdot \left[\frac{\left[G_c E_s h^3[1+e(c-a)]^2\right]^{n_2} - \left[3\left[T_{max}(h+t_a)\right]^2\right]^{n_2}}{\left[3\left[T_{max}(h+t_a)\right]^2\right]^{n_1} - \left[G_{th}E_s h^3[1+e(c-a)]^2\right]^{n_1}}\right] \tag{9.10}$$

The integration limits are the initial flaw size, a_o, and the final crack length, a_f, where rapid crack growth and failure occurs.

From the TDCB testing, the values of D, n, n_1, n_2, G_{th} and G_c are known. The geometry of the lap joint and the material properties of the adherends give e, h, t_a, c and E_s. Thus if expressions for a_o and a_f can be found, then we can predict N_f for a given maximum load per unit width, T_{max}.

Fracture mechanics methods can be used to find a_o, from the Griffith Equation[39],

$$a_o = \frac{E_a G_c}{\pi \sigma_a^2} \tag{9.11}$$

where σ_a is the tensile strength of the adhesive. For the 'AV119' adhesive used in the current work, a_o = 85 μm. The values of E_a, G_c, and σ_a are given in Section 9.2.5.4 (Table 9.4) with all the other data required for the analytical and finite element methods.

Rearranging Equation 9.8, putting G_{max} equal to G_c, gives the crack length at failure. This is a_f, and

$$a_f = c - \frac{1}{e}\left[\left(\frac{3\left(T_{max}[h+t_a]\right)^2}{E_s h^3 G_c}\right)^{1/2} - 1\right] \tag{9.12}$$

(As cracks are assumed to grow equally from both ends of the joint, a_f c.)

Thus we now have an analytical expression to predict the number of cycles to failure of a single lap joint in terms of the fracture mechanics data, the material properties and the joint geometry, i.e.

$$N_f = \int_{a_o}^{a_f} \frac{\left[E_s h^3 [1+e(c-a)]^2\right]^{n-n_2}}{D G_c^{n_2}\left[3[T_{max}(h+t_a)]^2\right]^{n-n_1}} \cdot \left[\frac{\left[G_c E_s h^3 [1+e(c-a)]^2\right]^{n_2} - \left[3[T_{max}(h+t_a)]^2\right]^{n_2}}{\left[3[T_{max}(h+t_a)]^2\right]^{n_1} - \left[G_{th} E_s h^3 [1+e(c-a)]^2\right]^{n_1}}\right]$$

where $a_o = \frac{E_a G_c}{\pi \sigma_a^2}$

and $a_f = c - \frac{1}{e}\left[\left(\frac{3\left(T_{max}[h+t_a]\right)^2}{E_s h^3 G_c}\right)^{1/2} - 1\right]$

9.2.5.3 Finite Element Approach

Lap Joint Finite Element Model

A finite element model of the single lap joint was set up using the 'ABAQUS' package, as shown in Figure 9.16. As the transverse stresses caused by Poisson's ratio strains in the adherends do not significantly affect the stresses in the direction of the applied load, the problem can be reduced to a two-dimensional one[164]. The steel adherends were modelled as an elastic-plastic material, with an elastic adhesive. The material properties used are given in Appendix 4. The model used six elements through the thickness of each adherend and four through the adhesive. A fine mesh, with an element size of 85 μm, was used for the adhesive and the overlap regions of the adherend. A coarser mesh was used for the less critical areas of the adherend, away from the overlap region, thus reducing the processing time required. The model has approximately 6000 degrees of freedom. The adhesive layer nodes were released in turn to simulate a crack propagating through the adhesive. A sample stress distribution plot is shown in Figure 9.17.

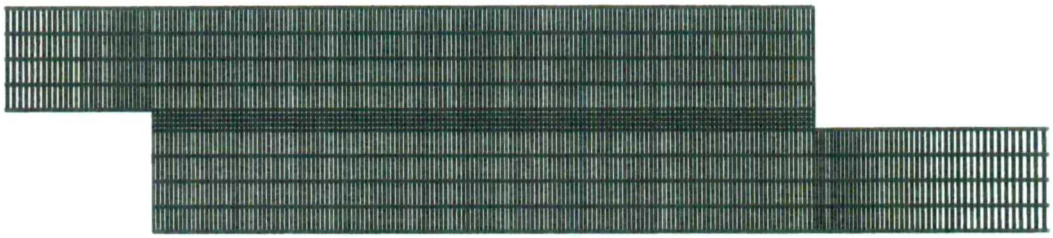


Figure 9.16: Finite element model of single lap joint, detail of joint overlap.

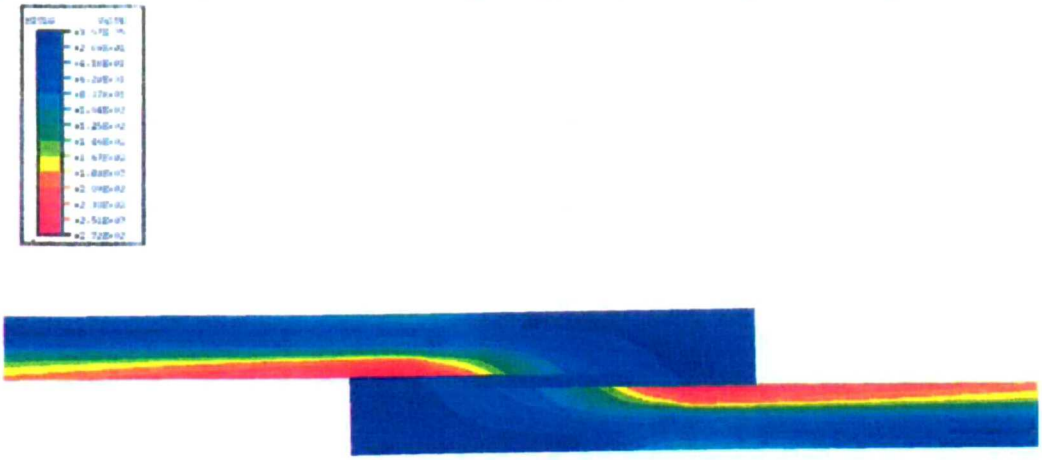


Figure 9.17: Von Mises' stress distribution in cracked lap joint. Applied load 183 kN/m, corresponding to 60 % of nominal failure stress measured using constant displacement rate tests. Crack length 2.5 mm from both ends of joint. Crack growth is cohesive-in-adhesive from both ends of joint.

The universal crack closure method, as discussed in Section 6.7.2, was used to calculate values of G_{max} for a range of crack lengths and applied loads. Each value of G_{max} was calculated by summing the mode I and mode II components of the strain energy release rate. Crack lengths between 85 μm and 5.1 mm were used. The applied loads corresponded to between 40 and 90 % of the nominal failure stress measured experimentally using the constant displacement rate tests. The variation of G_{max} with crack length at 60 % of this nominal stress is shown in Figure 9.18. Similar data calculated using the analytical approach described in Section 9.2.5.2 are also shown. The data shown in this Figure assume that failure occurs by cohesive-in-adhesive crack growth from both ends of the joint, and through the middle of the adhesive layer. These data are given in Appendix 6, for an applied load equivalent to 60% of the nominal stress measured using the constant displacement rate tests.

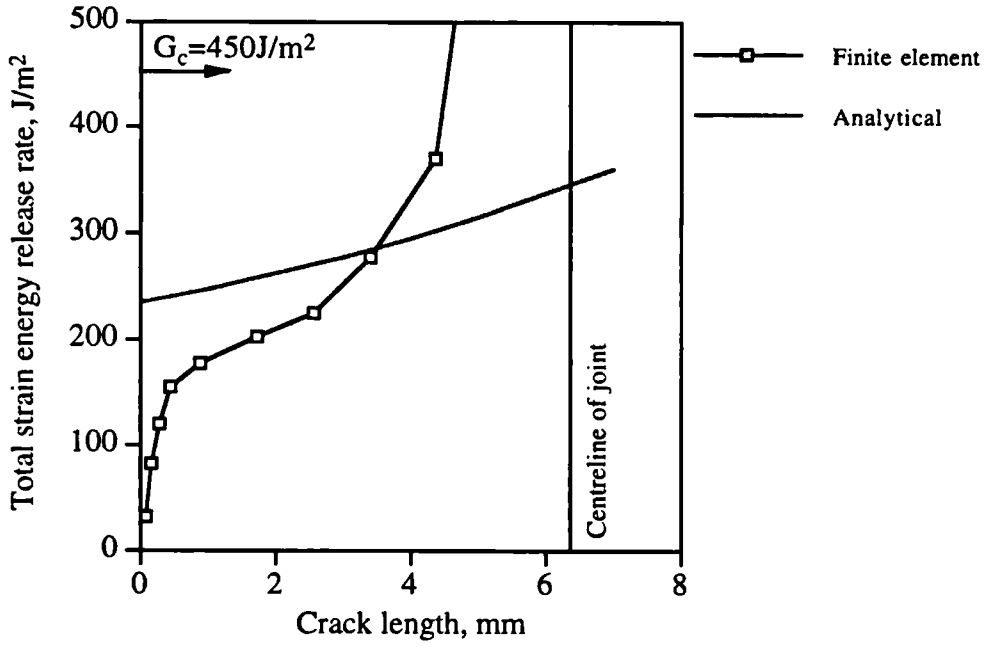


Figure 9.18: Variation of strain energy release rate with crack length for lap joint at 60 % of nominal failure stress from constant displacement rate tests. Analytical and finite element solutions are shown.

Modelling the Finite Element Model Data

The strain energy release rate is a function of both the crack length and the applied load per unit width, T_{max}. This function was formulated in two parts. First, values of T_{max} were plotted against the calculated value of G_{max}, for each crack length, see Figure 9.19. The form of the relationship between T_{max} and G_{max} is approximately linear for a given crack

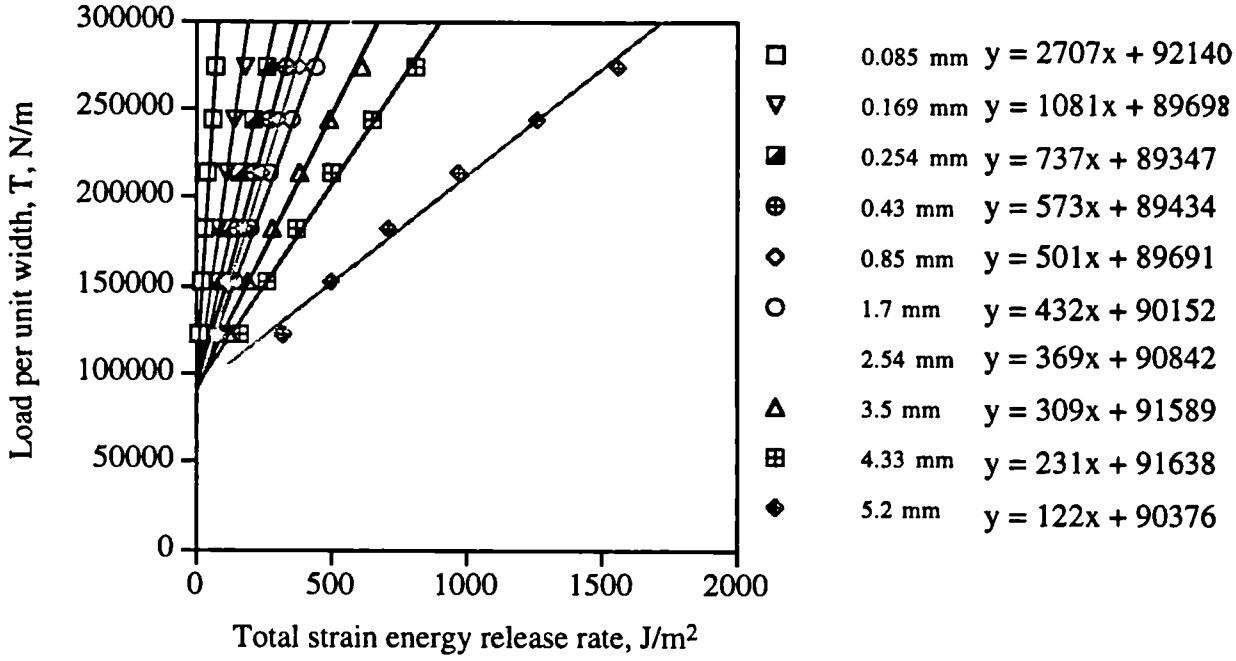


Figure 9.19: Graph of maximum load per unit width, T_{max}, versus maximum applied strain energy release rate, G_{max}, for cracked lap joint. Data from finite element model, assuming cohesive-in-adhesive crack growth from both ends of joint. Linear fits to data, $T_{max} = MG_{max} + C$, are shown.

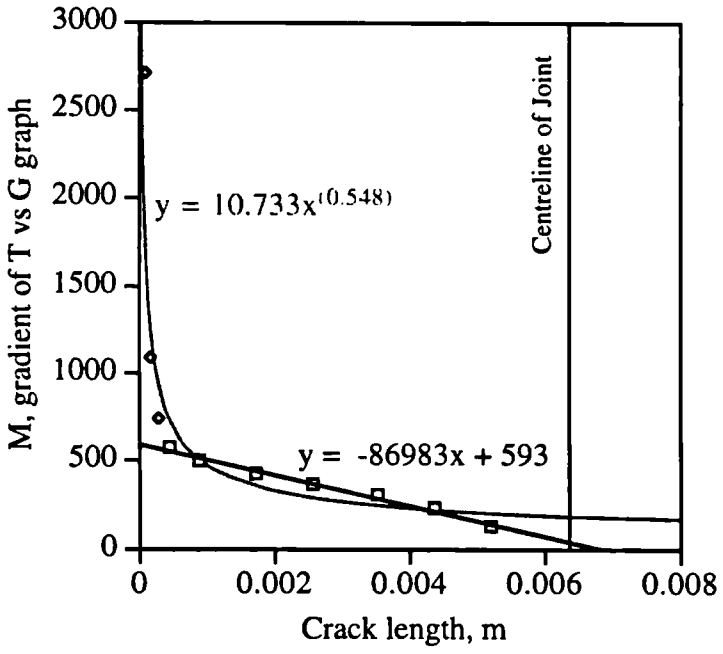


Figure 9.20: Graph of M (gradient of T_{max} versus G_{max} graph, from Figure 9.19) versus crack length, a, for cracked lap joint. Data for cohesive-in-adhesive crack growth from both ends of joint. Power law and linear fits to data are shown.

length over the range of values of interest. The intercept on the load axis is constant for the range of crack lengths used. Thus the data can be modelled as

$$T_{max} = MG_{max} + C \tag{9.13}$$

where C is a constant. The gradient of the lines, M, was then plotted against crack length, see Figure 9.20. This Figure shows that the value of M varies with crack length. The choice of the model for the T_{max} versus G_{max} data is discussed further in Chapter 12, which considers future work.

The variation of M with crack length is linear at crack lengths of greater than 0.4 mm. However, at small crack lengths the gradient of the T_{max} versus G_{max} graph increases rapidly. Thus the relationship between M and a may be modelled either linearly, neglecting the points at crack lengths of less than 0.4 mm, or with a power law. This latter method describes the whole relationship between M and a, and is of the form

$$M = p.a^r \tag{9.14}$$

where p and r are constants. The linear model is of the form

$$M = fa + k \tag{9.15}$$

where f and k are constants.

The effect of the choice of the model for the relationship between M and a will be discussed later in this Chapter. The values of the constants used in Equations 9.14 and 9.15, assuming cohesive-in-adhesive crack growth from both ends of the joint, are listed in Table 9.3 and shown in Figure 9.20. The effect of failure at the interface will be discussed in Section 9.2.7.3 as failure actually occurred through the oxide using both the lap joint and TDCB geometries. However, there was little difference between the predicted results for cohesive-in-adhesive or interfacial failure.

Rearranging Equation 9.13, the variation of G_{max} with T_{max} and crack length can be modelled as

$$G_{max} = \frac{T_{max} - C}{M} \tag{9.16}$$

where M is a function of crack length as described in Equation 9.14 or 9.15.

Table 9.3: Constants used for lap joint finite element model prediction using linear or power law fit to M versus a data. Data for cohesive-in-adhesive crack growth from both ends of the lap joint.

	Power Law	Linear
C, N/m	90500	90500
p	10.73	-
r	-0.548	-
f, m^{-1}	-	-86983
k, m	-	593

Hence, for the power law fit to the M versus a data,

$$G_{max} = \frac{T_{max} - C}{p.a^{r}} \tag{9.17}$$

Similarly, for the linear fit

$$G_{max} = \frac{T_{max} - C}{fa + k} \tag{9.18}$$

The predicted number of cycles to failure, N_f, can be calculated by inverting the expression for da/dN given in Equation 9.9, and integrating,

$$N_f = \int_{a_o}^{a_f} \frac{1}{DG_{max}^{n}} \cdot \frac{1}{\left\{ \frac{1 - \left(\frac{G_{th}}{G_{max}} \right)^{n_1}}{1 - \left(\frac{G_{max}}{G_c} \right)^{n_2}} \right\}} \cdot da \tag{9.19}$$

The integration is performed between the limits a_o and a_f, using the 'Mathcad' computer package. This splits the integral into two intervals and uses the trapezium rule to calculate N_f. Each interval is then split in half again and a new value of N_f is calculated. This process is repeated until the two subsequent values of N_f differ by less than the specified tolerance. The default tolerance used by the 'Mathcad' software is 1 x 10^{-3} cycles, though for some calculations near to the threshold this was increased to its maximum value of 1 cycle to reduce the calculation time.

A threshold value of T_{max} occurs when N_f tends to infinity, i.e. when the denominator of Equation 9.19 equals zero. This occurs when $G_{max} = G_{th}$, and can be calculated using Equation 9.17 or 9.18 for the power law and linear models respectively. Similarly, final failure occurs when $G_{max} = G_c$, thus allowing a value of a_f to be calculated using Equation 9.17 or 9.18. It is important to calculate a_f and the threshold value of T_{max} before performing the integration, as values of T_{max} below the threshold give negative numbers of cycles to failure. However, as these are simply subtracted from the positive part of the prediction, the effect may not be obvious. Hence, erroneous, though believable, lifetimes may be predicted. The same is true if the integration is performed to crack lengths greater than a_f. The value of a_o is calculated using the Griffith equation, as for the analytical approach described in Section 9.2.5.2. For the 'AV119' adhesive used in the current work, $a_o = 85$ μm.

Thus, we now have an integral expression to predict the number of cycles to failure using the finite element approach, with two expressions for G_{max}, one using a power law and one using a linear fit to the M versus a data, plus the analytical approach. However, before the values of N_f can be calculated it is necessary to model the TDCB fatigue data using the modified Paris law relationship as discussed previously.

9.2.5.4 Modelling the Fracture Mechanics Durability Data

The fatigue data from the TDCB tests relate the rate of crack growth, da/dN, to the maximum applied fracture energy, G_{max}. These data can be split into three sections, as was shown in Figure 8.2 These comprise a lower threshold section (I), where the fracture energy is denoted by G_{th}, a linear rising section (II), and the upper threshold (III), equal to G_c, as shown in Figure 9.21. Removing the threshold points, i.e. those at less than 10^{-6} mm/cycle leaves the rising section, where linear regression can be used to fit a simple Paris law, and hence find D and n from Equation 8.3 as discussed in Chapter 8. The data obtained from the 'wet' tests on steel TDCB specimens bonded with the 'AV119' adhesive give D and n values of 1.37×10^{-13} m^2/N.cycle, and 3.64 respectively. This simple Paris law relationship is shown dotted in Figure 9.21, with the experimental data.

Suitable values of n_1 and n_2, the modified Paris law parameters, were calculated by substituting a high and a low experimental value of the fracture energy, with its corresponding crack growth rate, into Equation 9.9, see Figure 9.21. This gives a pair of simultaneous equations which can be solved by iteration. The values of n_1 and n_2 are not unique, but depend on the chosen values of G_{max} and da/dN. However, the predicted number of cycles is largely unaffected by the choice of these values, as will be discussed in Section 9.2.7.3. The experimental data and the modified Paris law model (solid line)

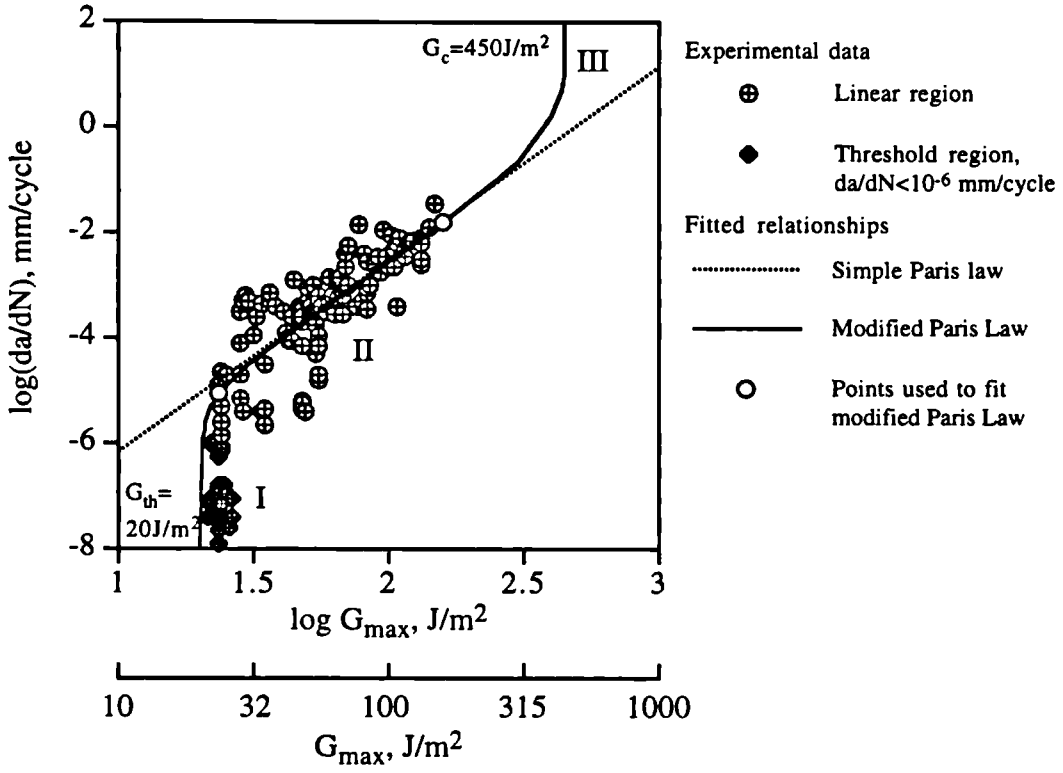


Figure 9.21: Modified Paris law fit to TDCB data for steel specimens bonded with 'AV119' tested in the 'wet' environment.

are shown in Figure 9.21. The data required for the lifetime prediction model are summarised in Table 9.4. The adhesive properties are taken from the literature[146].

9.2.6 Comparison of Theoretical Predictions and Experimental Results

The predicted lifetimes and the experimental results for the single lap joints are shown in Figure 9.22, calculated using the data given in Table 9.4. The agreement between the analytical method and the experimental results is only moderate. The fatigue life is underestimated, and the predicted threshold of approximately 20 % of the nominal failure stress is considerably lower than the 30 to 35 % observed experimentally. Thus, the prediction is a conservative one. This method of failure prediction has been shown to fit the experimental data very well for some adhesive/adherend combinations[65, 107], but poorer matches have also been found[157].

The predictions using the finite element approach to model the variation of G_{max} with crack length, using Equation 9.19, lie much closer to the experimental data than those

Table 9.4: Values of constants used for lap joint prediction models, steel adherends bonded with 'AV119' adhesive, tested 'wet'. Adhesive properties are taken from[146].

Adhesive fracture energy	G_c, J/m^2	450
Threshold fracture energy	G_{th}, J/m^2	20
Modified Paris law coefficient	D, m^2/N.cycle	1.37 x 10^{-13}
Modified Paris law exponent	n	3.64
Threshold region curve fitting constant	n_1	5.89
Fast fracture region curve fitting constant	n_2	2.10
Adherend modulus	E_s, GN/m^2	210
Adherend thickness	h, mm	2.0
Adherend Poisson's ratio	υ	0.35
Adhesive modulus	E_a, GN/m^2	3.0
Adhesive fracture stress	σ_a, MN/m^2	70
Adhesive thickness	t_a, mm	0.4
Half overlap length	c, mm	6.35
Griffith flaw size (from Equation 9.11)	a_o, μm	85

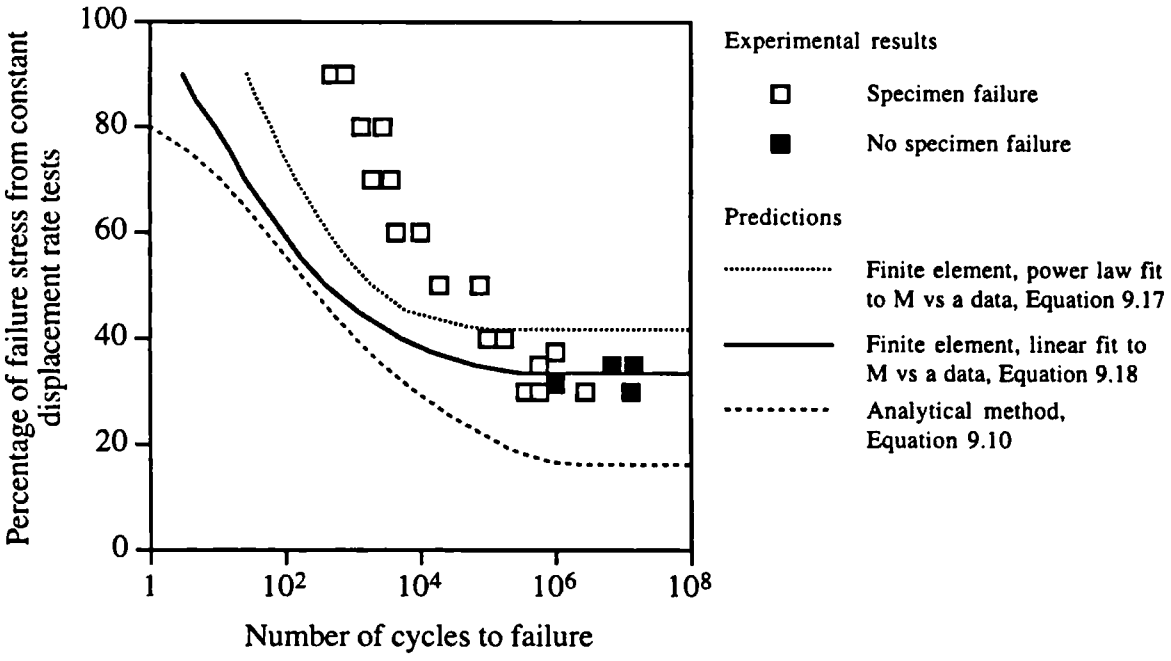


Figure 9.22: Predicted and experimental lifetimes for steel single lap joints bonded with 'AV119' adhesive, tested 'wet'. Predictions assume that crack growth is cohesive-in-adhesive from both ends of joint.

using the analytical method. A threshold of approximately 33 % is predicted using the linear fit to the M versus a data, using Equation 9.18, which compares well with the 30 to 35 % observed experimentally, as shown in Figure 9.22. The predictions using the power law fit to the M versus a data, using Equation 9.17, agree more closely than the linear data with the experimental results at higher applied stress levels. However, the threshold value is slightly overestimated using the power law model.

As the gradient of the relationship between the rate of crack growth and the applied fracture energy measured using the fracture mechanics tests is so steep[54], once a crack reaches a detectable size, failure will occur relatively quickly (unless the joint is monitored continuously). Unlike metals, where the gradient of the fracture mechanics data is shallow, the crack cannot be left to grow 'safely' for a time before the component is removed from service. Further, the single lap joints only show long lifetimes close to the threshold applied stress. Thus the threshold applied stress is the critical parameter to predict. Applied stresses below this critical value give a safe loading level. Hence the finite element approach using the linear model of the M versus a data gives the best agreement with the experimental results.

The next Section will consider how sensitive these predictions are to the assumptions made in the modelling, for example the effect of changing the initial flaw size or the parameters used for the modified Paris law model to the TDCB fatigue data. The sensitivity of the analytical model has been discussed by Osiyemi[106] and Jethwa[65], hence the present work will consider the FE predictions.

9.2.7 Effect of Boundary Conditions on Predicted Lifetimes

9.2.7.1 Introduction

The following Sections investigate the robustness of the finite element approach to the lifetime prediction of the lap joints. It considers the effect of changing the boundary conditions used, for example the initial flaw size, the parameters used to fit the modified Paris law to the TDCB data, n_1 and n_2, and the joint failure locus.

9.2.7.2 Effect of Initial Flaw Size

The initial flaw size, a_0, calculated from Equation 9.12 is 85 μm, using the values given in Table 9.4. However, it is useful to consider how critical this value is to the predicted number of cycles to failure. The integration performed to calculate N_f was repeated using a range of values of a_0, between 10 μm and 1 mm. Both the power law and the linear fits to the M versus a data were used. The predicted numbers of cycles to failure are shown in

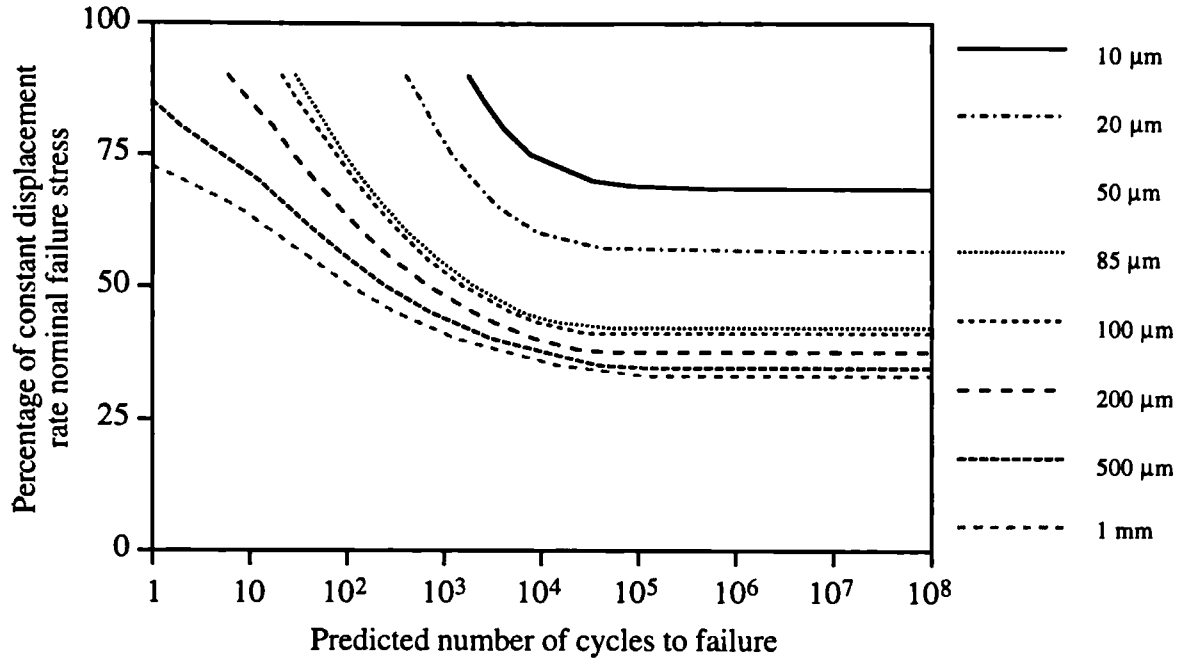
Figure 9.23. It can be seen that the linear model is relatively insensitive to the choice of a_0. The fatigue threshold remains virtually unchanged, and the numbers of cycles to failure at high stress levels are only noticeably altered at large a_0 values. Further, this reduction may simply be due to the reduction in bonded area, as a 1 mm crack from each end of the joint reduces the bonded area by 15 %.

The power law model is very sensitive to the choice of a_0. A small initial flaw size increases the number of cycles to failure, and increases the threshold value considerably. This is due to the steep gradient of the relationship between M and a at very small crack lengths. The increase in this gradient at crack lengths of less than 0.25 mm may an artefact of the finite element model as it occurs within only 3 elements from the edge of the joint. It would be necessary to refine the mesh in this area and repeat the modelling process to investigate whether this is a real effect or simply an artefact. Due to time constraints, this is an area for future work. Further, as the relationship between the rate of crack growth and fracture energy is so steep, the threshold is the parameter of interest. Thus, due to this uncertainty and the sensitivity of the power law model, the linear model only will be used for further comparisons in the current work. It was also shown Section 9.2.6 that this model gives the best agreement with the experimental data.

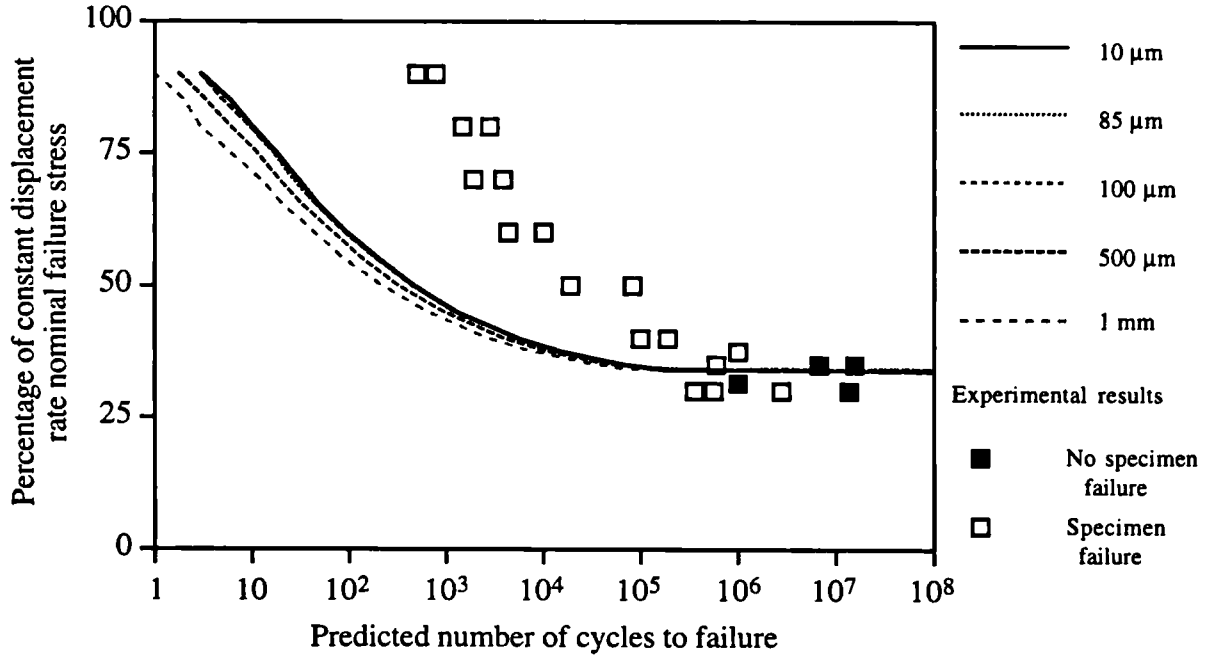
9.2.7.3 Effect of Modified Paris Law Parameters n_1 & n_2

To check the sensitivity of the model to the choice of the values of n_1 and n_2, the finite element prediction was repeated using the values of n_1 and n_2 shown in Figures 9.24 and 9.26. These Figures show the modified Paris law fit to the TDCB data obtained for the values listed. The predictions for number of cycles to failure, assuming crack growth is cohesive-in-adhesive from both ends of the joint, using the linear M versus a model, are shown in Figures 9.25 and 9.27.

If the values of n_1 and n_2 are chosen such that $n_1 = n_2$, and $0.1 \leq n_1, n_2 \leq 10$, then the value chosen has little effect on the predicted lifetimes. The value of the fatigue threshold is unaffected. Where $n_1 \neq n_2$, and $0.1 \leq n_1/n_2 \leq 10$, the fatigue threshold value is also unaffected by the choice of n_1 and n_2 values. However, if any of the values chosen is small, i.e. $n_1, n_2 \leq 0.1$, then the fit to the TDCB data moves away from the original simple Paris law fit. Thus the model does not accurately describe the experimental TDCB data, as shown in Figures 9.24 and 9.26. However, as can be seen from Figures 9.25 and 9.27, the effect on the predicted numbers of cycles to failure is small. Further, the predicted threshold value is unaffected by the choice of the modified Paris law parameters.



(a) Power law fit to M versus a data.



(b) Linear fit to M versus a data.

Figure 9.23: Effect of initial flaw size, a_0, on predicted number of cycles to failure for single lap joint, finite element approach, (a) power law fit to M versus a data, (b) linear fit to M versus a data.

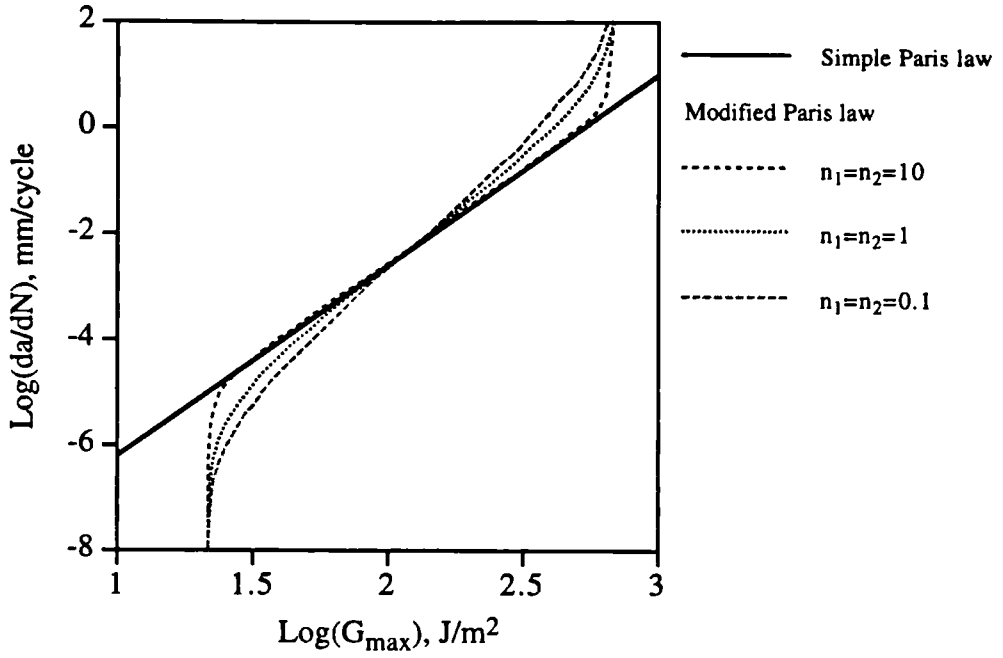


Figure 9.24: Fit to TDCB data, using Equation 9.9, for range of n_1 and n_2 values, when $n_1 = n_2$.

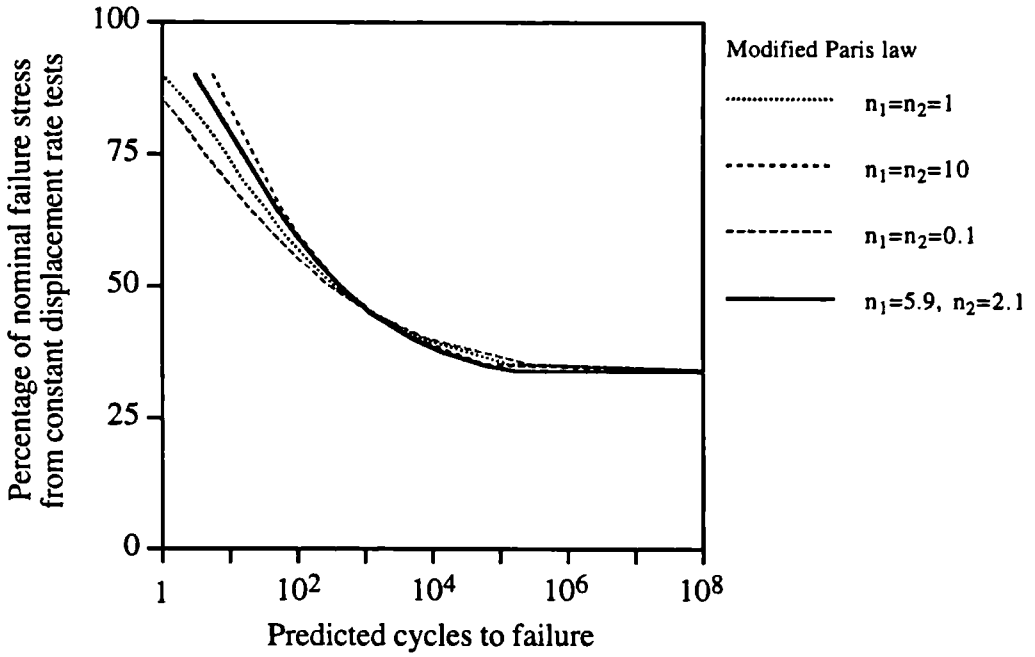


Figure 9.25: Lifetime predictions, using Equations 9.18 and 9.19, using range of n_1 and n_2 values.

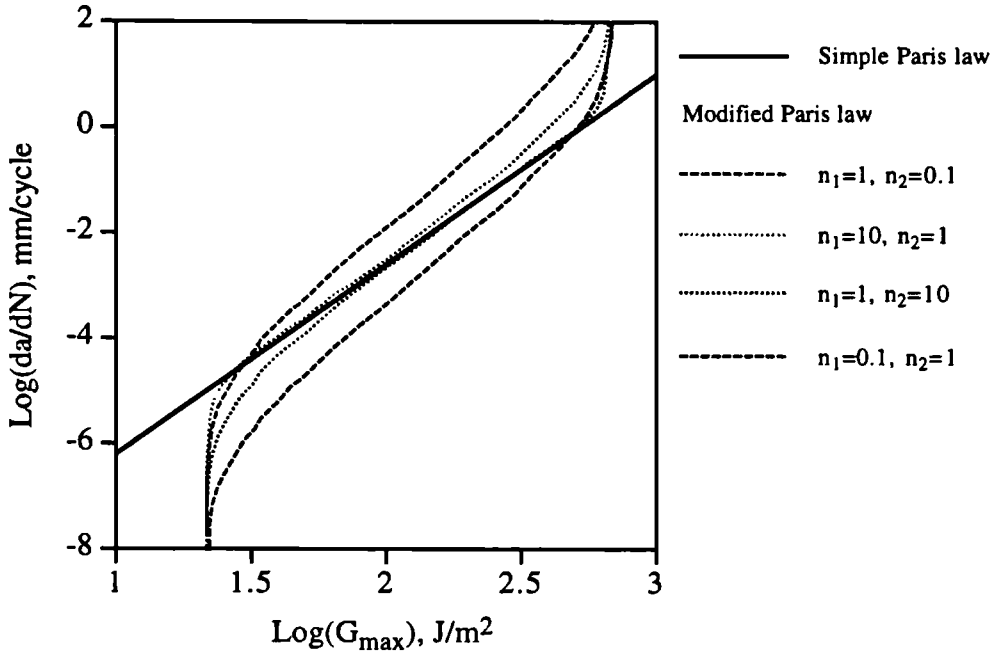


Figure 9.26: Fit to TDCB data, using Equation 9.9, for range of n_1 and n_2 values, when $n_1 \neq n_2$.

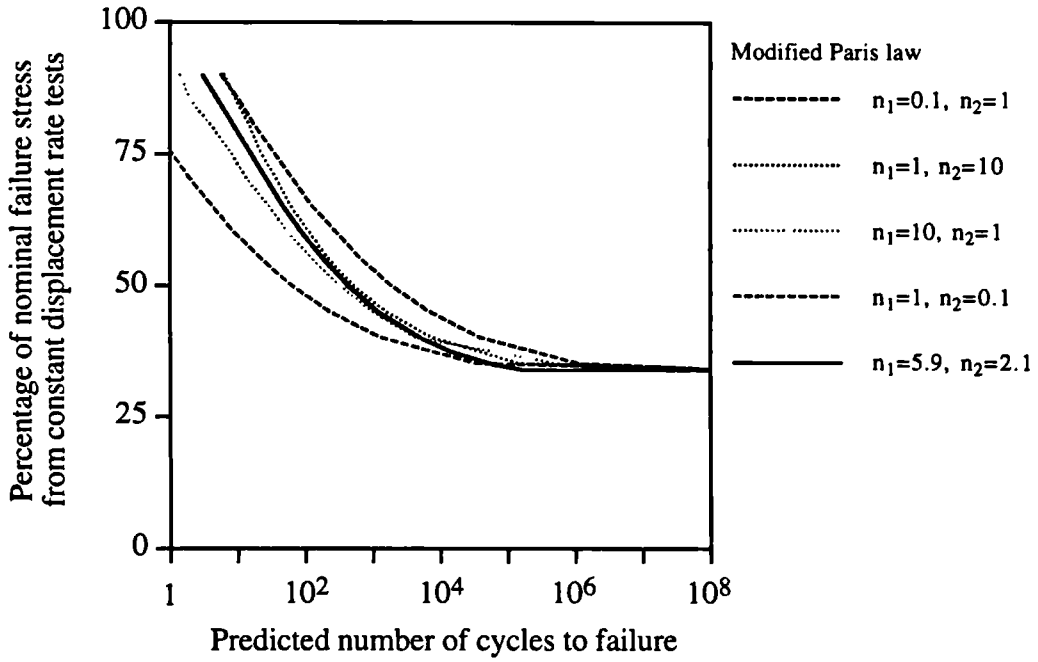


Figure 9.27: Lifetime predictions, using Equations 9.18 and 9.19, using range of n_1 and n_2 values.

9.2.7.4 Effect of Single Crack or Interfacial Failure

The above analyses assume that crack growth is in a cohesive-in-adhesive manner from both ends of the joint. However, the experimental data discussed earlier in this Chapter showed that this is not necessarily the case with these specimens. Thus it is useful to investigate if there is any effect of either only one crack propagating through the adhesive, or of a change of failure locus.

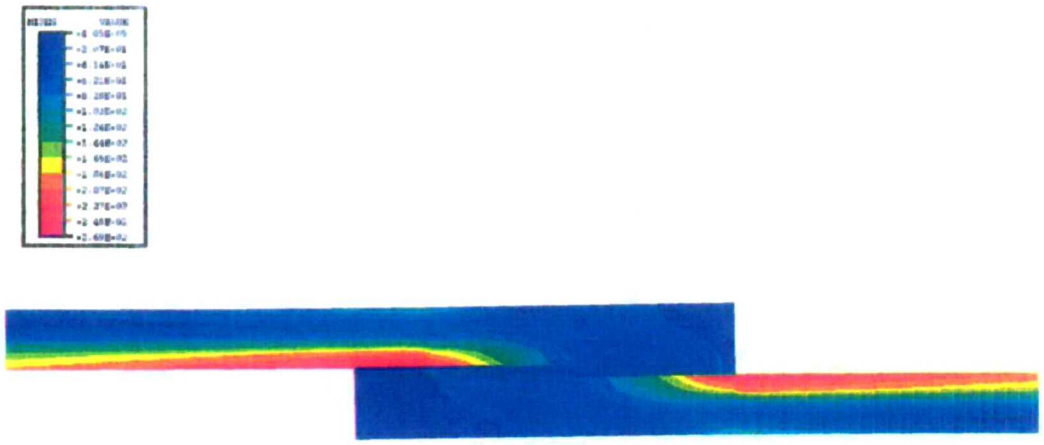
To investigate the effect of a single crack, the finite element modelling described in Section 9.2.5.4 was repeated, but the nodes in the centre of the adhesive layer were released from one end only. Values of G_{max} were calculated for crack lengths between 85 μm and 6.8 mm for between 40 and 90 % of the nominal failure stress from the constant displacement rate tests. A sample stress distribution is shown in Figure 9.28a.

The experimental results discussed earlier in this Chapter showed that many failures occurred close to the interface at the end of the overlap, as shown in Figure 9.5. The finite element modelling was repeated, allowing cracks to propagate along these interfaces, as shown in Figure 9.28b. Once again values of G_{max} were calculated for a range of T_{max} and crack length values.

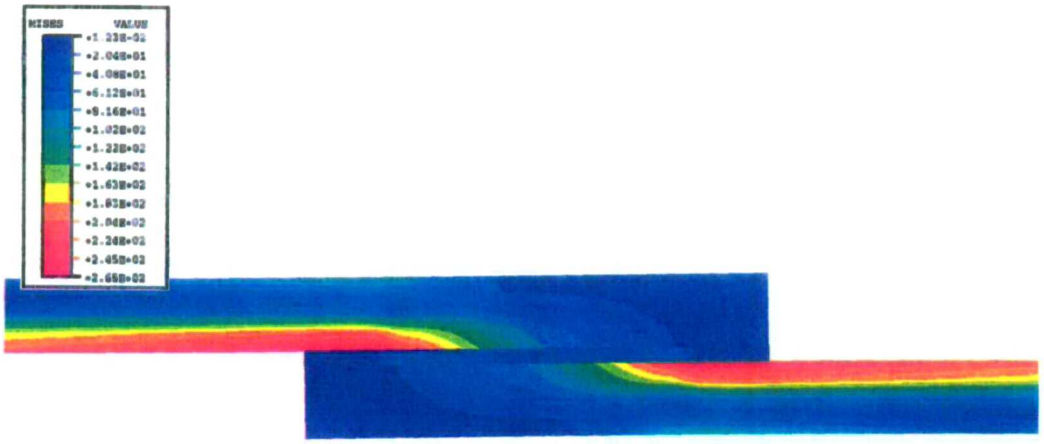
The stress distributions for all three types of crack growth, as shown in Figures 9.17 and 9.28, are very similar. The relationships between G_{max} and crack length are also similar for all three types of crack growth, see Figure 9.29.

As above, graphs of T_{max} versus G_{max}, and M versus a, were plotted for these two cases. Linear fits were used to model the relationships between M and a for the reasons discussed above, as shown in Figure 9.30 and Table 9.5. The predicted number of cycles to failure were calculated using Equation 9.19.

The predicted lifetimes and the experimental data are shown in Figure 9.31. This shows that there is very little difference between the predictions, whether crack growth is from both ends of the joint or only one, or if it occurs at the interface. However, there is a slight increase in the predicted fatigue threshold if crack growth only occurs from one end of the joint.



(a) Single crack.



(b) Interfacial crack from both ends of overlap.

Figure 9.28: Von Mises' stress distribution predicted by finite element model, crack length 2.5 mm, 60 % of nominal stress from constant displacement rate tests, (a) single crack, (b) interfacial crack from both ends of overlap. Compare with Figure 9.17.

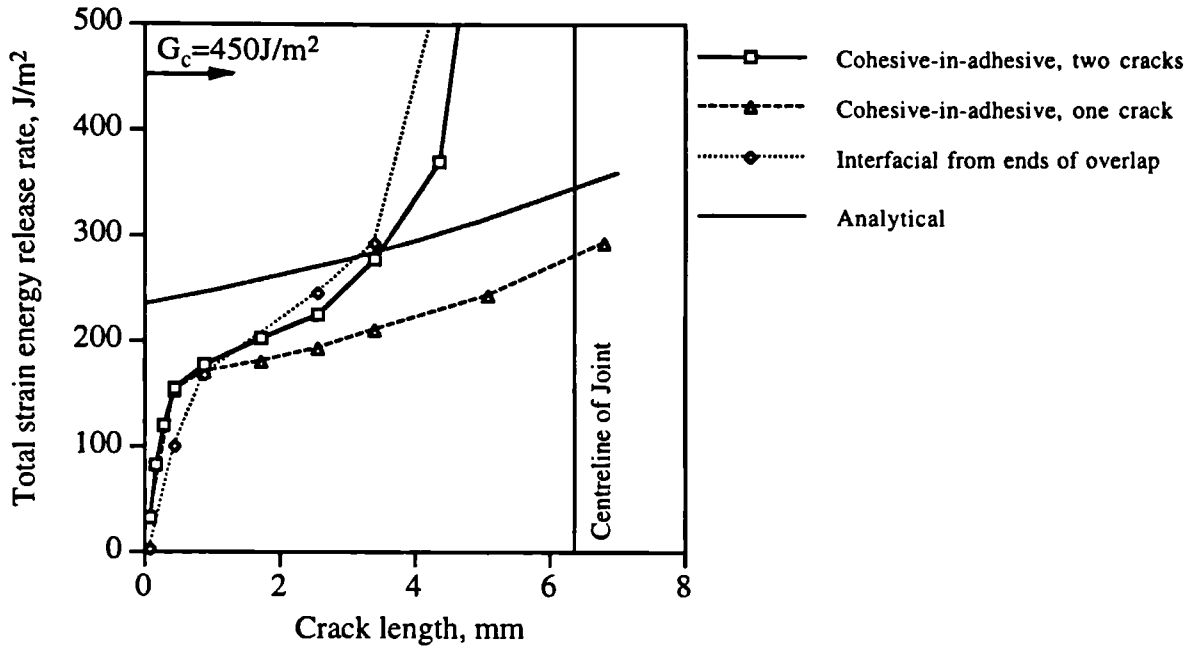


Figure 9.29: Graph of G_{max} versus crack length for various types of failure, finite element and analytical models.

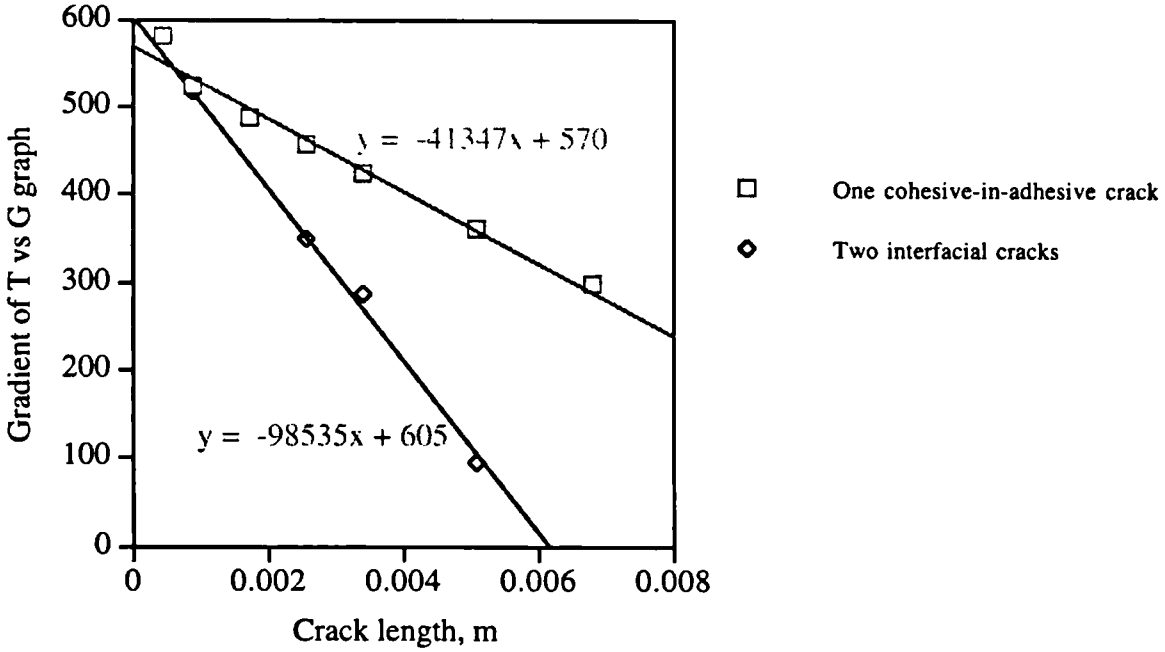


Figure 9.30: Gradient of T_{max} versus G_{max} graph, M, versus crack length for steel single lap joint bonded with 'AV119', assuming crack growth is cohesive-in-adhesive from one end, or interfacial from both ends of overlap.

Table 9.5: Fitting parameters used for linear fit to M versus a data, one or two cohesive-in-adhesive cracks or two interfacial cracks.

	Two cracks	One crack	Interfacial
C, N/m	90500	89800	96800
f, m^{-1}	-86983	-41347	-98535
k, m	593	570	605

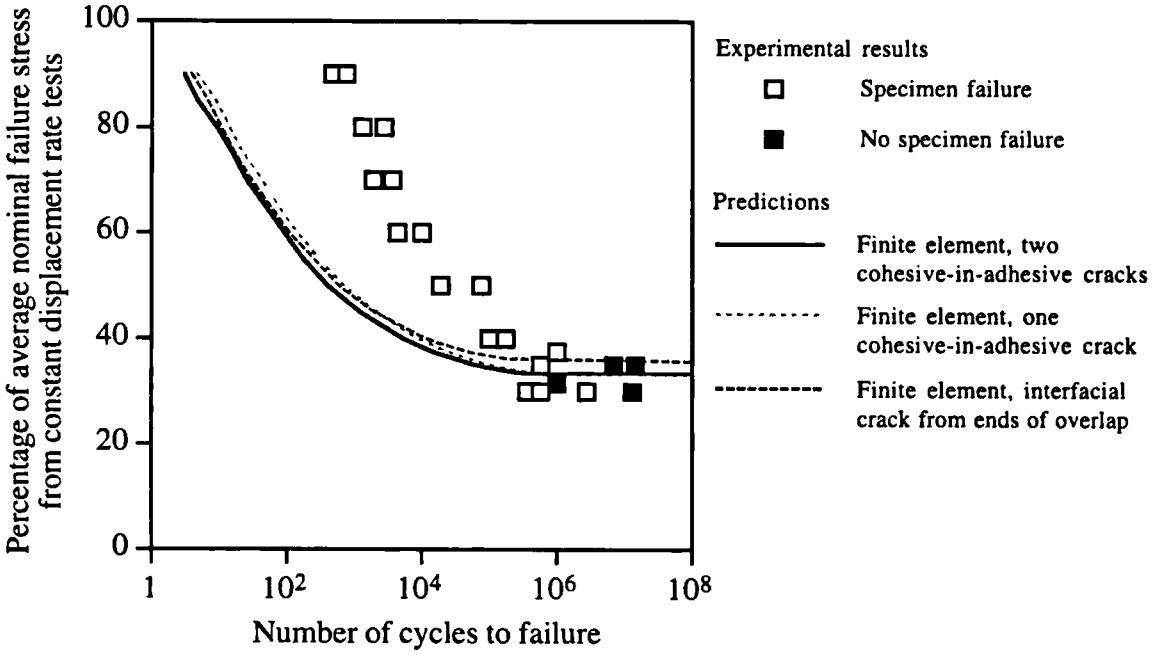


Figure 9.31: Predicted numbers of cycles to failure for steel lap joints bonded with 'AV119' adhesive, predicted using finite element models. (In all cases a linear model used to describe the M versus a data, see Equation 9.18.)

9.2.7.5 Dominant Mode of Failure

The lifetime predictions models discussed above assume that failure is dominated by mode I loading. The universal crack closure technique used with the finite element model gives the mode I and mode II components of fracture energy, which are summed to give the value of G_{max}. Hence it is possible to calculate the proportion of G_I and G_{II} that a crack experiences as it grows through the joint. Figure 9.32 shows how the mode I proportion of G_{max} varies with crack length. This shows that at crack lengths of less than

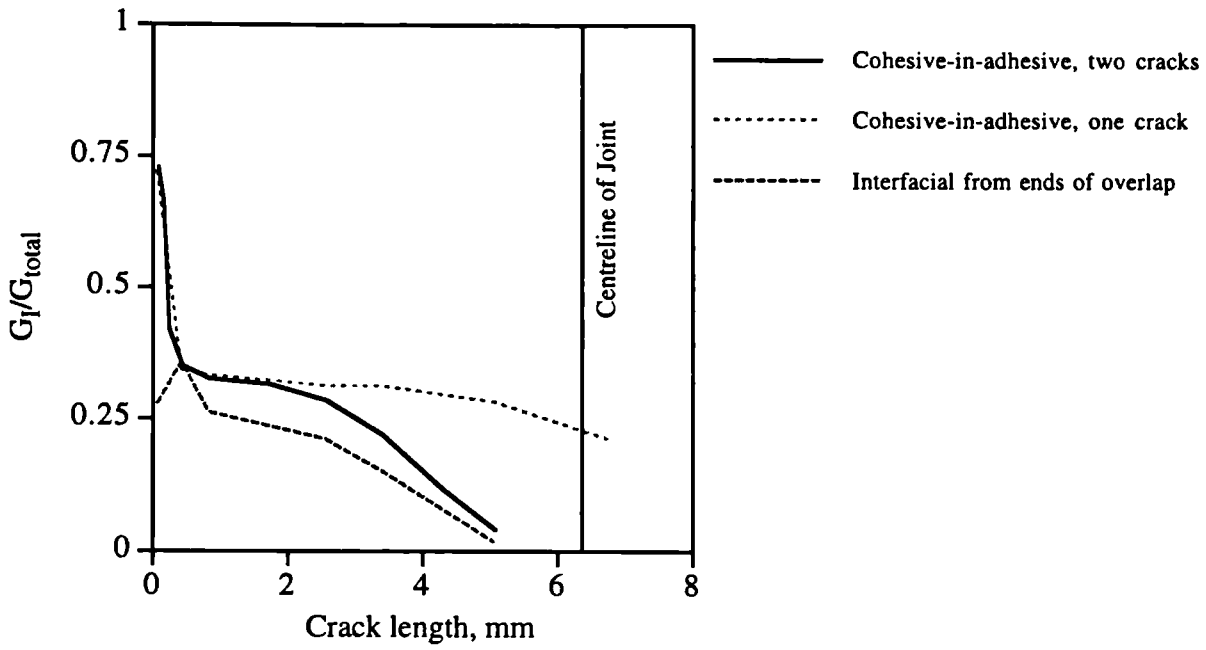


Figure 9.32: Mode I fracture energy as proportion of total fracture energy for finite element approach. Applied nominal stress 60 % of constant displacement rate nominal failure stress.

0.4 mm the loading is dominated by the mode I component, but then the mode II component becomes dominant. At large crack lengths the mode I component barely contributes to G_{max}.

However, Figure 9.32 is slightly misleading because the crack growth rate increases considerably as the crack grows through the specimen. Thus it perhaps better to plot the proportion of the predicted cycles to failure that occur under mode I dominated conditions. These data are presented in Figure 9.33. Note that for interfacial crack growth G_I never contributes more than 50 % of G_{max}. This Figure shows that predicted life of joints using the model with the power law fit to the M versus a data is predominately mode I loading. For those models that used the linear fit to the M versus a data, either for a single crack or two cracks, the joint life is dominated by mode II loading, except at high loads.

However, the TDCB fatigue data is not strictly only mode I, as failure occurred through the metal oxide at the interface between the adhesive and the adherend. Charlambides et al[165] have shown that when failure occurs at the interface, $G_{II}/G_I = 0.25$. Further, Duer et al[166] have shown that there is no measurable difference between the value of the fracture energy when failure occurs at the interface, for a range of mode-mixes (i.e.

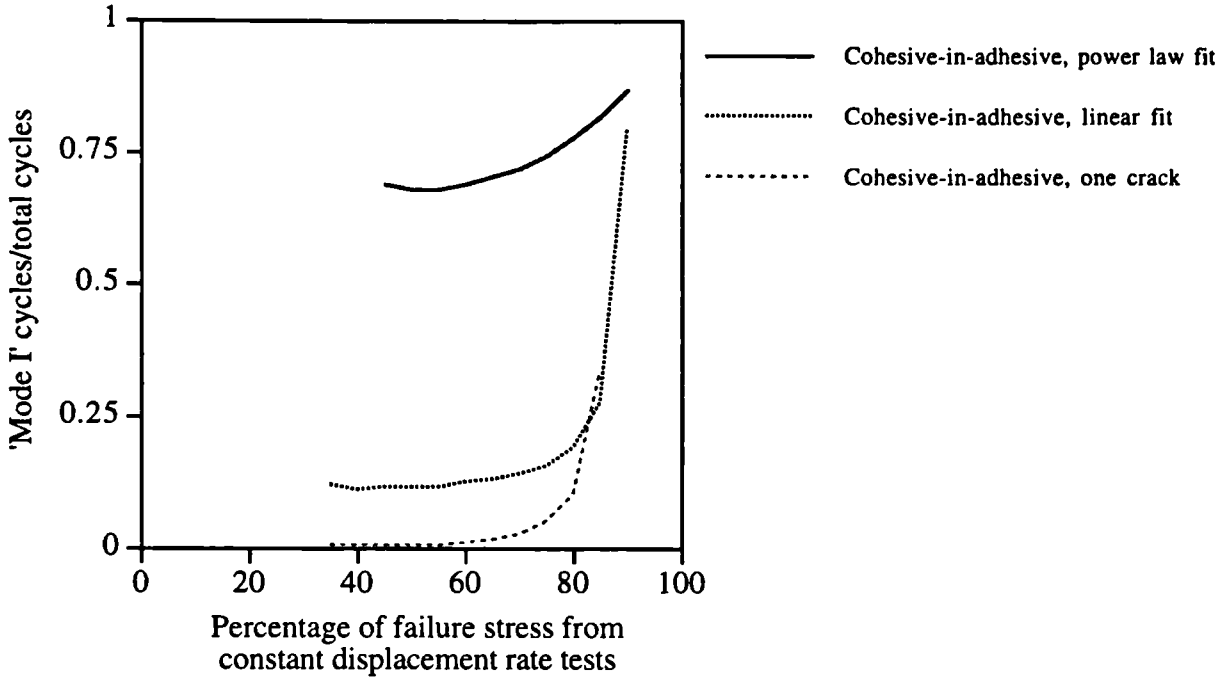


Figure 9.33: Proportion of predicted number of cycles to failure under mode I dominated conditions (i.e. when $G_I > G_{II}$) versus percentage of failure stress (or T_{max}) from constant displacement tests. Predictions assume cohesive-in-adhesive crack growth.

various values of G_I/G_{II}). Thus the nominally mode I TDCB data can be used to predict the fatigue life of the nominally mixed-mode lap joint.

9.2.8 Lap Joint Summary

Constant displacement rate testing of 'AV119'/steel lap joints gave a nominal failure stress of 24 MN/m^2. 'Wet' fatigue testing showed short joint lives at high applied stress levels (less than 10000 cycles down to 60 % of the nominal failure stress). The joint life increased with decreasing applied stress. Evidence of a threshold at around 30 to 35 % of the nominal failure stress was indicated by fatigue lives of more than 1.5 x 10^7 cycles. The use of a backface strain technique showed crack growth occurred for greater than 75 % of the life of the lap joints.

Lifetime prediction models have been used to estimate the number of cycles to failure of single lap joints from data obtained from the fracture mechanics (TDCB) fatigue tests. An analytical model, proposed by Kinloch and Osiyemi[107], was used to predict the variation of G_{max} with crack length.

Additionally, a finite element approach was used. The value of G_{max} was found to vary with both the crack length, a, and the maximum applied load, T_{max}. However, the relationship between T_{max} and G_{max} was linear. Thus the gradient, M, of the T_{max} versus G_{max} data was plotted against the crack length. The M versus a data were modelled using a power law and a linear relationship. Thus two expressions for G_{max} were formulated, Equations 9.17 and 9.18.

The TDCB fatigue data was modelled using a modified Paris law. Substitution of the expressions for G_{max} and integration allowed the number of cycles to failure of the lap joints to be predicted. Due to the steepness of the fracture mechanics data, the critical lap joint parameter to predict is the threshold applied stress, as unless the joint is instrumented, once a crack has reached a detectable size, the remaining joint life is limited.

All the methods gave good predictions of the fatigue life. The analytical method of prediction produced the most conservative values of the lifetime, and underestimated the threshold stress by approximately 10 %. The finite element method predicted lifetimes which agreed more closely with those observed experimentally, though using the power law model of the M versus a data gave a threshold value approximately 10 % higher than that observed experimentally. The predictions using the linear model of the M versus a data were closest to the experimental data. These were found to be insensitive to the initial flaw size, the modified Paris law fitting parameters, and to the locus of joint failure using the linear model of the M versus a data. A threshold value of 33 % of the nominal failure stress was predicted using this linear model, compared with the 30 to 35 % observed experimentally.

9.3 Bonded Components

9.3.1 Introduction

Section 9.2 has shown that the lifetime of a bonded lap joint subjected to fatigue loading can be predicted using fracture mechanics data from the TDCB fatigue tests. The work presented in this Section extends this work to a more complicated bonded component. A steel stiffener-type component was chosen, with an end-loaded 'top-hat' section bonded to a base plate using the 'AV119' adhesive, as shown in Figure 9.34. The variation of the strain energy release rate, G, with crack length in the component will be calculated using a finite element model. These data, combined with the TDCB data presented in Chapter 8, will allow the rate of fatigue crack growth to be predicted. The predictions will be compared to experimental data.

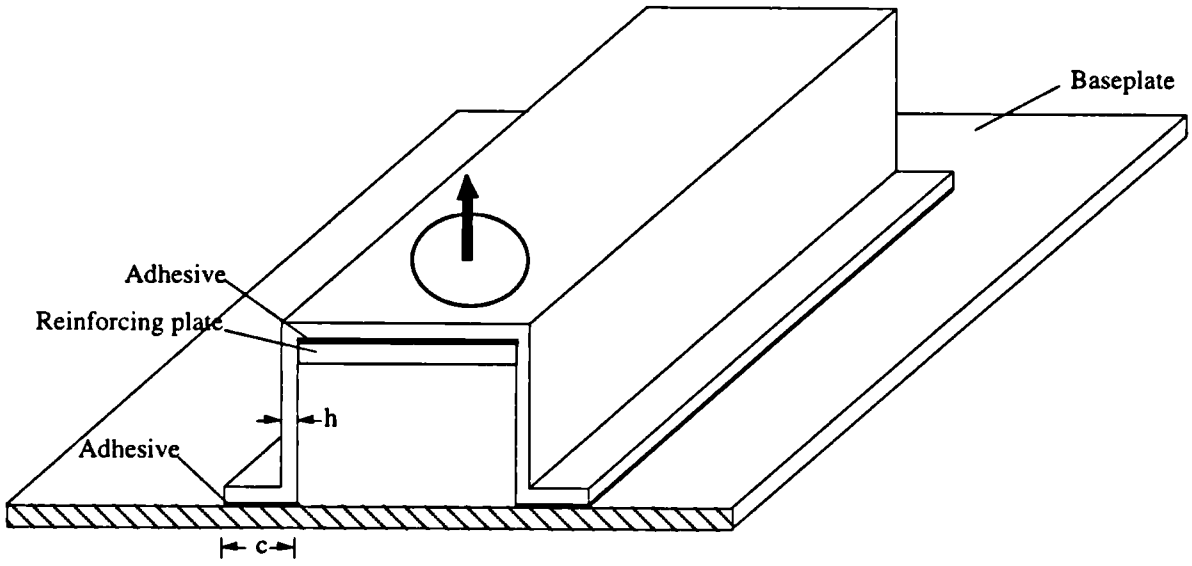


Figure 9.34: Schematic of bonded component, end loaded 'top-hat' section bonded to baseplate. Steel adherends bonded with 'AV119' adhesive. Adherend thickness, h, is 2 mm, and bonded width, c, is 15 mm.

9.3.2 Experimental Procedure and Results

9.3.2.1 Specimen Manufacture

The 'top-hat' section of the component was made from 2 mm thick mild steel. This was cut to size and bent to the required profile, the dimensions of which are shown in Figure 9.35. A reinforcing plate was used under the 'top-hat' section to prevent plastic deformation. The underside of the 'top-hat' was gritblasted and degreased where the reinforcing plate would be bonded on. Adhesive was applied to this area and to the reinforcing plate. These were brought together, and cured.

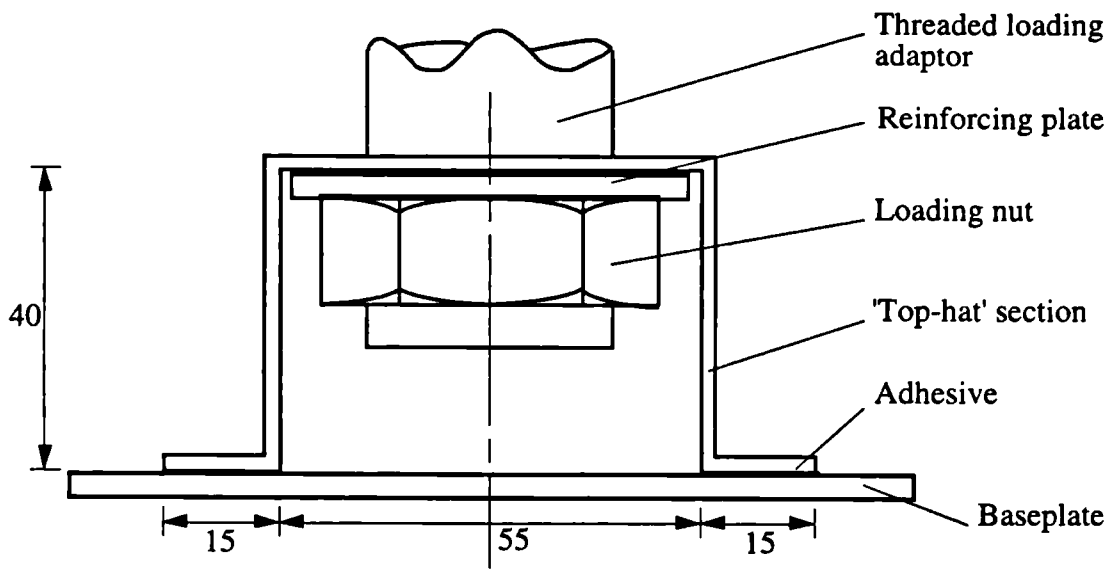


Figure 9.35: End view of bonded component showing loading arrangement, and dimensions used. All dimensions in millimetres. Component length 250 mm, adhesive thickness 0.4 mm.

The baseplate was made from 3 mm thick mild steel. This was cut to size, approximately 600 mm square, and the desired position of the 'top-hat' marked out. The areas to be bonded on the 'top-hat' and the base plate were gritblasted and degreased, as described in Chapter 3. The adhesive was applied, and 0.4 mm stainless steel wires placed at either end to give a constant adhesive layer thickness. A sheet of PTFE was placed at one end to act as a starter crack, 80 mm long. The two halves were assembled and pressure was applied using weights. Any excess adhesive was removed, and the component was cured.

Once the component had cured, holes were drilled through the baseplate to allow the component to be bolted onto the crosshead of the testing machine, see Figure 9.36. A hole was also drilled through the reinforced 'top-hat' section to enable the component to be loaded. The outside edges of the adhesive layer were sprayed with a thin layer of white paint to allow the crack tip to be followed during testing. To load the component, a nut was placed under the reinforcing plate, and a threaded adaptor screwed into it, see Figure 9.35.

9.3.2.2 Constant Displacement Rate Tests

A bonded component was tested on a screw-driven 'Instron' testing machine at a constant displacement rate of 0.5 mm/min. The force versus displacement response was recorded.

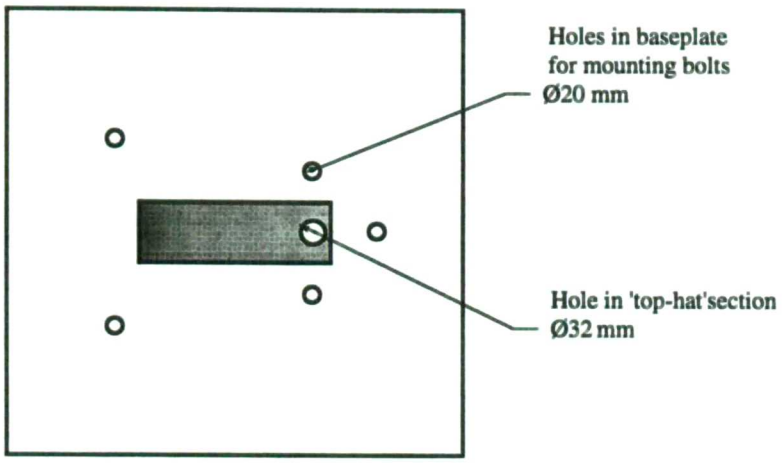


Figure 9.36: Bonded component, plan view, showing positions of holes for mounting bolts.

The component tested at a constant displacement rate exhibited stick/slip crack growth, as shown in Figure 9.37. The first initiation occurred at a load of 1750 N and a displacement of 1.7 mm. There was no plastic deformation of the adherends. The initiation and arrest lines are clearly visible on the fracture surfaces. These were curved, the crack length on the inside of the beam being longer than the outside. Approximately six initiation/arrest lines are visible on the 'smooth' fracture surface, and seven on the 'ribbed' (including initiation from the starter foil), see Figure 9.38. This compares with seven initiation points on the force versus displacement trace. Thus in some cases the cracks in both arms of the component propagate at the same time, whilst at others only one crack propagates.

The locus of failure was apparently interfacial visually. One arm of the specimen showed a similar failure to that seen in the TDCB tests - the adhesive remaining on the 'top-hat' while the baseplate was apparently free of adhesive, see Figure 9.38. The other arm of the component showed ribs of adhesive on both fracture surfaces, as shown in Figure 9.38. These are similar to those seen in the IWP tests where there was unstable failure of the 'AV119' adhesive. SEM of the fracture surfaces showed that failure occurred close to the interface. Adhesive was clearly visible on the 'top hat' half of the component, with cavitated rubber particles present, as shown in Figure 9.39. The baseplate is mostly free of adhesive, but areas of residual adhesive are present, see Figure 9.39.

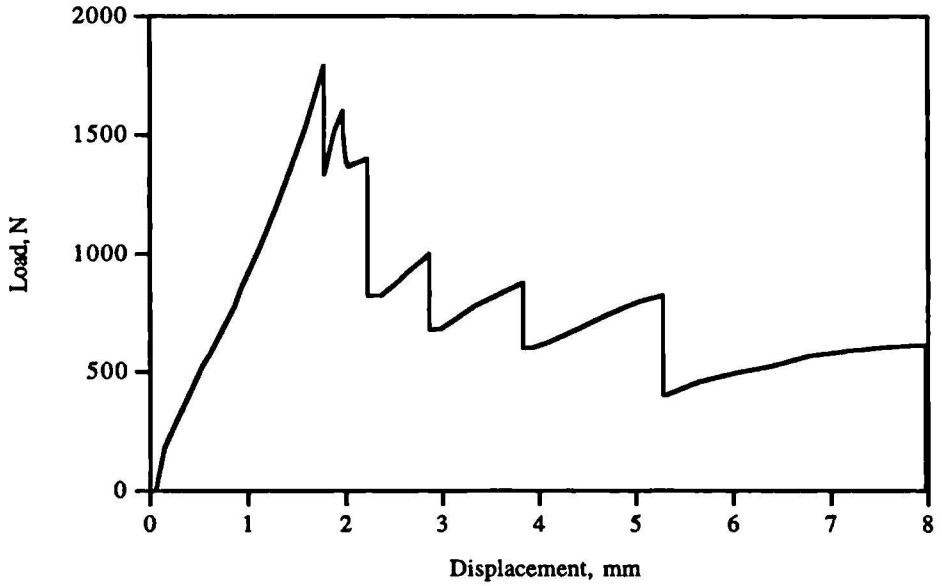
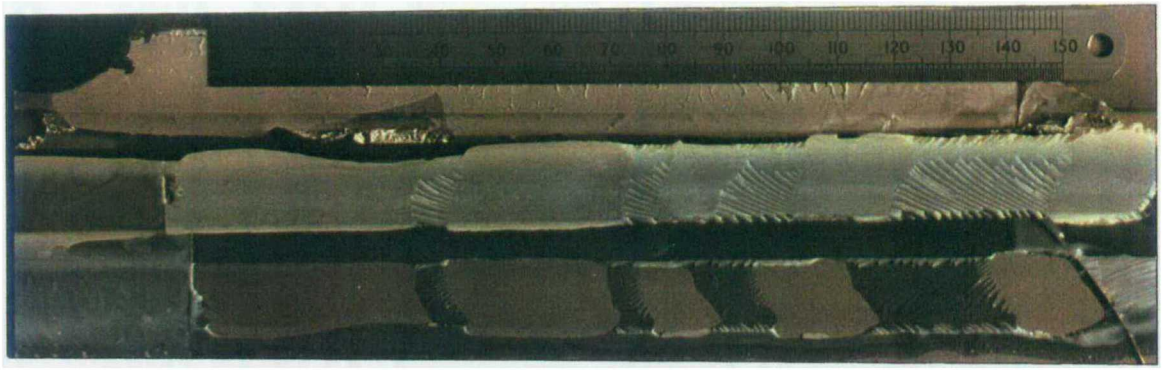
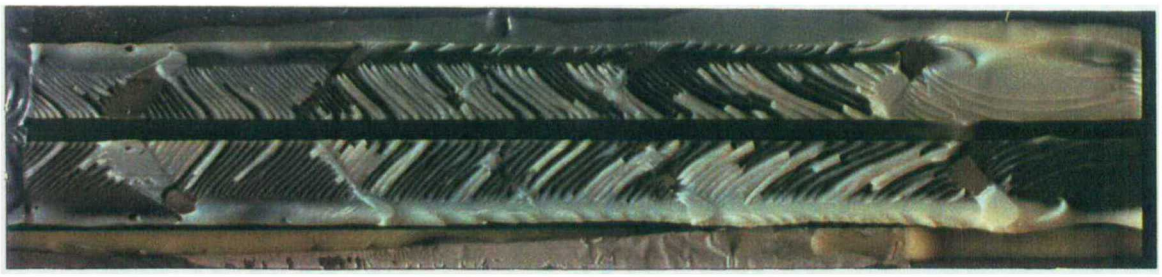


Figure 9.37: Force versus displacement response of bonded component, constant displacement rate test at 0.5 mm/min, showing initiation and arrest events due to stick/slip crack growth.

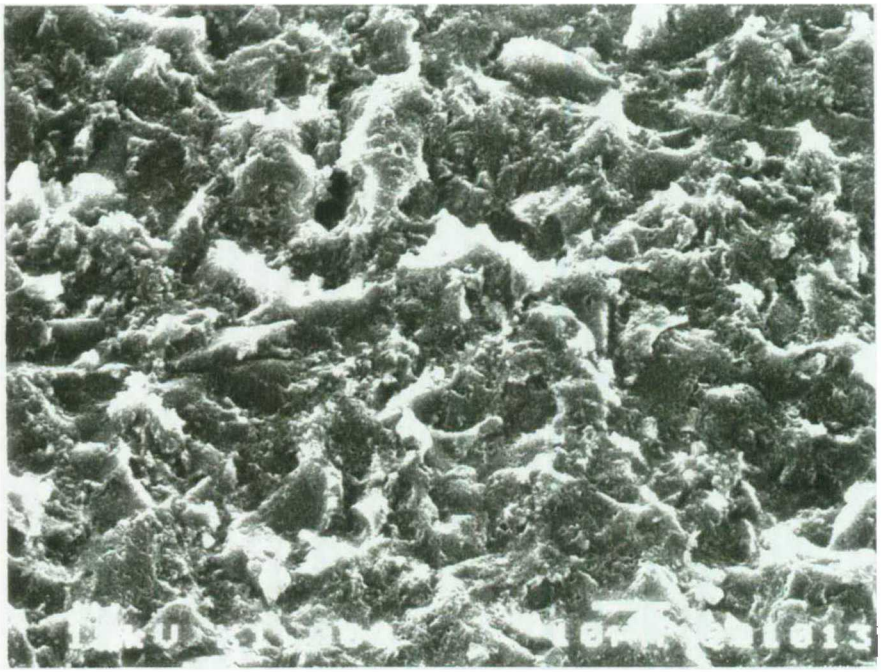


(a) Right-hand side of component ('smooth').

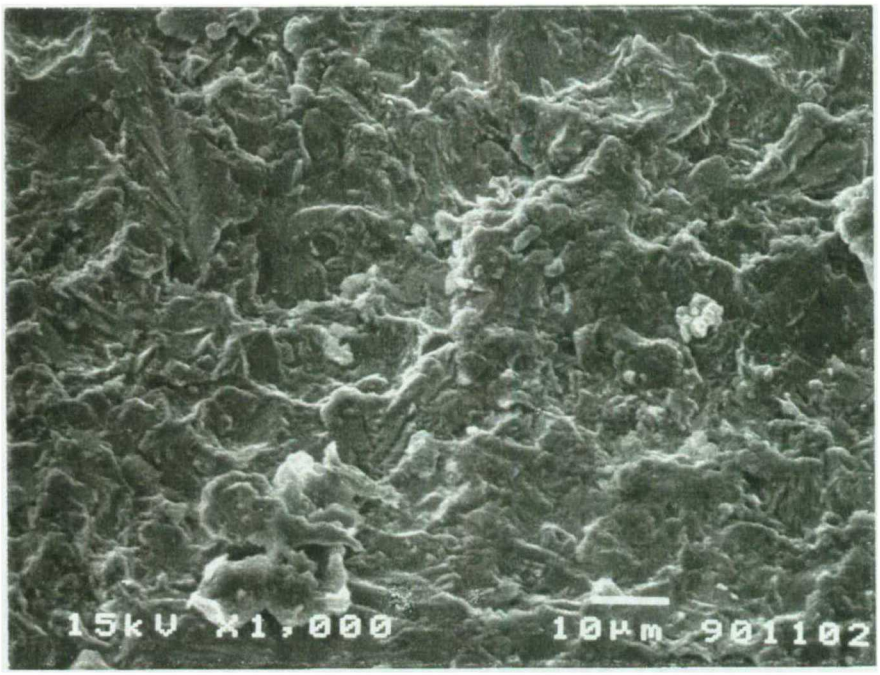


(b) Left-hand side of component ('ribbed').

Figure 9.38: Fracture surfaces of bonded component tested at constant displacement rate, showing apparent interfacial failure and initiation/arrest lines from stick/slip failure, (a) right-hand side ('smooth'), and (b) left-hand side ('ribbed'). (Crack propagation is from left to right.)



(a) 'Top hat' half of component (adhesive).



(b) Baseplate half of component (apparent interfacial).

Figure 9.39: Micrographs of fracture surfaces of bonded component tested at constant displacement rate, showing (a) 'top hat' half of component (adhesive), and (b) baseplate half of component (apparent interfacial). (Crack propagation is from left to right.)

9.3.2.3 Fatigue Tests

A bonded component was tested in 'dry' fatigue using an 'ESH' servo-hydraulic testing machine. A constant maximum displacement of 1.2 mm was used. Tests were performed at 5 Hz, using $u_{min}/u_{max} = 0.5$. The crack length in the arms of the specimen was monitored using a pair of travelling microscopes, see Figure 9.40.

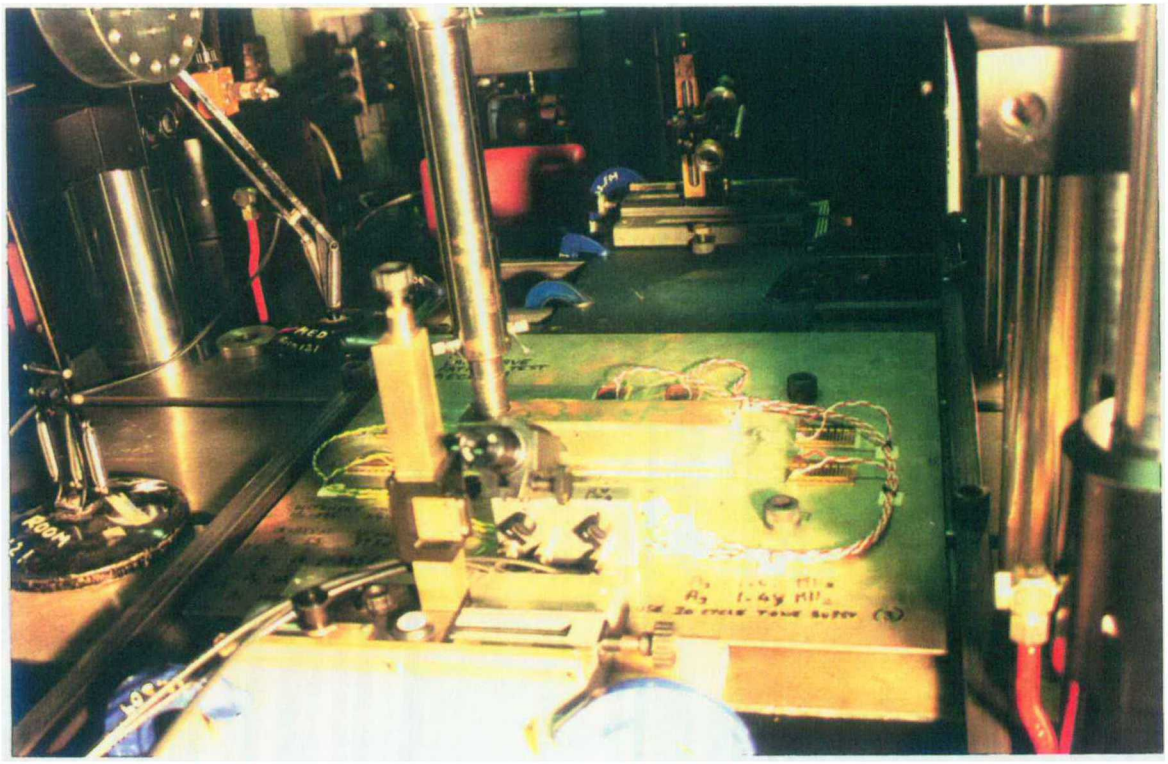


Figure 9.40: Bonded component during fatigue testing, showing travelling microscopes used to measure crack length.

The crack length in the two arms of the specimen was found to be unequal, see Figure 9.41, probably due to some eccentricity in the loading or the shape of the 'top-hat' section. The measured force decreases as the cracks grow, due to the increased compliance of the component, see Figure 9.42.

The rate of crack growth per cycle, da/dN, in each arm of the component was calculated from the crack length data, and are shown in Figure 9.43. As the cracks grow, the rate of crack growth decreases.

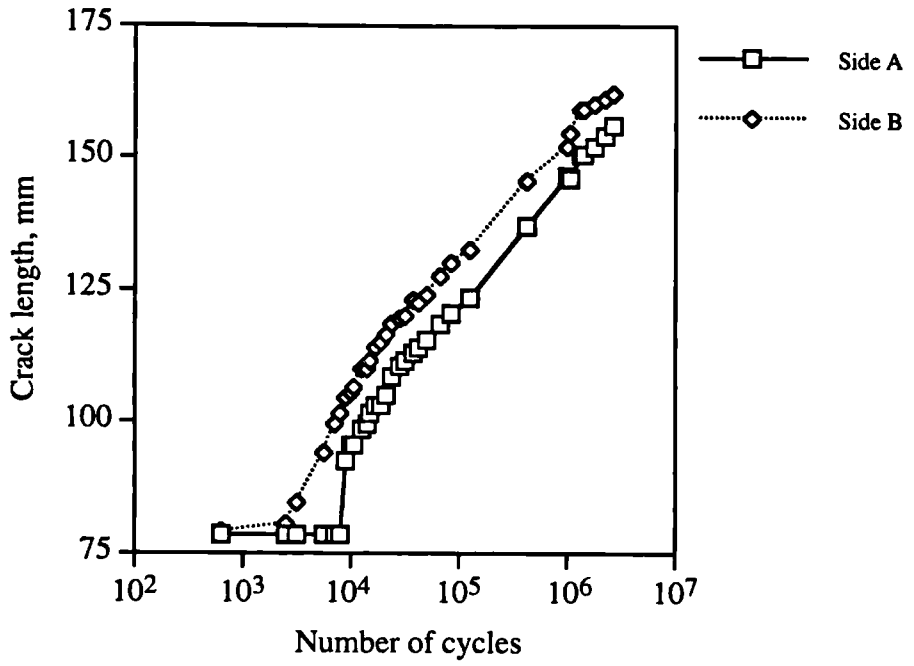


Figure 9.41: Experimental results from bonded component tested in fatigue, showing measured crack length versus number of cycles.

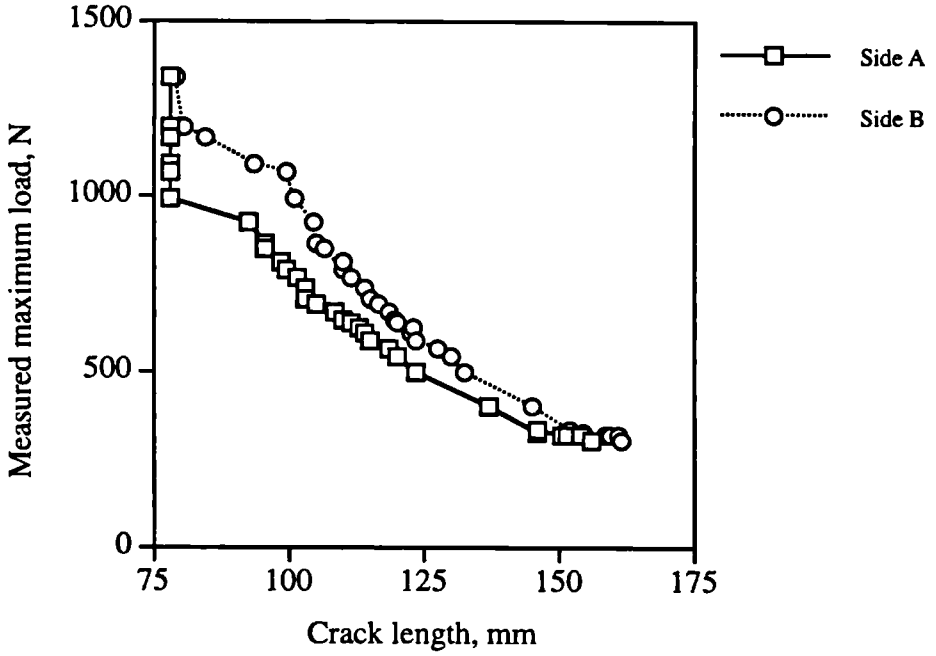


Figure 9.42: Graph of measured force versus crack length for component in fatigue, steel adherends bonded with 'AV119' adhesive, tested 'dry'.

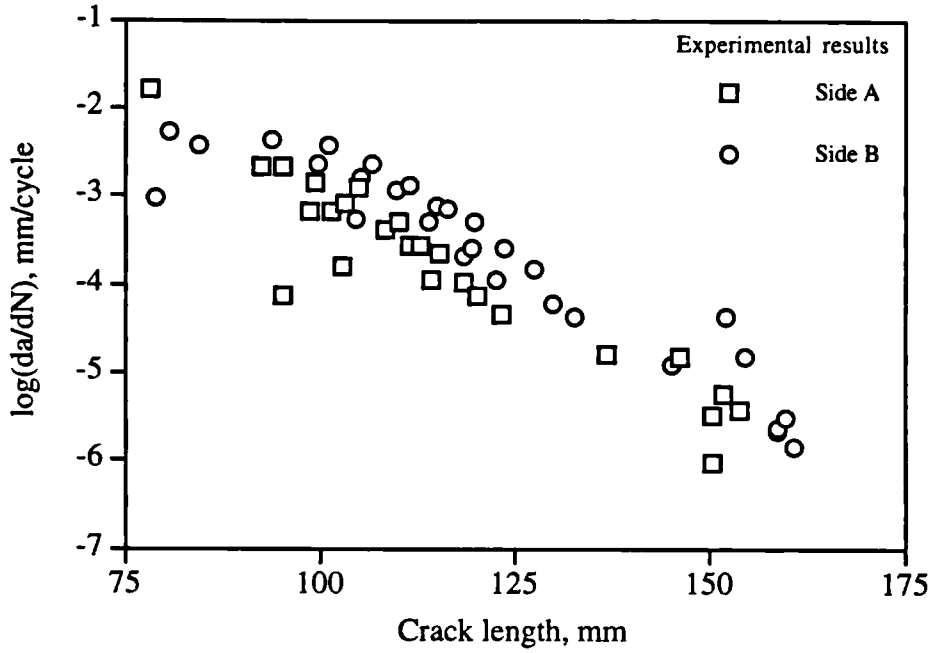
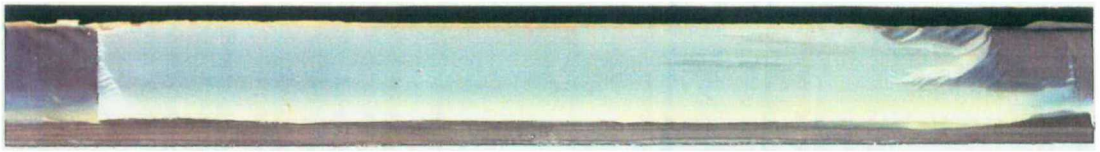


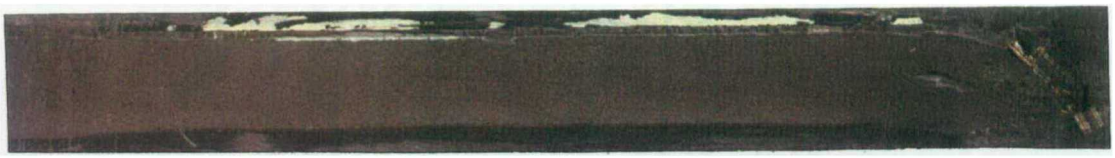
Figure 9.43: Graph of rate of fatigue crack growth, da/dN, versus crack length (log-linear axes) for bonded component in fatigue, steel adherends bonded with 'AV119' adhesive, tested 'dry'.

The fracture surfaces of the bonded component are shown in Figure 9.44. The failure is apparently interfacial visually, with the adhesive remaining on the 'top-hat' half of the component.

SEM of the fracture surfaces showed that adhesive was clearly visible on the 'top-hat' half of the component, with cavitated rubber particles present, see Figure 9.45. Analysis of the baseplate showed that there appeared to be no adhesive present. It appears that failure occurred close to the interface. The surfaces are very similar to those seen for the 'dry' TDCB fatigue tests on steel adherends bonded with the 'AV119' adhesive, as discussed in Section 8.6.3.3. Thus it may be concluded that the same locus of failure is observed for both the TDCB and the bonded component tests. Thus the fracture mechanics data from the TDCB tests may be used to predict the bonded component crack growth rate.

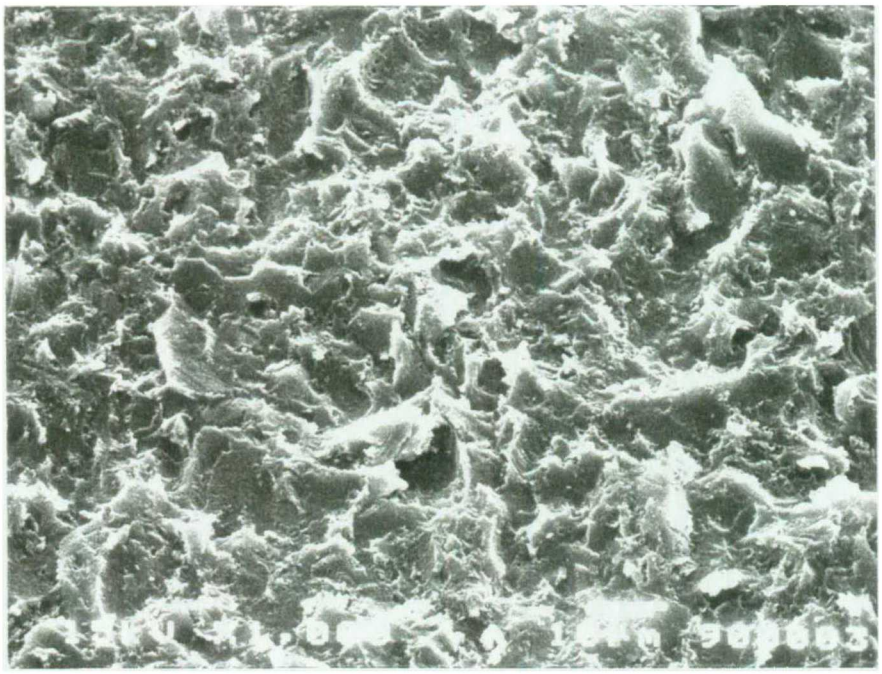


(a) 'Top-hat' half of component (adhesive).

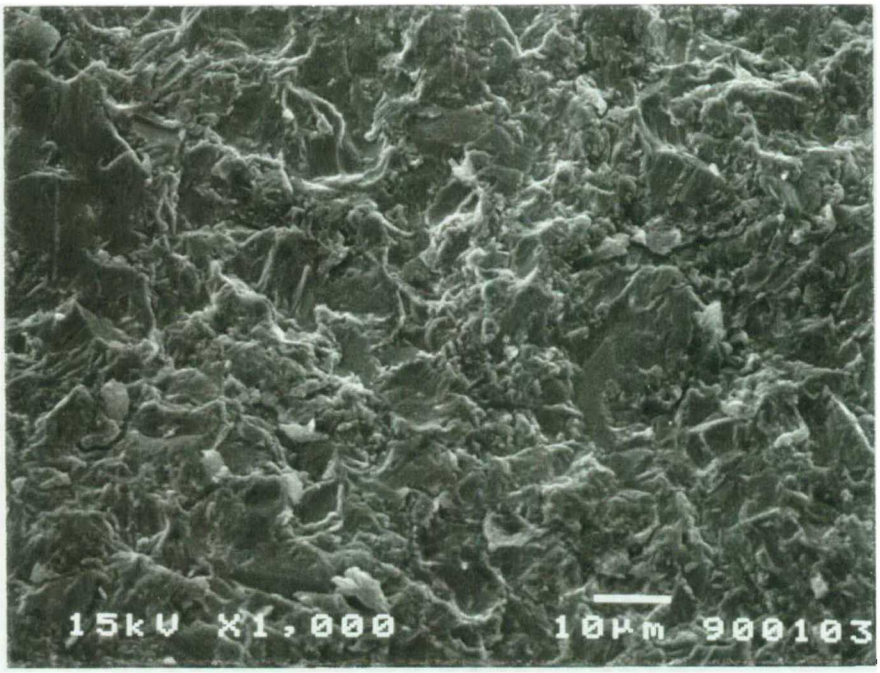


(b) Baseplate half of component (apparent interfacial).

Figure 9.44: Fracture surfaces of bonded component tested under 'dry' fatigue, (a) 'top-hat' section, and (b) baseplate half of component (apparent interfacial). (Crack propagation is from left to right.)



(a) 'Top-hat' half of component (adhesive).



(b) Baseplate half of component (apparent interfacial).

Figure 9.45: Micrographs of fracture surfaces of bonded component, tested in fatigue, showing (a) 'top-hat' half of component (adhesive), and (b) baseplate half of component (apparent interfacial). (Crack propagation is from top to bottom.)

9.3.3 Lifetime Prediction Modelling

9.3.3.1 Finite Element Modelling

A three-dimensional finite element model of the component was developed[167], see Figure 9.46. The steel and adhesive were assumed to be purely elastic, as no plastic deformation was observed experimentally. The material properties used are shown in Appendix 1. A fixed displacement of 1.2 mm was applied, and the nodes at the interface between the adhesive and the steel were released in turn. The model assumes that the crack length is equal in both arms of the component. The strain energy release rate at the outside edge of the adhesive layer was calculated using the universal crack closure method, as described in Chapter 6. The total strain energy release rate, G_{max}, was calculated by adding the mode I, mode II and mode III components. The variation of G_{max} with crack length is shown in Table 9.6.

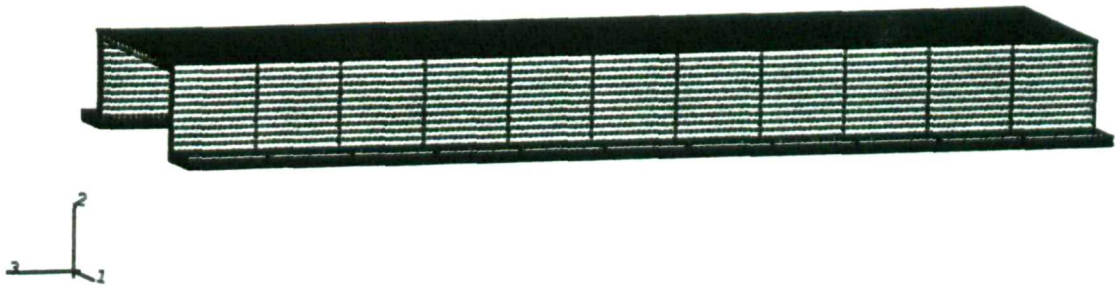


Figure 9.46: Three-dimensional finite element model of bonded component.

Table 9.6: Variation of strain energy release rate, G_{max}, with crack length calculated using finite element model. Values calculated at outside edge of component adhesive layer.

Crack length, mm	G_{max}, J/m^2
90	237
112.5	167
135	119
157.5	115
180	83

The strain energy release rate was found to be approximately constant across the width of the adhesive, though it tended to be higher at the inside edge than at the outside. For example, at a crack length of 157.5 mm, the calculated value of G_{max} was 142 J/m^2 at the inside of the component, and 115 J/m^2 at the outside. However, this was found to make little difference to the predicted values of the rate of crack growth. The mode mix also varies across the width of the adhesive layer. At the inside edge, the total strain energy release rate is dominated by the Mode I component, however at the outside, Mode II conditions dominate, see Figure 9.47. However, as discussed in Section 9.2, the fracture mechanics data from the TDCB tests is not purely mode I, as failure occurred close to the interface. Thus the data obtained in Chapter 8 can be used to predict the crack growth rate in the bonded component tests.

The difference between the calculated strain energy release rates at the inside and outside edges of the component explains the experimental observation that the crack length is longer at the inside of the component than the outside. The same strain energy release rate value is calculated for a longer crack at the inside of the component than the outside, hence the crack front is curved to maintain a constant fracture energy across the width of the adhesive layer.

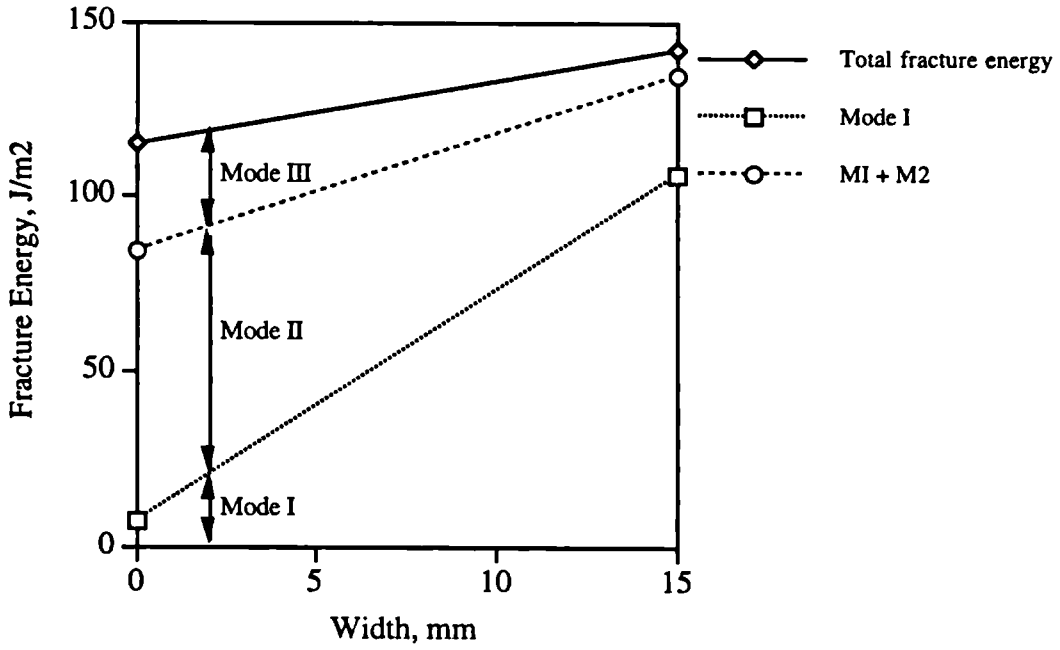


Figure 9.47: Mode mix across width of adhesive layer, bonded component. Zero width denotes outside of adhesive layer.

Hence, the FE model gives the relationship between G_{max} and crack length. Thus to predict the crack growth rate we require the relationship between da/dN and G_{max}. This can be obtained from the TDCB fatigue data discussed in Chapter 8.

9.3.3.2 Modelling the Fracture Mechanics Data

The TDCB fatigue data for steel adherends bonded with the 'AV119' adhesive, when tested 'dry', were modelled using a simple Paris law relationship of the form

$$\frac{da}{dN} = D(G_{max})^n \qquad (8.2)$$

where D and n are calculated by linear regression to the log(da/dN) versus log(G_{max}) data, neglecting the threshold data, as discussed in Section 9.2.5.4. The experimental data and the model are shown in Figure 9.48. The data from the model, plus the G_c and G_{th} values obtained from the TDCB testing, are given in Table 9.7. It should be noted that as the strain energy release rates calculated using the finite element model are greater than the measured G_{th} value, it is not necessary to model the data using the full modified Paris law, i.e. using n_1 and n_2 values.

Table 9.7: Simple Paris law model variables from TDCB test data, used with the finite element approach to predict the fatigue crack growth rate for the bonded component in 'dry' fatigue.

Adhesive fracture energy	G_c, J/m^2	450
Threshold fracture energy	G_{th}, J/m^2	85
Paris law coefficient	D, m^2/N.cycle	3.64 x 10^{-14}
Paris law exponent	n	5.61

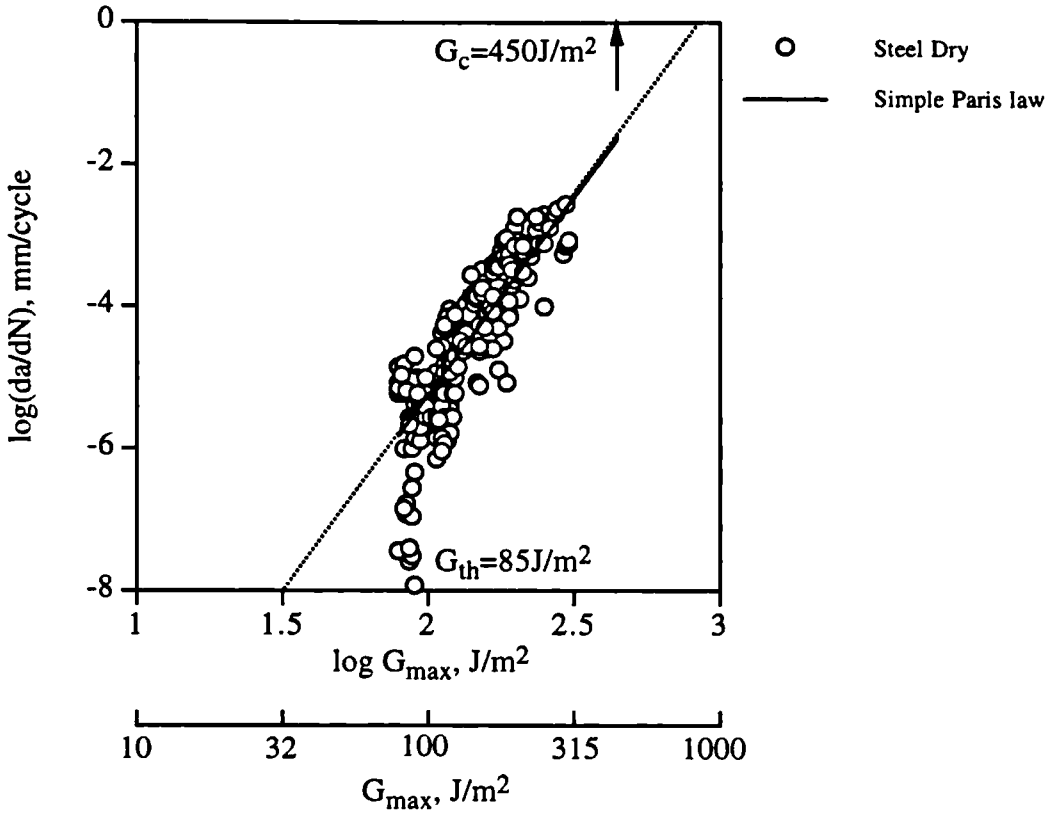


Figure 9.48: TDCB fatigue data for 'AV119' adhesive used to bond steel adherends, tested 'dry', and simple Paris law model. Also see Table 9.7.

9.3.5 Comparison of Predictions and Experimental Results

The predicted rate of crack growth per cycle, for a given crack length, was calculated using Equation 8.2, the simple Paris law

$$\frac{da}{dN} = D(G_{max})^n \qquad (8.2)$$

where D and n are obtained from the fit to the TDCB data, see Table 9.7 and Figure 9.48, and G_{max} is the value of fracture energy calculated from the finite element model at a given crack length, as shown in Table 9.6.

The experimental results and the predictions are shown in Figure 9.49. The agreement between the predicted values and the experimental data is very good. The fracture energy values were calculated at the outside edge of the component, those at the inside edge are slightly higher. Thus using the average value, or that calculated at the centre of the adhesive layer, would improve the agreement between the predictions and the experimental data.

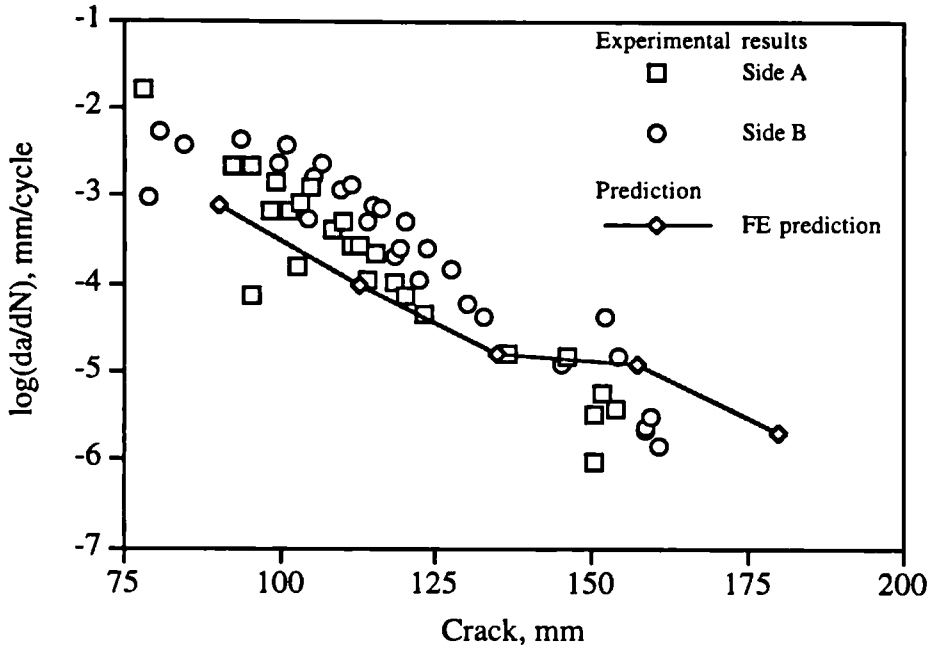


Figure 9.49: Graph of rate of crack growth per cycle versus crack length for the bonded component (log-linear axes), showing finite element predictions, using the TDCB fatigue data, and the experimental results.

9.3.5 Component Summary

Bonded components, comprising a steel 'top-hat' section bonded to a baseplate using the 'AV119' adhesive, were tested at a constant displacement rate and under fatigue loading. At a constant displacement rate failure was by stick/slip crack propagation, with an apparently interfacial locus of failure. No plastic deformation of the components was observed. The fatigue tests were conducted using a constant maximum displacement. The measured load decreased as cracks grew along the length of the component. The crack growth rate was also observed to decrease with increasing crack length. The cracks in the two arms of the component were not co-linear, probably due to some eccentricity in the loading or the component itself.

The component was modelled using a three-dimensional finite element model, allowing the variation of strain energy release rate with crack length to be calculated. The experimental fatigue fracture mechanics data was modelled using a Paris law relationship. These data allowed the rate of crack growth in the component to be predicted. The theoretical predictions were compared with the experimental results, and the agreement was found to be very good.

9.4 Conclusions

Steel lap joints bonded with the 'AV119' adhesive were tested at a constant displacement rate. These tests gave an average nominal failure stress of 24 MN/m^2. 'Wet' fatigue testing of the joints showed short lives at high applied stress levels. For example, at 60 % of the nominal failure stress from the constant displacement rate tests, joint lives of less than 10000 cycles were observed. The joint life increased with decreasing applied stress. Evidence of a threshold at around 30 to 35 % of the nominal failure stress was indicated by fatigue lives of greater than 1.5×10^7 cycles. The use of a backface strain technique showed crack growth for at least 75 % of the life of the lap joints, and in many cases almost the entire joint lifetime.

Lifetime prediction models were used to estimate the number of cycles to failure of the single lap joints from data obtained from TDCB fatigue tests. An analytical approach and a finite element approach were used to calculate the variation of strain energy release rate with crack length in the joints. The analytical approach produced conservative values of the lifetime, and predicted a threshold at about 20 % of the nominal failure stress. The threshold applied stress is the important parameter to predict as only close to this value does the lifetime of the joints become long, i.e. greater than 1×10^6 cycles. The joint lifetimes predicted using the finite element approach agreed more closely with the lifetimes observed experimentally. The predictions using both the power law and linear fits to the M versus a data gave excellent agreement with the experimental results. A threshold value of 33 % of the nominal failure stress was predicted using the linear fit to the M versus a data, compared with the 30 to 35 % observed experimentally. The predictions using this method were found to be insensitive to the initial flaw size, locus of joint failure, and whether the joint failed due to the propagation of one or two cracks.

However, further work is required to determine whether the linear relationship between M, the gradient of the load per unit width versus fracture energy data, and the crack length is indeed linear as was assumed (if not then the power law model should be used). If it is shown that the large values of M at small crack lengths are not an artefact of the FE model used, then factors such as the initial flaw size may need to be considered. However, these have been shown to have little effect on the predicted numbers of cycles as the model stands, and to have no effect on the predicted threshold.

Bonded components, consisting of a 'top-hat' section bonded to a baseplate, were tested at a constant displacement rate and using fatigue loading. Constant displacement rate tests gave a stick/slip mode of failure, with an apparently interfacial locus of failure. The components tested in 'dry' fatigue also gave an apparently interfacial failure, the adhesive remaining on the 'top-hat' section. A three-dimensional finite element model was

developed to calculate the variation of fracture energy with crack length in the component. These data, combined with the fatigue data from the TDCB tests, allowed the crack growth rate to be predicted as cracks propagated along the length of the component. The theoretical predictions were compared to the experimental data, and the agreement was found to be very good.

Thus, the present work has shown that the fatigue failure of the lap joints is dominated by propagation of cracks, and the joint can be successfully modelled using a finite element method. This allows the joint lifetime to be predicted from the fracture mechanics data obtained from TDCB tests. Further, this method can be used to predict the crack growth rate in more complex components.

Chapter Ten

Durability Performance: Summary

10.1 Introduction

This part of the present work has been concerned with the durability performance of two structural epoxy adhesives. A fracture mechanics approach was used to investigate the effect of fatigue loading in a 'dry' (55 % relative humidity at 23°C) environment. The effect of conducting the tests 'wet' (water immersion at 28°C) was also studied. The tapered double-cantilever beam (TDCB) specimen geometry was used for these tests.

The crack growth rate per cycle versus fracture energy data obtained from these tests were used to compare the durability performance of the 'LMD1142' and 'AV119' adhesives. The former is a modern, high fracture toughness adhesive, and the latter is an older generation adhesive with a low fracture toughness. These adhesives were chosen as they had been identified in the present work as possessing relatively 'good' and 'poor' impact performance respectively. Further, no durability test results have previously been published using the 'LMD1142' adhesive. Aluminium-alloy and steel adherends were used. The aluminium-alloy adherends were prepared using a chromic-acid etch (CAE), or a gritblast and degrease (GB&DG), surface treatment. Steel adherends were gritblasted and degreased.

The fracture mechanics data were also used to predict the lifetimes of single lap joints in 'wet' fatigue, and to predict the crack growth rate in a stiffener-type bonded component. The variation of applied strain energy release rate with crack length for each of these geometries was modelled using a finite element or analytical approach. These data were combined with the fracture mechanics data obtained from the TDCB tests, allowing the variation of crack growth rate with crack length to be calculated. Hence the lifetimes of the joints were predicted. The predictions were compared to experimental results.

10.2 Fracture Mechanics Tests

10.2.1 Constant Displacement Rate Tests

Constant displacement rate testing of bonded TDCB specimens at 10^{-5} m/s gave adhesive fracture energy, G_c, values of 4590 J/m^2 for the 'LMD1142' adhesive and 700 J/m^2 for the 'AV119' adhesive. For these joints, which used CAE aluminium-alloy adherends, the locus

of failure was cohesive-in-adhesive, i.e. approximately through the centre of the adhesive layer. Stick/slip crack growth occurred with the 'AV119' adhesive using the steel and the GB&DG aluminium-alloy adherends. In both cases the locus of failure was apparently interfacial and the measured fracture energy was reduced, compared to the cohesive-in-adhesive value, as shown in Table 10.1.

Table 10.1: Durability fracture mechanics data summary table, showing constant displacement rate fracture energy, G_c, values, and threshold fracture energy, G_{th}, values from fatigue tests.

Adhesive	Adherend	Surface treatment	Fracture energy G_c, J/m^2	Fatigue threshold fracture energy, G_{th}	
				'Dry', J/m^2	'Wet', J/m^2
'AV119'	Aluminium-alloy	CAE	700 C	160 C	175 O
	Aluminium-alloy	GB&DG	520 I	85 I	25 O
	Steel	GB&DG	450 I	85 I	20 O
'LMD1142'	Aluminium-alloy	CAE	4590 C	510 C	290 I

Notes:

1. Test conditions:

'Dry' 23°C, 55 % relative humidity.

'Wet' 28°C, water immersion.

2. Surface treatments:

CAE Chromic-acid etch.

GB&DG Gritblast and degrease.

3. Failure loci:

C Cohesive-in-adhesive.

I Close to interface.

O Oxide.

10.2.2 'Dry' Fatigue Tests

'Dry' fatigue tests were conducted using the TDCB specimens. All tests showed a threshold value of the fracture energy, G_{th}, below which crack growth does not occur. The value of this threshold depended on the adhesive, adherend, surface treatment and test environment used. The threshold fracture energy was far lower than the adhesive fracture energy, G_c, measured at a constant displacement rate. For example, the 'AV119' adhesive was found to have a G_c value of about 700 J/m^2, however in 'dry' fatigue (23°C and approximately 55 % relative humidity) a threshold fracture energy of 160 J/m^2 was measured. Similarly, the threshold fracture energy of the 'LMD1142' adhesive was measured to be 510 J/m^2, compared with a G_c value of 4590 J/m^2. In these cases, the failures were cohesive-in-adhesive. These data are summarised in Table 10.1.

Scanning electron microscopy (SEM) of the fracture surfaces of both adhesives after constant displacement rate and 'dry' fatigue testing showed that the locus of failure was cohesive-in-adhesive in both cases, using the CAE aluminium-alloy adherends. The fracture surfaces of the specimens tested at a constant displacement rate of 10^{-5} m/s showed large numbers of cavitated rubber particles. However, there were few cavitated rubber particles present on the fracture surfaces after fatigue testing. Thus the reductions in fracture energy, from a constant displacement rate to a threshold value in 'dry' fatigue, are due to the reduction in the amount of rubber particle cavitation. Hence the toughening mechanisms are less effective, and less energy is absorbed during fracture, under fatigue loading.

When failure occurred close to the interface, using the 'AV119' adhesive with the steel or the GB&DG aluminium-alloy adherends, the threshold fracture energy was reduced to 85 J/m^2. The lower value of the fracture energy associated with this locus of failure is expected, as the plastic zone size will be restricted by the presence of the adherend. Further, this value is approximately half that measured when cohesive-in-adhesive failure occurs, as would be expected when the plastic zone was approximately half the size due to the presence of the adherend.

10.2.3 'Wet' Fatigue Tests

The 'wet' fatigue tests were conducted in water at 28°C, and a reduction in the threshold fracture energy value was measured in most cases, as may be seen from Table 10.1. The exceptions were the specimens using the 'AV119' adhesive to bond chromic-acid etched (CAE) aluminium-alloy adherends, where the value of G_{th} was virtually unaffected, and actually increased slightly from 160 to 175 J/m^2. The threshold fracture energy value for the GB&DG surface treatment using both the aluminium-alloy and steel adherends was

reduced, from 85 J/m^2 (in both cases under 'dry' conditions) to 25 and 20 J/m^2 respectively under 'wet' conditions. The locus of failure for all the 'wet' tests using the 'AV119' adhesive was through the metal oxide, although XPS and AES did indicate that some residual adhesive was present on the fracture surfaces.

The value of G_{th} for the 'LMD1142' adhesive was reduced from 510 J/m^2 to 290 J/m^2 by the 'wet' environment, as shown in Table 10.1, using the CAE treated aluminium-alloy adherends. However, these values are both considerably lower than the G_c value of 4590 J/m^2 measured at a constant displacement rate. It is thought that a combination of adhesive displacement from the interface and weakening of the oxide by the presence of water cause the reductions in joint performance under the 'wet' fatigue conditions.

The TDCB fatigue data are summarised in Table 10.1, which lists the measured values of G_c and the threshold fracture energies. The 'AV119' adhesive shows better durability than the 'LMD1142' adhesive (using the CAE treated aluminium-alloy adherends) if the G_{th} values are expressed as a proportion of the constant displacement rate, G_c, value. For 'AV119' both the 'dry' and 'wet' G_{th} values are approximately 0.25 of G_c. However, the G_{th} values for the 'LMD1142' are 0.11 and 0.06 of G_c respectively. Thus, on this comparative basis, the adhesive with the lower G_c value, and the poor impact performance exhibits the better durability. The specimens using the CAE surface treatment for the aluminium-alloy adherends exhibited better durability than those using the GB&DG treatment. This may be due to improved wetting, or the oxide produced by the CAE treatment may be intrinsically stronger. The TDCB fatigue data are summarised in Table 10.1, which lists the measured values of G_c and the threshold fracture energies, G_{th}.

10.3 Predicting the Lifetime of Bonded Joints

10.3.1 Introduction

The fracture mechanics data obtained using the TDCB tests were used to predict the lifetime of two types of bonded joint geometries. The single lap joint and a stiffener-type bonded component were chosen. For each of these geometries, the variation of applied strain energy release rate, G, with crack length was modelled using a finite element or an analytical approach, and the fracture mechanics data used to predict the lifetime of the joint. The mechanics of crack propagation in the single lap joints were also investigated.

10.3.2 Crack Mechanics

A backface strain technique was used to investigate the crack growth in the single lap joints under fatigue loading in a 'wet' environment. This work encountered some

problems using strain gauges under water immersion, as the water could cause short-circuits. However, crack growth, either from one or both ends of the joint, was detected for at least 75 % of the joint life, and for almost 100 % in many cases. Thus most of the joint life is associated with the propagation, rather than the initiation, of cracks.

10.3.3 Lap Joints

Steel lap joints bonded using the 'AV119' adhesive were tested at a constant displacement rate, and a nominal failure stress of 24 MN/m^2 was measured. 'Wet' fatigue tests were performed at between 30 and 90 % of this nominal failure stress. This work showed an increasing joint life with decreasing applied stress, and indicated a fatigue threshold, below which failure does not occur, at 30 to 35 % of the nominal failure stress.

Lifetime prediction models were developed and used to predict the fatigue lives of the bonded lap joints, using the fracture mechanics data from the 'wet' TDCB fatigue tests. This approach modelled the variation of strain energy release rate with crack length in the lap joints using an analytical and a finite element method. Knowledge of the crack growth rate for a given fracture energy from the TDCB tests allowed the joint lifetimes to be predicted. The analytical method produced conservative values of the lifetime, and predicted a fatigue threshold at about 20 % of the nominal failure stress. The joint lifetimes predicted using the finite element method agreed more closely with those observed experimentally. This novel approach predicted a fatigue threshold value of about 33 % of the nominal failure stress, which compares well with the 30 to 35 % measured experimentally. This value was found to be relatively insensitive to the initial flaw size, and whether failure occurred by the propagation of either one or two cracks.

10.3.4 Component

A finite element method was also used to predict the rate of crack growth in a bonded component, using the fracture mechanics data from the TDCB fatigue tests. This novel work used a finite element model to calculate the variation of strain energy release rate, G, versus crack length. Hence the predicted rate of crack growth could be calculated using the fracture mechanics data. The agreement between the rate of crack growth values predicted using this method and the experimental data was found to be very good.

Chapter Eleven

Conclusions

11.1 Introduction

The increasing use of adhesives in many industries has shown that it is necessary to evaluate in detail the performance of adhesive joints, especially as the mechanical properties of the joints tend to decrease with impact loading, with fatigue loading, and with exposure to moisture. The main aims of the present work were therefore to investigate how structural epoxy adhesives perform under these conditions when used to bond steel or aluminium-alloy adherends.

The present work can be conveniently divided into two parts. Firstly, various methods were used to evaluate the impact performance of a range of rubber-toughened structural epoxy adhesives. Secondly, the effect of cyclic loading (i.e. dynamic fatigue loading) and an aqueous environment on the performance of a high and a low impact performance adhesive system was investigated. A theme that is common to both parts of the work is the use of a fracture mechanics approach (i) to quantify the performance of the joints, (ii) to study the mechanisms of failure, and (iii) to predict the behaviour and lifetime of bonded joints and components.

11.2 Impact Performance

11.2.1 Introduction

The impact testing studies investigated the effect of increasing the test rate on the performance of a range of structural epoxy adhesives. Three test methods were used: firstly the tapered double-cantilever beam (TDCB) test, secondly the three-point bend (TPB) test, and thirdly the impact wedge-peel (IWP) test. The first two of these are fracture mechanics methods, and the values of the adhesive fracture energies, G_c, obtained were compared. The three-point bend test was additionally used to compare the performance of bulk adhesive and joint specimens. The impact wedge-peel test is a recently introduced International Standard test method, which is becoming popular in industry to evaluate the impact properties of combinations of adhesives and adherends. The values obtained from the fracture mechanics tests were compared to the IWP cleavage-force values, measured using the IWP test, to investigate whether any correlations could be drawn between the methods.

11.2.2 Tapered Double-Cantilever Beam Tests

The adhesive fracture energies, G_c, of a range of structural epoxy adhesives were measured using the tapered double-cantilever beam (TDCB) geometry over a range of test rates between 10^{-5} and 1 m/s. A range of analysis methods were used to calculate the adhesive fracture energy, and good agreement was found between all the analysis methods used. Thus at test rates of 1 m/s and below, any of the methods of analysis described in the present work may be used to calculate the fracture energy for the TDCB test. However, the simplest analysis method to use is the force method, as only the force versus time data are required. Other methods of analysis using the test rate and average crack velocity may be also be used successfully, although these require data to be obtained using high-speed photography.

All the adhesives tested showed a reduction in the adhesive fracture energy with increasing test rate. A maximum reduction of 36 % was measured as the test rate was increased from 10^{-5} to 1 m/s, i.e. as the crack velocity was increased from approximately 10^{-4} to 20 m/s. Scanning electron microscopy showed that the reduction in performance was caused by a reduction in the amount of rubber particle cavitation, and hence in the extent of the toughening mechanisms occurring around the crack tip within the adhesive.

11.2.3 Three-Point Bend Tests

Three-point bend (TPB) tests were performed using bulk adhesive and joint specimens using the 'AV119' adhesive. At the high test rates used (0.3 to 2 m/s), large oscillations in the force versus time response of the three point bend specimens were recorded, due to dynamic effects. These were more significant using the pendulum testing machine than using the servo-hydraulic machine, probably because in the former case the striker is falling freely rather than being driven. These oscillations were reduced by damping the contact between the striker and the specimen.

The data showed a reduction in the adhesive fracture energy with increasing test rate and decreasing time to failure. The agreement between the fracture energies obtained using the bulk and joint specimens, and using the two testing machines, was excellent for a given time to failure, i.e. for a similar effective loading rate.

11.2.4 Comparison of Test Methods

All the joints were found to fail via cohesive-in-adhesive fracture, i.e. approximately through the centre of the adhesive layer. The adhesive fracture energy, G_c, values obtained using the TDCB tests were compared to those obtained using the TPB tests. The

agreement between the data from the two different tests, when the G_c values were plotted against the test rate, was found to be very good; thus the fracture energy of the adhesive is predominantly dependent on the test rate. However, the TPB test method is more time-consuming than the TDCB test, requiring a large number of specimens to be tested. Thus, the tapered double-cantilever beam test is the simpler method of measuring the adhesive fracture energy, G_c, as a function of test rate.

11.2.5 Impact Wedge-Peel Tests

The impact wedge-peel (IWP) test is a relatively new International Standard method for the impact testing of adhesive joints, and is becoming a popular test in industry. The present work has shown that the ISO Standard method for the analysis of the data from these tests can give misleading results in some cases. An improved method for analysing the experimental data has been identified in the present work. This calculates the average cleavage-force over an interval of 25 to 90% of the test, if only stable crack growth occurs during this period. If unstable failure occurs, then a zero value should be quoted. Further, this improved method of analysis gives results that are independent of the specimen profile used, and thus improves the precision of the results.

The results from the impact wedge-peel tests (using this improved method of analysis) showed a linear correlation between the wedge cleavage-force and the adhesive fracture energy, G_c, measured using the TDCB tests for equal crack velocities of 2 m/s. Further, this relationship is unique for each set of test conditions, e.g. test temperature, test rate and adherend material. The gradient of this correlation is dependent on the adherend material used; the use of steel adherends results in a steeper gradient than using aluminium-alloy adherends due to the higher modulus of the steel. The concept of a limiting value of the adhesive fracture energy in order to obtain stable crack propagation has also been identified. The limiting value is dependent on the test conditions, and increases with increasing test rate and decreasing temperature. It is dependent on the adherend properties, the limiting fracture energy value increasing with the yield stress of the adherend. This value has the potential to be used as a design criterion.

A finite element model was developed and used to predict the IWP cleavage-force from the measured value of the adhesive fracture energy, G_c. The agreement between the predicted values and the experimental results was very good, for both the steel and the aluminium-alloy adherends.

Thus, it has been found that the impact wedge peel test gives an indication of the performance of the adhesive/adherend combination, data which cannot be obtained

directly from the other test methods. However, the impact wedge-peel performance may be quantitatively modelled from a knowledge of the fracture energy of the adhesive, assuming that failure is cohesive-in-adhesive, as is observed experimentally.

11.3 Durability Performance

11.3.1 Introduction

The durability studies presented in the present work have investigated the effect of fatigue loading, in both 'dry' and 'wet' environments, on the measured fracture energies of two structural epoxy adhesives. Chromic-acid etched or gritblasted and degreased aluminium-alloy, or gritblasted and degreased steel, adherends were used. The data obtained were used to compare the durability performance of two adhesives, the 'LMD1142' and 'AV119' adhesives. The former is a modern, high fracture toughness adhesive, and the latter is an older generation adhesive with a relatively low fracture toughness. These adhesives were chosen as they had been identified in the present work as possessing 'good' and 'poor' impact performance respectively.

The fracture mechanics data obtained using the fatigue tests were also used to predict the lifetime of two bonded joint geometries. The single lap joint and a stiffener-type component were chosen. For each of these the variation of applied strain energy release rate with crack length was modelled, allowing the fracture mechanics data to be used to predict the lifetimes of the joints. The mechanics of crack propagation in the single lap joints were also investigated.

11.3.2 Fracture Mechanics Fatigue Tests

Constant displacement rate testing of bonded TDCB specimens at 10^{-5} m/s gave adhesive fracture energy, G_c, values of 4590 J/m^2 for the 'LMD1142' adhesive and 700 J/m^2 for the 'AV119' adhesive, using chromic-acid etched aluminium-alloy adherends. These were for cohesive-in-adhesive failure. Stick/slip failure occurred with the steel specimens, and using the GB&DG aluminium-alloy adherends, with the 'AV119' adhesive, and the measured fracture energy was reduced, compared to the cohesive-in-adhesive value, due to the change on the locus of failure to an apparently interfacial one.

'Wet' and 'dry' cyclic fatigue tests were conducted using the TDCB specimens. All tests showed a threshold value of the fracture energy, G_{th}, below which crack growth does not occur. The value of this threshold depended on the adhesive, adherend, surface treatment and test environment used. The threshold fracture energy was far lower than the constant displacement rate adhesive fracture energy, G_c. For example, the 'AV119' adhesive was

found to have a G_c value of about 700 J/m^2, however in 'dry' fatigue the threshold fracture energy was 160 J/m^2. Both failures were cohesive-in-adhesive. Scanning electron microscopy showed that the reductions in performance were caused by reductions in the extent of the toughening mechanisms occurring within the adhesive, due to less rubber particle cavitation.

The results obtained in the present work, and those available in the literature, show that although some adhesives possess a very high constant displacement rate adhesive fracture energy, G_c, this does not imply that the fatigue performance will be good. Indeed, those adhesives with a low G_c value frequently perform better in fatigue. The two adhesives tested using fatigue loading in the present work rank as intermediate when the ratio of G_{th}/G_c is considered, where G_{th}/G_c is 0.11 for the 'LMD1142' adhesive and 0.23 for the 'AV119'. The data that are available in the literature give a range of G_{th}/G_c values of 0.03 to 0.33.

The value of G_{th} was reduced when the fatigue tests were conducted in water. For example, apparently interfacial failure occurred using the 'AV119' adhesive with gritblasted and degreased aluminium-alloy adherends, and a G_{th} value of only 25 J/m^2 was recorded. This compares with a G_c value of 520 J/m^2. Thus there is a 95 % reduction between the value of G_c and the fatigue threshold, G_{th}, for a 'wet' fatigue test using the 'AV119' adhesive, with gritblasted and degreased aluminium-alloy adherends. This reduction is caused by the locus of failure moving to within the metal oxide, hence reducing the energy absorbed by the adhesive during fracture. Generally the chromic-acid etch treatment resulted in the better durability. This may be due to improved wetting, or the oxide produced by the CAE treatment may be intrinsically stronger. The TDCB fatigue data are summarised in Table 10.1, which lists the measured values of G_c and the threshold fracture energies, G_{th}.

11.3.3 Bonded Single Lap Joints

A backface strain technique was used to investigate the crack growth in single lap joints under fatigue loading. This work encountered some problems using strain gauges under water immersion, as the water could cause short-circuits. However, crack growth, either from one or both ends of the joint, was detected for at least 75 % of the joint life, and for almost 100 % in some cases. Thus most of the joint life is associated with the propagation, rather than the initiation, of cracks.

Steel lap joints bonded with the 'AV119' adhesive were tested at a constant displacement rate, and a nominal failure stress of 24 MN/m^2 was measured. 'Wet' fatigue tests were

performed at between 30 and 90 % of this nominal failure stress. This novel work showed an increasing joint life with decreasing applied stress, and indicated a fatigue threshold, below which failure does not occur, at 30 to 35 % of the nominal failure stress. The presence of this threshold allows a safe operating stress to be defined, such that failure of the joint will not occur.

Lifetime prediction models were developed and used to predict the fatigue lives of the bonded lap joints using the fracture mechanics data from the TDCB fatigue tests. The variation of strain energy release rate, G, with the length of the fatigue crack in the lap joints was modelled using an analytical and a finite element method. Knowledge of the crack growth rate for a given fracture energy from the TDCB tests allowed the joint lifetimes to be predicted. The analytical method produced conservative values of the lifetime, and predicted a fatigue threshold at about 20 % of the nominal failure stress. The joint lifetimes predicted using the finite element method agreed more closely with those observed experimentally. This approach, developed in the present studies, predicted a fatigue threshold value of about 33 % of the nominal failure stress, which compares well with the 30 to 35 % measured experimentally. This value was found to be insensitive to the initial flaw size, the locus of failure, and whether failure occurred by the propagation of either one or two cracks.

11.3.4 Bonded Component

A finite element model was developed and used to predict the rate of crack growth in a bonded component, using data from the TDCB fatigue tests. The model allowed the variation of strain energy release rate versus crack length to be calculated. Hence the predicted rate of crack growth could be calculated using the TDCB data. The agreement between the predicted values and the experimental data was found to be very good.

11.4 Concluding Remarks

The present work has shown that exposure to an aqueous environment is more detrimental to joint strength than impact conditions. The impact TDCB tests showed reductions in fracture energy of up to 36 % when the test rate was increased from 10^{-5} to 1 m/s. However cyclic fatigue in a 'dry' environment reduced the fracture energy by at least 70 %. Testing in a 'wet' environment, i.e. with the specimen immersed in water, could reduce the fracture energy by over 95 %. The values quoted for the durability tests represent the threshold values, below which crack growth does not occur. Such threshold values were identified for all test combinations.

Although the reduction in performance in fatigue and with exposure to water is greater than that for impact loading, the impact performance of adhesives is important, as the reduction in performance at high test rates can be large. Further, good durability performance does not imply good impact performance. Thus any reduction in performance should be evaluated; this is especially true for sectors such as the automotive industry, one of the major uses for structural adhesives being in cars and trucks.

The present work has shown that fracture mechanics can be used to quantify the performance of adhesives under a wide range of test conditions. Further, the data obtained can be used to predict quantitatively the performance of other joint geometries under similar test conditions, at high test rates, or using fatigue loading, either 'dry' or 'wet'. The ability to predict the performance of bonded structures is of critical importance to industry, and will result in more confidence in the use of adhesives in structural applications.

Chapter Twelve

Recommendations for Future Work

12.1 Introduction

The present work has shown that the performance of adhesively-bonded metal joints is reduced by impact and fatigue loading. A further reduction is caused by water immersion. Further, the modelling work has shown that the performance of joints may be predicted using fracture mechanics data. However, the present work has also identified areas where there is insufficient data available, or where more work is required than could be performed within the time constraints of the present work. This Chapter identifies these areas, and makes some recommendations as to how future work could address the issues raised.

12.2 Impact Wedge-Peel Tests

The present work has investigated the effect of test rate and temperature on the measured IWP cleavage-force using a range of epoxy adhesives. However, the ISO Standard allows a range of adherend thicknesses to be used, so future work should investigate the effect of the adherend thickness on the measured cleavage-force.

This work has identified that the IWP cleavage-force is dependent on the material properties of the adherends. However, it is not absolutely clear how differences in the modulus and yield stress of the adherends independently affect the measured values. Thus further tests using aluminium-alloy and steel adherends of the same thickness and modulus as those used in the present work, but with different yield stresses should be performed.

There are little data available concerning the effect of test rate on the properties of sheet metal adherends. Thus material property data at high test rates is required to enable the impact wedge-peel cleavage-force to be predicted at high rate using the finite element model of the impact wedge-peel test. It would also be useful to obtain data at all the temperatures used in the present work, i.e. -40, 20 and 60°C. This data would also confirm whether the changes in the measured force are indeed caused by changes in the modulus and yield stress of the adherends. To allow accurate comparisons to be made, it

would be useful to obtain the material property data at approximately the same strain rate as is observed using the IWP tests.

The lack of high rate material property data is probably because there is no Standard method governing how these data should be obtained. Thus work is required to identify a preferred method for obtaining these data.

The finite element model of the impact wedge-peel test also requires some changes to shorten the time taken to complete a prediction. Ideally the model should be programmed to calculate the strain energy release rate at the crack tip using the universal crack closure method automatically, make an adjustment to the time step (and hence the wedge displacement) used, and recalculate the IWP cleavage-force. This process would iterate until the calculated strain energy release rate was equal to the fracture energy of the adhesive. Currently the strain energy release rate is calculated manually, and the time step adjusted by the user. Thus the model requires constant attention. Further, the model should be simplified to reduce the time taken for a single run, currently approximately 2 hours. As it stands, it is quicker to measure the wedge cleavage-force experimentally than it is to use the finite element model to predict the cleavage-force.

It would also be useful to include a more realistic value of the contact stiffness between the wedge and the specimen in the FE model. The use of an elastic/plastic contact would be better than the rigid/elastic contact currently used. This would allow the initial slope of the force versus time response to be predicted more accurately.

12.3 Fracture Mechanics Durability Tests

The fatigue fracture mechanics tests using the TDCB specimens were successfully used to obtain the data required for the lifetime predictions. However, each test requires its own servo-hydraulic testing machine, a single test lasting for three or four weeks. Thus to enable repeat tests to be performed ties up equipment for a considerable length of time. Accelerating the tests, for example by increasing the temperature, is not advisable as the mechanism of failure may be changed, as discussed in Chapter 2. A better solution is to test several specimens using a single testing machine. As the TDCB tests are conducted using displacement control, the same displacement would be applied to each specimen, and the force measured using a load-cell attached to each specimen. This new testing arrangement would reduce the time required to obtain these data.

12.4 Crack Mechanics

It would be useful to calibrate the backface strain technique used to detect crack growth in the single lap joint fatigue tests against another method of measuring the crack length. This would allow the crack growth to be quantified. Possible non-destructive methods that may be used to measure the crack length include ultrasonics and dye penetrant, either visually or using x-rays. The penetrant method requires the joints to be fatigued until crack growth is detected using the backface strain technique. The test would then be stopped and the penetrant added. The visual penetrants could probably be used in-situ, though the joint must be removed from the testing machine if an x-ray penetrant is used. It is also possible to use ultrasonics in-situ, though poor resolution can be expected at short crack lengths and at the edges of the specimen. Alternatively the joint could be tested destructively, after immersing it in liquid nitrogen. The extent of the fatigue crack growth could then be measured from inspection of the fracture surfaces. However, destructive methods only allow a single crack length to be taken from each specimen, whereas non-destructive methods allow multiple readings to be taken. Another possible method is to mark the fracture surface at intervals by changing the frequency of the loading, a technique which is used during fatigue fracture testing of metals. However, the use of this method would require further investigation, as it is not certain how well this technique works with the structural epoxy adhesives used in the present work.

12.5 Lifetime Prediction Modelling

The lifetime prediction modelling of the bonded single lap joints was very successful. However, further work is required to determine whether the linear or power law model of the relationship between M, the gradient of the load per unit width versus fracture energy data, and the crack length is the more accurate. The gradient of the M versus crack length, a, relationship was found to increase rapidly at small crack lengths. However, this may be an artefact of the finite element model, which may be investigated by using a finer mesh at the ends of the joint overlap. If it is shown that the large values of M at small crack lengths are not an artefact of the finite element model used, then factors such as the initial flaw size may need to be considered. However, these have been shown to have no effect on the predicted numbers of cycles as the model stands. Alternatively, it may be better to use a different method of modelling the strain energy release rate versus applied load and crack length data, rather than using M.

It is also possible to model the relationship between G_{max} and T_{max} by plotting G_{max} versus $(T_{max})^2$. This relationship is even more linear over the range of values used than the G_{max} versus T_{max} relationship used in the present work. However, the use of this method

makes little difference to the predicted joint lifetimes. This requires some further work to investigate which is the preferred method.

The lifetime prediction modelling work assumed that the relationship between the rate of crack growth, da/dN, and the maximum applied fracture energy, G_{max}, is the same for mode II loading as that measured for mode I. It would be useful to perform mode II fracture mechanics tests using the 'AV119' adhesive to determine the relationship between da/dN and G_{max} under these conditions. These data would allow any effect on the predicted lifetimes to be evaluated.

The mesh used for the FE modelling of the bonded component could be refined to provide more detailed rate of crack growth predictions. A finer mesh would allow the fracture energy to be calculated at more points along the length of the component. The effect of the variation of the value of G_{max} across the width of the component should also be considered. Although this variation has been shown to be relatively small, its inclusion will improve the prediction, although the agreement between the prediction and the experimental data is already very good.

The present work has shown that fracture mechanics durability data can be used to predict accurately the lifetime of simple bonded joints and components. This work can now be extended to 'commercial' bonded joints, for example by testing an industrial product which contains a bonded joint and predicting its performance. A possible first step could be to use a component that includes bonded stiffeners, for example the doors or bonnets of cars and trucks, as the present work has shown that the crack growth rate in this type of component can be predicted.

References

1. International Standards Organisation, *Adhesives - Determination of Peel Resistance of High-Strength Adhesive Bonds Under Impact Conditions - Impact Wedge Method.* ISO, 1993. **11343**.

2. Dann, J.R., *Forces Involved in the Adhesive Process I: Critical Surface Tensions of Polymeric Solids as Determined with Polar Liquids.* J. Colloid Interf. Sci., 1970. **32**(2): pp. 302 - 320.

3. Dann, J.R., *Forces Involved in the Adhesive Process II: Nondispersion Forces at Solid-Liquid Interfaces.* J. Colloid Interf. Sci., 1970. **32**(2): pp. 321 - 331.

4. Comyn, J., *Contact Angles and Adhesive Bonding.* Int. J. Adhesion & Adhesives, 1992. **12**(3): pp. 145 - 149.

5. Poole, P. and Watts, J., *Effect of Alloy Composition and Surface Pretreatment on the Durability of Adhesive-Bonded Aluminium Alloy Joints.* Int. J. Adhesion & Adhesives, 1985. **5**(1): pp. 33 - 39.

6. Kinloch, A.J., *Adhesion And Adhesives: Science And Technology.* 1987, Chapman Hall: London.

7. Tabor, D. and Winterton, R.H.S., *The Direct Measurement of Normal and Retarded van der Waals Forces.* Proc. Roy. Soc. London, 1969. **A.312**: pp. 435 - 450.

8. Johnson, K.L., Kendall, K., and Roberts, A.D., *Surface Energy and the Contact of Solids.* Proc. Roy. Soc. London, 1971. **A.324**: pp. 301 - 313.

9. Israelachvili, J.N. and Tabor, D., *The Measurement of van der Waals Dispersion Forces in the Range 1.5 to 130 nm.* Proc. Roy. Soc. London, 1972. **A.331**: pp. 19 - 38.

10. Packham, D.E., *Engineering the Interface in Composites and Bonded Components.* J. Adhesion, 1995. **54**: pp. 133 - 143.

11. Critchlow, G.W. and Brewis, D.M., *Influence of Surface Macroroughness on the Durability of Epoxide-Aluminium Joints.* Int. J. Adhesion & Adhesives, 1995. **15**: pp. 173 - 176.

12. Vasenin, R.M., *Adhesion of High Polymers Part I: The Phenomenon of Adhesion.* Adhesives Age, 1965. (May): pp. 21 - 25.

13. Vasenin, R.M., *Adhesion of High Polymers Part II: Predicting Adhesion.* Adhesives Age, 1965. (May): pp. 30 - 35.

14. Vasenin, R.M., *Problems in the Diffusion Theory of Adhesion of Polymers,* in *Adhesion, Fundamentals and Practice.* 1969, McLaren & Son: London. pp. 29 - 36.

15. Voyutskii, S.S., *The Diffusion Theory of Adhesion.* Rubber Chem. Tech., 1960. **33**: pp. 748 - 756.

16. Currie, J. Depelsenaire, P., Goleau, R., and Sacher, E., *A Nuclear Scattering Evaluation of Organometallic Bonding in the Adhesion of Metallization to Polymers.* J. Colloid Interf. Sci., 1984. **97**(2): pp. 401 - 422.

17. Derjaguin, B.V. and Smilga, V.P., *Electronic Theory of Adhesion,* in *Adhesion, Fundamentals and Practice.* 1969, McLaren & Son: London. pp. 152 - 163.

18. Andrews, E.H. and Kinloch, A.J., *Mechanics of Adhesive Failure I.* Proc. Roy. Soc. London, 1973. **A.332**: pp. 385 - 399.

19. Andrews, E.H. and Kinloch, A.J., *Mechanics of Adhesive Failure II.* Proc. Roy. Soc. London, 1973. **A.332**: pp. 401 - 414.

20. Kinloch, A.J., *Interfacial Fracture Mechanical Aspects of Adhesive Bonded Joints - A Review.* J. Adhesion, 1979. **10**(3): pp. 193 - 219.

21. Gledhill, R.A. and Kinloch, A.J., *Environmental Failure of Structural Adhesive Joints.* J. Adhesion, 1974. **6**: pp. 315 - 330.

22. Gent, A.N. and Kinloch, A.J., *Adhesion of Viscoelastic Materials to Rigid Substrates. III. Energy Criterion for Failure.* J. Polymer Sci., 1971. **A2**(9): pp. 659 - 668.

23. Kinloch, A.J., Welch, L.S., and Bishop, H.E., *The Locus of Environmental Crack Growth in Bonded Aluminium Joints.* J. Adhesion, 1984. **16**: pp. 165 - 178.

24. Bishopp, J.A. and Thompson, G.E., *The Role of Electron Microscopy in the Study of Adhesion to Aluminium Substrates.* Surface Interface Anal., 1993. **20**: pp. 485 - 494.

25. Luksepp, T. and Janssen, I., *Personal Communication.* 1996, AB Volvo, Goteburg, Sweden.

26. Davis, R.E. and Fay, P.A., *Personal Communication.* 1995, Ford Motor Company, Basildon.

27. Bond, A.E., *A Review of Industrial Case Histories.* Report, 1995, MTS Adhesives Programme.

28. Mazza, J.J. *Grit Blast/Silane Surface Treatment for Structural Bonding of Aluminium,* in Proceedings of *Adhesion Society,* in Proceedings of *Nineteenth Annual Meeting of the Adhesion Society,* Myrtle Beach, USA. 1996, T.C. Ward, Editor. The Adhesion Society: Blacksburg, USA. pp. 94 - 97.

29. Hertzberg, R.W. and Manson, J.A., *Fatigue of Engineering Plastics.* 1980, Academic Press: New York, USA.

30. Kunz, S.C. and Beaumont, P.W.R., *Low-Temperature Behaviour of Epoxy-Rubber Particulate Composites.* J. Mater. Sci, 1981. **16**: pp. 3141 - 3152.

31. Huang, Y., *Microstructure-Property Relationships in Toughened Epoxy Polymers.* PhD Thesis, 1991, Imperial College of Science, Technology & Medicine: University of London.

32. Huang, Y. and Kinloch, A.J., *Modelling of the Toughening Mechanisms in Rubber-Modified Epoxy Polymers, Part I: Finite Element Analysis Studies.* J. Mater. Sci, 1992. **27**: pp. 2753 - 2762.

33. Huang, Y. and Kinloch, A.J., *Modelling of the Toughening Mechanisms in Rubber-Modified Epoxy Polymers, Part II: A Quantitative Description of the Microstructure-Fracture Property Relationships.* J. Mater. Sci, 1992. **27**: pp. 2763 - 2769.

34. Li, D., Li, X., and Yee, F.F., *The Role of Cavitation in Rubber Particles in the Deformation of Rubber Toughened Epoxy under Constrained Conditions,* in *American Chemical Society Division of Polymeric Materials: Science and Engineering.* 1990. American Chemical Society: Washington, USA.

35. Kinloch, A.J., Maxwell, D.L., and Young, R.J., *Micromechanisms of Crack Propagation in Hybrid-Particulate Composites.* J. Mater. Sci. Lett., 1985. **4**: pp. 1276 - 1279.

36. Kinloch, A.J., Maxwell, D.L., and Young, R.J., *The Fracture of Hybrid-Particulate Composites.* J. Mater. Sci, 1985. **20**: pp. 4169 - 4184.

37. Griffith, A.A., *The Phenomena of Rupture and Flow in Solids.* Phil. Trans. Roy. Soc. London, 1920. **221**: pp. 163 - 198.

38. Irwin, G.R., *Structural Aspects of Brittle Fracture.* Appl. Mater. Res., 1964. **3**(2): pp. 65 - 81.

39. Caddell, R.M., *Deformation and Fracture of Solids.* 1980, Prentice-Hall: Englewood Cliffs, USA.

40. Orowan, E., *Fracture and Strength of Solids.* Reports on Progress in Physics, 1948. **12**: pp. 185 - 232.

41. Irwin, G.R., *Fracture Strengths Relative to Onset and Arrest of Crack Propagation.* Testing Materials, 1958. **58**: pp. 640 - 657.

42. Westergaard, H.M., *Bearing Pressures and Cracks.* J. Appl. Mech., 1939. (June): pp. A-49 - A-53.

43. Dugdale, D.S., *Yielding of Steel Sheets Containing Slits.* J. Mech. Phys. Solids, 1960. **8**: pp. 100 - 104.

44. Industrial Advisory Group, *Minutes of Meeting.* 1995, (June). MTS Adhesives Programme.

45. Powell, P.C., *Engineering with Polymers.* 1983, Chapman & Hall: London.

46. Gordon, J.E., *The New Science of Strong Materials.* 1978, Penguin Books: London.

47. Blackman, B.R.K., *The Fracture Behaviour Of Bonded Polymeric Fibre-Composites.* PhD Thesis, 1993, Imperial College of Science, Technology & Medicine: University of London.

48. Williams, J.G., *Fracture Mechanics of Polymers.* 1984, Ellis Horwood: Chichester.

49. Kinloch, A.J., Kodokian, G.A., and Jamarani, M.B., *Impact Properties Of Epoxy Polymers.* J Mater. Sci, 1987. **22**: pp. 4111 - 4120.

50. American Society for Testing and Materials, *Standard Test Method for Impact Strength of Adhesive Bonds.* ASTM, 1982. **D950**.

51. British Standards Institute, *Determination of Impact Resistance of Adhesive Bonds.* BS, 1986. **5350**.

52. Taylor, A.C., *Impact Testing of Adhesive Joints.* Report, 1996, MTS Adhesives Programme.

53. Adams, R.D. and Harris, J.A., *A Critical Assessment of the Block Impact Test for Measuring the Impact Strength of Adhesive Bonds.* Int. J. Adhesion & Adhesives, 1996. **16**: pp. 61 - 71.

54. Hart-Smith, L.J., *Designing to Minimize Peel Stresses in Adhesive-Bonded Joints.* ASTM STP, 1985. **876**: pp. 238 - 266.

55. Tomczyk, A.J., *Tensile Impact Testing of Adhesively Bonded Thin Lap Shear Joints.* Report, 1995, MTS Adhesives Programme:

56. Knott, J.F. and Elliott, D., *Worked Examples in Fracture Mechanics.* 1979, Institute of Materials: London.

57. American Society for Testing and Materials, *Standard Methods for Notched Bar Impact Testing of Metallic Materials.* ASTM, 1986. **E23**.

58. European Structural Integrity Society, *A Linear Fracture Mechanics (LEFM) Standard for Determining K_c and G_c for Plastics.* ESIS Protocol, 1990.

59. Kinloch, A.J. and Kodokian, G.A., *Impact Behaviour of Structural Adhesive Joints.* J. Mater. Sci. Lett., 1987. **6**: pp. 653 - 655.

60. Jamarani, F., Jakusik, R., Kinloch, A.J., and Kodokian, G.K.A. *Experimental and Analytical Studies of the Fracture Behaviour of Engineering Adhesives and Adhesive Joints Under Impact Loading,* in *Adhesion 14.* 1990. Elsevier Applied Science: London.

61. Williams, J.G., *The Analysis of Dynamic Fracture Using Lumped Mass-Spring Models.* Int. J. of Frac., 1987. **33**: pp. 47 - 59.

62. Williams, J.G. and Adams, G.C., *The Analysis of Instrumented Impact Tests Using a Mass-Spring Model.* Int. J. of Frac., 1987. **33**: pp. 209 - 222.

63. Gledhill, R.A., Kinloch, A.J., and Shaw, S.J., *A Model for Predicting Joint Durability.* J. Adhesion, 1980. **11**: pp. 3 - 15.

64. American Society for Testing and Materials, *Standard Test Method for Plane-Strain Fracture Toughness and Strain-Energy Release Rate of Plastic Materials.* ASTM, 1991. **D5045**.

65. Jethwa, J.K., *The Fatigue Performance of Adhesively-Bonded Metal Joints.* 1995, PhD Thesis, Imperial College of Science, Technology and Medicine: University of London.

66. Hashemi, S., Kinloch, A.J., and Williams, J.G., *The Analysis of Interlaminar Fracture in Uniaxial Fibre-Polymer Composites.* Proc. Roy. Soc. London, 1990. **A.427**: pp. 173 - 199.

67. Mostovoy, S. and Ripling, E.J., *Fracture Toughness of an Epoxy System.* J. Appl. Polymer Sci., 1966. **10**: pp. 1351 - 1371.

68. Jethwa, J.K. and Kinloch, A.J., *The Fatigue and Durability Behaviour of Adhesive Systems for Automobile Applications,* in Proceedings of *Nineteenth Annual Meeting of the Adhesion Society,* Myrtle Beach, USA. 1996, T.C. Ward, Editor. The Adhesion Society: Blacksburg, USA. pp. 469 - 473.

69. Kinloch, A.J., *Environmental Attack at Metal-Adhesive Interfaces,* in *Polymer Surfaces and Interfaces,* W.J. Feast & H.S. Munro, Editors. 1987, J. Wiley & Sons: New York, USA. pp. 75 - 97.

70. Kerr, C., MacDonald, N.C., and Orman, S., *Effect of Hostile Environments on Adhesive Joints, III. Role of Simple Alcohols with Unstressed Epoxide Adhesive.* British Polymer Journal, 1970. **2**: pp. 71 - 72.

71. Brewis, D.M., Comyn, J., Kinloch, A.J., and Raval, A.K., *Is There a Critical Relative Humidity for the Weakening of Joints in Wet Air?* in Proceedings of *Adhesion '90,* Cambridge. 1990, Plastics & Rubber Institute: London. pp. 28/1 - 28/6.

72. Davis, R.E. and Fay, P.A., *The Effect of a Tropical Environment and Stress on Bonded Steel Joints,* in Proceedings of *Adhesion '90,* Cambridge. 1990, Plastics and Rubber Institute: London. pp. 27/1 - 27/6.

73. Jackson, R.S., *The Effects of Water on the Peel Behaviour of Adhesive Joints.* PhD Thesis, 1997, Imperial College of Science, Technology & Medicine: University of London.

74. Dickie, R.A., DeBolt, M.A., and Ward, S.M., *Stress Durability Testing of Adhesively Bonded Steel.* SAE Technical Paper Series, 1995. **950128.**

75. Comyn, J., *Kinetics and Mechanisms of Environmental Attack,* in *Durability of Structural Adhesives,* A.J. Kinloch, Editor. 1983, Applied Science Publishers: London. pp. 85 - 134.

76. Anon., *Water Uptake in Adhesives.* Report, 1995, Oxford Brookes University.

77. Ebtahaj, K., *Personal Communication.* 1996. Oxford Brookes University.

78. Brewis, D.M., Comyn, J., and Tegg, J.L., *The Durability of Some Epoxide Adhesive-Bonded Joints on Exposure to Moist Warm Air.* Int. J. Adhesion & Adhesives, 1980. **1**: pp. 35 - 39.

79. Lefebvre, D.R. and Raju, V.R., *Degradation of Epoxy Coatings in Humid Environments: The Critical Relative Humidity,* in Proceedings of *Adhesion '90,* Cambridge. 1990. Plastics & Rubber Institute: London.

80. Bowditch, M.R., *The Durability of Adhesive Joints in the Presence of Water.* Int. J. Adhesion & Adhesives, 1996. **16**: pp. 73 - 79.

81. Anon., *Environmental Durability of Adhesive Bonds: Development of Experimental Database.* Report, 1994, DTI MTS Programme.

82. Bolger, J.C., *Acid Base Interactions between Oxide Surfaces and Polar Organic Compounds,* in *Adhesion Aspects of Polymer Coatings,* K.L. Mittal, Editor. 1983, pp. 3 - 18.

83. Gosselin, C.A., *Effect of Surface Preparation on the Durability of Structural Adhesive Bonds,* in *Polymeric Materials for Corrosion Control.* 1986, American Chemical Society: Washington, USA. pp. 181 - 193.

84. Watts, J.F., Castle, J.E., and Hall, T.J., *The Effect of Water on the Failure Mechanism of Adhesive Joints.* J. Mater. Sci. Lett., 1988. **7**: pp. 176 - 178.

85. Watts, J.F., Blunden, R.A., and Hall, T.J., *The Failure Mode of Adhesively Bonded Aluminium Following Aqueous Exposure.* Surface Interface Anal., 1990. **16**: pp. 227 - 235.

86. Kinloch, A.J., *Introduction,* in *Durability of Structural Adhesives,* A.J. Kinloch, Editor. 1983, Applied Science Publishers: London. pp. 1 - 39.

87. Minford, J.D., *Durability of Structural Adhesive Bonded Aluminium Joints.* Adhesives Age, 1978. **21**(March): pp. 17 - 23.

88. Davies, R.J. and Kinloch, A.J., *The Surface Characterisation and Adhesive Bonding of Aluminium.* Report, 1989, Imperial College of Science, Technology and Medicine: University of London.

89. Davis, G.D., Whisnant, P.L., and Venables, J.D., *Subadhesive Hydration of Aluminium Adherends and its Detection by Electrochemical Impedance Spectroscopy.* J. Adhesion Sci. & Tech., 1995. **9**: pp. 433 - 442.

90. Venables, J.D., *Adhesion and Durability of Metal-Polymer Bonds.* J. Mater. Sci, 1984. **19**: pp. 2431 - 2453.

91. Cayless, R.A., *Interfacial Chemistry and Adhesion: the Role of Surface Analysis in the Design of Strong Stable Interfaces for Improved Adhesion and Durability.* Surface Interface Anal., 1991. **17**: pp. 430 - 438.

92. Roberts, S.S.J. and Yates, T., *Property Measurement of Bulk Adhesives.* Report, 1994, DTI MTS Adhesives Programme.

93. Zanni-Deffarges, M.P. and Shanahan, M.E.R., *Bulk and Interphase Effects in Aged Structural Joints.* J. Adhesion, 1994. **45**: pp. 245 - 257.

94. Jurf, R.A. and Vinson, J.R., *Effect of Moisture on the Static and Viscoelastic Shear Properties of Epoxy Adhesives.* J Mater. Sci, 1985. **20**: pp. 2979 - 2989.

95. Mackie, R.I. and Su, N. *The Effect of Aging and Environment on the Performance of Adhesive Joints*, in Proceedings of *Structural Adhesives in Engineering III*, Bristol. 1992, Institute of Materials: London. pp. 29/1 - 29/6.

96. Crank, J., *Mathematics of Diffusion.* 1957, Oxford University Press: Oxford.

97. Zanni-Deffarges, M.P. and Shanahan, M.E.R., *Diffusion of Water into an Epoxy Adhesive: Comparison between Bulk Behaviour and Adhesive Joints.* Int. J. Adhesion & Adhesives, 1995. **15**(3): pp. 137 - 142.

98. Stevenson, A. and Priest, A.M., *Durability and Life Prediction of Adhesive Bonds in Severe Environments.* Rubber Chem. Tech., 1991. **64**(4): pp. 545 - 558.

99. Cognard, J., *Use of the Wedge Test to Estimate the Lifetime of an Adhesive Joint in an Aggressive Environment.* Int. J. Adhesion & Adhesives, 1986. **6**(4): pp. 215 - 220.

100. Brockmann, W., Hennemann, O.D., Kollek, H., and Matz, C., *Adhesion in Bonded Aluminium Joints for Aircraft Construction.* Int. J. Adhesion & Adhesives, 1986. **6**(3): pp. 115 - 143.

101. Bowditch, M.R. and Stannard, K.J., *Adhesive Bonding of GRP.* Composites, 1982. (July): pp. 298 - 304.

102. Anon., *Environmental Durability of Adhesive Bonds: Environmental Durability Test Procedures.* Report, 1993, MTS Adhesives Programme.

103. Critchlow, G.W. and Brewis, D.M., *Aspects of Metal-to-Metal Adhesion*, in Proceedings of *Structural Adhesives in Engineering IV*, Bristol, 1995. Institute of Materials: London. pp. 293 - 302.

104. Sharpe, L., *Some Aspects of the Performance of Adhesive Joints.* Applied Polymer Symposia, 1966. **3**: pp. 353 - 359.

105. Toh, T.C.K., *The Fatigue Behaviour of Adhesively Bonded Aluminium Lap Joints.* Report, 1994, Imperial College of Science, Technology and Medicine: University of London.

106. Osiyemi, S.O., *The Fatigue Performance of Adhesively Bonded Fibre-Composite Joints.* PhD Thesis, 1992, Imperial College of Science, Technology and Medicine: University of London.

107. Kinloch, A.J. and Osiyemi, S.O., *Predicting the Fatigue Life of Adhesively-Bonded Joints.* J. Adhesion, 1993. **43**: pp. 79 - 90.

108. Martin, R.H. and Murri, G.B., *Characterization of Mode I and Mode II Delamination Growth and Thresholds in AS4/PEEK Composites.* ASTM STP, 1990. **1059**: pp. 251 - 270.

109. Chang, T., Sproat, E.A., Lai, Y., Shephard, N.E., and Dillard, D.A., *Testing Methods for Accelerated Humidity Conditioning and Estimation of Adhesive Bond Durability.* J. Adhesion, to be published.

110. Jackson, R.S., Kinloch, A.J., Gardham, L.M., and Bowditch, M.R., *A Study of the Effects of Water Concentration on the Stability of Interfaces in Adhesive Joints.* in Proceedings of *Euradh '96,* Cambridge. 1996, Institute of Materials: London.

111. Harjoprayitno, W.W., *The Fatigue Performance of Adhesively Bonded Al-Alloy Joints.* MSc Thesis, 1993, Imperial College of Science, Technology and Medicine: University of London.

112. Luckyram, J. and Vardy, A.E., *Fatigue Performance of Two Structural Adhesives.* J. Adhesion, 1988. **26**: pp. 273 - 291.

113. Xu, X., Crocombe, A., and Smith, P., *Fatigue Crack Growth Rates in Adhesive Joints Tested at Different Frequencies.* J. Adhesion, 1995. **58**: pp. 191 - 204.

114. Blackman, B.R.K., *Personal Communication.* 1996, Imperial College of Science, Technology and Medicine.

115. British Standards Institute, *Aluminium and Aluminium Alloys - Sheets, Strips and Plates - Part 2 : Mechanical Properties.* BS, 1995. **EN-485-2.**

116. Alcan Plate, *Materials Data Sheet.* Alcan Plate, Birmingham.

117. British Standards Institute, *Aluminium and Aluminium Alloys - Chemical Composition and Form of Wrought Products - Part 3: Chemical Composition.* BS, 1994. **EN-573-3.**

118. Bull, S.J., Bellamy, B.A., Bishop, H.E., Watts, J.F., and Brewis, D., *The Role of Surface Analysis in Adhesive Bonding.* Report, 1995. MTS Adhesives Programme.

119. King, F., *Aluminium and its Alloys.* 1987, Ellis Horwood: Chichester.

120. Bishopp, J.A., Jobling, D., and Thompson, G.E., *The Surface Pretreatment of Aluminium-Lithium Alloys for Structural Bonding.* Int. J. Adhesion & Adhesives, 1990. **10**(3): pp. 153 - 160.

121. Critchlow, G., *Personal Communication.* 1996, Institute of Surface Science and Technology, Loughborough University.

122. American Society for Testing and Materials, *Fracture Strength in Cleavage of Adhesives in Bonded Joints.* ASTM, 1975. **D3433.**

123. Wang, Y. and Williams, J.G., *Dynamic Crack Growth in TDCB Specimens.* Int. J. Mech. Sci., 1996. **38**(10): pp. 1073 - 1088.

124. Mülhaupt, R. and Buchholz, U., *Compatibilized, Segmented Liquid Rubbers as Epoxy-Toughening Agents,* in *Toughened Plastics II: Novel Approaches in Science and Engineering,* C.K. Riew and A.J. Kinloch, Editors. 1996, American Chemical Society: Washington. pp. 75 - 94.

125. Kinloch, A.J. and Kodokian, G.A., *The Impact Resistance Of Structural Adhesive Joints.* J. Adhesion, 1987. **24**: pp. 109 - 126.

126. Sampson, T., *Personal Communication.* 1995, AEA Technology, Harwell.

127. Kalthoff, J.F., *On The Measurement Of Dynamic Fracture Toughness - A Review Of Recent Work.* Int. J. of Frac., 1985. **27**: pp. 277 - 298.

128. MacGillivray, H.J. and Chong, M.J.C., *Personal Communication.* 1996, Imperial College of Science, Technology and Medicine.

129. Marshall, G.P., Williams, J.G., and Turner, C.E., *Fracture Toughness and Absorbed Energy Measurements in Impact Tests on Brittle Materials.* J. Mater. Sci, 1973. **8**: pp. 949 - 956.

130. Holmes, B., *Personal Communication.* 1995, Ciba Polymers, Duxford.

131. Fay, P.A., Davis, R.E., and Suthurst, G.D., *Impact Testing and Performance of Bonded Automotive Structures,* in Proceedings of *Impact and Fatigue Testing of Adhesives*, London. 1990, Plastics and Rubber Institute: London.

132. Powell, J.H., *Impact Testing of Adhesives : Peel Joints,* in Proceedings of *Impact and Fatigue Testing of Adhesives*, London, 1990, Plastics and Rubber Institute: London.

133. Thouless, M., Adams, J., Kafkalidis, M., Ward, S., Dickie, R., and Westerbeek, G., *Determining the Toughness of Adhesives in Plastically-Deforming Joints.* J. Mater. Sci., to be published.

134. Dickie, R.A. and Ward, S.M., *Durability of Automotive Adhesive Bonds: Test Methods and Failure Mechanisms.* J. Adhesion Sci. & Tech., to be published.

135. Blackman, B.R.K., Dear, J.P., Kinloch, A.J., MacGillivray, H., Wang, Y., Williams, J.G., and Yayla, P., *The Failure of Fibre-Composites and Adhesively-Bonded Fibre-Composites Under High Rates of Test, Part I : Mode I Loading - Experimental Studies.* J. Mater. Sci, 1995. **30**: pp. 5885 - 5900.

136. Hashemi, S., Kinloch, A.J., and Williams, J.G., *The Effects of Geometry, Rate and Temperature on the Mode I, Mode II and Mixed-Mode I/II Interlaminar Fracture of Carbon-Fibre/Poly(ether-ether ketone) Composites.* Journal of Composite Materials, 1990. **24**: pp. 918 - 956.

137. Farruggio, C.S., *Experimental Studies of Neck Formation and Propagation in Polyethylene.* Report, 1996, Imperial College of Science, Technology and Medicine: University of London.

138. Saechtling, H., *International Plastics Handbook for the Technologist, Engineer and User.* 1987, Hanser: Munchen.

139. The Aluminium Federation, *The Properties of Aluminium and its Alloys.* 7th ed. Information Bulletin 2. 1973, The Aluminium Federation: Birmingham.

140. Crofton, S., *Personal Communication.* 1997, Imperial College of Science, Technology & Medicine.

141. ASM International Handbook Commitee, *Aluminium and Aluminium Alloys - ASM Speciality Handbook.* Davis, J.R., Editor, 2nd ed. 1994, ASM: Washington, USA.

142. Teed, P.L., *The Properties of Metallic Materials at Low Temperatures.* 1950, Chapman & Hall: London.

143. National Bureau of Standards, *Mechanical Properties of Metals and Alloys.* 1943, United States Department of Commerce: Washington, USA.

144. Wang, Y., *Personal Communication.* 1995, Imperial College of Science, Technology and Medicine.

145. Ashby, M.F. and Jones, D.R.H., *Engineering Materials I: An Introduction to their Properties and Applications.* 1980, Pergamon Press: Oxford.

146. Dean, G.D. and Duncan, B.C., *Tensile Behaviour of Bulk Specimens of Adhesives.* Report, 1995, MTS Adhesives Programme.

147. Rybicki, E.F. and Kanninen, M.F., *A Finite Element Calculation of Stress Intensity Factors by a Modified Crack Closure Integral.* Eng. Frac. Mech., 1977. **9**: pp. 931 - 938.

148. Greer, A. and Hancock, D.J., *Tables, Data and Formulae for Engineers.* 1984, Stanley Thornes: Cheltenham.

149. Jethwa, J.K. and Kinloch, A.J., *The Fatigue Performance of Adhesively Bonded Metal Joints,* in *Conference Proceedings of Adhesion '93*, Cambridge. 1993, Institute of Materials: London. pp. 197 - 202.

150. Fernando, M., Harjoprayitno, W.W., and Kinloch, A.J., *A Fracture Mechanics Study of the Influence of Moisture on the Fatigue Behaviour of Adhesively-Bonded Aluminium-Alloy Joints.* Int. J. Adhesion & Adhesives, to be published.

151. Liaw, P.K., Hartmann, H.R., and Helm, E.J., *Corrosion Fatigue Crack Propagation Testing with the Krak-Gage in Salt Water.* Eng. Frac. Mech., 1983. **18**(1): pp. 121 - 131.

152. Oba, T., *Personal Communication.* 1996. Imperial College of Science, Technology and Medicine.

153. Watts, J.F., *An Introduction to Surface Analysis by Electron Spectroscopy.* 1990, Oxford Science Publications: Oxford.

154. Watts, J.F., *X-Ray Photoelectron Spectroscopy.* Vacuum, 1994. **45**(6/7): pp. 653 - 671.

155. Dyson, I.N., Fernando, M., Kinloch, A.J., and Shaw, S.J., *Unpublished Data.* .

156. Gettings, M., Baker, F.S., and Kinloch, A.J., *Use of Auger and X-Ray Photoelectron Spectroscopy to Study the Locus of Failure of Structural Adhesive Joints.* J. Appl. Polymer Sci., 1977. **21**: pp. 2375 - 2392.

157. Fernando, M. and Dyson, I.N., *Personal Communication.* 1996, Imperial College of Science, Technology and Medicine.

158. American Society for Testing and Materials, *Strength Properties of Adhesives in Shear by Tension Loading (Metal-to-Metal).* ASTM, 1983. **D1002**.

159. Harris, J.A. and Fay, P.A., *Fatigue Life Evaluation of Structural Adhesives for Automotive Applications.* Int. J. Adhesion & Adhesives, 1992. **12**(1): pp. 9 - 18.

160. Zhang, Z., Shang, J.K., and F.V. Lawrence, J., *A Backface Strain Technique for Detecting Fatigue Crack Initiation in Adhesive Joints.* J. Adhesion, 1995. **49**: pp. 23 - 36.

161. Imanaka, M., Haraga, K., and Nishikawa, T., *Fatigue Strength of Adhesive/Rivet Combined Lap Joints.* J. Adhesion, 1995. **49**: pp. 197 - 209.

162. Zhao, X., Adams, R.D., and Pavier, M.J. *A New Approach to Determining the Bending Moment Factors in Single Lap Joints.* in Proceedings of *Adhesion '90*, Cambridge. 1990. Plastics and Rubber Institute: London.

163. Williams, J.G., *On the Calculation of Energy Release Rates for Cracked Laminates.* Int. J. of Frac., 1988. **36**: pp. 101 - 119.

164. Adams, R. and Peppiatt, N., *Effect of Poisson's Ratio Strains in Adherends on Stresses of an Idealized Lap Joint.* J. Strain Anal., 1973. **8**(2): pp. 134 - 139.

165. Charlalambides, M., Kinloch, A.J., Wang, Y., and Williams, J.G., *On the Analysis of Mixed-Mode Fracture.* Int. J. of Frac., 1992. **54**: pp. 269 - 291.

166. Duer, R., Katevatis, D., Kinloch, A.J., and Williams, J.G., *Comments on Mixed-Mode Fracture in Adhesive Joints.* Int. J. of Frac., 1996. **75**: pp. 157 - 162.

167. Curley, A., *Personal Communication.* 1996. Imperial College of Science, Technology and Medicine.

168. Jeffrey, *Mathematics for Engineers and Scientists.* 1985, Billing & Sons: Worcester.

169 Kinloch, A.J., Shaw, S.J., and Hunston, D.L., *Deformation and Fracture Behaviour of a Rubber-Toughened Epoxy: 1. Microstructure and Fracture Properties.* Polymer, 1983. **24**(October): pp. 1341 - 1354.

Appendix One

Material Properties for FE Modelling

Material properties used for finite element modelling. Terms are defined in Figure A4.1, below. Modulus and yield data for adherend materials are from tensile tests. Epoxy adhesive data are taken from the literature[146]. The material models for the adherend materials are shown, along with example tensile test data, in Figures A4.2 and A4.3.

Epoxy adhesive, 'AV119'

Modulus	E_a, GN/m^2	3.0
Poissons ratio	υ	0.4

Aluminium-alloy 'EN AW 5251'

Modulus	E_s, GN/m^2	69
Yield stress	σ_y, MN/m^2	140
Plastic stress	σ_p, MN/m^2	160
Plastic strain	ε_p, %	0.6
Poissons ratio	υ	0.33

Steel 'EN 3A'

Modulus	E_s, GN/m^2	206
Yield stress	σ_y, MN/m^2	180
Plastic stress	σ_p, MN/m^2	250
Plastic strain	ε_p, %	1.1
Poissons ratio	υ	0.33

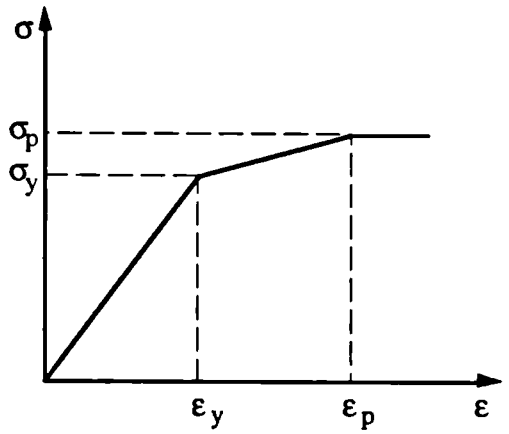


Figure A4.1: General material model used in finite element modelling.

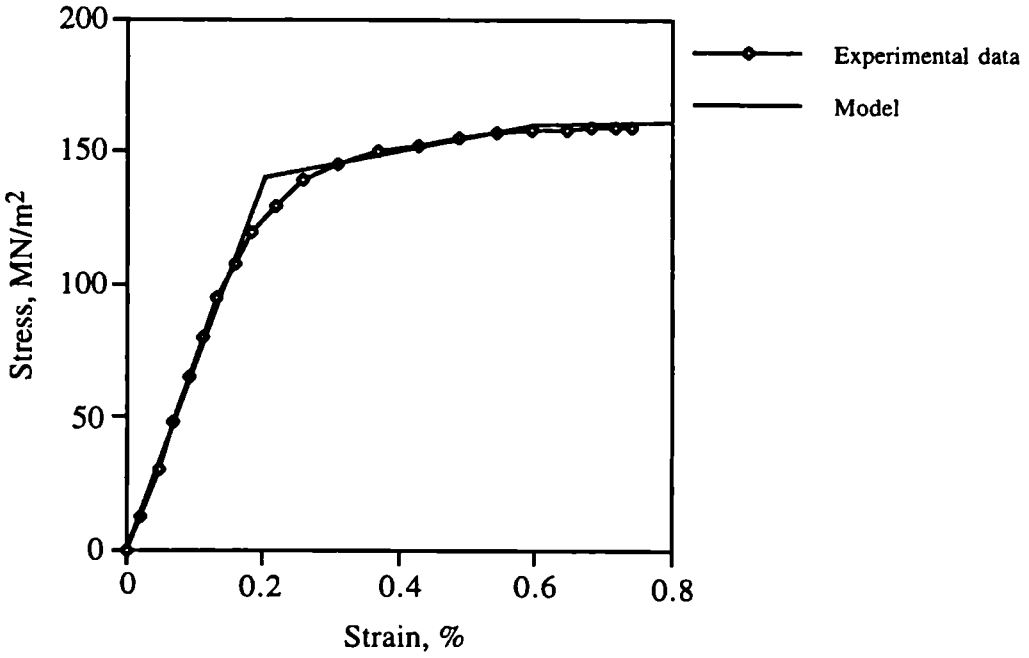


Figure A4.2: Material model for aluminium-alloy adherends ('EN AW 5251') superimposed on experimental data from tensile test at 10^{-5} m/s and 20°C.

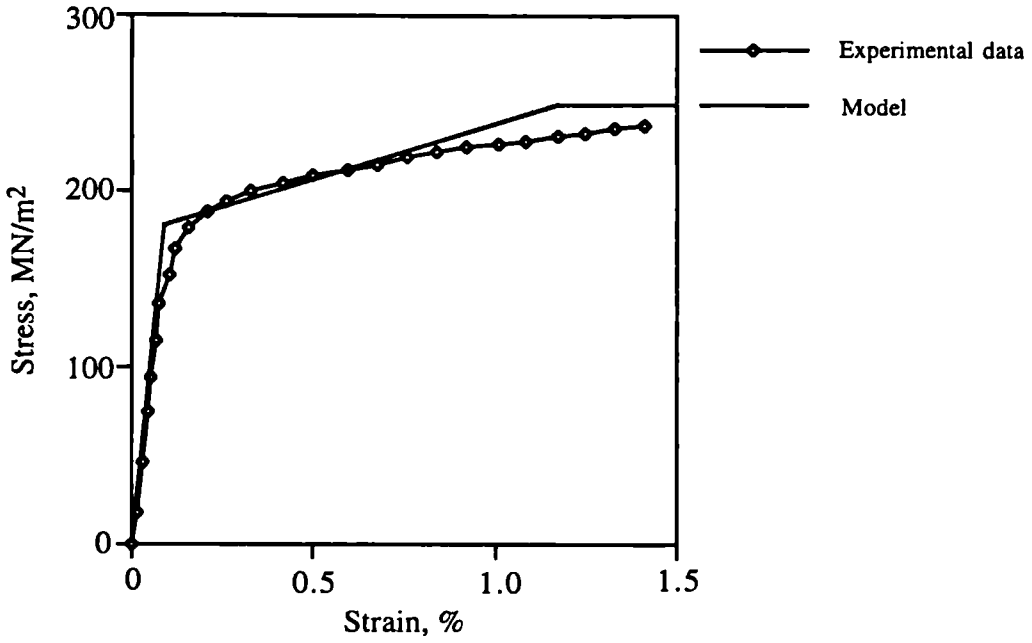


Figure A4.3: Material model for steel adherends ('EN 3A') superimposed on experimental data from tensile test at 10^{-5} m/s and 20°C.

Appendix Two

TDCB Impact Tests, Example Results

Table A2.1: Example results for 'LMD1142' adhesive at a test rate of 10^{-5} m/s, showing fracture energies calculated using methods described in Chapter 4. Average G_c using crack velocity method is 4.40 kJ/m^2.

Crack length, mm	Force, kN	Displacem. mm	Fracture energy, G_c, kJ/m^2			Crack velocity, mm/min
			Force	Force / displacem.	Displacem.	
	0	0				
75	1.85	2.76	3.76	3.34	2.96	
80	1.92	3.10	4.05	3.65	3.28	7.35
85	1.95	3.40	4.18	3.82	3.50	8.33
90	1.97	3.67	4.26	3.94	3.64	9.26
95	2.02	4.07	4.48	4.24	4.02	6.25
100	2.06	4.44	4.66	4.48	4.31	6.76
105	2.05	4.78	4.62	4.57	4.53	7.35
110	2.05	4.96	4.62	4.53	4.45	13.89
115	2.05	5.23	4.62	4.57	4.52	9.26
120	2.05	5.42	4.62	4.54	4.46	13.16
125	2.03	5.64	4.53	4.49	4.45	11.36
130	2.02	5.82	4.48	4.43	4.38	13.89
135	2.05	6.02	4.62	4.48	4.35	12.50
140	2.07	6.29	4.71	4.56	4.42	9.26
145	2.06	6.50	4.66	4.53	4.40	11.90
150	2.03	6.78	4.53	4.50	4.47	8.93
155	2.00	7.12	4.39	4.50	4.62	7.35
160	2.00	7.25	4.39	4.44	4.49	19.23
165	2.00	7.48	4.39	4.44	4.50	10.87
170	1.95	7.58	4.18	4.26	4.35	25.00
175	1.94	7.66	4.13	4.16	4.19	31.25
180	1.93	7.74	4.09	4.07	4.04	31.25
		Average	**4.51**	**4.47**	**4.43**	**11.15**

Appendix Three

Three Point Bend Tests, ϕ Values and Example Results

Table A3.1: Table of geometry factor for three point bend test, ϕ, as a function of the proportion of cracked depth, a/d, from[58]. Intermediate values may be obtained by interpolation.

a/d	ϕ
0.05	1.502
0.10	0.857
0.15	0.641
0.20	0.526
0.25	0.449
0.30	0.391
0.35	0.345
0.40	0.307
0.45	0.275
0.50	0.246
0.55	0.220
0.60	0.195
0.65	0.170
0.70	0.145
0.75	0.120
0.80	0.096
0.85	0.072
0.90	0.049
0.95	0.025

Table A3.2: Example three point bend test results, bulk 'AV119' specimens tested at 2 m/s on high speed servo-hydraulic machine. Calculated values for energy absorbed are given for all tests. The final column shows those tests where the dynamic effects were less than the ±5% specified by the ESIS protocol[58], see Figure 5.12.

Specimen	Notch, a, mm	Dimensions, mm Height, d	Width, b	a / d	ϕ	$bd\phi$, $m^2 \times 10^{-4}$	Damping, mm	Max. Force, N	Time to Fail., ms	Energy, J	<5% Dyn Energy, J
AV5-2	0.83	12.07	9.96	0.0688	1.2599	1.5146	0.25	534	0.30	0.1165	0.1165
AV5-3	1.34	12.12	10.17	0.1106	0.8114	1.0001	0.25	467	0.26	0.1081	-
AV5-4	2.42	12.13	10.15	0.1995	0.5271	0.6490	0.25	379	0.22	0.0930	0.0930
AV5-5	4.08	12.12	10.16	0.3366	0.3573	0.4400	0.25	287	0.25	0.0765	0.0765
AV5-5A	3.96	12.16	10.15	0.3257	0.3674	0.4535	0.40	599	0.30	0.0696	-
AV5-6	7.74	12.17	10.14	0.6360	0.1770	0.2185	0.40	115	0.25	0.0422	0.0422
AV6-2	0.88	12.13	10.00	0.0725	1.2111	1.4691	0.25	343	0.35	0.1007	-
AV6-3	1.34	12.11	9.99	0.1107	0.8110	0.9811	0.25	331	0.35	0.0921	0.0921
AV6-4	2.50	12.12	9.99	0.2062	0.5163	0.6257	0.25	231	0.30	0.0579	0.0579
AV6-5	4.06	12.10	10.04	0.3355	0.3583	0.4353	0.25	172	0.30	0.0409	-
AV6-5A	3.93	12.10	10.01	0.3248	0.3682	0.4460	0.40	158	0.26	0.0366	-
AV8-3	1.39	12.07	9.98	0.1152	0.7915	0.9534	0.25	553	0.32	0.1444	-
AV8-4	2.52	12.06	9.86	0.2090	0.5122	0.6091	0.25	217	0.30	0.0538	0.0538
AV8-4A	2.50	12.01	9.89	0.2082	0.5134	0.6099	0.25	188	0.28	0.0433	-
AV8-5	4.02	12.09	9.98	0.3325	0.3611	0.4357	0.25	149	0.24	0.0329	-
AV8-6	7.77	11.96	9.90	0.6497	0.1702	0.2015	0.25	56	0.10	0.0578	0.0578
AV11-3	1.29	12.08	10.13	0.1068	0.8277	1.0128	0.10	543	0.24	0.1082	0.1082
AV11-4	2.65	12.09	10.13	0.2192	0.4964	0.6080	0.25	425	0.27	0.1044	0.1044
AV11-5	4.09	12.13	10.14	0.3372	0.3568	0.4389	0.40	284	0.25	0.0643	-
AV11-6	8.12	12.07	10.13	0.6727	0.1586	0.1940	0.65	93	0.50	0.0324	-
AV11-6A	8.17	12.12	10.15	0.6741	0.1580	0.1940	0.65	97	0.40	0.0352	-

Appendix Four

Confidence Limits for Linear Regression

Linear regression using the least squares method allows a linear relationship to be fitted to experimental data, and a t-distribution may be used to find a confidence interval for the gradient of this fitted line[168]

The experimental data is composed of n pairs of observations (x_1, y_1), (x_2, y_2), ..., (x_i, y_i). We wish to fit a linear relationship of the form

$$Y = aX + b \tag{A4.1}$$

The least squares method minimises the sum of the squares of the deviation of the points from this linear relationship (the deviations are in the Y-direction). The sum of the squares of the deviations, S, is given by

$$S = \sum_{i=1}^{n} (ax_i + b - y_i)^2 \tag{A4.2}$$

To obtain the minimum value of S, we require that $S/a = 0$ and $S/b = 0$, thus

$$\sum_{i=1}^{n} (ax_i + b - y_i) = 0 \tag{A4.3}$$

and

$$\sum_{i=1}^{n} x_i (ax_i + b - y_i) = 0 \tag{A4.4}$$

Solving this pair of equations for the required parameters a and b gives the familiar expressions

$$a = \frac{\sum_{i=1}^{n} (x_i y_i) - n\overline{xy}}{\sum_{i=1}^{n} (x_i^2) - n\overline{x}^2} \tag{A4.5}$$

and

$$b = \bar{y} - a\bar{x} \tag{A4.6}$$

where $\bar{x}$ and $\bar{y}$ are the mean values of x_i and y_i respectively.

Although we have found the gradient, a, of the best linear relationship to the data, there is no indication of the likely variation. The value, a, that we have obtained is a sample estimate of the true gradient, $\tilde{a}$. Thus a confidence interval may be obtained for the true gradient $\tilde{a}$ of the regression line of Y on X. This assumes that the errors in y_i are normally distributed with the same variance, and that the n pairs of observations are independent.

The confidence interval for the true gradient $\tilde{a}$, of which a is the sample estimate is defined as

$$a - \alpha \leq \tilde{a} \leq a + \alpha \tag{A4.7}$$

where α is given by

$$\alpha = \beta \left[\frac{\sum_{i=1}^{n} \left[a(x_i - \bar{x}) - (y_i - \bar{y}) \right]^2}{(n-2)\sum_{i=1}^{n} \left[x_i^2 \right] - n\bar{x}^2} \right]^{1/2} \tag{A4.8}$$

where β is the parameter appropriate to the chosen confidence level, for a system with (n-2) degrees of freedom. The values of β are tabulated in Table A4.1.

The confidence intervals applied to the experimental data discussed in Chapter 5, the three point bend tests, are shown in Table A4.2.

Table A4.1: Values of parameter β for confidence levels of 90, 95 and 99 %, from[168].

Degrees of freedom (n-2)	Confidence level 90 %	95 %	99 %
2	2.920	4.303	9.925
4	2.132	2.776	4.604
6	1.943	2.447	3.707
8	1.860	2.306	3.355
10	1.812	2.228	3.169
20	1.725	2.086	2.845
30	1.697	2.042	2.750
40	1.684	2.021	2.704
50	1.678	2.011	2.682
∞	1.645	1.960	2.576

Table A4.2: Confidence limits for three point bend tests in present work, for confidence levels of 90 and 95 %.

Specimen type, test rate and testing machine used	a	90 % α	90 % a + α	90 % a - α	95 % α	95 % a + α	95 % a - α
Bulk 0.3 m/s HSSHM	950	143	1083	807	173	1123	777
Joint 0.3 m/s HSSHM	693	118	811	576	145	838	549
Bulk 0.5 m/s Pendulum	633	226	859	407	285	918	349
Bulk 2 m/s HSSHM	521	207	728	314	257	777	264
Joint 2 m/s HSSHM	256	39	296	217	49	305	208

Appendix Five

Impact Wedge-Peel Tests, Example Results

Example results from impact wedge peel tests on steel specimens bonded with 'XB5315' adhesive, test rate 2 m/s and 20°C. Results are calculated for the intervals as defined in Figure 6.16. The duration of these intervals and the average wedge-cleavage force are shown. The energy absorbed is also given, calculated by integration over the intervals. The mean values and standard deviation are calculated for the series of four tests.

Specimen number	Velocity, m/s	Whole			Peak		
		Time, ms	Energy, J	Force, N	Time, ms	Energy, J	Force, N
Beta 4-5	2.0	11.45	12.50	424	2.62	3.57	681
Beta 2-4	2.0	12.14	14.25	587	2.46	3.74	760
Beta 2-5	2.0	13.96	16.80	557	3.01	4.59	765
Beta 3-1	2.0	12.53	14.06	571	2.72	3.86	723
Mean		12.5	14.4	535	2.7	3.9	732
S.D.		1.1	1.8	75	0.2	0.5	39

Specimen number	Plateau whole			Plateau step		
	Time, ms	Energy, J	Force, N	Time, ms	Energy, J	Force, N
Beta 2-4	9.81	10.19	529	9.81	10.20	529
Beta 2-5	8.83	8.83	500	7.67	8.23	537
Beta 3-1	9.68	10.51	543	9.68	10.51	543
Beta 4-5	10.95	12.20	557	10.09	11.72	580
Mean	9.8	10.4	532	9.3	10.2	547
S.D.	0.9	1.4	24	1.1	1.4	23

Specimen number	Standard		
	Time, ms	Energy, J	Force, N
Beta 2-4	8.14	8.43	526
Beta 2-5	7.44	8.07	542
Beta 3-1	7.89	8.80	557
Beta 4-5	8.66	10.15	586
Mean	8.0	8.9	553
S.D.	0.5	0.9	26

Appendix Six

TDCB Durability Tests, Example Results

The Table below shows TDCB fatigue test data using steel adherends bonded with the 'AV119' adhesive. Tests conducted 'dry' at 5 Hz, using $u_{min}/u_{max} = 0.5$.

Cycles	Crack length, mm	log(da/dN), mm/cycle	G_{max}, J/m^2	log(G_{max}), J/m^2
1250	127.39	-2.570	296.5	2.472
3670	133.90	-2.894	263.4	2.421
7740	139.10	-3.135	248.3	2.395
10100	140.83	-3.131	239.4	2.379
11628	141.96	-2.760	233.1	2.368
12820	144.03	-3.200	227.2	2.356
16800	146.54	-3.595	220.9	2.344
20340	147.44	-3.114	217.6	2.338
22720	149.27	-3.142	214.7	2.332
24425	150.50	-3.235	210.5	2.323
26780	151.87	-3.588	206.2	2.314
28600	152.34	-3.086	202.7	2.307
30210	153.66	-3.296	199.7	2.300
31810	154.47	-2.902	198.0	2.297
32680	155.56	-3.648	196.0	2.292
34460	155.96	-3.738	193.1	2.286
36650	156.36	-3.943	190.6	2.280
38230	156.54	-3.249	188.5	2.275
40520	157.83	-3.828	186.9	2.272
41530	157.98	-5.077	185.3	2.268
43920	158.00	-3.299	183.9	2.265
46430	159.26	-3.542	180.5	2.256
59760	163.09	-4.305	175.1	2.243
66820	163.44	-3.393	170.4	2.232
74410	166.51	-4.074	163.7	2.214
94320	168.19	-4.114	139.3	2.144

383800	190.43	-4.475	120.4	2.081
399910	190.97	-5.794	119.3	2.077
418600	191.00	-5.453	117.8	2.071
449800	191.11	-4.159	116.8	2.068
473860	192.78	-5.892	116.3	2.066
489440	192.80	-4.187	115.6	2.063
511910	194.26	-4.832	114.7	2.060
524820	194.45	-4.937	106.8	2.028
1671490	207.72	-5.609	99.1	1.996
1728430	207.86	-5.836	98.6	1.994
1762720	207.91	-5.205	98.3	1.993
1817240	208.25	-5.069	97.6	1.989
2104240	210.70	-5.556	96.6	1.985
2165360	210.87	-5.047	96.0	1.982
2283520	211.93	-5.093	95.2	1.979
2533950	213.95	-5.410	94.0	1.974
2685520	214.54	-5.405	93.0	1.968
2964860	215.64	-5.014	91.0	1.959
3110410	217.05	-5.392	89.4	1.951
3401680	218.23	-5.502	89.6	1.952
3544720	218.68	-8.061	87.3	1.941
4695980	218.69	-6.968	84.2	1.925
4788790	218.70	-6.956	83.8	1.923
4879180	218.71	-6.798	84.2	1.925

Appendix Seven

Bonded Lap Joint Test Results

Table A7.1: Constant displacement rate test results, steel single lap joints bonded with 'AV119' adhesive. Tests conducted at crosshead speed of 0.5 mm/min.

Specimen number	Joint width, mm	Overlap length, mm	Bonded area, mm^2	Bondline thickness, mm	Failure load, N	Failure stress, MN/m^2	Average. stress, MN/m^2
SL 1-1	25.61	12.69	324.99	0.44	8400	25.85	
SL 1-2	25.49	11.91	303.59	0.42	7700	25.36	25.61
SL 2-1	25.61	12.64	323.71	0.42	7400	22.86	
SL 2-2	25.52	12.63	322.32	0.42	7300	22.65	22.75
SL 3-1	25.60	12.55	321.28	0.36	8600	26.77	
SL 3-2	25.63	12.60	322.94	0.37	8300	25.71	26.23
SL 4-1	25.41	12.42	315.59	0.43	6600	20.91	
SL 4-2	25.81	12.42	320.56	0.41	6820	21.28	21.09
Average	**25.59**	**12.48**	**319.37**	**0.41**	**7640**	**23.93**	
S.D.	0.12	0.25	6.97	0.03	743	2.26	

Table A7.2: Results of single lap joint fatigue tests, steel adherends bonded with 'AV119' adhesive. Tests conducted immersed in distilled water at 28°C at a frequency of 5 Hz and using $P_{min}/P_{max} = 0.5$.

Specimen number	% of nominal failure stress	Cycles	Log cycles	Failure ?
SL 1-8	90	478	2.68	Yes
SL 2-8	90	744	2.87	Yes
SL 1-4	80	1402	3.15	Yes
SL 2-7	80	2782	3.44	Yes
SL 2-3	70	3764	3.58	Yes
SL 3-3	70	1854	3.27	Yes
SL 1-7	60	9744	3.99	Yes
SL 3-4	60	4294	3.63	Yes
SL 1-5	50	19143	4.28	Yes
SL 2-4	50	79061	4.90	Yes
SL 1-6	40	101233	5.01	Yes
SL 3-7	40	183391	5.26	Yes
SF 5-5	37.5	992900	6.00	Yes
SF 5-6	37.5	8749680	6.94	No Failure
SL 2-5	35	586150	5.77	Yes
SF 5-2	35	6894100	6.84	No Failure
SF 5-3	35	15172990	7.18	No Failure
SF 5-1	31.5	1000000	6.00	No Failure
SL 1-3	30	354100	5.55	Yes
SL 3-6	30	2820000	6.45	Yes
SL 3-8	30	556400	5.75	Yes
SL 4-3	30	13497040	7.13	No Failure

Table A7.3: Lap joint lifetime prediction, fracture energies calculated using analytical and finite element approaches, (a) analytical approach, and (b) finite element approach. Applied load 183 kN/m, equivalent to 60% of the nominal failure stress measured from constant displacement rate tests.

(a) Analytical approach.

Crack length, mm	Fracture energy, G_{max}, J/m^2 Analytical
0	233.0
1	246.5
2	261.0
3	277.5
4	295.0
5	314.5
6	336.0
7	359.5

(b) Finite element approach.

Crack length, mm	Fracture energy, G_{max}, J/m^2		
	Cohesive-in-adhesive		Interfacial
	Two cracks	One crack	Two cracks
0.085	31.5	31.5	1.3
0.169	82.1		
0.254	119.0		
0.42	154.0	150.9	99.5
0.85	175.9	168.5	167.0
1.7	202.0	179.3	
2.54	224.3	191.6	244.6
3.4	276.9	207.7	291.2
4.33	368.1		
5.08	713.3	241.9	713.4
6.77		292.2	

Appendix Eight

Bonded Component, Fatigue Results

Fatigue data from bonded component test, showing number of cycles, crack length, maximum measured load, and calculated rate of crack growth, log(da/dN).

Cycles	Crack length, mm		Maximum load, N	Log(crack growth rate), mm/cycle	
	Side A	Side B		Side A	Side B
610	78.05	78.71	1338		
2430	78.05	80.41	1199		-3.030
3200	78.05	84.46	1167		-2.280
5600	78.05	93.55	1093		-2.422
7000	78.05	99.47	1065		-2.374
7700	78.05	101.04	992		-2.649
8600	92.36	104.39	925	-1.799	-2.429
9900	95.15	105.09	870	-2.668	-3.269
10700	95.21	106.38	852	-4.125	-2.793
12200	98.42	109.77	814	-2.670	-2.646
13600	99.37	109.76	790	-3.168	
15000	101.41	111.35	768	-2.836	-2.945
16800	102.64	113.77	736	-3.165	-2.871
18800	102.96	114.77	709	-3.796	-3.301
20800	104.63	116.26	692	-3.078	-3.128
23800	108.27	118.37	672	-2.916	-3.153
28000	110.01	119.25	650	-3.383	-3.679
30450	111.21	119.86	640	-3.310	-3.604
36000	112.73	122.64	623	-3.562	-3.300
40500	113.98	122.41	609	-3.556	
50700	115.11	123.54	589	-3.956	-3.956
64700	118.15	127.22	568	-3.663	-3.580
83400	120.11	129.91	542	-3.980	-3.842
125700	123.19	132.5	501	-4.138	-4.213
422100	136.73	145.1	402	-4.340	-4.372

1000440	146.07	151.99	331	-4.792	-4.924
1054000	145.98	154.3	329		-4.366
1337600	150.24	158.52	318	-4.823	-4.827
1411720	150.31	158.68	316	-6.025	-5.666
1800500	151.61	159.6	317	-5.476	-5.626
2198000	153.9	160.85	316	-5.240	-5.5027
2683000	155.75	161.54	302	-5.419	-5.847

Appendix Nine

Publications

Papers

Taylor, A.C., Blackman, B.R.K., Kinloch, A.J., and Wang, Y., *The Impact Testing of Adhesive Joints*, in Proceedings of *Structural Adhesives in Engineering IV*, Bristol. 1995, Institute of Materials: London.

Taylor, A.C., Blackman, B.R.K., Kinloch, A.J., and Wang, Y., *The Impact Testing of Adhesive Joints*, in Proceedings of *Nineteenth Annual Meeting of the Adhesion Society*, Myrtle Beach, USA. 1996, Adhesion Society: Blacksburg, USA.

Taylor, A.C., Blackman, B.R.K., Curley, A., Kinloch, A.J., and Wang, Y., *Impact Testing, Durability and Lifetime Prediction of Adhesive Joints*, in Proceedings of *Stress Analysis and Fracture in Adhesive Joints*, London. 1996, Institute of Materials: London.

Taylor, A.C., Kinloch, A.J., and MacGillivray, H.J., *Instrumentation of an Impact Test for Adhesive Joints*, in Proceedings of *British Society for Strain Measurement Annual Conference*, Exeter. 1996, British Society for Strain Measurement: London.

Kinloch, A.J., Blackman, B.R.K., Taylor, A.C., and Wang, Y., *The Failure of Adhesively-Bonded Joints under High Rates of Deformation*, in Proceedings of *EURADH '96*, Cambridge. 1996, Institute of Materials: London.

Reports

Taylor, A.C., *Impact Testing of Adhesive Joints, Interim Report*, Report, 1995, DTI MTS Adhesives Programme.

Taylor, A.C., *Impact Testing of Adhesive Joints, Final Report*, Report, 1996, DTI MTS Adhesives Programme.

Taylor, A.C., *Durability and Lifetime Prediction of Adhesive Joints, Final Report*, Report, 1996, DTI MTS Adhesives Programme.

BIBL. LONDON UNIV